Electronic and Adsorption Characteristics of Gaseous Molecules on Chemically Modified 2D Materials and van der Waals Structures

THESIS

Submitted in partial fulfilment

of the requirements for the degree of

DOCTOR OF PHILOSOPHY

by

Andru Sahithi

ID. No. 2018PHXF0413H

Under the Supervision of

Prof. K. Sumithra

BIRLA INSTITUTE OF TECHNOLOGY AND SCIENCE, PILANI

2024

BIRLA INSTITUTE OF TECHNOLOGY AND SCIENCE, PILANI

CERTIFICATE

This is to certify that the thesis titled "**Electronic and Adsorption Characteristics of Gaseous Molecules on Chemically Modified 2D Materials and van der Waals Structures**" submitted by **Andru Sahithi,** ID No **2018PHXF0413H** for award of Ph.D. of the institute embodies original work done by her under my supervision.

Signature of the Supervisor: K Sumitra.

Name in capital letters: PROF. K. SUMITHRA

Designation: PROFESSOR

Date: 18-03-2024

Acknowledgment

I am pleased to take this opportunity to express my heartfelt gratitude towards all the people who have contributed to the compilation of this thesis, academically as well as personally. First and foremost, I would like to thank my supervisor, Prof. K. Sumithra. It gives me immense pleasure to express my deep gratitude to her for allowing me to work under her as a Ph. D student. I am thankful for her excellent guidance, valuable advice, and critical remarks regarding the scientific works. Constant encouragement and immense freedom from her side made the work environment productive yet very relaxing. Her scientific temperament and pursuit of excellence have been a vital source of inspiration for me.

I would like to thank many people who helped me during this entire tenure of my Ph.D. with their valuable time, suggestions, and encouragement. I acknowledge my doctoral advisory committee (DAC) members, Prof. Jayanty Subbalakshmi and Prof. Balaji Gopalan, for their support and encouragement. I thank DRC convener Dr. Tanmay Chatterjee and former DRC convener Prof. Durba Roy for their helpful insights and valuable suggestions.

I thank Prof. Sounak Roy, Head of the Department (HOD), chemistry, and the entire faculty for their valuable support. I thank Prof. Manab Chakravarty, former HOD, for his encouragement.

I owe my sincere gratitude to BITS-Pilani Vice-chancellor Prof. V. Ramgopal Rao, former Vice-chancellor Prof. Souvik Bhattacharyya, and Director Prof. G. Sundar, for allowing me to pursue and carry out my doctoral research work on this campus.

I would like to express my sincere thanks to Prof. V. V. Vamsi Krishna, Associated Dean. Academic-Graduate Studies and Research Division (Ph. D. program), and former Associate Dean Prof. Vidya Rajesh for their constant support and encouragement throughout my research. I thank Mr. Praveen, AGSRD, for his support and for sharing timely information regarding coursework and other details. Financial support from BITS-Pilani, Hyderabad

campus is gratefully acknowledged.

This work was only possible with the computational facilities at BITS-Pilani, Hyderabad Campus. I thank the central HPC facility at BITS-Pilani, Hyderabad Campus, for their servers and for providing new compute nodes on Sharanga. I gratefully acknowledge their help and support. I thank Dr. Mudit Dixit and his research scholar, Priti, for their help in learning new programs.

I was fortunate enough to work in the B102 lab with Santosh Ranga. I appreciate him for his company, assistance in various ways, and providing a cheerful environment to work. I thank my seniors, Singireddy Srinivas Rao and especially Hima Bindu Di, for their constant encouragement, guidance, and moral support.

Friends are God's beautiful gift to us. And I am blessed to have friends like Varun Yaddanapudi, Ravalika, Yogesh, Kaja Sravani, Meenu, Reeshma, and Nilanjana, who were always with me in difficult times. They always gave me moral support, and it was so relaxing talking to them whenever I felt low.

Ranga Santosh, and Singi Reddy Srinivas Rao, Hima Bindu were in contact with me even after completing their Ph. D and always gave me valuable suggestions, guidance, and support.

I thank my dear brother, Sainath Reddy Andru, for helping me learn about Linux codes and fixing programs.

Last but not least, at every step, the unconditional love and support of my loving Anudeep Reddy Gouru and my respected parents, Dr. Andru Surender Reddy and Andru Sridevi, made this work possible. They always supported me through thick and thin and encouraged me to achieve my goals. Ultimately, I give my regards to the Almighty with all humility, for blessing me with patience, the ability to work hard, and courage to complete this work.

Abstract

The detection of gas molecules employing various 2D materials and van der Waals (vdW) structures has attracted significant interest across several disciplines. One area of particular focus in solid-state gas sensor technology is using graphene-based materials for gas sensing applications. The exceptional characteristics of graphene-based materials, including large surface area, thermoelectric conduction, and mechanical strength, have generated significant enthusiasm for detecting diverse gaseous species. Earlier studies have shown that intrinsic graphene is almost inert to most gases.

Consequently, research efforts have been focused on developing strategies to enhance the sensitivity of graphene by appropriate modifications. Numerous theoretical and experimental studies have revealed that the gas sensitivity of graphene may be significantly improved by incorporating suitable dopants. This study investigates the impact of gaseous molecular adsorbates on the structural and electronic characteristics of both pristine graphene surfaces and graphene doped with various heteroatoms. This research aims to assess the influence of different dopants on the electronic properties of graphene, with the ultimate objective of understanding the adsorption of gaseous molecules on its surface.

This thesis employs first-principles DFT calculations using the Vienna *Ab initio* Simulation Package (VASP), with plane wave basis and pseudopotentials, to describe the interactions between graphene surface and adsorbate molecules. The study examines the adsorption of individual gas molecules on graphene surfaces and investigates the impact of doping on the reactivity of graphene toward various gas molecules. The analysis focuses on parameters such as adsorption energies, charge density distribution, electronic band structure, and density of states of the graphene-gas molecule adsorption systems.

The adsorption of gas molecules on doped graphene surfaces may be determined by analyzing and comparing the structural and electronic characteristics of the surface before and

after gas adsorption. This thesis deals with the adsorption behavior of several small gas molecules (CO, NH_3, N_2O, NO, NO_2, and O_2) on graphene doped with boron and nitrogen. A thorough investigation explored graphene's structural, energetic, and electronic characteristics doped with boron and nitrogen at varying concentrations. An insight into the changes made in the electronic band structure due to intrinsic and extrinsic doping and through a combined effect of both is discussed.

With this regard, the adsorption of these gaseous moieties is investigated on substitutionally p- and n-doped graphene surfaces, doped with various mole fractions and having different configurational patterns on the surface. Even though the electronic properties are modified with various mole fractions of doping, they do not show a systematic increase with the increase in the dopant concentration. It is attributed to the sub-lattice-induced symmetry breaking for the dopant configurations where equivalent lattice sites are occupied on the surface. An appreciable band gap opening, to a maximum of 0.59 eV can be achieved by doping in specific lattice configurations in graphene. It is further improved on molecular doping, with CO and NH_3, where an increase up to 0.83 eV is noted with the adsorption of ammonia on graphene with 9.37% of dopant concentration. While both the molecules are physisorbed on nitrogen-doped surfaces, carbon monoxide is strongly physisorbed, and ammonia molecules are chemisorbed on a few boron-doped surfaces, resulting in notable changes in the adsorption energy.

Therefore, it is clear that changes in the transport properties can be brought about by the adsorption of these molecules on such surfaces, and this study indicates the invaluable prospects of such doped surfaces as potential sensors for these molecules. The calculations also indicate that B-doped graphene can be an excellent gas-sensing platform for detecting NO and NO_2. The electronic effects produced by molecular adsorption of some environmentally

potent oxides of nitrogen, N_2O, NO, and NO_2 oxides on chemically modified graphene surfaces are investigated, employing spin-polarized density functional calculations.

The graphene surface is modified chemically with substitutional doping through boron, nitrogen, and co-doping with a few combinations of boron and nitrogen. In the case of adsorption of the paramagnetic species, NO and NO_2, rather exotic effects on adsorption are observed, with unusual electronic structures leading to flat bands in the band structure. The significant alterations of the electronic structure are primarily due to the adsorbate-adsorbent orbital mixing. The adsorption-induced dispersion-less flat bands are produced, eventually turning some doped, semiconducting surfaces into metallic ones. These dispersion-less bands are due to substantial interactions of the gaseous molecule with the surface, leading to the localization of the molecule over the surface. It is observed that with the adsorption of paramagnetic oxides of nitrogen, the flat bands are introduced between the valence and the conduction band, resulting in the loss of dispersion. For some of the configurational patterns, chemically driven adsorption of molecules onto the doped graphene surface is characterized by strong adsorption energies and charge transfers.

The density functional calculations of electronic and structural properties of the adsorption of dioxygen on boron-doped graphene surfaces are conducted using spin-polarized density functional theory methods, including van der Waals correction. The results show significant differences in the adsorption characteristics of singlet and triplet oxygen on boron-doped graphene surfaces. Both triplet and singlet dioxygen offer weak attraction to intrinsic and singly doped graphene. The singlet oxygen adsorption on doped graphene shows fascinating features involving chemisorption with dioxetane-type ring formation with appreciable charge transfer. In contrast, the triplet oxygen is only weakly physisorbed on the boron-doped surfaces.

Chemisorption of singlet oxygen occurs with noticeable charge transfer and leads to almost featureless band structures, while the triplet oxygen physisorption proceeds with a well-defined band structure. Chemisorption of the singlet oxygen is attributed to the enormous mixing of π^* of dioxygen and the p-orbitals of dopant and carbon. Because of the difference in adsorption characteristics, chemically modified graphene can be used to detect and trap singlet oxygen, which has potential applications in photodynamic therapy.

Adsorption on 2D vdW structures like bilayer graphene is also explored, and p-type doping is done with boron. The adsorption of ammonia on pristine AB stacked graphene bilayers and also on p-doped surfaces of bilayer graphene are investigated. Modifications of the adsorption interactions and electronic structure effects due to doping and adsorption of ammonia are discussed. The adsorption of NH_3 is investigated for different dopant concentrations and varied configurational patterns on the bilayer. Some bilayer configurations have strong interactions with ammonia depending on the dopant pattern, evidenced by appreciable binding energies and charge transfer. The chemisorption is confirmed by the strong mixing of the non-bonding p-orbitals of ammonia and with the electron-deficient p-orbitals of the surface. The theoretical results on doped bilayer adsorption energies are higher than adsorption on doped monolayer graphene by about 0.65 eV. The boron-doped graphene bilayer induces the donor state above the Fermi level, making it helpful in sensing ammonia gas. The changes in the electronic properties of the system due to the interactions are expected to give a proper understanding of the development of novel gas sensor devices based on these materials.

We use first-principles DFT calculations to explore the geometric and electrical properties of phosphorene sheets that have been substitutionally doped with the elements B, N, S, and Si in different patterns and concentrations. The number of valence electrons in dopant atoms is shown to have a profound effect on the electronic characteristics of phosphorene. Phosphorene doped with odd valence electrons to achieve a semiconducting nature, whereas

doping with even valence electrons imparts metallic character to the surface. The significant hybridization of s-p orbitals between dopants and phosphorene is responsible for this even-odd oscillation behavior. First-principles simulations are used to thoroughly examine the sensing capabilities of both natural and N-doped phosphorene substrates for adsorbing the toxic gases HCN and HNC. According to the calculations, pure phosphorene has the potential to be used as an outstanding HCN and HNC sensor due to its modest adsorption energy, good charge transfer, high sensitivity, and selectivity. In addition, N-doped phosphorene shows some moderately intense reactivity toward HCN and HNC gases, suggesting it may find use as a metal-free catalyst for catalyzing the activation of HCN or HNC adsorbates. Based on the data, the electronic attributes of phosphorene are significantly affected by the adsorption of HCN or HNC gas molecules. The phosphorene molecule is more sensitive to gas molecules along its zigzag direction than its armchair route. These findings provide a fascinating strategy for controlling the transport parameters of phosphorene-based optoelectronic devices.

The findings presented in this study provide a promising approach for modulating the band-gap of 2D materials and vdW materials by the incorporation of boron (B) and nitrogen (N) dopants, specifically by altering the dopant concentrations distributed in different patterns. It is further found to adsorb many toxic gases and, therefore, could be a potential sensor for these molecules. Therefore, this study has significant potential for developing graphene-based nanoelectronic devices in the future.

Table of content

List of Tables

List of Figures

Abbreviations

vdW	-	van der Waals
LCD	-	Liquid crystal displays
IC	-	Integrated circuits
TMDs	-	Transition metal dichalcogenides
2DLMs	-	Two-dimensional layered materials
2D	-	Two-dimensional
HBN	-	Hexagonal Boron Nitride
GO	-	Graphene oxide
rGO	-	Reduced graphene oxide
LDOS	-	Local density of states
CMOS	-	Complementary metal oxide semiconductor
GFETs	-	Graphene-based field effect transistors
E_F	-	Fermi level
CVD	-	Chemical vapor deposition
AFM	-	Atomic force microscopy
TEM	-	Transmission electron microscopy
HOPG	-	Highly oriented pyrolytic graphite
BZ	-	Brillouin zone
DOS	-	Density of states
CNTs	-	Carbon nanotubes
BP	-	Black phosphorus
FET	-	Field-effect transistor
DFT	-	Density functional theory
NEGF	-	Non-equilibrium Green's function method
QM	-	Quantum mechanical
CI	-	Configuration Interaction
LSDF	-	Local spin density functional
KS	-	Kohn-Sham
LDA	-	Local density approximation
HEG	-	Homogenous electron gas

GGA	-	Generalized gradient approximations
PBE	-	Perdew-Burke-Ernzerhof
KS-DFT	-	Kohn-Sham density functional theory
PAW	-	Projected Augmented Wave
PSPW	-	Pseudopotential plane-wave
US-PP	-	Ultra-soft pseudopotentials
LEDs	-	Light-emitting diodes
E_a /A.E	-	Adsorption energy
PDOS	-	Partial Density of States
ORRs	-	Oxygen reduction reactions
DMC	-	Diffusion Monte Carlo
PG	-	Pristine graphene
BG	-	Single boron doped graphene
DG	-	Defective graphene
BLG	-	Bilayer graphene
MG	-	Monolayer graphene
ALD	-	Atomic layer deposition
PMMA	-	Polymethylmethacrylate

Chapter 1

Introduction

1.1. Introduction

The material most frequently used currently in the semiconductor industry is crystalline silicon. It is the primary component of solar cells, liquid crystal displays (LCDs), and integrated circuits. Silicon qualifies as the fundamental component of directional, gate-controlled conducting devices in digital electronics due to its moderate band-gap of 1.11 eV at ambient temperature and a Fermi level that the extrinsic doping concentration can modify. The need to build denser logic components in integrated circuits has driven the downsizing of semiconductor transistors over the past few decades. However, scaling down Si semiconductors will surely provide challenges, including substantial subthreshold leakage, dangling bond-induced undesirable scattering, the diffraction limit in lithography tools, etc.

Consequently, transition metal dichalcogenides (TMDs) and graphene, two-dimensional (2D) materials, are introduced as potential alternatives for next-generation electronics [1]. Due to their covalent bonding between single-layered atoms, 2D materials are smooth and ultra-thin. The unique physical and chemical characteristics of atomically thin 2D materials have made them suitable for applications in ultra-thin transistors, highly responsive sensors, and spintronic devices [2].

There has been a significant interest in two-dimensional (2D) materials since the first successful separation of graphene sheets by micro-mechanical exfoliation of highly oriented pyrolytic graphite in 2004 [3]. Graphene, an ultra-thin layer consisting of a single sheet of carbon atoms arranged in a hexagonal crystal lattice, has exhibited significant potential in various fields, including electronics, photonics, energy conversion and storage, medicine, chemical and biological sensing, among others. It is primarily attributed to its intriguing array of exceptional physical, chemical, electrical, optical, thermal, and mechanical characteristics. Numerous experimental and theoretical studies have been conducted on gas sensors fabricated using graphene and its derivatives, including graphene oxide (GO) and reduced graphene oxide

(rGO) [4–7]. These investigations have consistently demonstrated the potential of graphene and its derivatives as highly effective sensing materials for advanced gas sensing systems. The remarkable performance of graphene, a 2D material, in gas sensing and several other applications, has sparked significant research interest in isolating additional 2D materials. These materials are characterized by their stacked layers in bulk crystals, which are firmly bonded together. These are explored to understand their prospective uses.

Many distinct 2D materials exhibiting exceptional characteristics have been identified [8]. These materials encompass allotropes of diverse elements, such as graphene, silicene, germanene, phosphorene, etc. Compounds like TMDs, including MoS_2, $MoSe_2$, WTe_2, TaS_2, $TaSe_2$, and others, and germanane and hexagonal boron nitride (HBN), have also been studied. Two-dimensional materials exhibit favorable characteristics such as high optical transparency, exceptional mechanical flexibility, significant mechanical strength, and distinctive electrical properties. These attributes make them suitable for many applications in electronics and optoelectronics [9]. Using 2D materials has great potential in advancing gas sensors as they exhibit ultra-high sensitivity and exceptional selectivity. It is achieved by modifying the abundant surface chemistry of these materials while preserving their distinct optical and electrical characteristics.

Nevertheless, as indicated by the semiconductor industry roadmap, it is anticipated that traditional silicon-based electronics would face inherent constraints when operating at spatial scales smaller than 10 nm. Consequently, there is a need for alternate materials that may replace silicon to overcome these restrictions. Graphene, a two-dimensional carbon allotrope characterized by a honeycomb lattice structure, emerges as a prospective option for developing future electronic devices [3,10]. The material demonstrates ballistic transport at a submicron scale and may undergo substantial doping via either gate voltages or molecule adsorbates without compromising the mobility [3].

Furthermore, recent investigations [4] have shown the promise of graphene in solid-state gas sensors and the potential for detecting single molecules. One of the preliminary investigations on graphene has demonstrated the potential to introduce charge carriers to this material by adsorbing several gases such as NH_3, H_2O, and NO_2 [4]. The primary focus of this thesis is to elucidate the underlying physics governing the phenomena of doping and gas-sensing. These investigations aim to facilitate the enhancement of gas detection and electrical devices in future applications. The doping in graphene-related systems has garnered significant attention and research efforts in recent years [11]. Carbonaceous materials, including pristine graphene (PG), GO, and rGO, have shown notable gas sensing capacity, as evidenced by previous literature. Nanotechnology has facilitated remarkable advancements in oxide nanostructures, conducting polymers, carbon nanostructures, and 2D materials [12]. The improvement, as mentioned above, may be seen by the escalating quantity of scientific publications that have been published, as shown in Figure 1.1, with a notable surge occurring in recent years.

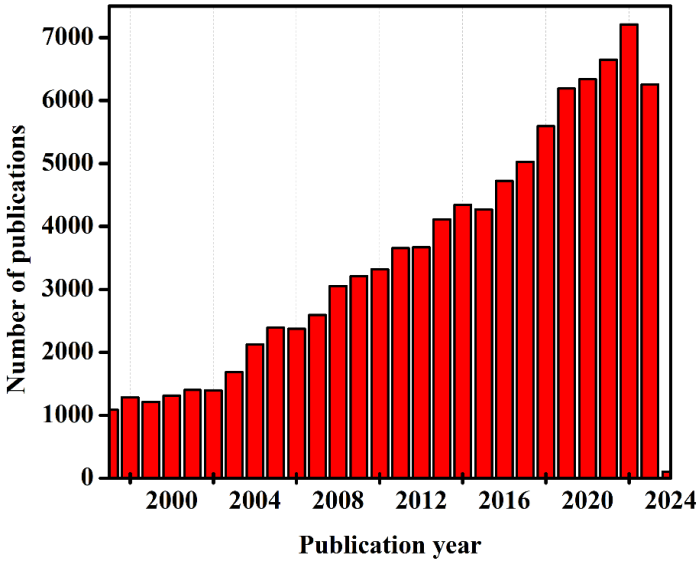

Fig. 1.1. The literature on gas sensing application of graphene from 1997 to present (a check of Scopus on November 08, 2023). The search terms are gas sensor.

The adsorption of gas molecules significantly influences electron transport through

graphene-based materials due to their two-dimensional structure [4,13]. The alteration in the electrical conductivity of graphene results from the adsorption of gas molecules on its surface. This change is attributed to the modification in the local carrier concentration caused by the surface adsorbates, which function as either electron donors or acceptors [4]. The various materials exhibit distinct electrical conductivity and diverse surface functional groups, significantly influencing the gas sensing method. For example, as pure graphene has high electrical conductivity even in the absence of charge carriers, few charge carriers produced by the gas adsorbates lead to considerable changes in charge carrier density, resulting in noticeable changes in electrical conductivity [4].

Some exciting reviews of 2D materials have explored their distinctive physical and chemical characteristics and applications [1]. Some of this research delves into the latest advancements in synthesis methods. It examines the diverse range of applications of these materials in various fields, such as electronics, optoelectronics, energy conversion, storage, and gas storage [1,14]. In recent years, there has been a notable increase in the investigations on gas sensors that use graphene and graphene-related materials. These investigations primarily concentrate on the characteristics of these materials concerning gas sensing, the underlying processes of sensing, and the many modifications employed to improve the sensing capabilities of graphene [15]. This chapter aims to provide a comprehensive overview of recent advancements in gas sensor studies, specifically focusing on utilizing graphene and other 2D materials as sensing materials. The primary focus is to study toxic gas adsorption on graphene and chemically modified graphene surfaces. This chapter elucidates the distinctive characteristics of 2D materials, namely graphene and phosphorene, which render them highly appropriate for potential use in gas sensor systems. Furthermore, this chapter also examines the adsorption behavior of different gas molecules on the above two-dimensional materials by computational investigations.

1.2. Two-Dimensional Materials for Gas Sensing

Two-dimensional materials refer to materials that consist of a single layer with a thickness of a few nanometers or less [8]. The extensive surface area shown by 2D materials offers many reactive sites, rendering them very effective in many applications such as sensing, catalysis, and energy storage technologies. The crucial significance of 2D materials in future gas detection systems is attributed to their vast surface area, large electrical conductivities, and low noise levels. The considerable alterations in electrical conductivity may be attributed to the minor variations in carrier concentration resulting from gas exposure, facilitated by the high electrical conductivity and little electrical noise. The combination of these characteristics, including the transfer of charge between gas molecules and these materials with the adsorption of gas molecules, renders these materials very appropriate for developing gas sensors [16].

The use of graphene and modified graphene as potential sensors for gaseous adsorbates has emerged as a prominent area of interest. The sensing capability of graphene may be ascribed to its planar structure, which offers exceptional characteristics, including a maximum surface area to volume ratio and a heightened sensitivity of electron transport on the adsorption of gas molecules [17]. The remarkable gas-sensing capabilities shown by graphene have prompted researchers to explore the gas-sensing properties of other two-dimensional materials. 2D materials such as MoS_2, ZnO, WO_3, CuO, NiO, SnO_2, etc., depend on electrical conductivity alterations resulting from their interaction with gaseous species [18,19]. This phenomenon arises from the induced charge transfer facilitated by gas molecules in the surrounding environment. Two-dimensional nanostructures, such as TMDs (for example, $MoSe_2$, WTe_2, TaS_2, $TaSe_2$, etc.), germanane, hexagonal boron nitride (BN), phosphorene, etc., have shown efficacy as sensing materials and have shown potential for use in the construction of gas sensors [18,19]. The essential characteristics of graphene and phosphorene are discussed in the following sections.

1.2.1. Graphene-Early history

The field of graphene research has experienced significant growth over the past decade, evolving into a well-established area that encompasses solid-state physics, materials science, and engineering [20,21]. Moreover, this research has generated considerable enthusiasm for exploring various two-dimensional layered materials (2DLMs) with distinct electronic properties [22,23]. Despite the numerous exceptional properties exhibited by graphene, which make it an outstanding platform for investigating low-dimensional physics and developing advanced electronic devices with atomically thin structures and unparalleled speed and flexibility, challenges still need to be addressed [24]. This study's primary focus and central objective is to enhance graphene's zero band-gap characteristic. The graphical representation of the electronic band structure of graphene is shown in Figure 1.2. The degeneracy of the P_x and P_y orbitals in Figure 1.2a is a consequence of the hexagonal symmetry inside the plane. The formation of sp^2 hybrid orbitals in the graphene plane occurs via the combination of the s-orbital with the degenerate P_x and P_y orbitals, resulting in σ bonds. The remaining P_z orbitals out of the sp^2 hybrid orbitals are responsible for forming π bonds perpendicular to the graphene plane. The P_z orbitals form bonding orbitals (π) and anti-bonding orbitals (π*) positioned below and above the Fermi energy level. These two bands possess a zero bandgap and intersect at a single point inside the momentum space, precisely at the Fermi energy.

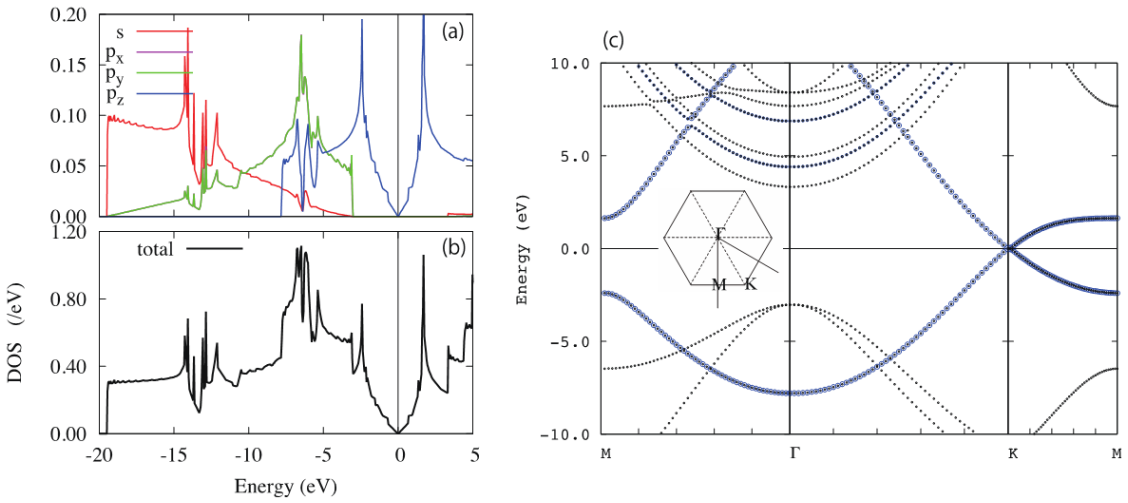

Fig. 1.2. (a) The figure represents the local density of states (LDOS) projected onto graphene's

s, P_x, P_y, and P_z orbitals. (b) The total density of states for graphene. The projected local density of states (LDOS) onto the P_x and P_y orbitals exhibits degeneracy. (c) The band structure of monolayer graphene. The blue lines in the diagram correspond to the wave functions associated with P_z orbitals. It is adapted from [25].

The band exhibits linearity in the vicinity of this point, resulting in an electron having an effective mass of zero. The term "Dirac point" is used to describe this particular point due to its resemblance to the band structure of a mass-less Dirac particle, as seen in the solution of the Dirac equation in the context of relativistic quantum mechanics. The Dirac point is essential in graphene physics, the significant characteristic of graphene results in high electron mobility. Theoretical calculations indicate that the mobility of graphene is estimated to be 1000 times greater than silicon. However, experimental observations suggest that the actual mobility is at least 100 times higher than the theoretical prediction. The substantial electron mobility graphene shows are a crucial factor contributing to its anticipated role as a prominent material for future nano-devices. The electronic characteristics of graphene are primarily influenced by the adsorption of atoms or molecules due to its two-dimensional nature, with the P_z-orbitals playing a significant role. The doping effect caused by some of the molecular adsorptions is interesting.

Nevertheless, most electrical applications are limited by the lack of a semiconducting band-gap in pristine graphene. For instance, the low static power consumption of complementary metal oxide semiconductor (CMOS) technology is lost in devices constructed of zero-bandgap, i.e., graphene, since they are more challenging to turn off. In terms of quantitative analysis, it has been shown that the I_{on}/I_{off} ratios of graphene-based field effect transistors (GFETs) are below 100 GHz. [26]. Hence, creating a substantial and finely-tuned energy bandgap in graphene poses a notable obstacle to developing graphene electron devices.

Hence, to harness the potential of this promising material for specific applications, it is

essential to exercise control over the characteristics of graphene. Extensive research has examined the regulation of charge carrier concentration by manipulating the Fermi level (E_F), also known as doping. As an atomically thin surface, graphene's Fermi level can be perturbed by interactions with many substances, including underlying substrates, and even minor environmental fluctuations. It can result in unintended and uncontrolled doping effects.

1.2.2. Synthesis of graphene

At present, graphene is synthesized by three distinct methods: micromechanical fracturing of graphite [27], epitaxial growth on SiC substrates, and chemical vapor deposition (CVD). Alternate approaches are also developed for the synthesis of graphene [26]. One of the ways used is the well-recognized old technique of micromechanical fracturing of graphite.

1.2.2. (a). Micromechanical Cleavage

The fundamental methodology for isolating a single layer of graphene rather looks straightforward, though it is not, for which the Andre Geim and Kostya Novoselov were awarded the Nobel Prize in Physics "for groundbreaking experiments regarding the two-dimensional material graphene". The process is often called micromechanical cleavage, exfoliation technique, or scotch tape method. It uses sticky tape to remove thin layers from three-dimensional graphite [3] delicately. Within these flakes, sheets with a single layer may be found. The graphene sheets are concealed in thousands of thick graphite flakes, making this search difficult. The process involves depositing these components onto a silicon substrate with a certain thickness and afterward using an optical microscope to locate the areas of graphene [16].

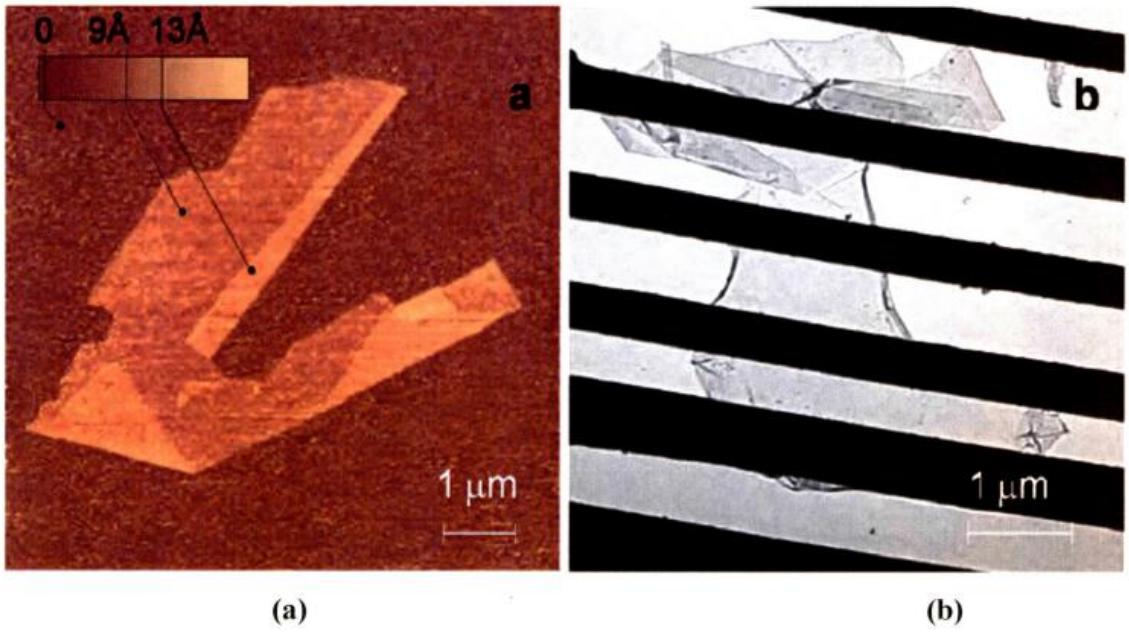

Fig. 1.3. (a) An atomic force microscopy (AFM) picture depicting a graphene flake on a SiCF substrate. (b) An image obtained by transmission electron microscopy (TEM) showcasing free-hanging graphene. The photographs were captured by the study group of Novoselov *et al.* [10] and copied from the same reference.

Geim *et al.*[3] used a mechanical exfoliation technique to produce graphene layers with a thickness of up to 10 pm. This method included the repetitive peeling tiny stacks of highly oriented pyrolytic graphite (HOPG). The above technique is determined to provide a high degree of reliability. Films with a thickness greater than 3 nm exhibited sizes of up to 100 pm, as shown in Figure 1.3., making them visible to the unaided human eye. Individual graphene patches may be identified based on their distinct coloration in contrast to regions containing multilayer graphite. Following the process of fine-tuning, this technology produces graphene crystallites of exceptional quality, with diameters reaching up to 100 pm which is generally sufficient for a wide range of research applications. The problem associated with this methodology is the need for graphene crystallites on the substrate. Scanning probe microscopy is inadequate for the investigation of graphene due to its limited throughput while scanning electron microscopy is deemed unsuitable due to the absence of distinct indicators for

determining the number of atomic layers. The approach described is often used to generate samples for research investigations.

1.2.3. Gas adsorption on graphene: An overview

There have been numerous experimental [4] and theoretical investigations [28–33] on the adsorption of gaseous molecules on pristine graphene. Several research groups used pristine graphene for sensing gas molecules such as CO_2, NH_3, NO_2, NO, N_2O, O_2, SO_2, H_2O, etc., [5,28,34–37]. The first micrometer-sized graphene sensor to detect gases at the ultimate concentration (single molecule level) at room temperature was shown by Schedin *et al.*[4] in their ground-breaking demonstration of graphene's single molecule sensitivity for NO_2 and NH_3. This micrometer-sized sensor could detect a single molecule of NO_2 even under a high vacuum environment. The basis for the functioning of graphene-based gas sensors is the variation in electrical resistivity brought about by the surface adsorbates, which take on the function of electron donors or acceptors and alter the local carrier concentration. It is found that electron acceptors, such as NO_2 and H_2O, and electron donors, such as CO and NH_3, can be distinguished by examining their impact on resistivity. Specifically, the resistivity decreases due to increased hole concentration caused by electron acceptors, while it increases due to heightened electron concentration caused by electron donors. The shown sensitivity, reaching the level of detecting individual molecules, highlights the significant promise of graphene in gas detection.

The increased sensitivity of pristine graphene to different gases may be ascribed to the chemical doping of graphene resulting from contamination of the graphene surface during device construction [14]. Furthermore, it is demonstrated that the inherent sensitivity of pristine graphene remains modest even when exposed to potent adsorbates. Ko *et al.* [38] have fabricated a NO_2 gas detector using intrinsic graphene as the sensing material. The graphene layers, obtained by mechanical exfoliation with a thickness ranging from 3.5 to 5 nm, are

deposited on a SiO_2/Si substrate. This sensor exhibited rapid response, excellent selectivity, reliable repeatability, reversible behavior, and high sensitivity (with a ratio of around 0.09) when exposed to 100 parts per million of NO_2 gas at room temperature. However, when exposed to elevated temperatures, the surface becomes unsuitable for detecting these gases, limiting its use as a sensor.

In their theoretical investigations employing first-principles simulations based on density functional theory (DFT) computations, Leenaerts *et al.* [35] studied the interactions between pristine graphene and several gas molecules, including H_2O, NH_3, CO, NO_2, and NO. They have found that gaseous adsorbates like carbon monoxide (CO), ammonia (NH_3), nitrogen dioxide (NO_2), water (H_2O), and nitric oxide (NO) exhibit physical adsorption on the surface of intrinsic graphene. Furthermore, the investigation of charge transfer shows compatible data with the experimental observations made by Schedin *et al.* [4], as shown in Table 1.1.

Table 1.1. The already established adsorption energy values and charge transfers of different gas molecules on intrinsic graphene. The data is obtained from the studies of Schedin *et al.* [4] and Leenaerts *et al.* [35].

Type of gas	Adsorption energy (eV)	Charge transfer (e)	reference
NH_3	0.031	0.027	[4]
H_2O	0.047	−0.025	[35]
NO_2	0.067	−0.099	[35]
CO	0.014	0.012	[4]
NO	0.029	0.018	[35]

These molecular adsorptions may result in either n-type or p-type doping of graphene. Notably, NO_2 induces a significant p-type doping effect, while the NO molecule, despite its similarities

with NO_2, results in n-type doping. The observed discrepancy may be attributed to the reciprocal influence of charge donation and back-donation between the graphene and the adsorbates [35]. However, in contrast to the pronounced acceptor properties of NO_2, the dimer N_2O_4, which is often present in the gaseous form due to its equilibrium, exhibits only a modest donor behavior. Consequently, the adsorption of N_2O_4 on graphene does not result in a substantial doping impact, as shown by previous studies [39].

The precise and effective control of n-type or p-type doping in graphene, brought about by molecular adsorption, enables the desired charge carrier concentration and opens up numerous potential applications. These include photodetectors, photovoltaics, sensors, organic light-emitting diodes, organic thin-film transistors (OTFTs), supercapacitors, catalytic applications, etc. Fermi level engineering is a common practice in which introducing or removing electrons in graphene leads to n-type or p-type doping, respectively [40].

1.2.4. Gas adsorption on chemically doped graphene: An overview

Graphene has a unit cell with two atoms, consisting of the A and B sites, as shown in Figure 1.4a. However, it should be noted that the graphene lattice does not conform to the definition of a Bravais lattice when considering the carbon atoms as indistinguishable. In the context of pristine graphene, the Fermi energy is a boundary that distinguishes the valence and conduction bands at the Dirac points. Consequently, graphene may be classified as a semi-metal or semiconductor without a band-gap, exhibiting an extremely low density of states around the Fermi level. Several methods have been identified to modify the concentration of charge carriers, including introducing charged impurities via doping, applying an electric field, changing temperature, and adsorption of atoms and molecules [5,41,42]. Although the absolute changes in electron density may be relatively small, introducing dopants in graphene, either through extrinsic means such as substrate or adsorbate interactions or through intrinsic effects like doping of the graphene itself, can result in significant alterations in conductivity [42].

These changes can occur even as the carrier mobility undergoes modifications.

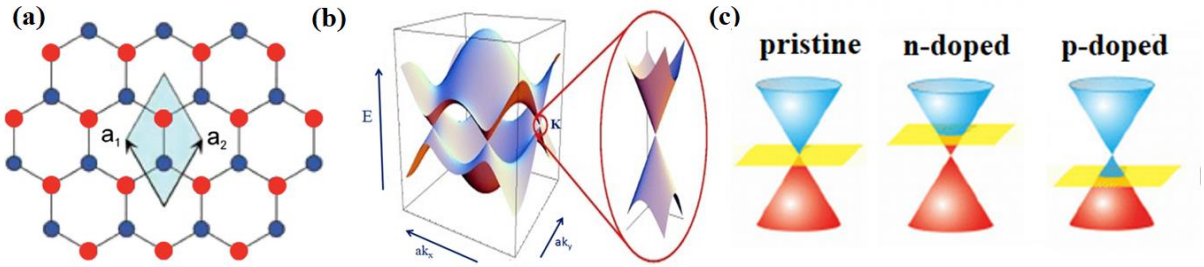

Fig. 1.4. (a) The honeycomb lattice structure of graphene can be characterized by a unit cell composed of the unit vectors a1 and a2, along with a diatomic basis consisting of atoms A and B; (b) The band structure of graphene has been computed, revealing the presence of occupied states and unoccupied states. These states intersect each other at six specific points, known as K-points, within the first Brillouin zone (BZ); (c) In the vicinity of the K-points and the Fermi level, the band structure of graphene can be simplified, allowing for an examination of the charge carrier's concentration dependence. Introducing either n-type or p-type doping may result in generating charge carriers that exhibit electron-like or hole-like behavior. This Figure is adapted from reference [5].

Although molecular adsorption gives graphene an extrinsic doping effect, pure graphene does not significantly alter its electronic characteristics even after the adsorption of these gaseous molecules, limiting the material's device-based applications. Different methods have been used to improve the semiconducting characteristics of graphene by altering its band-gaps to create high-performance graphene devices. A practical method for adjusting graphene's electronic characteristics is doping. The sp^2 hybridization of carbon atoms is affected by substitutional doping of graphene with other atoms (e.g., B, N, and B-N co-doping). In an intrinsic modification of graphene, there are two primary strategies. The first involves the replacement of carbon atoms with heteroatoms, while the second entails the introduction of dopants by physical or chemical adsorption onto the surface of graphene [43].

The stability of substitution with heteroatom in graphene is primarily attributed to the

covalent bond formation between the dopant and the graphene lattice. This substitution process may disrupt graphene's distinctive honeycomb structure, leading to defects and disorder [44]. This phenomenon leads to a reduction in electronic mobility, resulting in a decline in the operational efficiency of electronic equipment. On the other hand, the replacement of interacting dopants with graphene induces a localized disturbance in the graphene structure, therefore achieving the intended doping effect [11]. Various dopants have been incorporated into graphene, including sulfur (S), phosphorus (P), selenium (Se), oxygen (O), silicon (Si), iodine (I), as well as metals. The inclusion of dopants such as chromium and manganese increases the sensitivity of pristine graphene towards SO_2, which has been investigated by Shao et al. [45].

Graphene subjected to modifications by introducing defects and incorporating transition metal dopants, such as Ca, Co, and Fe, has shown a significantly enhanced affinity towards H_2S [46]. The high interaction energies of the order of -2 eV between transition metals and hydrogen sulfide (H_2S) result in significant alterations in graphene's electronic and magnetic characteristics. In another research using DFT, it was observed that the introduction of transition metals, such as Fe, Co, Ni, Ru, Rh, Pd, Os, Ir, and Pt, into graphene, resulted in the chemisorption of O_2 onto the transition metal-doped graphene [47]. The study found that graphene doped with titanium (Ti) showed significant adsorption energies, ranging from -1 eV to -4 eV, with several gas molecules, including carbon monoxide (CO), nitrogen oxide (NO), sulfur dioxide (SO_2), and formaldehyde (HCHO), in comparison to pristine graphene and defective graphene [48].

In contrast, boron and nitrogen have gained significant interest from the scientific community due to their atomic radii, which resemble carbon in size. It is anticipated that the lattice will maintain its structural integrity. Graphene is often subjected to doping with boron (B) [49] and nitrogen (N) [50] due to their comparable atomic radii (B: 87 pm; N: 56 pm) to

that of carbon (C) (67 pm), which allows for the preservation of the planar geometry [40]. A theoretical study [40] has shown that the band-gap of graphene may be effectively modified by substitutional doping, wherein carbon atoms are replaced with boron or nitrogen atoms. This substitution induces distinct p-type or n-type semiconductor properties in the material. Nitrogen, the first dopant incorporated into graphene, has been extensively used to generate n-type conductivity, therefore serving as a crucial component in advancing microelectronic gadgets. From an electrical perspective, boron may be seen as the contrasting counterpart of nitrogen due to its lower electronegativity, which is even lower than carbon.

Consequently, boron can produce p-type conductivity in graphene. While the inclusion of boron, akin to nitrogen, can induce intriguing chemical and electrochemical behavior in the basal plane of graphene, the investigation of boron-doped graphene (BG) has progressed at a slower pace compared to nitrogen-doped graphene (NG). Only recently has the research on BG caught up in synthesis methodologies, examination of physicochemical characteristics, and practical utilization in various applications.

The sensitivity of graphene-based gas sensors has been significantly enhanced by introducing defects and dopants, as shown by the theoretical studies above. This enhancement is attributed to the more significant adsorption of gas molecules on defective and doped graphene than pristine graphene [15]. Employing DFT simulations, Zhang *et al.* [15] investigated the interactions between several small gas molecules, including NO_2, CO, NO, and NH_3. There are modified forms of graphene, including boron-doped graphene (BG), nitrogen-doped graphene (NG), and defective graphene (DG). These gas molecules exhibited more pronounced interactions with the modified graphene structures (BG, NG, and DG) than pristine graphene. The adsorption energies of gas molecules on modified graphene are higher than on pristine graphene.

The investigation of formaldehyde adsorption on graphene modified with dopants such

as B, N, S, and defects has revealed that vacancy-defected graphene is a favorable option for the precise detection of formaldehyde [51]. Though the defective and S-doped graphene have shown encouraging outcomes, some drawbacks exist. Specifically, S-doping leads to structural deformation, whereas defects do not exhibit the anticipated level of response. Numerous software tools based on DFT are used to investigate gaseous molecules' adsorption behavior on graphene surfaces [15,52]. Most of these experiments demonstrate pronounced chemisorptive behavior, resulting in comprehensive modifications to the electronic characteristics of graphene.

Nevertheless, it is anticipated that the metallic nature of a semi-metal, when doped with a transition metal or a metal, would persist, rendering it unsuitable for use in semiconductor-based sensing devices. Graphene, when doped with boron (B), nitrogen (N), or silicon (Si), has shown significant sensing capabilities towards a wide range of commonly encountered gases, including hydrogen (H_2), water vapor (H_2O), oxygen (O_2), carbon dioxide (CO_2), carbon monoxide (CO), nitrogen dioxide (NO_2), nitric oxide (NO), sulfur dioxide (SO_2), ammonia (NH_3), and nitrogen (N_2) [52]. Further, the modulation of charge carrier type and density may be achieved by doping at several locations with distinct mole fractions [40]. The adsorption of various small gaseous molecules on pristine and modified graphene by doping are discussed below.

1.2.4. (a). H_2O adsorption on graphene

Graphene exhibits p-doping due to the adsorption of H_2O and O_2 in the atmosphere [5]. However, theoretical investigations by Wehling *et al.* [39] indicate that intrinsic graphene does not exhibit sensitivity towards water molecules. It is suggested that the process of doping graphene with water molecules necessitates the presence of strongly orientated H_2O clusters [35]. Water molecules have a higher chance of adsorption in the carbon rings' central positions and on bridge sites located between two carbon atoms [35]. The sensitivity of graphene to its

surrounding environment is determined by the behavior of its π electrons, which are immediately exposed to molecules present in the ambient surroundings. The adsorption of ammonia, atomic hydrogen, fluorine, and chlorine is expected to exhibit a distinct preference for top adsorption sites, in contrast to the above phenomenon.

The interactions between water and graphene indicate that applying graphene as a coating does not result in substantial modifications [53]. The minor impact of graphene on wetting behavior may be attributed to its thin atomic structure, uniform composition, and lack of reactivity. This combination of properties can be compared to a "transparency" towards surface wetting, and therefore, graphene can be used as a covering material. This finding is substantiated by research on the hydration of graphene [54], which further demonstrated the impermeability of water molecules through a graphene layer [55]. Hydroxyl ions exhibit a size that exceeds the permissible limits for penetration through the graphene film.

A*l*-doping [56] has shown potential benefits in transforming the hydrophobic nature of graphene into a hydrophilic one. At ambient temperature, the presence of A*l*-doped graphene leads to a significant reduction in the dissociative barrier of H_2O molecules on the graphene surface. This alteration in the electronic properties of graphene results in a spontaneous transition in its wettability from hydrophobic to hydrophilic and preserves its conductivity. The above phenomenon operates because aluminum (A*l*) may enhance the dissociative adsorption of water (H_2O) on graphene through hybridization between its p orbital and the 1b1 orbital of the H_2O molecule. The impact of A*l*-doping on the dissociative adsorption of H_2O molecules on graphene is being investigated to assess the potential use of graphene as an electrode material for supercapacitors and biomaterial supports. It is particularly relevant in applications where hydrophilic and conductive graphene is desired.

1.2.4. (b). NH_3 adsorption on graphene

Multiple experiments have provided evidence that the adsorption of NH_3 on graphene often

results in n-type doping [57]. According to theoretical investigations, NH_3 has been identified as a significant electron donor, exhibiting an electron transfer to graphene (0.03e) [35]. This electron transfer is comparatively higher than that of other electron donor molecules like CO [15]. However, it is essential to acknowledge that the adsorption geometry plays a crucial role in this phenomenon. Additionally, the correlation between ammonia and graphene, facilitated by the creation of many p-n-p connections, is shown to be significantly influenced by the number of graphene layers [58]. It is found that graphene flakes with a few layers had a much greater reaction to ammonia adsorption than single-layer graphene, with a difference in magnitude ranging from 1 to 8 orders of magnitude [58].

The ammonia molecules show weak physical adsorption onto the pure graphene [34]. It may be attributed, at least in part, to the weak van der Waals interactions between ammonia and graphene [35]. Furthermore, it is noteworthy that the minimum distance observed between the adsorbed molecule and graphene is 3.17 Å respectively. This distance suggests that pure graphene has limited effectiveness in ammonia adsorption. Chemical doping is used to enhance the suitability of graphene for ammonia adsorption. Numerous investigations have been conducted on the surfaces of graphene doped with transition metals. However, a drawback associated with incorporating transition metal dopants in graphene is their tendency to induce metallic behavior to the graphene surface, resulting in increased adsorption energies that ultimately modify the physical characteristics of the surface [59]. To address this limitation, the graphene material is subjected to substitutional doping with boron and nitrogen [60]. The results of this modification revealed that boron-doped graphene has favorable characteristics for ammonia sensing [60].

1.2.4. (c). CO adsorption on graphene

It is found that carbon monoxide (CO) is adsorbed onto graphene by physisorption [35]. The carbon monoxide (CO) molecule consistently functions as a donor. The capacity of CO

adsorption can be significantly increased by doping graphene with aluminum (A*l*) [56]. A significant alteration in electrical conductivity is observed, which is attributed to the change in electrical conductivity due to the introduction of a substantial number of shallow acceptor states resulting from the absorption of CO. Therefore, the A*l*-doped graphene material exhibits promising potential for CO gas sensing [56], as the adsorption of CO induces a significant structural modification in A*l*-doped graphene, resulting in the protrusion of the A*l* atom from the graphene plane by approximately 1.38 Å. However, few studies show that carbon monoxide (CO) on transition metal-doped graphene surfaces is not universally stable. It is found to be stable on osmium (Os) and iron (Fe) doped graphene surfaces [61].

However, a significant challenge associated with introducing transition metal dopants into graphene is the complete modification of its transport characteristics and strong adsorption energies. Doping of graphene with boron and nitrogen is considered to be the most stable for sensing of CO [60].

1.2.4. (d). NO_2 adsorption on graphene

Nitrogen dioxide (NO_2) and ammonia (NH_3) are well recognized as electron acceptor and donor species, respectively, and can potentially engage in charge transfer processes when interacting with graphene. There have been few investigations of the adsorption of these molecules on pristine graphene and its derivatives [62,63]. However, it has been shown that pure graphene-based sensors have certain limitations, such as low response signals, extended recovery time, and inadequate selectivity towards NO_2. These limitations have hindered the practical use of pristine graphene-based sensors [64]. Leenaerts *et al.* [35] studied the adsorption characteristics of NO_2 on pure graphene using DFT calculations. The results revealed a low adsorption energy of 0.067 eV and a charge transfer of -0.099 e, suggesting a weak interaction between NO_2 and pristine graphene [35]. In contrast, the use of noble nanoparticle doping has been shown as a straightforward and efficient approach for enhancing the NO_2 sensing by

graphene [15].

In a study conducted in 2019, Yang *et al.* [65] demonstrated that introducing group 10 transition metals into graphene significantly increased the sensitivity of the materials towards NO_2 and H_2S. Among the transition metals, Ni and Pt are renowned for their robust adsorption capabilities with NO_2 [65]. Another study demonstrated that NO_2 exhibits strong chemisorption on Ag-doped graphene and that significant Mulliken charge transfers occur from graphene to NO_2 [66]. Introducing a transition metal dopant onto the graphene surface results in an irreversible modification after the adsorption of NO_2 gas. This modified surface may then be used to detect additional gases. It is now established that boron-doped graphene exhibits optimal suitability for NO_2 adsorption due to the strong interaction between the boron (B) and nitrogen (N) atoms [67]. This interaction results in notably high adsorption energy of -1.37 eV and the formation of a tightly bonded B-N structure characterized by a bond distance of 1.67 Å. Additionally, this adsorption process involves a discernible charge transfer of 0.34e from the B-doped graphene to NO_2.

1.2.4. (e). NO adsorption on graphene

Surprisingly, whereas NO_2 generates rather significant p-type doping, the comparable NO molecule induces n-type doping. The charge transfers and back-donation interaction between graphene and adsorbates cause this difference [35]. The adsorption process of NO on pristine graphene exhibits the lowest exothermicity, with a value of -0.30 eV. Additionally, the distance between the NO molecule and the graphene sheet is measured to be 2.43 Å, suggesting that the interaction between NO and pristine graphene is physisorption. This finding resembles previous studies on NO adsorption on carbon nanotubes [68]. Zhang *et al.* [15] proposed that the enhancement of sensitivity and selectivity in sensors based on graphene may be significantly achieved by introducing dopants or defects into the graphene material. Graphene doped with boron and sulfur has promising potential as a sensor for detecting harmful gases,

namely NO and NO_2 [67]. In the context of boron-doped graphene, the considerable interaction between B and NO results in significantly enhanced adsorption energy (-1.52 eV) and a strong B-N bond (with a bond distance of 1.52 Å). This contact is followed by an observable charge transfer of 0.15e from NO to the graphene sheet. For the N-doped graphene, the adsorption energy is -0.40 eV, and the closest distance is 2.32 Å.

1.2.4. (f). N_2O adsorption on graphene

The N_2O, naturally present in the gaseous form at equilibrium, has a higher acceptor character than NO_2. However, N_2O works as a weak donor when adsorbed on graphene and does not result in a significant doping impact, as reported in previous studies [5]. The NO_2 molecule, characterized by a single, open-shell configuration, has a pronounced affinity for accepting electrons. Conversely, when N_2O is in its gaseous equilibrium form, it assumes a weak dopant role and has no substantial doping impact. In contrast to the paramagnetic monomer, the dimer N_2O lacks unpaired electrons and exhibits diamagnetic properties following its synthesis from two monomers. N_2O and NO_2 can induce p-type doping in graphene, but there is a significant difference. The individual open-shell monomer has a far higher affinity for accepting graphene electrons than the dimer. It is essential to acknowledge that while the DOS at the Fermi level is substantial, the dimer and the monomer lack Jahn-Teller activity due to the absence of orbital degeneracy [69].

1.2.4. (g). O_2 adsorption on graphene

Among the potential gas adsorbates/molecules, oxygen (O_2) holds considerable significance due to its ability to induce significant changes in material properties through doping [70]. Additionally, as the second most prevalent gas in the atmosphere, oxygen will impact the performance of devices in practical applications. Theoretical simulations have been done to study the interaction between O_2 molecules and O atoms with 2D materials [71]. However, the accuracy of the obtained adsorption energies has been compromised by conflicting results,

due to the inability of the approximation functionals used to describe the dispersion forces. It is crucial to understand the accurate value of the adsorption energy since it indicates the degree to which the adsorbate interacts with the 2D material and how much of its characteristics are changed.

The oxygen adsorption characteristics of graphene vary depending on the dopants. Oxygen adsorbs only weakly to boron and nitrogen-doped graphene surfaces, preventing the doped graphene's oxidation. Chemical adsorption of A*l*-, Si-, P-, Cr-, and Mn-doped species onto graphene has been reported [47]. The chemical adsorption of oxygen may alter doped graphene's electronic structure and local spin polarization. Specifically, the chemical adsorption of O_2 on Cr-doped graphene exhibits antiferromagnetic behavior [70]. It has been shown that the physical adsorption of O_2 molecules may occur on both graphene and N-doped graphene surfaces [70]. Also, oxygen undergoes chemisorption on defective graphene [72]. However, a significant drawback of defective graphene is its tendency to decrease the transport characteristics.

1.2.5. Bilayer graphene

The principle of bilayer graphene fundamentally diverges from the mere superposition of one layer of carbon atoms onto another. To comprehend the notable distinctions between bilayer and single-layer graphene, it is crucial to consider the relative locations, also known as stacking order, and the electron hopping energy between atoms in distinct layers [73]. Two prevalent forms seen in bilayer graphene are AA stacking and Bernal stacking. In the first scenario, the layers are arranged precisely aligned on top of the corresponding atoms in the other layer so that the atoms of both layers have identical lateral coordinates [74]. Conversely, in the second scenario, the top layer is displaced laterally with the bottom layer, referred to as AB-stacking [75]. The orientation and stacking order of bilayer graphene, as seen in Figure 1.5, have the potential to impact its electronic and optical characteristics. The AB bilayer graphene structure

consists of a hexagonal carbon lattice, whereby the top layer is composed of A atoms, and the bottom layer is designated as B atoms [76]. AB-stacking or Bernal stacking is the predominant arrangement in naturally occurring bilayer graphene samples [77]. Experimental observations have confirmed the existence of both stacking configurations [78]. It has been shown that AB stacking is energetically favored over AA stacking by a margin of 5 meV per carbon atom [76]. Furthermore, it is now possible to generate high-quality, large-area samples of this configuration [79]. The AA-stacked structure exhibits metallic properties, but the AB-stacked configuration has characteristics typical of a semiconductor material [80].

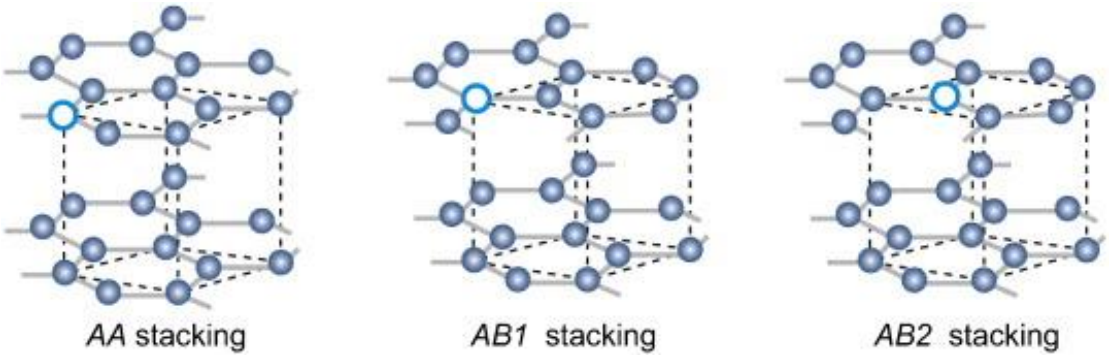

Fig. 1.5. Three distinct variations of bilayer graphene doped with boron and nitrogen are shown. Boron or nitrogen atoms are substituted at one carbon atom in the upper layer. The replacement sites containing boron and nitrogen atoms are shown by the open circles. This illustration is adapted from [81].

It is not unexpected that several characteristics of bilayer graphene exhibit similarities to those seen in monolayer graphene [82]. These characteristics encompass exceptional electrical conductivity, with room temperature mobility reaching up to 40,000 $cm^2\ V^{-1}\ s^{-1}$ in air [83]. The electrical properties can also be adjusted by modifying the carrier density through gating or doping [84]. Furthermore, they exhibit a high thermal conductivity, with a room temperature value of approximately 2800 $W\ m^{-1}\ K^{-1}$ [85]. These materials also possess mechanical stiffness, strength, and flexibility, with an estimated Young's modulus of around 0.8 TPa [86]. Moreover, they demonstrate high transparency, transmitting approximately 95%

of white light [87], exhibit impermeability to gases, and can be chemically functionalized [88]. Similar to monolayer graphene, bilayer graphene shows potential for various applications in different fields. These applications encompass transparent and flexible electrodes for touch screen displays, high-frequency transistors, thermoelectric devices, photonic devices such as plasmonic and photodetectors , energy-related applications like batteries, composite materials, etc. [89].

It is important to emphasize that bilayer graphene has characteristics that set it apart from monolayer graphene. Similar to a monolayer, an intrinsic bilayer lacks a band-gap between its conduction and valence bands. However, the low-energy dispersion in an intrinsic bilayer is quadratic, in contrast to the linear dispersion seen in a monolayer. Additionally, the quasiparticles in an intrinsic bilayer are characterized by their large chirality, as opposed to the massless nature of quasiparticles in a monolayer [90]. Bilayer graphene is considered the most minimal form of an intercalated material due to its two-layer structure [91]. The independent manipulation of individual layers in bilayer graphene can provide novel functions, such as the ability to modulate an energy band-gap of about 300 meV via processes such as doping or gating [92]. Recently, the band-gap has been used to fabricate devices using the technique of electrostatic confinement utilizing gates. Bilayer or multilayer graphene devices may be more advantageous than monolayer devices in situations where more material is needed to be used to enhance electrical or thermal conductivity, strength, or optical characteristics [93].

To date, a moderate body of literature exists about the investigation of boron and nitrogen-doped monolayer graphenes and nanotubes [15,52,94]. This research has been motivated by B, C, and N elements possessing comparable structural characteristics [95]. The effects of introducing a single boron or nitrogen atom into AB stacked bilayer graphene have been examined previously [81,96]. Previous research has shown that the energy required for boron and nitrogen doping is lower in the bilayer than in the monolayer [97]. It included doping

both the top and hollow sites, which refer to the position of the dopant atom relative to the other layer. It has been observed that similar electronic band structures are present for both sites. It is found that, the boron and nitrogen prefer hollow sites over top sites, with a difference in energy of 11 meV and 16 meV, respectively [97]. In AB stacked bilayer graphene, the total energy exhibits a notable decrease as the distance between the two dopant atoms increases when one nitrogen atom is present in each layer. Conversely, when doping is carried out using boron atoms, there is little to no observed dependency of the total energy on the distance [98]. The co-doping of boron and nitrogen in monolayer graphene is energetically advantageous when boron and nitrogen atoms are paired in the ortho position. Specifically, the energy difference between boron-nitrogen pairings in the ortho position and their next closest neighbors is around 20 meV, as reported earlier [99]. There has also been a study of bilayer graphene with a single boron atom in one layer and a single nitrogen atom in the other [100]. This study suggests that the electronic characteristics of this system are based upon the occupied sublattice rather than the relative distance between the atoms.

The modification of electronic characteristics in graphene and carbon nanotubes (CNTs) by the introduction of boron and/or nitrogen atoms has led to the use of chemically doped carbon nanomaterials for sensing gases [15,52,61,66,101]. Despite several theoretical studies on gas adsorption on impurity-doped monolayer graphene and carbon nanotubes, our current understanding of gas adsorption onto bilayer graphene still needs to be explored [81]. The impact of toxic gas adsorption on the energetics and electronic characteristics of single B-doped and single N-doped bilayer graphenes is done. Using first-principles electronic-structure calculations within the density-functional theory framework [102]. The adsorption of carbon monoxide (CO), carbon dioxide (CO_2), nitrogen monoxide (NO), and nitrogen dioxide (NO_2) are considered. These molecules do not show any affinity with the N-doped bilayer graphene. The adsorption of NO and NO_2 molecules onto B-doped bilayer graphene occurs via the

formation of chemical bonds, but CO and CO_2 molecules do not undergo chemical adsorption. Based on the analysis of the energy-band structures, it is shown that the NO and NO_2 molecules generate the presence of acceptor states positioned above the Fermi energy level. Simultaneously, the charge transfer occurs between the NO or NO_2 molecule and the B-doped graphene layer. In this scenario, electrons are transferred from the NO molecule to the B-doped graphene layer. On the other hand, with NO_2 adsorption, electrons are transported from the B-doped graphene layer to the NO_2 molecule [102]. The recent investigation of ammonia adsorption on p-doped bilayer graphene shows a strong interaction with ammonia depending on the dopant pattern and is evidenced by appreciable binding energies and charge transfer [102].

In general, the prospects for bilayer graphene and its derivatives in gas adsorption and sensing are favorable, with potential applications in gas storage and capture. There is still a significant amount of work to be undertaken to understand the impact of dopants on the adsorptive behavior of diverse non-toxic gases, including CH_4, H_2O, H_2, and O_2.

1.2.6. Phosphorene

Among the 2D vdW materials in recent years, black phosphorus (BP) nanostructures have gained attention as semiconductor nanomaterials due to their optical absorption, high carrier mobility, etc [103]. Inside the phosphorene layer, each phosphorus atom covalently bonds to three neighboring phosphorus, forming a puckered honeycomb structure similar to graphene, as shown in Figure 1.6 [103]. The surface possesses the inherent ultrahigh surface-to-volume ratio due to sp^3 hybridization, and the unique features make it a suitable candidate for the adsorption of gases. Moreover, it is flat enough to confine electrons so that charge flows quickly, with a relatively high mobility and chemical activity [103]. Due to these unparalleled features, the phosphorene may be superior to the many other 2D materials, for adsorption application. Furthermore, phosphorene's electronic structure and properties can be tuned via

substitutional doping. [104].

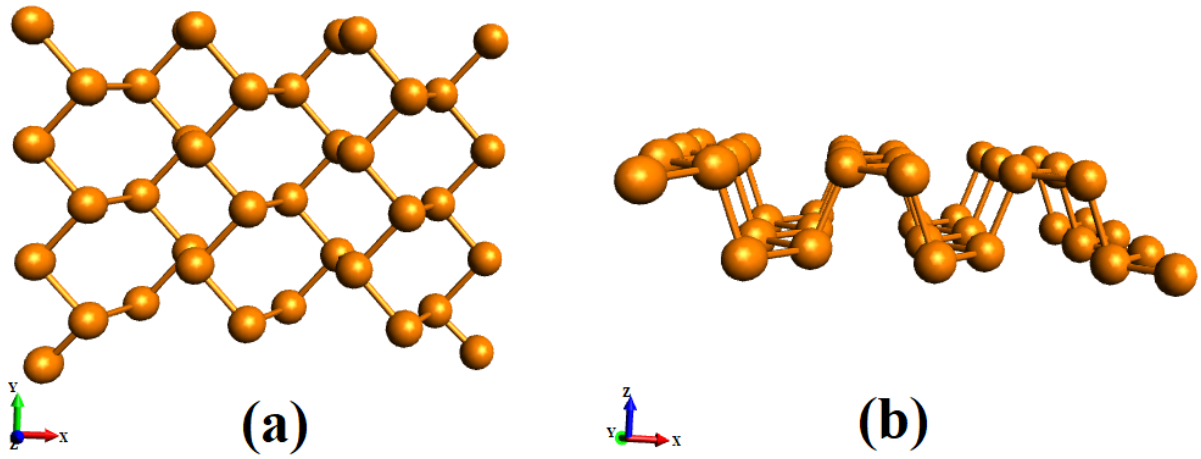

Fig. 1.6. The (a) top and (b) side view of the single-layer phosphorene structure represents armchair (AC) and zigzag (ZZ) along the x-axis and y-axis respectively.

In particular, small molecules such as CO_2, H_2O, NH_3, NO_2 and O_2 physisorbed in phosphorene have been investigated for applications in gas sensing, and the interactions are found to change the polarity and density of carriers [19]. Two-dimensional BP, which exhibits a high carrier mobility of about 1000 $cm^2\ V^{-1}\ s^{-1}$ and an adjustable direct band-gap, has gained greater acceptance compared to other two-dimensional semiconductors [105]. Moreover, phosphorene has other favorable characteristics, including anisotropic attributes and a substantial on-off ratio, therefore setting it apart from other two-dimensional materials [106]. Several disciplines have extensively acknowledged these outstanding properties, including transistors, photovoltaics, photocatalysis, solar cells, etc. [106]. The band-gap of phosphorene exhibits a high degree of sensitivity to variations in the number of atomic layers and external factors and falls within the range of 0.6–1.5 eV [107]. It also has enhanced ductility under x-axial stress, ultimately transitioning from a semiconductor to a metallic state. The above fascinating characteristics of phosphorene may contribute to its potential for developing innovative electronic devices. Pristine black phosphorus (BP) is inert towards greenhouse gases [108]. However, in order to expand its range of applications, defects and impurities may

be introduced which can significantly alter its electronic, thermal, and mechanical characteristics [109].

1.2.6.1. Anomalous doping effects on phosphorene

The adsorption characteristics of phosphorene can be improved by intrinsic and extrinsic doping [110]. Phosphorene exhibits p-type behavior and demonstrates enhanced stability by calcium doping. Ammonia (NH_3) has a high affinity for the Ca-doped BP structures when oriented along the armchair direction. It has been shown that including substitutional dopants with an odd number of valence electrons, such as those from group IIIA (boron), may effectively maintain the semiconducting properties of the material [111]. The semiconducting features and anisotropic transport properties of black phosphorene may be preserved by iso-valence doping with nitrogen from group VA [111].

Consequently, the absence of magnetism is attributed to valence electron pairing between the dopant and the adjacent phosphorus atoms [111]. A further DFT study demonstrates that introducing nitrogen doping results in chains composed of alternating nitrogen and phosphorus atoms, denoted as –N–P–P–P–N–. The introduction of doping elements such as carbon (C), silicon (Si), and germanium (Ge) from group IVA, which possess an even number of valence electrons, not only imparted metallic characteristics to black phosphorene but also resulted in significantly anisotropic transport properties [111]. According to ab initio total energy calculations, it has been hypothesized that the substitutional carbon dopant establishes chemical bonds with three adjacent phosphorus atoms at the grain boundary defects by sp^2-like hybridization.

A small amount of boron impurity causes black phosphorene to transition from semiconductors to semi-metal/metal, increasing chemical reactivity [112]. These doped systems are anticipated to exhibit thermodynamic stability [111]. The introduction of boron as a dopant does not result in the induction of magnetism in black phosphorene. It may be

attributed to the robust electron pairing and hybridization of s-p orbitals between the n-type dopant and the neighboring phosphorus atoms [113].

The introduction of boron into phosphorene and the increased reactivity due to the same have shown promise for metal-free catalysis of SO_2. However, the strong adsorption associated with this process limits its suitability for sensing applications [114]. As shown in previous studies [115], the B-doped system exhibited an indirect bandgap and significant anisotropy, which is irrelevant for developing optical devices.

1.2.7. Gas adsorption phosphorene- an overview

In early 2014, the successful synthesis of a monolayer of black phosphorus, also referred to as phosphorene, was achieved [103]. Theoretical investigations [116] along with experimental studies [117] have indicated its potential as a promising candidate for gas sensors. Phosphorene has the advantageous characteristics of a direct band-gap property and a buckled structure [118], rendering it particularly well-suited for gas molecule adsorption and sensing, hence overcoming the limitations associated with zero band-gap materials. There is a limited body of literature about the adsorption of gas molecules on phosphorene, of which the majority focus on the pure form of phosphorene. Numerous studies have focused on using first-principles computations to investigate the adsorption of CO, CO_2, NH_3, NO, NO_2, SO_2, H_2S, and CH_4 molecules on phosphorene. These adsorption studies show that there are noticeable alterations in the transport and electrical properties of phosphorene. Some of the previous studies [119] show that defects impact phosphorene's electronic properties and geometry.

The molecule NO_2 at the concentration of 5 ppb adsorbed on the monolayer and a few layers of phosphorene in a dry environment was carried out by Abbas *et al.* [120] and checked this system's capability as a field-effect transistor (FET). Using both DFT and non-equilibrium Green's function method (NEGF), the selectivity and anisotropic $I - V$ response of gas adsorption (CO, CO_2, NH_3, NO, and NO_2) on phosphorene monolayer was also done [19].

They have observed the anisotropic properties shown by phosphorene along its armchair and zigzag orientations. Phosphorene offers slightly favorable properties on chemical alterations via doping and consequent adsorptions. It can be seen as an alternate method to improve its electronic and optical properties. Many methodologies have been proposed for incorporating dopants into nanomaterials, including chemical vapor deposition, electron beam irradiation, and pulsed laser deposition [121].

Zhang *et al.* [122] conducted a theoretical investigation on the interactions between electron donor and acceptor molecules on BP. The use of calcium-doped and calcium-decorated phosphorene as the fundamental substrate was studied for the adsorption of carbon dioxide (CO_2), methane (CH_4), hydrogen (H_2), and ammonia (NH_3) molecules. [110]. The essential research in the adsorption of small gaseous molecules on doped phosphorene is reviewed below. It is suggested in a recent study that Si- and S-phosphorene devices may provide benefits over pristine phosphorene for sensing CO, NO, NO_2, and NH_3. Using a combination of DFT and NEGF methods, the transport properties of both devices have been investigated. The substitutional doping of Si or S into phosphorene can induce the metallic feature due to the unpaired valence electron on the Si atom or the non-bonding electrons of the neighboring phosphorus atom around the sulfur atom [123].

A search for novel CO_2 capture materials based on phosphorene doped with Fe, Co, Ni, Ti, Cu, Au, Ag, Ca, Cr, Pd, Pt, V, Sr, Mn, B, C, N, O, Si, Ge, Se, and S were done using first-principles calculations. The interactions between CO_2 and pristine phosphorene are usually low (around 0.2 eV), and metallic dopants help improve the interaction energy. However, non-metallic dopants do not significantly change the interactions between CO_2 and phosphorene. Computational studies consider Fe-, Ti-, and Cr- doped phosphorenes as promising candidates for CO_2 detection and removal [124]. A theoretical analysis of the adsorption properties between methanol gas molecule and pristine or heteroatom-doped

phosphorene like B, N, C, and O were done by Wang *et al.* [125]. N-doped and O-doped phosphorene are found to have larger charge transfer values with shorter adsorption distances and larger adsorption energies for the adsorption of methanol compared to pristine phosphorene.

In contrast, B-doped and C-doped phosphorene are unsuitable for methanol adsorption. In a previous study, the pristine phosphorene is sensitive to SO_2 gas molecules with moderate adsorption energy [114]. Doping phosphorene with either B or Si atom exhibits significantly high reactivity towards SO_2 via strong chemisorption, thus presumably unsuitable as an SO_2 gas sensor. They can be applied as metal-free catalysts for activating or catalyzing SO_2 adsorbate. Doping with N or S is redundant without improving the SO_2 sensing performance of phosphorene.

1.3. Conclusions

Despite the initial promise of graphene as a possible substitute for silicon in next-generation electronics, its zero band-gap has been a significant barrier to its practical deployment in this field. Graphene-based FETs have low on-off ratios [126] due to their gapless band structure. For the concepts of graphene-based FETs to be viable, it is necessary to induce a band-gap inside the graphene material. One of the primary focuses in graphene research is the exploration of methods to introduce a band-gap in graphene while preserving its inherent characteristics.

Various techniques have been developed to manufacture graphene devices with enhanced semiconducting characteristics by manipulating band-gaps. Among the several methods used for controlling the band-gap of graphene, doping methodologies have shown the most significant potential in their applicability on an industrial scale. The primary consequence of doping in graphene is generating a band-gap, rendering graphene suitable for various applications. In addition, introducing electron-deficient and electron-rich heteroatoms into

graphene may alter its affinity for binding with other molecules, such as ammonia.

The study encompasses several types of graphenes, including intrinsic graphene, doped graphene, doped and undoped graphene bilayers, and phosphorene. This work investigates the impact of doping on the structural and electrical characteristics of graphene when it interacts with gas molecules. Specifically, the adsorption energies, charge density distribution, band structure, and density of states of graphene-gas molecule adsorption systems are examined. The present study employs a first-principles method based on density functional theory to analyze the interactions between multiple gas molecules and graphene sheets that are either intrinsic or doped with heteroatoms.

Comprehending the principles behind the adsorption process of gas molecules onto the surface of graphene has considerable importance in advancing gas sensors based on graphene. Examining charge transfers, electronic band structures, and electronic DOS describes the adsorption processes. The alterations in the electronic configurations of graphenes resulting from the physical or chemical adsorption of gas molecules onto the surface of graphene can be assessed by examining charge distribution and studying band structure diagrams.

The efficacy of doped graphenes as gas sensors is contingent upon their sensitivity to different constituents in the atmosphere. The findings derived from investigating the impacts of adsorbed atmospheric elements on doped graphene structures suggest the appropriateness of using doped graphenes as sensors for detecting dangerous gases in the air. The investigation of the energy stabilities, structural characteristics, and electronic band structures of boron and nitrogen substitutional dopants in graphene is undertaken due to their importance in nanoelectronic device applications. A thorough investigation examined the relationship between the energy stability and band-gaps in graphene for varying concentrations and configurations of B- and N- dopants. The outcomes derived from the computations provide the potential to customize the band-gap according to specific requirements, hence facilitating

the use of doped graphene in electronic applications.

1.4. Broad Outline of thesis

The thesis is divided into eight chapters. **The first Chapter** of the thesis contains a general introduction to two-dimensional materials like graphene, bilayer graphene, and phosphorene and their unique electronic features. A comprehensive literature review on chemical modifications of the surfaces and adsorption phenomena on these modified surfaces are also discussed. It is followed by a detailed write-up on the computational methodology and density functional theory for elucidating the electronic and adsorption behavior in **Chapter 2**. This chapter also included details about exchange-correlation functional, band structure, charge transfer calculations, adsorption energy calculations, etc.

Chapter 3 discusses our calculations regarding the effects of individual B and N doping on the structure and electronic properties of graphene sheets. The obtained results are compared with pure graphene and other previous results. The distance between adsorbate and adsorbent, adsorption energy, and band-gap are calculated for different hetero-graphene structures with increasing concentration of boron (nitrogen) doping and by varying the doping sites. Further, the chapter details the investigation of the adsorption of CO and NH_3 on these chemically modified surfaces. The effects of paramagnetic molecules like NO, NO_2, and diamagnetic N_2O adsorption on chemically modified graphene surfaces are discussed in **Chapter 4**. It also includes graphene surfaces co-doped with boron and nitrogen in different mole fractions. The study is also extended for various doping patterns and mole fractions.

The electronic properties of oxygen in its natural and singlet state upon adsorption on pure and boron-doped graphene are discussed in detail in **Chapter 5.** In this chapter, the structural properties of the adsorption of dioxygen on boron-doped graphene surfaces are also conducted using spin-polarized density functional theory methods, including van der Waals correction. **In Chapter 6,** how adsorption and electronic properties vary upon adsorption of

ammonia on bilayer graphene is discussed. In this chapter, a discussion of how electronic properties vary upon doping and increasing concentration with different patterns of doping on bilayer graphene is explored. In **Chapter 7**, the adsorption studies are carried out on another essential two-dimensional surface, phosphorene. In this chapter, black phosphorus is doped with different p-block elements and made the best phosphorene semiconductors and metals upon doping. Further adsorption of HCN and HNC on these modified surfaces of phosphorene was also done. Finally, all results and conclusions are summarized in **Chapter 8** followed by bibliography.

1.5. Scope and limitations

There are various techniques, such as Raman spectroscopy, that may be used to investigate materials and their electronic characteristics; however, DFT approaches with different suitable functionals and vdW corrections are considered as the most effective computational approach.

This thesis primarily focuses on the doping of 2D materials like graphene and phosphorene, adsorption of small gaseous molecules and its subsequent electronic structural alterations. However, the transport characteristics, such as electrical conductivity are not studied. Moreover, we have not studied the specificity and selectivity of these surfaces towards the gas molecules. Nevertheless, this work provides a thorough knowledge of the electronic properties and adsorption of gas molecules on chemically modified graphene and similar surfaces, making it a valuable fundamental research.

Chapter 2

Computational methodology

This chapter overviews the computational methods employed in the electronic structure calculations involving various systems, including different adsorbates on intrinsic and chemically modified two-dimensional adsorbents.

2.1. Introduction

Materials are essential to modern civilization since they support our current technologies, buildings, transportation, clothing, food supply, health, etc. Complex interactions occurring within material on various time and length scales are the source of successful new uses for the material. Solid-state materials are highly sought-after due to their distinct qualities and technological benefits. Due to the advancements in contemporary material science, there is an ever-growing demand to understand phenomena that describe the atomistic-level features of materials and processes that occur in materials.

The field of computational material science focuses on using computational methods and techniques to study and understand the properties and behavior of materials. Material science, an area expanding quickly, has much potential for managing multidisciplinary simulations in physics, chemistry, and engineering under realistic settings. Completing complex, multi-body problems that were unsolvable a few years ago now requires using quick, compelling computer systems rather than mathematical approximations used in analytical theory. The utilization of computational methods in material science enables researchers to acquire an essential understanding of their structural, magnetic, optical, and electrical properties. Additionally, these methods aid in investigating phenomena related to materials design, characterization, and utilization through quantum mechanical simulations.

The utilization of quantum mechanical principles in theoretical computation enables the analysis of systems that pose challenges in experimental characterization and the prediction of physical properties for materials that have yet to be synthesized. This technique can effectively identify and design nanoscale materials for particular applications by examining the

structure-property correlation of these materials. One approach to investigating complex many-body systems involves conducting computer simulations utilizing classical and quantum mechanical (QM) methodologies. Classical methodologies encompass force field or semi-empirical methods, wherein the forces governing atomic interactions are specified to replicate experimental outcomes accurately. However, it should be noted that these techniques are limited in their applicability since they are only suitable for a specific group of molecules.

Furthermore, their effectiveness relies on the availability of trustworthy data, which must be obtained beforehand from closely comparable systems. In cases where the parameters remain unknown or when a system exhibits atypical behavior, it is advisable to depend on *ab initio* calculations. *"Ab initio*" originates from Latin and translates to "from the commencement."

DFT has emerged as a significant advancement in quantum mechanical *ab initio* simulations [1]. It serves as the fundamental framework for atomic-scale computational materials science, enabling the incorporation of electron-electron interactions within a single particle Schrödinger equation through the exchange-correlation functional [2]. Today advances in exchange-correlation functional and higher-level post-DFT approaches and their use in highly efficient computer codes make DFT-based computations a valuable tool for material characterization and processes.

2.2. *Ab initio* methods

Material science covers several computational techniques, including molecular mechanics, semi-empirical, and *ab initio* approaches. These methods are distinguished by their respective use of approximations, resulting in varying degrees of accuracy in the obtained conclusions. Molecular mechanics use principles of classical physics to simulate the behavior of molecular systems, as opposed to solving the Schrödinger equation. This method is vastly helpful for biomolecules and other macromolecules, where the electronic structure of the individual

molecules is less critical. Consequently, the outcomes obtained by this approach are defined with less accuracy. The energy expression consists of simple classical equations, such as the harmonic oscillator equation in order to describe the energy associated with bond stretching, bending, rotation and intermolecular forces, such as van der Waals interactions and hydrogen bonding. All of the constants in these equations must be obtained from experimental data or an ab initio calculation. Determining all constants included in the conventional equations necessitates their solving via either *ab initio* computations or experimental methods. Semi-empirical methodologies use principles from quantum physics and include empirically acquired empirical parameters inside the mathematical framework. Due to the various approximations of the Schrödinger equation, these approaches provide less precise outcomes; however, they exhibit much enhanced computational efficiency. These approaches may be effectively used for computations in organic and inorganic chemistry, mainly involving a limited number of moderately sized components.

As the *ab initio* methods are derived from basic principles, the calculations exhibit a high computational cost, although they provide excellent qualitative and quantitative outcomes. These computations do not use empirical parameters except for fundamental constants and the atomic numbers of the atoms involved. This technique uses quantum mechanical principles to compute the molecular characteristics of the systems. One prevalent category of *ab initio* approaches uses Hartree-Fock calculations [3], where the central-field approximation is employed. The Hartree-Fock technique incorporates the exchange interaction between electrons while neglecting the explicit treatment of electron-electron repulsion (correlation). Instead, the computation accounts for the average impact of this repulsion, and the correlation can be included by the Configuration Interaction (CI) approach, but at the cost of increased computational time with system size.

2.2.1. Density functional theory

DFT, established by Hohenberg, Kohn, and Sham, presents a more reliable and versatile method for calculating electronic structure. It is a frequently used computational approach in physics and chemistry to investigate the electronic configuration of complex systems such as atoms, molecules, and solids. This method is prevalent in materials science, which can predict fundamental characteristics of many-body systems, such as the total energy, atomic structure, electronic configuration, etc.

Computational solid-state physics simulations have gained significant popularity since the 1970s. Before the 1990s, DFT was not considered precise for quantum-chemical computations. Including exchange and correlation interactions in the approximations used in DFT has made this theory suitable for specific quantum chemical applications [4]. This approach provides significant advantages over traditional *ab initio* wave function methods, like HF methods and its successors that rely on the complex many-electronic wave function, since they can deliver comparable results at much-reduced computing expenses. The cost-effectiveness and performance of DFT make it a more favorable choice for analyzing larger molecular systems compared to electron-correlated, wave function-based, *ab initio* methods like Møller–Plesset perturbation theory [5] or coupled cluster method [6]. DFT provides a satisfactory level of accuracy and demonstrates significant predictive capabilities. The DFT has established a solid foundation for developing computational methodologies to obtain valuable insights into atoms' and molecules' energetic, structural, and property characteristics. It is an exceptionally efficient methodology for characterizing the fundamental features of solids in their ground states. According to this theoretical framework, the aspects of a system consisting of several particles may be effectively elucidated using electron density functionals. The technique developed by Hohenberg and Kohn aims to address the many-body Schrödinger equation by formulating the system's total energy relative to the overall electron density. The

fundamental concept of DFT involves substituting the electronic density as the fundamental entity instead of the wave function, to characterize the features of a system of interacting fermions. In a solid with N electrons, subject to the Pauli principle and Coulomb interactions, the fundamental quantity representing the system is a function of just three spatial coordinates (x, y, and z) rather than the extensive 3N degrees of freedom. DFT finds relevance not only in the study of conventional bulk materials but has also found applications in the investigation of intricate structures like bio-molecules and functionalized nanostructures. The basic DFT has been extended to include a wide range of systems, including but not limited to spin-polarized systems, nuclei, superconductors exhibiting electron pairing processes, relativistic electrons, time-dependent phenomena [7,8], excited states, bosons, molecular dynamics, etc.

The first formulation of DFT is attributed to the pioneering work of Thomas and Fermi in the 1920s [9]. The Thomas-Fermi equation needed to be revised in terms of accuracy due to its failure to include the exchange energy of an atom, as predicted by the Hartree-Fock theory. The concept of exchange energy functional was first developed by Dirac in 1928 [10].

2.2.2. Density functional theory- The Kohn-Sham approach

Within the framework of DFT, it is postulated that the overall energy of a given system is only described by the electron density of the ground state. Essentially, the total energy of a system composed of atoms can be articulated as a function that depends on the density of its electrons.

$$\boldsymbol{E} = \boldsymbol{E}[\boldsymbol{\rho}] \tag{2.1}$$

According to the fundamental Hohenberg-Kohn theorem, determining various characteristics of a molecule in its lowest energy electronic state can be accomplished by employing the electron density function associated with the ground state, denoted as ρ_0(x, y, z). It implies that density ρ_0 enables the computation of diverse ground-state attributes relevant to the system being examined, such as its energy. It can be represented as,

$$\boldsymbol{E_0}\ [\boldsymbol{\rho_0}(\boldsymbol{x}, \boldsymbol{y}, \boldsymbol{z})] \tag{2.2}$$

meaning that E_0 is a functional of the electron density $\rho_0(x, y, z)$. The first Hohenberg-Kohn theorem postulates that any characteristic of a molecule's ground state may be expressed as a functional relationship with the electron density function of the ground state. According to the second Hohenberg-Kohn theorem, the energy obtained from any trial electron density function will be greater than or equal to the actual ground-state energy. Within the context of DFT computations, the electronic energy arising from a certain trial electron density is precisely characterized as the energy associated with the motion of electrons within the potential field generated by the atomic nuclei. The term "external potential" can denote the nuclear potential, which can be represented as v(r). It can be expressed as,

$$\boldsymbol{E_v[\rho_t] \geq \ E_0[\rho_0]} \tag{2.3}$$

Here, ρ_t represents a trial electronic density, whereas $E_0[\rho_0]$ denotes the actual ground-state energy functional. The trial density must adhere to the specified criterion.

$$\boldsymbol{\int \rho_t(\overrightarrow{r})\, d\vec{r} = n} \tag{2.4}$$

where n is the number of electrons in the molecule.

The non-relativistic Hamiltonian operator $\hat{H}_{tot}$ for a many-particle system can be written as the sum of electronic, nuclear, and mixed terms as follows:

$$\boldsymbol{\hat{H}_{tot} = \hat{T}_e + \hat{T}_N + \hat{V}_{Ne} + \hat{V}_{ee} + \hat{V}_{NN}} \tag{2.5}$$

In this context, T denotes the kinetic energy, V represents the potential energy, and e and N symbolize electrons and the nucleus, respectively.

Another approximation often used in quantum mechanics is the Born-Oppenheimer or adiabatic approximation [11]. This approximation requires separating the degrees of freedom related to the movement of nuclei and electrons. The nuclei, because of their greater mass relative to electrons, nuclei are much slower compared to the electrons. Consequently, the contribution of the nuclei's kinetic energy component might be considered insignificant within the context of the Schrödinger equation. Hence, the total electronic energy of the actual

molecule in its ground state is determined by the combined contributions of electron kinetic energies, nucleus-electron attraction, and electron-electron repulsion energies. The ground-state electronic energy may be expressed using the following equation,

$$\boldsymbol{E_0} = \langle \boldsymbol{T}[\boldsymbol{\rho_0}] \rangle + \langle \boldsymbol{V_{Ne}}[\boldsymbol{\rho_0}] \rangle + (\boldsymbol{V_{ee}}[\boldsymbol{\rho_0}]) \tag{2.6}$$

The focus is placed on the middle term, which pertains to the potential energy between the nucleus and electrons. It includes the summation of the potential energy for each of the 2n electrons, accounting for the attraction between an electron and all nuclei as,

$$\langle \boldsymbol{V_{Ne}} \rangle = \sum_{\boldsymbol{i=1}}^{\boldsymbol{2n}} \sum_{\boldsymbol{nuclie}} -\frac{\boldsymbol{z_A}}{\boldsymbol{r_{iA}}} = \sum_{\boldsymbol{i=1}}^{\boldsymbol{2n}} \boldsymbol{v}(\boldsymbol{r_i}) \tag{2.7}$$

The symbol $v(r_i)$ represents the external potential. Therefore, it may be stated that,

$$\int \boldsymbol{\psi} \sum_{\boldsymbol{i=1}}^{\boldsymbol{2n}} \boldsymbol{f}(\boldsymbol{r_i}) \boldsymbol{\psi} \boldsymbol{dt} = \int \boldsymbol{\rho}(\boldsymbol{r}) \boldsymbol{f}(\boldsymbol{r}) \boldsymbol{dr} \tag{2.8}$$

The function $f(r_i)$ represents the dependence on the coordinates of the 2n electrons inside the investigated system. The average nuclear-electron attraction can be written as,

$$\langle \boldsymbol{V_{Ne}} \rangle = \int \boldsymbol{\rho_0}(\boldsymbol{r}) \mathbf{v}(\boldsymbol{r})\, \boldsymbol{dr} \tag{2.9}$$

Therefore, Eq. 2.6 may be expressed as the following equation,

$$\boldsymbol{E_0} = \int \boldsymbol{\rho_0}(\boldsymbol{r}) \mathbf{v}(\boldsymbol{r}) \boldsymbol{dr} + \langle \boldsymbol{T}[\boldsymbol{\rho_0}] \rangle + \langle \boldsymbol{V_{ee}}[\boldsymbol{\rho_0}] \rangle \tag{2.10}$$

Due to the lack of knowledge about $\langle T[\rho_0] \rangle$ and $\langle V_{ee}[\rho_0] \rangle$, it is impossible to use this equation's current version for energy. To maximize the utilization of Eq. 2.10, Kohn and Sham introduced the concept of a reference system consisting of non-interacting electrons. They have defined a $\Delta\langle T[\rho_0] \rangle$ as the variation between the actual kinetic energy $\langle T[\rho_0] \rangle$ and the kinetic energy of the reference system $\langle T_r[\rho_0] \rangle$,

$$\boldsymbol{\Delta}\langle \boldsymbol{T}[\boldsymbol{\rho_0}] \rangle = \langle \boldsymbol{T}[\boldsymbol{\rho_0}] \rangle - \langle \boldsymbol{T_r}[\boldsymbol{\rho_0}] \rangle \tag{2.11}$$

Similarly, $\Delta\langle V_{ee}[\rho_0] \rangle$ is defined as the difference between the actual electron-electron repulsion energy and the classical charge-cloud coulomb repulsion energy. The classical electrostatic repulsion energy may be expressed as the sum of the repulsion energies between pairs of finite volume elements $\rho(r_2)dr_2$ and $\rho(r_1)dr_1$, separated by a distance r_{12}. This energy is then

multiplied by a factor of ½ to get,

$$\boldsymbol{\Delta\langle V_{ee}[\rho_0]\rangle = \langle V_{ee}[\rho_0]\rangle - \frac{1}{2}\iint \frac{\rho_0(r_1)\rho_0(r_2)}{r_{12}} dr_1 dr_2} \quad (2.12)$$

Therefore,

$$\boldsymbol{E_0 = \int \rho_0(r)\mathrm{v}(r)dr + \langle T_r[\rho_0]\rangle + \frac{1}{2}\iint \frac{\rho_0(r_1)\rho_0(r_2)}{r_{12}} dr_1 dr_2 + \Delta\langle T[\rho_0]\rangle + \Delta\langle V_{ee}[\rho_0]\rangle} \quad (2.13)$$

The term "exchange-correlation energy functional" or "exchange-correlation energy E_{xc}" refers to the combined deviation in kinetic energy from the reference system and the deviation in electron-electron repulsion energy from the classical system can be written as,

$$\boldsymbol{E_{xc}[\rho_0] = \Delta\langle T[\rho_0]\rangle + \Delta\langle V_{ee}[\rho_0]\rangle} \quad (2.14)$$

The symbol $\Delta\langle T\rangle$ is used to describe the kinetic correlation energy of the electrons, whereas the symbol $\Delta\langle V_{ee}\rangle$ symbolizes the potential correlation energy.

Hence, by using Eq. 2.13 and 2.14, it is possible to write,

$$\boldsymbol{E_0 = \int \rho_0(r)\mathrm{v}(r)dr + \langle T_r[\rho_0]\rangle + \frac{1}{2}\iint \frac{\rho_0(r_1)\rho_0(r_2)}{r_{12}} dr_1 dr_2 + E_{xc}[\rho_0]} \quad (2.15)$$

In Eq. 2.15, four variables need more explanation. If the value of ρ_0 is known, the integrals of the terms may be easily computed. The second element in the equation indicates the expectation value of the sum of the kinetic energy operators for individual electrons, summed over the ground-state wave function of the reference system. The third part corresponds to the energy associated with classical electrostatic repulsion and may be computed given the value of ρ_0. The E_{xc} word refers to the exchange-correlation energy functional of the system. The primary focus within the framework of DFT is on identifying and selecting accurate exchange-correlation functionals that can effectively compute the energy term based on the electron density function.

Eq. 2.15 is now expressed as,

$$\boldsymbol{E_0 = -\sum_{nuclei\ A} Z_A \int \frac{\rho_0(r_1)}{r_1 A} dr_1 - \frac{1}{2}\sum_{i=1}^{2n}\langle \psi_i^{ks}(1)|\nabla_1^2|\psi_i^{ks}(1)\rangle + \frac{1}{2}\iint \frac{\rho_0(r_1)\rho_0(r_2)}{r_{12}} dr_1 dr_2 + E_{xc}[\rho_0]} \quad (2.16)$$

where ψ_i^{ks} refers to the Kohn-Sham spatial orbitals. The energy in Eq. 2.16 is exact. The KS equations are derived using the variation principle and the second Hohenberg-Kohn theorem. It is postulated that the electron density of the reference system is equivalent to that of the actual system. Hence, the electron density may be expressed as

$$\boldsymbol{\rho_0 = \rho_r = \sum_i \left|\psi_i^{ks}\right|^2} \tag{2.17}$$

By substituting Eq. 2.17 into Eq. 2.16 and varying E_0 with respect to ψ_i^{ks}, the KS equation can be written as,

$$\left[-\frac{1}{2}\boldsymbol{\nabla_i^2} - \boldsymbol{\sum_{nuclei\ A}\frac{Z_A}{r_1 A}} + \boldsymbol{\int\frac{\rho(r_2)}{r_{12}}dr_2} + \mathbf{v_{xc}(1)}\right]\boldsymbol{\psi_i^{ks}(1)} = \boldsymbol{\in_i^{ks}\ \psi_i^{ks}(1)} \tag{2.18}$$

In this context, the symbol $v_{xc}(1)$ represents the exchange-correlation potential, specifically assigned to electron number 1. This assignment is arbitrary because the Kohn-Sham equations consist of a collection of equations for individual electrons, denoted by the subscript 'i' ranging from 1 to n. The exchange-correlation potential v_{xc} may be defined as the functional derivative of $E_{xc}[\rho(r)]$ with respect to $\rho(r)$ as,

$$\mathbf{v_{xc}(r)} = \frac{\boldsymbol{\delta E_{xc}[\rho(r)]}}{\boldsymbol{\delta\rho(r)}} \tag{2.19}$$

The KS equations can now be written as,

$$\boldsymbol{\hat{h}^{ks}(1)\psi_i^{ks}(1) = \in_i^{ks}\ \psi_i^{ks}(1)} \tag{2.20}$$

Where $\hat{h}^{ks}$ is Kohn-Sham potential energy, expressed as $\left[-\frac{1}{2}\nabla_i^2 - \sum_{nuclei\ A}\frac{Z_A}{r_1 A} + \int\frac{\rho(r_2)}{r_{12}}dr_2 + v_{xc}(1)\right]$ in Eq. 2.18.

2.3. Spin polarization

Until now, the discourse on DFT has been limited to scenarios without spin polarization. Nevertheless, specific systems, such as magnetic transition metals or molecules like O_2, involve unpaired electrons or molecular radicals, necessitating a spin-polarized approach. In these systems, the count of electrons with "spin-up" can differ from that of electrons with "spin-down." The fundamental quantities in the local spin density functional (LSDF) theory include

the electron density, denoted as ρ, and the spin density, represented as σ. The spin density is operationally defined as the variation between the densities of the spin-up and spin-down electrons relative to the overall electron density.

$$\boldsymbol{\sigma(r) = \sigma_{\uparrow}(r) - \sigma_{\downarrow}(r)} \tag{2.21}$$

According to the LSDF hypothesis, the exchange-correlation potential for spin-up electrons often exhibits distinctions from the potential associated with spin-down electrons. Therefore, the spin-polarized Kohn-Sham equations may be expressed as,

$$\left[\frac{-\hbar^2}{2m}\nabla^2 + V_{eff}^{\sigma}(\varepsilon_i^{\sigma})\right]\Psi_i^{\sigma}(r) = \varepsilon_i^{\sigma}\Psi_i^{\sigma}(r), \sigma = \uparrow or \downarrow \tag{2.22}$$

where

$$V_{eff}^{\sigma}(r) = V_c + \mu_{xc}^{\sigma}[\rho(r), \sigma(r)] \tag{2.23}$$

The exchange-correlation potential in LSDF theory depends on both the electron density and the spin density, as given by Eq. 2.23. Here μ_{xc}^{σ} refers to the exchange-correlation potential operator. There are two sets of single-particle wave functions, one about electrons with spin-up orientation and the other about electrons with spin-down orientation. Each set is accompanied by its respective one-electron eigenvalues. In the scenario when the densities of spin-up and spin-down particles are equal, the spin density is uniformly zero throughout all spatial regions, resulting in the equivalence of LSDF theory and the LDF method. It is essential to observe that inside spin-polarized computations, the occupancy of single-particle states is restricted to 1 or 0. However, despite this distinction, there remains only a single Fermi energy. Magnetic systems are expected to designate the electrons with spin-up and spin-down as the "majority" and "minority" spin systems, respectively.

2.4. Exchange Correlation functional and approximations

Although DFT offers a somewhat accurate depiction of ground state features, its practical implementation relies on exchange-correlation functionals. The exchange-correlation potential

is a theoretical framework that accounts for the influence of the Pauli exclusion principle and the Coulomb potential, specifically regarding the electrostatic interaction among electrons. One of the challenges associated with the DFT is the need for knowledge of the precise functionals for exchange and correlation, except for the free electron gas. Nevertheless, using certain approximations makes it possible to compute specific physical values with a high degree of accuracy. The computation with DFT often involves three sorts of approximations. The first aspect conceptualizes KS eigenvalues and orbitals, interpreted as physical energies and wave functions. The numerical approximation, the second form of approximation, is used in the methodologies aimed at effectively solving the differential equation. One crucial factor to consider is the selection of appropriate basis functions. The third type of approximation involves the formulation of an equation for the unknown xc functional $E_{xc}[n]$, which encompasses all the many-electron characteristics of the problem under consideration [12]. There currently needs to be a precise explanation of the exchange-correlation terms in the present theory. The local density approximation (LDA), which approximates the total energy of the multi-electron system, is the first simple form that Kohn and Sham developed. The necessary approximations for the calculation of E_{xc} are discussed below.

2.4.1. Local Density Approximation (LDA)

Local-density approximations (LDA) refer to a category of approximations utilized in DFT to estimate the exchange-correlation energy functional, E_{xc}. This approximation relies exclusively on the electronic density value at each spatial point without considering factors such as density derivatives or the Kohn-Sham orbitals. Many methodologies may provide localized approximations to the E_{xc}. Nevertheless, the local approximations have significantly succeeded, mainly using the homogenous electron gas (HEG) model. In this context, it is often understood that LDA is analogous to functionals that rely on the HEG approximation and are afterward used to study practical systems such as molecules and solids. The exchange-

correlation energy using a local-density approximation, for the spin-unpolarized system, is,

$$E_{xc}^{LDA}[\rho] = \int \rho(r)\epsilon_{xc}(\rho(r))dr \quad (2.24)$$

where $\rho(r)$ represents charge density. In systems characterized by gradual variations in density, the LDA demonstrates favorable performance, effectively reproducing chemical trends [13]. LDA exhibits significant inaccuracies in systems characterized by high correlations, where the assumption of independent particles is no longer valid. For example, the transition metal oxides XO (where X represents Fe, Mn, or Ni) which are insulators, are predicted to be either semiconductors or metallic according to LDA [14]. The LDA algorithm often fails to accurately identify the correct ground state in several basic scenarios, for example, LDA yields an incorrect ground state prediction for the titanium atom. It fails to include the influence of van der Waals bonding and provides an inadequate depiction in many cases, for e.g., hydrogen bonding.

2.4.2. Generalized Gradient Approximation (GGA)

The LDA is ineffective when the density varies quickly, such as in molecules, since it calculates the actual density's energy using the energy of a local constant density. One of the best ways to improve is to consider DFT calculations that employ gradient-corrected functionals that incorporate both the electron density and its gradient, represented by the first derivative of ρ with respect to its position. These functionals are commonly referred to as generalized gradient approximations (GGA). The fundamental concept underlying these schemes involves incorporating components into the exchange-correlation expressions based on the electron density gradient rather than solely relying on its value at individual spatial points. Hence, these adjustments are occasionally denoted as "non-local" potentials. In this particular scenario, the exchange and correlation functional exhibits dependence on the charge magnitude and the charge gradient. Consequently, the functional is formulated as,

$$E_{xc}^{GGA}[n(r), \nabla n(r)] = \int \epsilon_{xc}^{GGA}(n(r), |\nabla n(r)|)n(r)dr \quad (2.25)$$

E_{xc}^{GGA} is the exchange and correlation energy density per particle in a homogeneous electron gas of density n(r). The corresponding potential can be expressed as,

$$\boldsymbol{v_{xc}^{GGA}(r) = \frac{\delta E_{xc}^{GGA}[n]}{\delta n(r)} = \left(\frac{\partial F_{xc}[n]}{\partial n} - \sum_{\alpha=1}^{3} \partial_\alpha \left(\frac{\partial F_{xc}[n]}{\partial(\partial_\alpha n)}\right)\right)\Big|_{n=n(r)}} \quad (2.26)$$

where F_{xc} (n, |∇n|) = ϵ_{xc}^{GGA} (n (r), |∇n (r)|) and ∂α stands for the αth component of the gradient. This novel approximation method effectively addresses several challenges encountered in LDA and has demonstrated successful applications in various domains, including surfaces, molecules, and materials. Several proposals have been made for multiple versions of F_{xc} (n, |∇n|) = ϵ_{xc}^{GGA} (n (r), |∇n (r)|), with the PBE [15] being the most often used. However, despite its popularity, the GGA still faces significant challenges as it remains a semi-local approximation that does not incorporate long-range interactions due to its inherent structure. The necessary modifications can be done to address these shortcomings, which are discussed in the next section.

Although the LDA method has just one type, the GGA method has several parameterizations available. Specific models in this context may be classified as semi-empirical since they use experimental data, such as atomization energies, in their derivation process. Some of them are exclusively generated using the first principles approach. The GGA functionals often used in research include the PW91 functional, developed by Perdew and Yang [16], and BLYP, PBE, and B3LYP [17,18].

While there are many GGA functionals, the Perdew-Burke-Ernzerhof (PBE) functional is much preferred due to its non-empirical nature and ability to provide reasonably accurate results for a broad spectrum of systems. The PBE functional stands out as the most widely used and favored one among researchers in computational material science. The GGA refers to a collection of functionals rather than a single functional.

2.5. DFT corrections

It is apparent that traditional Kohn-Sham density functional theory (KS-DFT) approximations, as shown by previous studies [4], are inadequate in accurately characterizing London-dispersion interactions [19,20]. These interactions are non-local in nature and are asymptotically regulated by a well-known relation [21].

$$\boldsymbol{E_{disp}} \propto -\frac{\boldsymbol{C_6}}{\boldsymbol{R^6}} \tag{2.27}$$

Eq. 2.27 demonstrates that in the long-range domain, characterized by minimal electron cloud overlap between two molecular or atomic fragments, the dispersion energy (E_{disp}) exhibits the sixth-power dependence on the distance (R) separating these fragments. The coefficient C_6 represents the sixth-order dispersion coefficient. It has been shown that typical density functional approximations cannot accurately account for the long-range tail of the dispersion energy, mainly owing to their semi-local character. This situation presented a specific difficulty, considering that KS-DFT has emerged as a fundamental approach in Quantum Chemistry. However, we must also consider London dispersion's widespread and substantial significance in chemical processes. Therefore, several variations/modifications of DFT corrections, such as DFT-D1, DFT-D2, and DFT-D3, are available.

In 2010, Grimme introduced two refined versions [22] that may be seen as advancements of his previous studies on the less complex DFT-D1[23] (2004) and DFT-D2 [24] (2006) variations. The incorporation of additive corrections, namely the DFT-D3 versions, also significantly changed the understanding of DFT methods [25] and has now been widely used in quantum-chemical applications. The following section describes DFT-D2 and DFT-D3.

2.5.1. DFT-D2

The corrected DFT method, DFT-D2, incorporates a multipole term that exhibits a sixth-order dependence on the R_{AB} distance between two atoms, A and B. In other words, the DFT-D2 method considers all potential atom pairs within a particular chemical system and assigns a

dispersion contribution to each pair based on London's formula (Eq. 2.27). Contributions from the atom-pair are then added together to get the molecular dispersion correction.

$$\boldsymbol{E_{disp}^{DFT-D2}} = -\frac{\mathbf{1}}{\mathbf{2}}\boldsymbol{s_6}\sum_{A\neq B}\frac{\boldsymbol{C_6^{AB}}}{\boldsymbol{R_{AB}^6}}\boldsymbol{f_{damp}^{DFT-D2}}(\boldsymbol{R_{AB}}) \tag{2.28}$$

The symbol C_6^{AB} represents the average, isotropic sixth-order dispersion coefficient for the atom pair AB. $f_{\text{damp}}^{\text{DFT-D2}}$ corresponds to a damping function, while s_6 signifies a global scaling parameter. The inclusion of a prefactor of one-half is necessary in order to prevent the occurrence of duplicate calculations.

It should be noted that while DFT-D2 guarantees a decline of the dispersion contribution up to the sixth order in the long-range area, the short-range region, which is characterized by the overlapping electron clouds of the non-covalently bound fragments, is primarily influenced by the underlying density functional approximation. To prevent any potential duplication of calculations inside the specified area, applying a damping factor to the DFT-D2 contribution is necessary. Furthermore, having a smooth and uninterrupted connection in the regions between the short-range and long-range components is vital. This area will be referred to as the "medium-range region" in subsequent discussions. Both of these prerequisites are satisfied by using a damping function denoted as $f_{\text{damp}}^{\text{DFT-D2}}$, which is characterized by the following mathematical expression:

$$\boldsymbol{f_{damp}^{DFT-D2}}(\boldsymbol{R_{AB}}) = \frac{\mathbf{1}}{\mathbf{1}+\boldsymbol{e}^{-\mathbf{20}(\frac{\boldsymbol{R_{AB}}}{\boldsymbol{R_r}}-\mathbf{1})}} \tag{2.29}$$

The value of R_r represents the summation of van der Waals radii, which were obtained via restricted-open-shell Hartree-Fock density contour plots and afterward adjusted by a scaling factor of 1.10. The selection of this number is motivated by the objective of enhancing intermolecular distances, especially in systems that include heavier atoms. The choice of the exponent of 20 in Eq. 2.29 was made to have more substantial corrections for distances that are neither very close nor exceptionally far.

The C_6^{AB} dispersion coefficients used in DFT-D2 are empirical and derived from element-specific coefficients (C_6^{AB} and C_6^{B}) by calculating a geometric mean.

$$\boldsymbol{C_6^{AB} = \sqrt{C_6^A C_6^B}} \tag{2.30}$$

Undoubtedly, DFT-D2 can be considered a significant addition to the DFT [25]. Although there were some empirical components, the approach offered a simple, straightforward method for addressing non-covalent interactions within the framework of KS-DFT. Additionally, it is user-friendly and does not need much technical expertise, making it accessible to non-experts. The utilization of DFT-D2 corrected treatments has facilitated a more precise characterization of non-covalent interactions, but, more significantly, the outcomes from these corrections have contributed to a deeper understanding of the significance of London dispersion in thermochemistry [26]. Moreover, these findings have gradually challenged the misconception that dispersion effects are insignificant due to their perceived smallness [27].

However, it is also essential to address the limitations of this technique. The determination of van der Waals radii and C_6 coefficients was limited to the main-group elements, only up to xenon. The values for scandium have been allocated to all 3d transition metals, whereas the values for yttrium have been given to all 4d metals. However, it is well acknowledged that C_6 coefficients are influenced by factors such as hybridization or oxidation states [28]. Specific issues have also been documented with both charged and neutral compounds of alkaline metals [22]. As elucidated in the subsequent section, the above concerns have paved the way for developing DFT-D3 corrections.

2.5.2. DFT-D3

DFT-D3 is envisaged as an enhanced version of DFT-D2. The method's applicability extends to the first 94 elements of the periodic table. In contrast to the DFT-D2 approach, both main-group elements and transition metals are now addressed equally. The primary distinction from its previous version is adaptability and dependence on the system of its dispersion coefficients,

hence providing a means for broader application and increased robustness. The distinguishing characteristic of DFT-D3 lies in its coefficients solely dependent upon the specific molecular geometry provided. The idea of fractional coordination numbers (CNs) is introduced to determine the coordination number for each atom A in the system. It is calculated using the following formula:

$$\mathbf{CN^A} = \sum_{B \neq A} \frac{1}{1+e^{-16\left(\frac{4\left(R_{A.COV}+R_{B.COV}\right)}{3R_{AB}}-1\right)}} \tag{2.31}$$

The covalent radii, denoted as R_{cov}, are determined using a self-consistent additive methodology developed by Pyykkö and Atsumi [29], which combines theoretical calculations and experimental observations. Determining the fractional coordination number for a particular atom is mainly influenced by the atoms located in its immediate surroundings. The improvised DFT-D3, namely the DFT-D3(BJ) variation, was introduced in 2011, and it uses a rational damping function provided by Becke and Johnson [30].

$$E_{disp}^{DFT-B3(BJ)} = -\frac{1}{2}\sum_{A \neq B}\sum_{n=6,8} s_n \frac{C_n^{AB}}{R_{AB}^n + \left[f_{damp}^{DFT-D3(BJ)}(R_{BJ}^{AB})\right]^n} \tag{2.32}$$

Although the DFT-D3(BJ) formulation (Eq. 2.32) is similar to the DFT-D2 corrections, it is distinguished by the inclusion of two multipole terms. The first term is the well-known sixth-order component that incorporates isotropic dispersion coefficients C_6^{AB} for every pair of atoms. In contrast, the subsequent term is of eighth order and involves dispersion coefficients C_8^{AB}. This term exhibits a diminishing trend as interatomic distances decrease, ultimately approaching zero. Its formulation is specifically tailored to include the influence of medium-range phenomena. In this context of the subject matter, the damping function is

$$f_{damp}^{DFT-D3(BJ)}\left(R_{BJ}^{AB}\right) = a_1 R_{BJ}^{AB} + a_2 \tag{2.33}$$

The adjustable parameters a1 and a2 control the dispersion correction within the short- to medium-range regimes. The following equation in the DFT-D3(BJ) framework introduces the parameter R_{BJ}^{AB}, which directly correlates with the dispersion coefficients.

$$R_{BJ}^{AB} = \sqrt{\frac{C_8^{AB}}{C_6^{AB}}} \tag{2.34}$$

To include DFT-D3 in periodic systems, it is necessary to carry out an extra summation over the translation vectors T of the system's unit cell.

$$E_{disp} = -\frac{1}{2}\sum_{AB}\sum_{n=6,8}\sum_{T} s_n \frac{C_n^{AB}}{|R_{AB}+T|^n+\left(a_1 R_{BJ}^{AB}+a_2\right)^n} \tag{2.35}$$

The distance between atoms A and B inside the same unit cell is called R_{AB}. The parameters and variables that have not been previously defined have the exact definition as those specified before for the molecular scenario. The essential differences between the DFT-D2 and D3 methods are summarized in Table 2.1.

Table 2.1. The significant differences between DFT-D2 and DFT-D3 [31].

Sl.no	Properties	DFT-D2	DFT-D3(BJ)
1	Multipole terms	R_{AB}^{-6}	R_{AB}^{-6} and R_{ABJ}^{-8}
2	It can be used for	The first 34 main-group elements; limited applicability to 3d and 4d metals	The first 94 elements in the periodic table
3	Dispersion coefficients	Empirical: fixed for each element	Based on fractional atomic coordination numbers, Flexible and system-dependent
4	vdW/cut-ff radii	Fixed for each element	Fixed for each atom pair
5	Fit parameters	s_6 in Eq. 2.28	s_8 in Eq. 2.32 and a_1, a_2 in Eq. 2.33

2.6. Basis Sets

A basis set refers to a set of functions, also known as basis functions, that are combined by

linear combinations to construct molecular orbitals in quantum chemical computations. Since these functions are often atomic orbitals centered on atoms but can be of any unknown function [32], expressing them as a series of well-known functions is conventional. In quantum chemistry, computational calculations are often performed using a finite set of basis functions. The finite basis can be expanded using a complete set of functions so that calculations approach the basis set limit. This expansion can be represented as,

$$\boldsymbol{\psi_i(r)} = \sum_{j=1}^{\infty} \boldsymbol{C_j \phi_j(r)} \tag{2.36}$$

where $\{\phi_j\}$ makes a complete set.

2.6.1. Plane-wave basis sets

Plane-waves can be described as basis functions that are both periodic and delocalized. In the quantum chemical computation of solid-state materials, plane-wave basis sets may be extended to complement the existing localized basis sets. Generally, a limited set of plane-wave functions is used, including just those plane-waves with kinetic energy below a designated cut-off energy threshold, which is selected for a given computational analysis. In some cases, plane-wave basis functions may facilitate the coding process for integrals and operations, as compared to the localized basis set.

One of the challenges connected with using plane-wave basis sets is the discontinuity in the number of basis states when the energy cut-off is changed [32]. However, this issue may be resolved by using dense sets of k-points. In practice, using plane-wave basis sets in conjunction with an 'effective core potential' or pseudo-potential is common. This approach allows the plane-waves to reflect the valence charge density. The observed phenomenon can be attributed to the inner electrons' inclination to congregate close to the atomic nuclei. As a result, there is a significant expansion of the wave function and gradients of density near the nuclei. Describing these characteristics employing a plane-wave basis set becomes challenging unless a high energy cut-off corresponding to a small wavelength is employed. Using a plane-

wave basis set in conjunction with a core pseudo-potential is sometimes called a pseudo-potential plane-wave (PSPW) computation.

Moreover, plane-wave basis sets do not exhibit basis-set superposition errors due to the orthogonal nature of all functions inside the basis and their lack of association with any specific atom. Another significant benefit of using a plane-wave basis is its built-in capacity to converge smoothly and monotonically towards the desired wave function. The locations of atomic nuclei do not influence plane waves. Hence, correction factors are unnecessary for force calculations, unlike localized basis sets. One limitation of this approach is the need for an extensive set of basis functions for accurate computations. Additionally, pseudo-potentials are necessary due to the fast variation of the core wave functions.

2.7. Pseudo-potentials

Hellmann first proposed the pseudo-potential methodology in 1934 [33]. The pseudo-potential method accounts for the intricate dynamics associated with the movement of the core, specifically the non-valence electrons and the nucleus of an atom. This method involves substituting the conventional Coulombic potential term for core electrons, typically present in the Schrödinger equation, with a modified effective potential term referred to as a pseudo-potential. The valence wave function produced is made to be orthogonal with all core states. This approach explicitly considers just the chemically engaged valence electrons, whereas the core electrons are considered "frozen" and evaluated with the nuclei as hard, non-polarizable ion cores. Norm-conserving pseudo-potentials are formulated by selecting an atomic state as a reference and ensuring that the pseudo- and all-electron valence Eigen states possess identical energies and amplitudes, maintaining consistent densities beyond a specific core cut-off radius r_c.

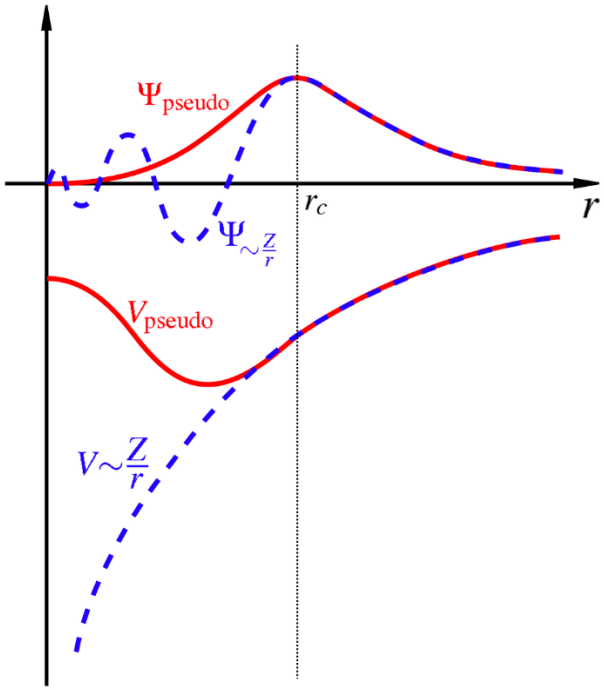

Fig. 2.1. The diagram illustrates the schematic representation of both all-electron potentials (represented by solid lines) and pseudo-potentials (shown by dashed lines), together with their respective wave functions [32]. The point where the values of all-electron and pseudo-potential intersect is often referred to as the critical radius, denoted as r_c.

Hence, it is possible to consider the core electron states fixed and develop a pseudo-potential for each atomic species that incorporates the influences of the nucleus and core electrons [34]. It does not represent the rapid oscillations, significantly reducing the number of plane-waves required to describe them (See Figure 2.1). A pseudo-potential is generated to accurately represent the real potential beyond a certain radius, known as the core radius. It is expected that every pseudo-wave function would exhibit a match with its respective actual wave function beyond a certain distance. It is also essential that the charge densities acquired outside the core area show similarity to the actual charge density. Therefore, it is necessary to integrate the squared amplitudes of the actual and pseudo-wave functions across the core area to be equivalent and is often called norm-conservation [35].

Pseudo-potentials are first computed for an isolated atom generated using an *ab initio* approach. The wave functions that accurately represent an isolated atom's quantum state are determined by using an all-electron DFT approximation. The valence wave functions created in this process are then adjusted inside the core area to eliminate oscillations while still adhering to the norm-conservation constraint. The Schrödinger equation is then used reversely to get the pseudo-potential that would accurately generate the pseudo-wave functions. This pseudo-potential can be used in a diverse range of systems, in contrast to semi-empirical potentials specifically designed to define a particular atomic environment. The projector-augmented wave technique put forward by Bloch [36] is a more efficient way to do DFT calculations.

2.7.1. Projected Augmented Wave (PAW) approach

It is an extension of the linear augmented plane-wave and pseudo-potential methods. It is more precise and efficient than ultra-soft pseudo-potentials (US-PP) and norm-conserving pseudo-potentials. The basis of the augmented wave approach is that the real electron wave functions exhibit distinct spatial behaviors, such as fast oscillations around the nucleus and smooth conduct in the interstitial area. Considering a partial wave expansion of the Kohn-Sham wave function $|\psi\rangle$, which is an all-electron wave function,

$$|\boldsymbol{\psi}\rangle = \sum_i |\boldsymbol{\phi_i}\rangle \boldsymbol{C_i} \tag{2.37}$$

where ϕ_i are solutions of the Schrodinger equation, which are difficult to compute because they vary rapidly near the core region. Therefore, we transform $|\phi_i\rangle$ into practically convenient pseudo-wave functions using the transformation operator τ. The PAW method is centred on a change that maps the physical full all-electron wave function $|\psi\rangle$ onto the nonintersecting pseudo-wave functions $|\breve{\psi}\rangle$.

$$|\boldsymbol{\psi}\rangle = \boldsymbol{\tau}|\breve{\boldsymbol{\psi}}\rangle \tag{2.38}$$

Given the knowledge of the transformation τ, it is possible to compute physical quantities based

on the expected value.

$$\langle \boldsymbol{A} \rangle = \langle \boldsymbol{\psi} | \boldsymbol{A} | \boldsymbol{\psi} \rangle = \langle \widetilde{\boldsymbol{\psi}} | \boldsymbol{\tau}^{\dagger} \boldsymbol{A} \boldsymbol{\tau} | \boldsymbol{\psi} \rangle \quad (2.39)$$

To achieve the difference between $|\psi\rangle$ and $|\breve{\psi}\rangle$ in the vicinity of the core by accumulating local atom-centered contributions, we have

$$\boldsymbol{\tau} = \mathbf{1} + \sum_{\boldsymbol{R}} \boldsymbol{\tau}_{\boldsymbol{R}} \quad (2.40)$$

The variable $\tau_R$exhibits a non-zero value only inside the augmentation area Ω_R. We can now create pseudo partial waves using the expanded pseudo-wave function.

$$|\widetilde{\boldsymbol{\psi}}\rangle = \sum_{\boldsymbol{i}} |\widetilde{\boldsymbol{\phi}}_{\boldsymbol{i}}\rangle \boldsymbol{C}_{\boldsymbol{i}} \quad (2.41)$$

The coefficients C_i may be expressed as an inner product with a collection of projector functions, $|p_i\rangle$, because the operator τ is linear.

$$\boldsymbol{C}_{\boldsymbol{i}} = \langle \boldsymbol{p}_{\boldsymbol{i}} | \widetilde{\boldsymbol{\psi}} \rangle \quad (2.42)$$

In the area of augmentation, they have to fulfill

$$\langle \boldsymbol{p}_{\boldsymbol{i}} | \widetilde{\boldsymbol{\phi}_{\boldsymbol{j}}} \rangle = \boldsymbol{\delta}_{\boldsymbol{ij}} \quad (2.43)$$

Therefore, it is necessary to have three quintiles for the transformation τ, which are outlined as follows:

(i) The real or full-electron partial waves may be represented as $|\phi_i\rangle$.

(ii) Pseudo partial waves, denoted as $|\widetilde{\boldsymbol{\phi}}_{\boldsymbol{i}}\rangle$, are being considered.

(iii) The functions of a projector may be represented as $|p_i\rangle$.

Furthermore, it is possible to articulate this concept in a written format.

$$\boldsymbol{\tau} = \mathbf{1} + \sum_{\boldsymbol{i}} (|\boldsymbol{\phi}_{\boldsymbol{i}}\rangle - |\widetilde{\boldsymbol{\phi}}_{\boldsymbol{i}}\rangle \langle \boldsymbol{p}_{\boldsymbol{i}}| \quad (2.44)$$

The PAW technique is often used with the frozen core approach, whereby the core states are assumed to remain unperturbed by the surrounding ion environment.

2.8. K-point sampling

The electronic states in a solid are restricted to a certain set of k points, which are determined by the boundary constraints that apply to the bulk material. The distribution of permissible k

points exhibits a direct proportionality to the volumetric characteristics of the material. An unlimited number of k points is necessary to accommodate the infinite number of electrons present in the material. However, it is important to note that at each k point, only a finite number of electronic states are occupied. The Bloch theorem [37] enables the transformation of the task of computing an infinite set of electronic wave functions into the scheme of computing a finite set of electronic wave functions at an infinite set of k places. The electronic potential in a bulk solid is influenced by the occupied states at each k point, necessitating a substantial number of computations to determine this potential accurately. However, the electrical wave functions at k sites near exhibit high similarity. Therefore, it is feasible to characterize the electronic wave functions throughout a specific area of k space by using the wave functions at a singular k-point. In this particular case, it is sufficient to consider the electronic states at a limited number of k points to calculate the electronic potential and then ascertain the overall energy of the solid. Various techniques have been developed to provide very accurate estimations of the electronic potential and the contribution of a filled electronic band to the overall energy. These methods include determining electronic states at certain k points inside the Brillouin zone (BZ) [38].

The theory behind the fundamental concepts of electrical energy bands is greatly influenced by the Brillouin zone, a significant topic in materials science. The area inside the k-space, represented by an imaginary plane with coordinates k_x and k_y, where low-k electrons may exist without experiencing diffraction, is referred to as the first Brillouin Zone and is shown in Figure 2.2. The next Brillouin zone is seen in the illustration, including electrons defined by k values ranging from π/a to $2\pi/a2$. These electrons are in motion along the ±x and ±y directions, and the range of permissible *k* values becomes progressively narrower as the diagonal orientations are approached.

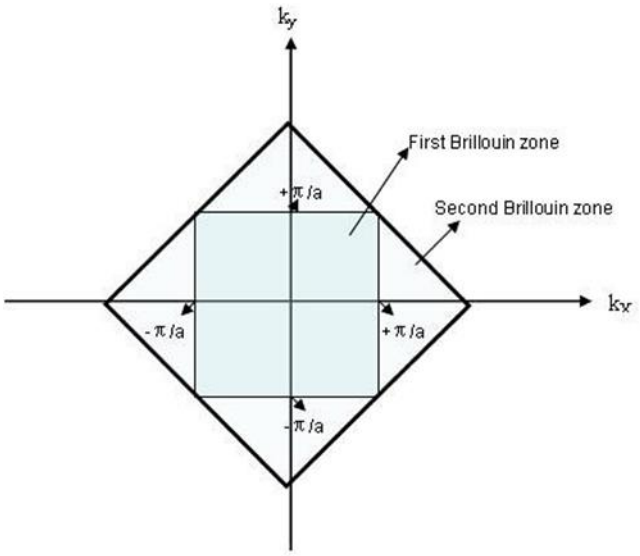

Fig. 2.2. The first and second Brillouin zones of a two-dimensional square lattice [39].

In a generic context, the construction of a Brillouin zone may be achieved by adhering to the principle that a wave incident upon a lattice would experience significant scattering in the presence of a reciprocal lattice vector K under certain conditions like

$$\boldsymbol{k}.\ \boldsymbol{K} = \frac{\mathbf{1}}{\mathbf{2}}\boldsymbol{K}^{\mathbf{2}} \tag{2.45}$$

The initial region refers to the collection of points closer to the origin than any other reciprocal lattice point. The second zone comprises the group of points accessed by passing a single border of a zone. The third zone includes the collection of points attained by traversing at least two boundaries between zones. The process of constructing Brillouin zones for a three-dimensional lattice becomes more complex. As an example, it can be seen that the first Brillouin zone of a basic cubic lattice has a simple cubic shape. However, in contrast, the first Brillouin zones of a body-centered cubic (bcc) and a face-centered cubic (fcc) lattice exhibit much more intricate characteristics. Figure 2.3 illustrates the first Brillouin zone of a basic cubic lattice, including the symmetry points.

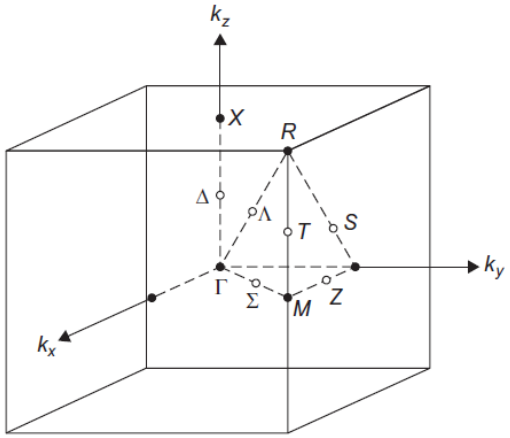

Fig. 2.3. The Brillouin zone of the simple cubic lattice [40].

The point Γ is located near the center of the zone, as seen in Figure 2.3. The point R is located at one of the corners of a cube, which is linked to the other seven corners so that all eight corners coincide at a single point. Both Γ and R may be represented by the same mathematical structure, known as the cubic group. Point X is located at the point of intersection between the k_z axis and the bottom face of the cube. Point M is located at the intersection of the k_{ey} plane and the vertical edges, with three corresponding points to M. Both M and X possess the same symmetry elements of 4/mmm. T is equal to the three points located on the remaining vertical edges. Both points T and Δ belong to the same point group, 4mm. The point Λ has a point group of 3m. The points Σ and S exhibit holomorphicity for the 2mm symmetry group. Point Z exhibits the presence of two mirror planes and a two-fold axis. Figure 2.4 illustrates the Brillouin zone of the hexagonal close-packed structure, specifically in the context of graphene, showcasing the symmetry points.

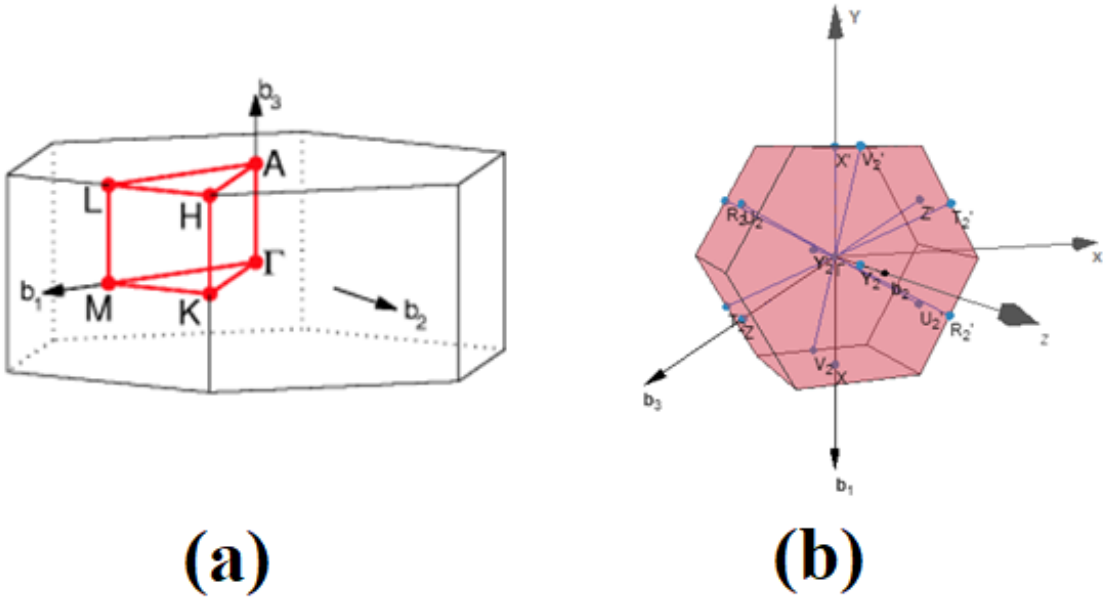

Fig. 2.4. (a) Brillouin zone of a hexagonal lattice. Path: **Γ-M-K-Γ**-A-L-H-A|L-M|K-H. (b) Module obtained from seek-path to visualize band paths in the Brillouin zone of graphene structures.

The two locations, K and K', located at the corners of the graphene Brillouin zone, as seen in Figure 2.5, have significant relevance in graphene physics. These structures are often referred to as Dirac points. The locations of the particles in momentum space are determined by

$$\boldsymbol{K} = \left(\frac{2\pi}{3a}, \frac{2\pi}{3\sqrt{3}a}\right), \boldsymbol{K'} = \left(\frac{2\pi}{3a}, -\frac{2\pi}{3\sqrt{3}a}\right) \tag{2.46}$$

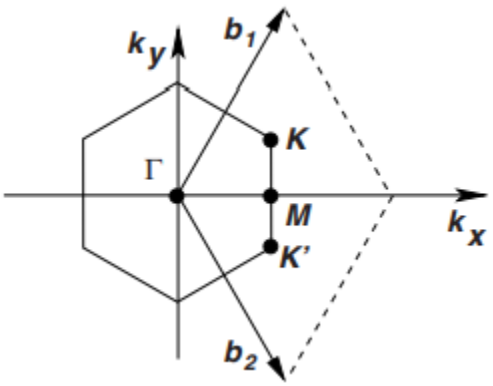

Fig. 2.5. The Brillouin zone corresponding to the Dirac cones is located at the K and K′ points [41].

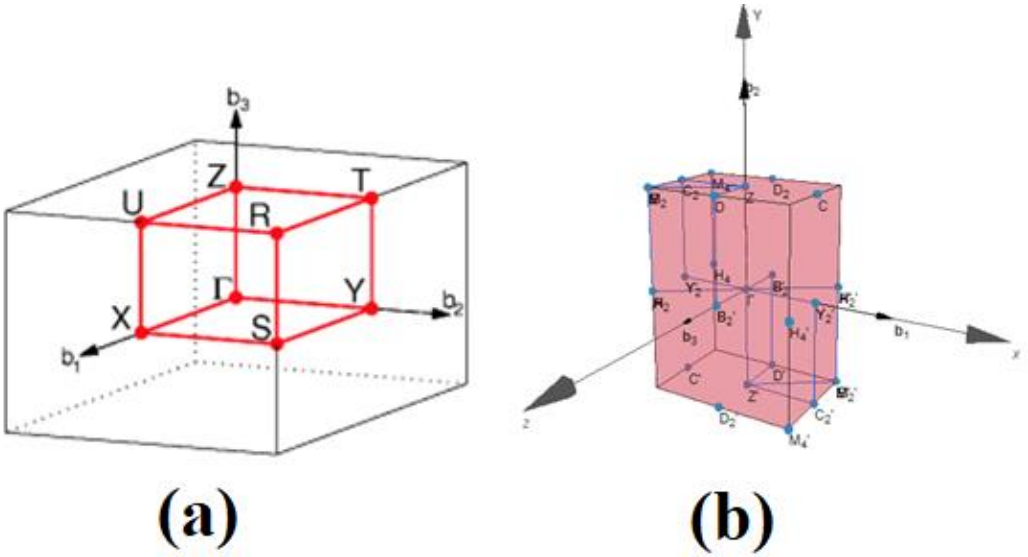

Fig. 2.6. (a) Brillouin zone of Orthorhombic lattice. Path: **Γ-X-S-Y-Γ**-Z-U-R-T-Z|Y-T|U-X|S-R. (b) Module obtained from seek-path to visualize band paths in the Brillouin zone of phosphorene structures. An example of band structure using this path can be seen in Chapter 7.

2.9. Band structure

The band theory is a theoretical framework in solid-state physics that offers a quantum description of the potential energy levels available to electrons inside a solid material. This model also provides valuable insights into the phenomenon of electrical conductivity. The concept originates from the principles of molecular orbital theory. By using the above procedures, it is possible to get a proficient estimate of the electronic potential and total energy of an insulator or semiconductor by calculating electronic states at a reduced quantity of k locations. Calculating the electronic potential and total energy becomes more challenging in metallic systems due to the need for a denser collection of k points to accurately describe the Fermi surface.

The energy levels permitted inside a solid are restricted to a band, the width of which is typically on the scale of an electron volt. The crystal structure and the degree of overlap between atomic orbitals dictate this width. The energy band, as its name suggests, represents

a much broader range in which electrons are allowed to exist. In the context of solid-state physics, the conduction band refers to the highest energy band inside a solid material, whereby electrons are not confined to the atomic nucleus's influence, enabling their unrestricted mobility. An energy gap is present between the conduction band and the valence band in solids, depending on their inherent characteristics, resulting in the exclusion of electrons. The occupation of energy bands is determined by using Fermi-Dirac statistics, whereby electrons at a temperature of absolute zero (0 K) occupy all energy levels below the Fermi level.

2.9.1. Direct and indirect band structure

The band-gap measures the minimal energy separation between the maximum energy of valence band and the minimum energy of the conduction band. However, it is important to note that the valence band's highest energy level and the conduction band's lowest energy level do not often occur at the same electron momentum value. In a direct band gap semiconductor, the momentum values at the top of the valence band and the bottom of the conduction band are equal, as seen in Figure 2.7.

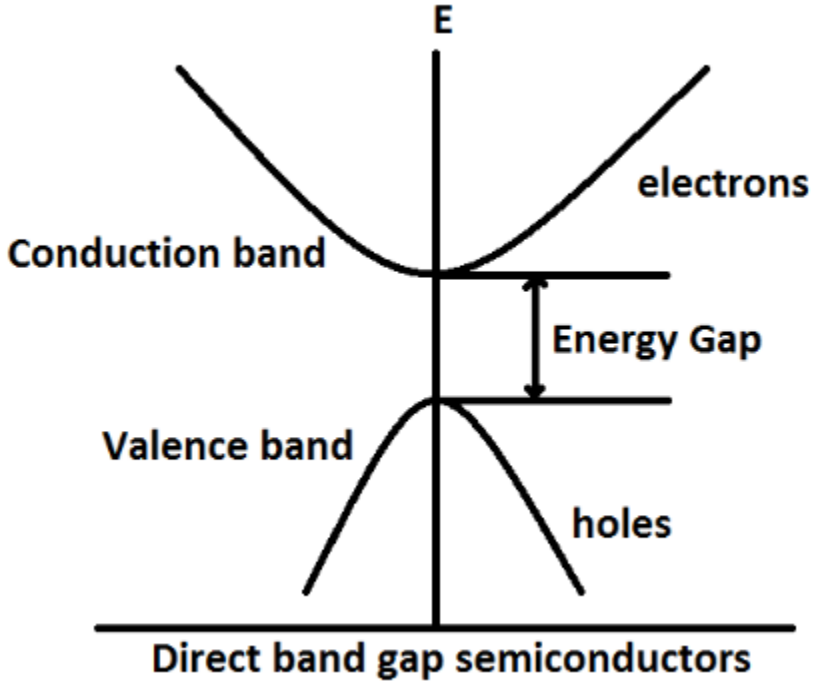

Fig. 2.7. The figure depicts direct band-gap [42].

In the context of an indirect band-gap semiconductor, as seen in Figure 2.8, it is observed that the peak energy of the valence band is situated at a distinct momentum value from that of the lowest energy point in the conduction band. The distinction between the two entities has significant relevance in optical devices, primarily due to the photon's capacity to provide the requisite energy for generating an electron-hole pair. In a direct band-gap semiconductor, generating an electron-hole pair may be facilitated by a photon with energy, E_g, denoting the band-gap energy. This process is rather effortless due to the small velocity required for the electron. Nevertheless, it is essential for an electron to substantially alter its momentum in order for a photon with energy E_g to generate an electron-hole pair in an indirect band-gap semiconductor. It is feasible but contingent upon the electron's interaction with a photon for energy acquisition and a phonon, a lattice vibration, for momentum alteration.

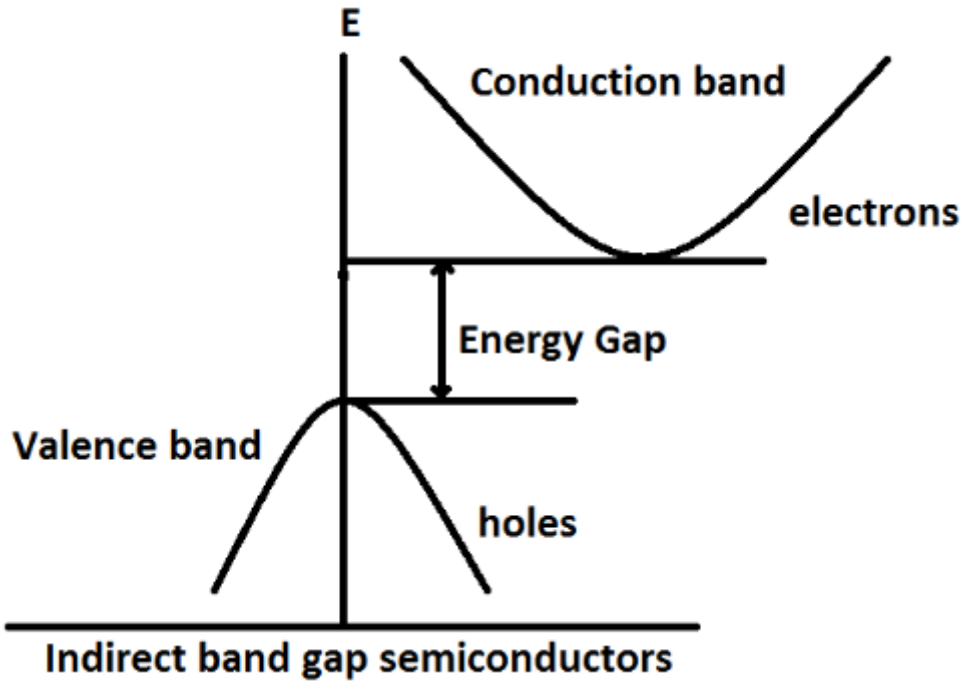

Fig. 2.8. The figure depicts indirect band-gap [42].

The progress of the indirect process is much slower due to the need for three things - an electron, a photon, and a phonon to intersect in order for the process to advance concurrently. This phenomenon may be likened to chemical processes, whereby a specific phase of a reaction

exhibits a much higher rate when involving the interaction between two molecules compared to a process that deals with the interaction of three molecules. This idea also applies to the process of electron-hole recombination, which results in the emission of photons. The efficiency of the recombination process is much higher in direct band-gap semiconductors than indirect band-gap semiconductors since the former may undergo recombination directly. At the same time, the latter necessitates mediation via a phonon. Due to these above factors, gallium arsenide and other direct band-gap semiconductors, such as graphene and phosphorene, are used in the fabrication of optical devices such as light-emitting diodes (LEDs) and semiconductor lasers, as well as gas sensors. Conversely, silicon, an indirect band-gap semiconductor, is not utilized for these purposes.

2.10. Adsorption energy calculations

In the adsorption process, an atom, ion, or molecule (adsorbate) is bonded to the surface of a solid (adsorbent), and the resulting decreased energy is known as "adsorption energy." Adsorption energy, E_a, can be computed by subtracting the energy of the adsorbed structure from the sum of the energy calculated individually for each structure that makes up the adsorption complex, which could be written as

$$\boldsymbol{E_a} = \left[\boldsymbol{E_{system}} - (\boldsymbol{E_{adsorbent}} + \boldsymbol{E_{adsorbate}})\right] \tag{2.47}$$

Therefore, to determine the adsorption energy (E_a), it is necessary to compute the energies for the three models outlined below.

1. A supercell configuration characterizes the structure of the adsorbent.
2. The adsorption structure refers to the arrangement of a surface structure, including the adsorbent, which constitutes the adsorption system.
3. The adsorbate inside the vacuum (referred to as adsorbate).

To determine the energy of the surface structure, it is advisable first to optimize the unit cell and then construct the supercell based on the optimized unit cell. Due to the presence of a

vacuum, the calculation time for a surface structure is very lengthy. However, this issue may be mitigated by using an optimized structure, which reduces the overall calculation time. When calculating an adsorption structure, it is essential to exercise caution in selecting appropriate calculation choices. In contrast to bulk unit cells, the computational time required for surface calculation is notably longer. The model's symmetry reduction is attributed to the presence of the adsorbate. To reduce the computational time, it is possible to use a strategy of breaking the calculation into many sequential parts. In this study, we have used a precise energy cut of 520 eV for graphene computations and 450 eV for phosphorenes, ensuring reliable results.

To determine the energy of the adsorbate, it is necessary to position it inside a sufficiently large vacuum space. The interaction between periodic images may affect the computation if the cell size is insufficient due to the assumption of periodic boundary conditions where the cell (consisting of lattice and basis) is infinitely replicated. Therefore, it is essential to appropriately and adequately adjust the cell dimensions to ensure that the spacing between regularly replicated molecules is equal to or greater than 10 Å. To prevent further contact between surfaces, a vacuum of 15 Å along the z-axis was implemented for the graphene system. In contrast, a vacuum of 20 Å was used for the phosphorene system calculations.

2.11. Charge calculations: Bader charge analysis

To further study the effects of adsorbed molecules on the electronic properties of graphene, charge density surfaces are calculated for the systems with and without the adsorption for the visualizing the various interactions between the adsorbate and adsorbent. The charge transfers between the gas molecule and the surface is calculated with Bader charge analysis [43]. For the system of gas molecules adsorbed on various surfaces, the charge density difference $\Delta\rho$ is calculated as the charge density variation of gas molecules before and after the adsorption as in Eq. 2.48,

$$\Delta\rho = \rho\,(adsorbed\ complex) - (\rho(surface) + \rho\,(gas\ molecule)) \quad (2.48)$$

Where ρ refers to charge density, the Bader charge analysis, commonly known as the atoms-in-molecules hypothesis, involves partitioning molecules into individual atoms based on the concept of zero flux surfaces. A zero flux surface may be described as a two-dimensional surface where the charge density reaches its minimal value after traversing the surface. The Bader charge of an atom refers to the aggregate charge contained inside the atomic volume, also known as the Bader volume, of each atom.

2.12. Available software codes for *ab initio* calculations

In recent decades, there has been substantial growth in the scope of first-principle simulations within the field of condensed matter physics. These simulations have now extended beyond the domains of physics and chemistry, including disciplines such as life sciences, earth sciences, nanoscale sciences, and materials sciences. This achievement may be attributed to the simultaneous advancements in computer efficiency and the widespread use of DFT methodologies. Despite the considerable work needed for program creation, many programs have been documented in the existing literature. In this context, our focus is limited to software applications designed for broad molecular computations used by a diverse community of chemists and physicists. Some examples of computational chemistry software packages include ONETEP, Gaussian, GAMESS, VASP, QUANTUM-ESPRESSO, DMol3, etc. There are variations in the implementation of the above codes, as some codes demonstrate greater compatibility with some specific issues and materials than others. VASP utilizes plane-wave basis sets for its applications in computational material science.

2.12.1. VASP application

The code was written by Kresse and Furthmuller in 1995 at the University of Vienna in Austria. VASP 5 offers a robust and efficient platform that grants advanced access to VASP, a prominent first-principles DFT code well-recognized in the industry. MedeA VASP 5 [44] is a software program incorporated within the MedeA atomistic simulation environment. It offers

a range of features, including extensive structural databases, tools for model construction, and fully automated modules for property analysis. The software also provides a user-friendly graphical interface, allowing easy navigation and interaction. Additionally, VASP 5 offers access to automation and large-scale high-throughput capabilities, enabling efficient processing of large datasets. It also facilitates efficient calculation of properties and allows for interactive analysis of the obtained results.

To run VASP with minimum configuration, the following input files are necessary: the INCAR file, the POTCAR file, the POSCAR file, and the KPOINTS file.

The INCAR file serves as the primary input file for VASP, playing a pivotal role in specifying the tasks to execute and the corresponding methodologies. The INCAR tags, as provided in the INCAR file, select algorithms and define parameters that VASP uses during the computation.

The POTCAR file is a crucial component that includes the pseudo-potential for each atomic species used in the computational analysis. If the number of species exceeds one, it is customary to merge the POTCAR files of each species using concatenation. The POTCAR file further contains pertinent details on the atoms, such as their mass, valence, and the energy associated with the reference configuration used in the construction of the pseudo-potential. In the case of POTCAR files containing several species, the computation uses the maximum cut-off values (ENMAX or ENMIN).

The POSCAR file is an essential input file for the VASP software. The file in question is a plain text format that includes, at minimum, the lattice geometry and the locations of the ions. Additionally, initial velocities for a molecular dynamics simulation may be optionally supplied in this section. The format of this file is identical to that of the VASP output file CONTCAR.

The KPOINTS file specifies the Bloch vectors, also known as k points, that are used for

sampling the Brillouin zone. The convergence of this sampling is a crucial undertaking in several computations about electronic reduction. The selection of k points is often accomplished by using a regular mesh.

VASP 5 is effectively included inside the MedeA Environment, offering a model development process led by a graphical user interface, quick execution of calculations, and comprehensive analysis functionalities.

All the charge transfer calculations were done with the help of VESTA (short for Visualisation for Electronic Structural Analysis) software. It offers a 3D visualization tool for structural models, volumetric data such as electron/nuclear densities, and crystal morphologies.

Almost all the structures are modeled with the help of Virtual NanoLab. Its graphical interface presents a method of atomic-scale modeling that is user-friendly. The program includes interactive tools that enable the user to create nanosystems, set up and run numerical computations, and see the results. With a few mouse clicks, molecules, nanotubes, crystalline systems, and two probe systems (a nanostructure connected to two electrodes) may be created.

2.13. Conclusions and discussions

Adsorption of gas molecules on two-dimensional surfaces and van der Waals heterostructures can be investigated using various ab initio electronic structure calculations. DFT is the most popular choice currently employed to study properties like binding energy, adsorbate distance from the surface, electronic band-gaps, density of states, and charge transfers [45].

To study the adsorption characteristics of gaseous molecules, we have used the density functional calculations, employing periodic boundary conditions. We have considered supercells of monolayer graphene, bilayer graphene, and phosphorene two-dimensional materials. In our analyses, we have used each simulated system consisting of 4×4 and 5×5 graphene supercells to see the supercell size effects by checking the results against the available experimental results. For the studies of black phosphorene, we have considered 3×3 supercell

(36 phosphorous atoms) representing an isolated sheet for which different doping concentrations and configurations are contemplated.

All the DFT calculations, geometry optimizations, and electronic structure calculations have been performed using the Vienna ab initio simulation package (VASP) as integrated in the MedeA® computational environment with the projector augmented wave (PAW) basis sets and periodic boundary condition. We have mainly used plane-wave basis sets in our quantum chemical stimulations as they converge smoothly to the target function, contrasting with the localized basis sets.

The plane-wave basis sets are popular in calculations involving periodic boundary conditions. They have the advantage in the DFT stimulations: they are orthogonal, computationally simple, and low scaling methods allow easy transformation between real and reciprocal space. Certain integrals and operations are much easier to carry out with plane-wave basis functions than with the localized counterparts. In practice, plane-wave basis sets are often combined with an effective core potential or pseudo potential so that the plane-waves are only used to describe the valance charge density. It is because the core electrons tend to be concentrated close to the atomic nuclei, resulting in significant wave function and density gradients near the nuclei. These are only easily described by a plane-wave basis set if a very high energy cut-off is used. The projector augmented wave method (PAW) is used in *ab initio* electronic structure calculations. It is a generalization of the pseudo-potential and linear augmented-plane-wave methods and allows for DFT calculations to be performed with greater computational efficiency [32].

Valence wave functions tend to have rapid oscillations near ion cores due to the requirement that they be orthogonal to core states; this situation is problematic because it requires many Fourier components (or, in the case of grid-based methods, a very fine mesh) to describe the wave functions accurately. The PAW approach addresses this issue by

transforming these rapidly oscillating wave functions into smooth wave functions, which are more computationally convenient and provide a way to calculate all-electron properties from these smooth wave functions. This approach is somewhat reminiscent of a change from the Schrödinger picture to the Heisenberg picture.

We have employed the GGA-PBE with the Perdew–Burke–Ernzerhof (PBE) [18] exchange-correlation functional in the DFT framework to investigate the adsorption properties of various molecules on the chemically doped nanostructures. Though there are many GGA functions the most popular and preferred function is the PBE. GGA (Generalized Gradient Approximation) is a group of functional, not a particular one. PBE0 is a hybrid functional (different class from GGA) based on PBE. Hybrid functionals include an additional term representing the HF exchange, which is not present in GGA functionals. In short, the Perdew-Burke-Ernzerhof (PBE) functional is very popular because it is a non-empirical functional with reasonable accuracy over a wide range of systems. While PBE is typically not the most accurate GGA (generalized gradient approximation) functional for a given system, it usually is not too far off either.

By tallying with experimental results, we have used van der Waals corrections like DFT-D2 and DFT-D3 (BJ-damping). The kinetic energy cut-off of the plane-wave expansion is 520 eV to represent the wave function, and for the charge density with a convergence criterion of 0.01 eV^{-1} is kept throughout the calculation in the case of graphene and while considering black phosphorene calculations, kinetic energy is maintained 450 eV.

Chapter 3

Electronic modification of chemically doped graphene surfaces on adsorption of NH_3 and CO

3.1. Introduction

Adsorption of gases on graphene has gained much interest recently and has been the focus of many theoretical and experimental investigations due to the wide variety of applications [1,2]. Such adsorption studies can significantly modify the electronic and other transport characteristics of pristine graphene [3,4]. As graphene-based electronic devices have the disadvantage of being a zero band-gap semi-metallic conductor, a lot of research, both experimental [5] and theoretical [6–8], is dedicated to modulating or engineering its band-gap to change it into the semiconducting regime to tailor its optoelectronic properties. The most important ways to change the electronic band-gap are intrinsically doping the graphene [7–10] with p- and n-type dopants and extrinsically by adsorbing various molecular species on its surface [11–14]. One of the most crucial ways to improve the sensing property of graphene surfaces has been the introduction of foreign atoms or dopants on the graphene layer [11–15]. It is well established that pristine graphene is insensitive or chemically inert to the presence of almost all environmental gaseous molecules [16,17]. Therefore, there is a lot of interest in adsorption on doped graphene and its application as sensors for gaseous species [11–15,18,19].

Some of the previous literature shows that the interaction of graphene with adsorbed gaseous species can drastically alter the electronic properties and, therefore, be used to design ultra-sensitive gas sensors [18,20]. The fact that sensors based on graphene can be used even for sensing individual gas molecules is already established through some experiments [15], as these surfaces have high sensitivity to chemical doping and show remarkable fluctuations in conductivity in the presence of gaseous molecules [18] This invaluable result has also been supported theoretically by Wehling *et al.* [20]. Such adsorbate/adsorbent systems are reported to show changes in the transport properties initiated by controlled surface adsorption of gaseous species [21]. Most adsorption studies deal with strong chemisorption on metal-doped or transition metal-doped graphene [22–25], with very high adsorption energy, as anticipated.

This has been established by a few of the previous adsorption studies of gaseous molecules like CO, NH_3, O_2, NO_2, O_3, SO_2, SO_3, etc., on doped and co-doped graphene surfaces [22–27]. Most of these studies show assertive chemisorptive behavior, where the entire electronic properties of graphene get altered. However, a semi-metal doped with a transition metal or a metal is expected to remain metallic and will not be suitable for semiconductor based sensing devices. Therefore, the primary interest is to modulate the band-gap of graphene through doping and molecular adsorption to improve its selectivity and sensitivity even with traces of adsorbates. It has been shown by a recent theoretical investigation [7] that the band-gap of graphene can be opened up by substitutional doping by replacing carbon atoms with boron or nitrogen, thus inducing p-type or n-type semiconducting characteristics. The type and the density of charge carriers can also be modulated by doping at different sites with different mole fractions [7,8].

The previous adsorption studies on doped graphene surfaces focus only on surfaces with a single dopant [27] and also mainly on transition metal-doped surfaces [22–27]. Our principal interest in the current work involves the study of molecular adsorption on graphene surfaces doped with boron and nitrogen, with varied concentrations of the dopants. In particular, the significant objectives deal not only with the electronic structure alterations with increased dopant concentrations but also with the different configurational patterns on which adsorptions of CO and NH_3 are considered. It is interesting to explore how chemically modified graphene can be sensors for toxic environmental gaseous species like CO and NH_3. One of our previous investigations showed that boron-doped SWCNT could be a potential sensor for gases like NH_3 [28].

Even though there are a few adsorption studies on singly doped surfaces, the aspect of adsorption onto surfaces with different mole fractions of dopants and varied configurations has yet to be explored, making this study distinctive and relevant. It is of interest to have the band-

gap of the semi-metal graphene changed to a semiconducting regime, and the study may open up its potential applications in new technologies in nanoscale electronic devices. Such doped graphene surfaces will have an additional advantage over the conventional indirect band-gap semiconductor, silicon, of being a direct band-gap semiconductor. Therefore, the study on chemically modified graphene and its molecular adsorptions are fascinating and pave the way for creating direct band materials for applications in optoelectronic devices. Moreover, studying the adsorption of potent gaseous molecules like carbon monoxide and ammonia on surfaces where the transport properties can be governed may find application as potential sensors for these molecules.

3.2. Results and discussion

To study the gaseous molecules' adsorption characteristics, we have used the first principle density functional calculations, employing periodic boundary conditions. Each simulated system consists of a 4×4 graphene supercell (32 carbon atoms) representing an isolated graphene sheet for which different doping concentrations and configurations are considered. In the case of a singly doped graphene sheet, a boron atom or nitrogen has substituted a carbon atom. The respective concentration of dopants when one carbon atom is substituted is 3.12%. Furthermore, increased concentrations of the dopants are also considered, where the different arrangements of boron yielded different surface configurations, as shown in Figure 3.1. For the adsorption studies, we construct a cubic supercell of height 15 Å with a single adsorbate molecule inside. We have implemented DFT calculations with a force convergence criterion of 0.01 eV $Å^{-1}$ and an energy convergence precision of 10^{-2} eV for the adsorption systems. Additionally, only the Gamma point is sampled in its Brillouin zone. Adsorption of a single molecule of CO and NH_3 is considered on the different patterns where the most important physical quantity to define the strength of adsorption interactions is the binding or adsorption energy, and is calculated with the help of Eq. 2.47 in Chapter 2, described

as,

E_{ad} = E (CO/NH_3–graphene complex) - (E (graphene surface) + E (CO/NH_3 molecule)).

Here, E (CO/NH_3–graphene complex), E (graphene surface), and E (CO/NH_3 molecule) are the total energies of the adsorbed system, intrinsic/doped graphene surface, and the gas molecule, respectively. According to this definition, the negative value of the adsorption energy implies favorable adsorption and vice versa.

3.2.1. Boron-doped graphene

Doping with boron and nitrogen is the most appropriate for graphene as the two-dimensional structure is least disturbed by including similarly sized dopants [28]. Boron is chosen as a favorable dopant because no substantial distortions in surface lattice geometry are noticed, and the planarity of the surface is retained. The boron carbon distance is found to be 1.42 Å, and after optimization, it has increased in the range of 1.45–1.48 Å, and the C–C bond length in the vicinity of doping is 1.45 Å and 1.39 Å away from it. A system of 4×4 supercells, with 32 carbon atoms, is constructed with the doping of impurities like boron to study the adsorption characteristics of common pollutant gases like CO and NH_3 on such a surface. We examine three different concentrations of doping, 3.12, 6.25, and 9.37%, and seven different doping patterns for boron-doped graphene. Except for the single boron doped, these patterns are defined in Figure 3.1 for 6.25 and 9.37% dopant concentrations of boron. The graphene surface with a 3.12% boron concentration is abbreviated to as BG; a similar surface with the same nitrogen concentration is called NG.

To understand the effect of p- and n-type doping on the semi-metallic Dirac cone material graphene, we have initially calculated the band structure of boron doped and nitrogen doped graphene (3.12% of doping concentration). The main idea of doping is to modify the electronic and optical properties. The electronic band structure diagrams for boron and nitrogen doped graphene along with that of pristine graphene are plotted in Fig. 3.2.

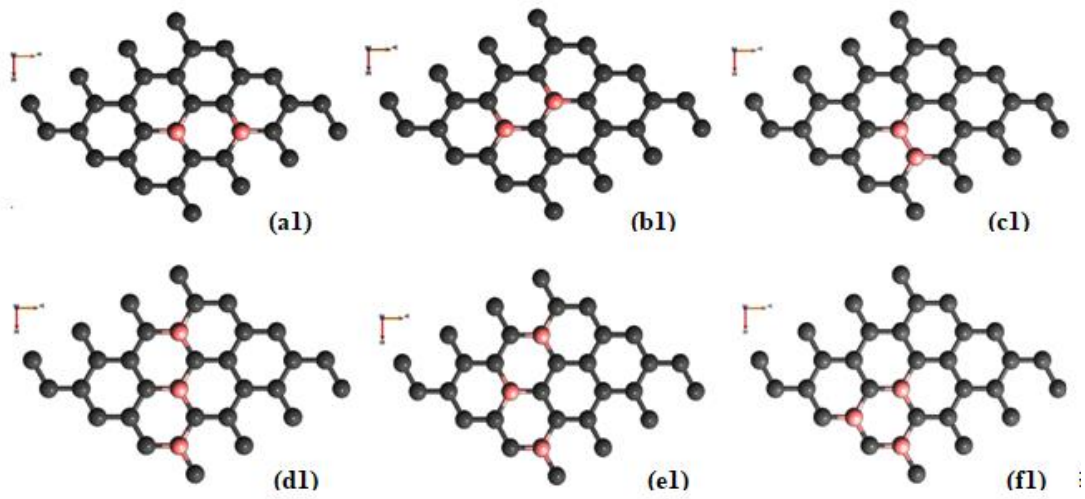

Fig. 3.1. The ball and stick model of 6.25% and 9.37% boron-doped graphene surfaces in three different configurations of the doped boron depicted by the names, 'a1-f1', respectively. The grey color represents the carbon atoms, while pink represents the boron atom.

The band-gap for graphene with a boron concentration of 3.12% is 0.14 eV and corresponds to p-type doping with Dirac cones appearing above the Fermi level, forming hole states in the valence band. The band-gaps are measured as the difference between the maximum of the valence band and the minimum of the conduction band at the high symmetry point 'K'. This result coincides with the previously reported band-gap opening of 0.14 eV for single boron-doped graphene [7] and also with the experimental value [29]. Using angle-resolved photoemission spectroscopy (ARPES) Vyalikh *et al.* [29] found out the band-gap for the freestanding boron-doped graphene surface is found to be 0.13 eV, close to the theoretical value of 0.14 eV.

In addition to the band-gap, the boron-carbon distance of 1.48Å and the charge transfer of -1.85e (from boron to carbon) also coincide with the previous investigations [7]. The charge transfers of -1.85e are attributed to the hole creation and associated mobility through hole transport due to electron deficiency. The cyan line in the figures corresponding to the band structure represents the Fermi level and is uniformly followed throughout all the chapters.

The electronic band structure diagrams for all boron-doped systems corresponding to

various configurations, from ‘a1’ to ‘f1’, with different doping concentrations, are given in Figure 3.3. When it enters the lattice, the doping atom makes covalent bonds with the carbon atom and changes the structure of graphene. It would modify the electronic structure of graphene and suppress the density of states near the Fermi level; thus, a gap is opened between the valence and the conduction bands.

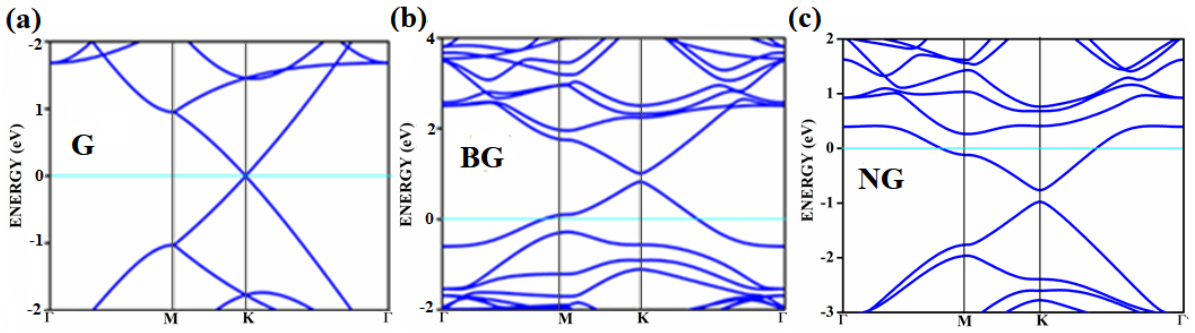

Fig. 3.2. The band structure of pristine graphene (a), showing the Dirac cones with zero band-gap. Parts (b) and (c) correspond to the band-gap opening with the substitutional doping of one carbon on the surface with boron (BG) and nitrogen (NG), respectively.

To confirm the dependability of our procedure, we have also looked into the Fermi level shift of about 0.7– 0.8 eV in the band structure, below the Dirac point in the case of boron-doped systems. In all the above cases, with p-type doping, the Fermi level shifts below the Dirac point, as boron is electron deficient. It is interesting to see how the electrical band-gaps change due to doping.

The electronic band-gaps of graphene, doped with boron and nitrogen, for the various configurations are compiled in Table 3.1. Interestingly, the band-gaps for specific surface configurations are improved drastically compared to the un-doped (0 eV) or singly doped surface (0.14 eV for boron doped and 0.21 eV for nitrogen-doped graphene). Upon doping with boron (creating hole states), the Dirac point shifts above the Fermi level, and a gap appears, making it a p-type system. The n-type substitutional doping of graphene is done with a nitrogen atom with five electrons. The boron orbitals contribute more in the additional levels

created near the Fermi due to the p-type dopant for all the configurations shown in Figure 3.4.

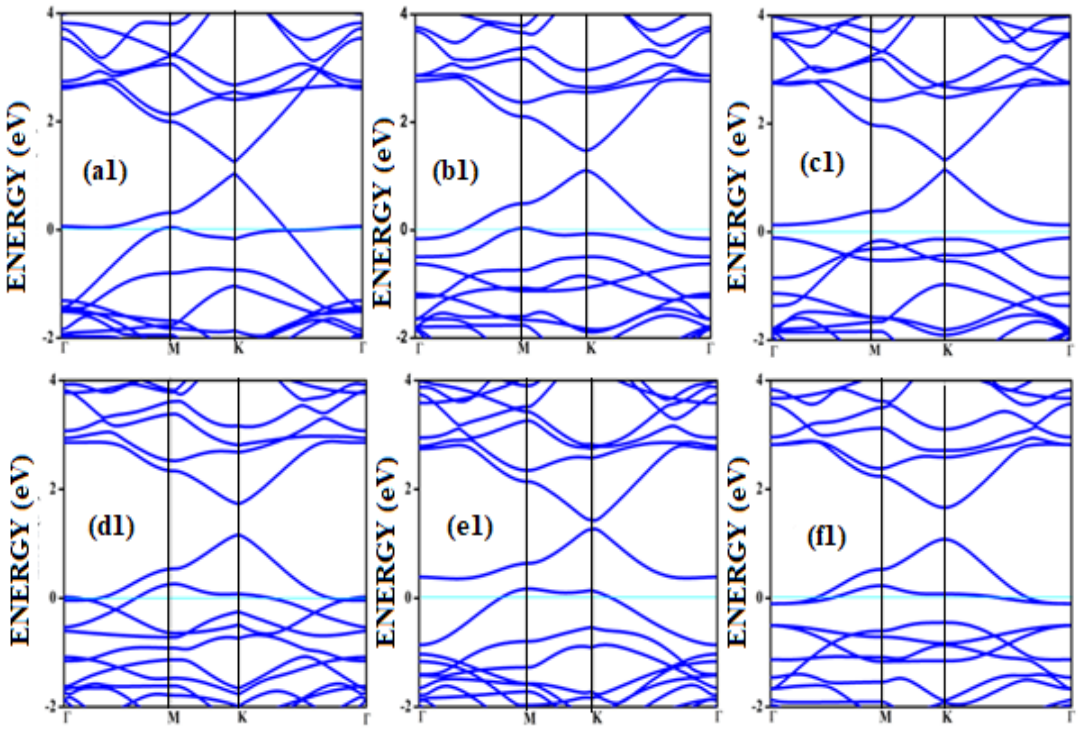

Fig. 3.3. The band structures corresponding to 6.25% (a1, b1, and c1) and 9.37% (d1, e1, and f1) boron-doped graphene surfaces.

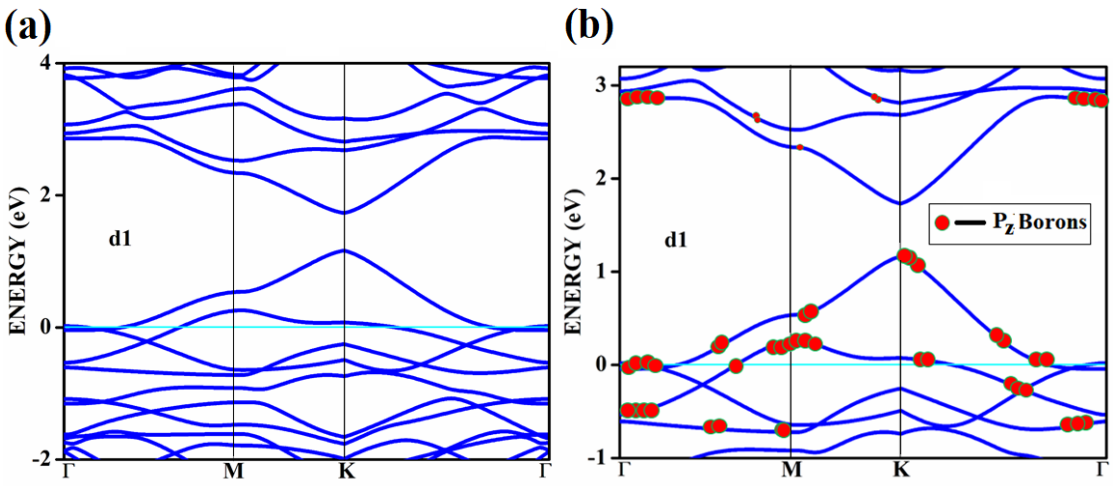

Fig. 3.4. The band structure of the 'd1' surface with the orbital contribution (a) Band structure of 'd1' surface (b) Boron P_z orbitals contribution.

For the doping patterns labeled 'b1', with two borons, the band-gaps are 0.37eV. On further doping, with 9.37%, the band-gaps are further increased to 0.57 and 0.58 eV for the surface configurations mentioned in 'd1' and 'f1'. Interestingly, the linear dispersion near the

Dirac point remains almost unaffected for single-doped graphene and is affected moderately for 6.25 and 9.37% of doping. For specific configurations where the atoms are placed adjacent, i.e., when the dopant atoms are at alternate sub-lattice positions, as in the 'c1' configuration, the band-gap is reduced to smaller values in the case of boron-doped surfaces. Such effects are due to the introduction of symmetry by the dopants in the sub-lattices. Similar results were also observed by Rani et al. [7] in their studies on doped systems.

Table 3.1. The band-gaps for the various configurations were studied for the different doping concentrations. One boron (BG) and nitrogen-doped (NG) surfaces; 3.12%, a–c; (6.24%) and d–f; (9.37%).

Structure	**Band-gap (eV)**	**Structure**	**Band-gap (eV)**
BG	0.14	NG	0.21
BG Literature [7]	0.14	NG Literature[29]	0.21
a1	0.21	a2	0.22
b1	0.37	b2	0.40
c1	0.15	c2	0.0
d1	0.57	d2	0.57
e1	0.16	e2	0.15
f1	0.58	f2	0.59

The band-gaps for 6.25% boron doping are checked with the available literature, with

6% dopant concentration calculated with a 6 × 6 supercell [7]. The band-gap corresponding to configurations ‘a1’, ‘b1’, and ‘c1’ are 0.21, 0.37, and 0.15 eV, and the corresponding values found in the matching configurations in the literature are 0.19, 0.43, and 0.17 eV, respectively. The results almost match, and minor changes can be attributed to supercell size effects. From our results, it is clear that the type of configuration or the isomer plays a part in the opening of the band-gap in addition to the increased dopant concentration. The dopants are placed at the same sub-lattice positions for a similar type of doping as in 'b1', 'd1', and 'f1'. It confirms that the band-gap is created through the symmetry-breaking phenomena. This remarkable band-gap opening which turns graphene into a semiconductor, is achieved via sub-lattice-induced symmetry breaking. Similar sub-lattice-induced symmetry breaking leading to band-gap opening has been reported in a few earlier studies [7,30]. In the case of configurations where the dopants are placed at the non-equivalent sites, no appreciable changes in the band-gap are observed, as in configurations ‘a1’, ‘c1’, and ‘e1’. Rani et al. [7] also studied similar doping patterns on doped graphene surfaces, and our band-gap calculations yielded identical values.

3.2.2. Nitrogen-doped graphene

Similar to the boron doping mentioned in the previous section, we have also done n-type doping on the surface with nitrogen. For the nitrogen-doped systems, no significant changes are observed in the planarity of the surface as the radii of carbon and nitrogen are almost similar. It shows that the primary two-dimensional structure of the surface remains unaffected, with a minor change in the bond lengths adjacent to the dopants. Similar to the B-doped graphene system of 4 × 4 supercell, with 32 carbon atoms, is constructed, and substitution doping with nitrogen is carried out to study the effect of n-type doping on the adsorption characteristics of common pollutant gases like CO and NH_3. The different concentrations of nitrogen doping considered are 3.12, 6.25, and 9.37%, with six different doping patterns. These patterns are defined in Figure 3.5 for 6.25 and 9.37% dopant

concentrations of nitrogen are mentioned as ‘a2’to ‘f2’, respectively, and correspond to the similar patterning as in Figure 3.1. The graphene surface with 3.12% nitrogen concentration is referred to as NG.

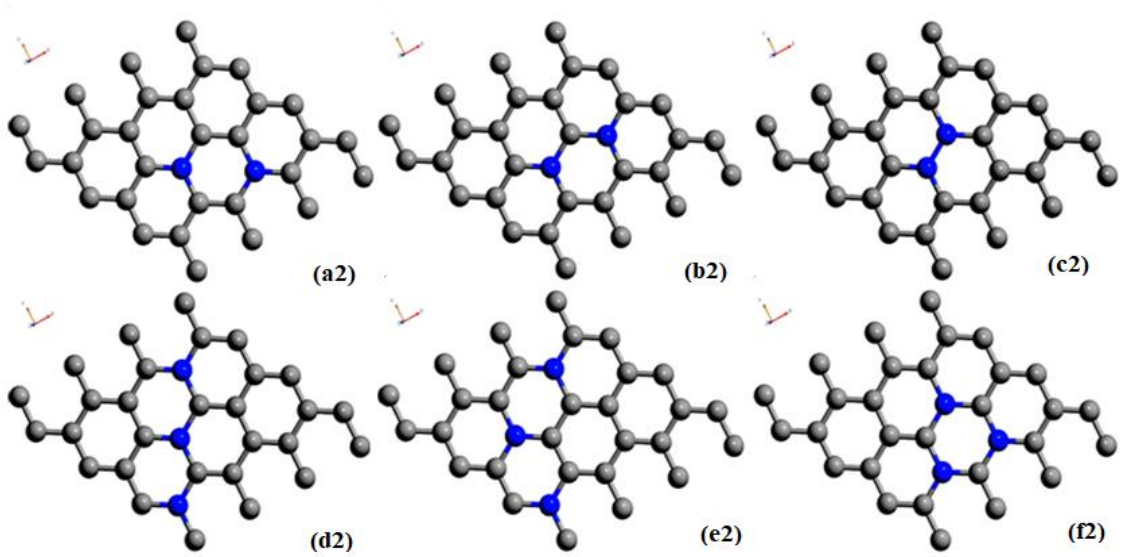

Fig. 3.5. The ball and stick model of 6.25% and 9.37% nitrogen-doped graphene surfaces in three different configurations of the doped nitrogen depicted by the notations, ‘a2’, ‘b2’etc till ‘f2’. Grey color represents the carbon atoms, while blue represents the nitrogen atom.

The results of the band structure calculations of N-doped surfaces are summarized in Figure 3.6. The studies were carried out with nitrogen-doped graphene for various doping concentrations. As expected, the Dirac point is about 0.9 eV below the Fermi level due to n-type doping.

Similar to studies with boron-doped surfaces, the different doping patterns with nitrogen are conducted, and their electronic band-gap is noted in Table 3.1. Interestingly, the band-gaps for specific surface configurations, like in boron doping, are improved drastically compared to the un-doped (0 eV) or singly doped surface (0.21 eV for nitrogen-doped graphene). Our values coincide with the previous investigation for 3.17% nitrogen-doped with a gap of 0.21 eV [31]. Similarly, charge transfers of 1.15e (from carbon to nitrogen) are observed for

graphene with singly doped nitrogen, which coincides with the values of 1.16e in the literature and is attributed to the electronic transport [7,30] due to n-type doping.

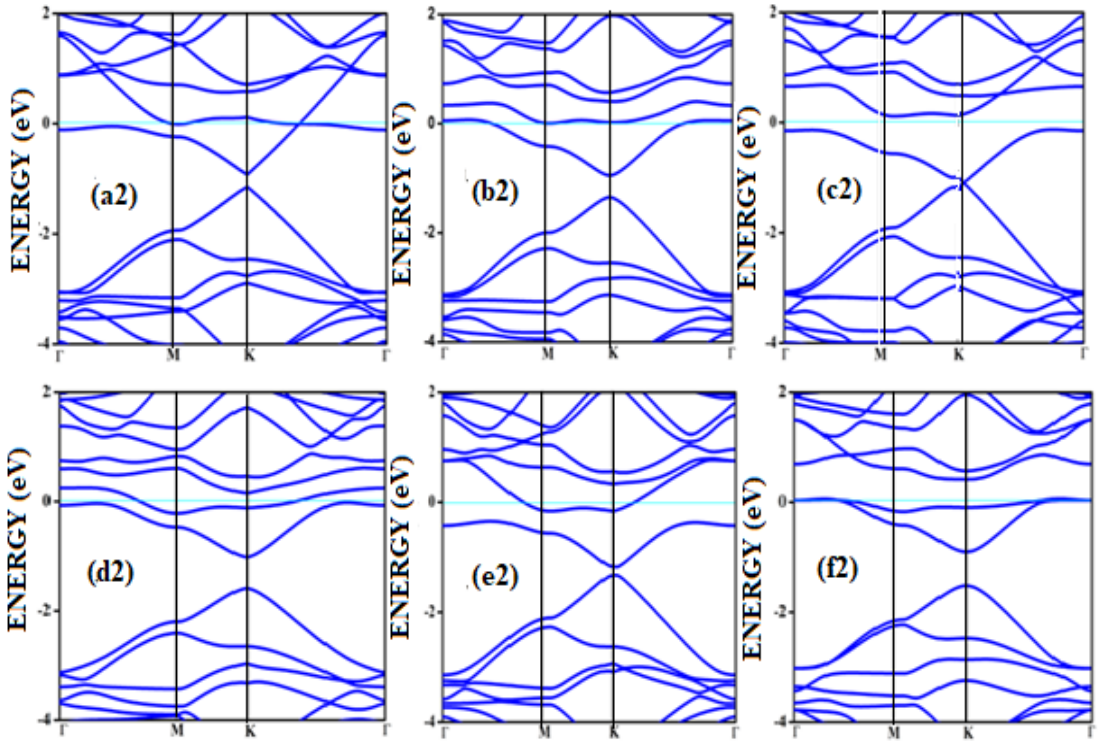

Fig. 3.6. The band structures corresponding to 6.25% (a2, b2 and c2) and 9.37% (d2, e2 and f2) nitrogen doped graphene.

For the doping pattern ‘b2’, where two nitrogen atoms are doped, the band-gap is 0.4 eV. On doping with 9.37%, the band-gaps are further increased to 0.57 and 0.62 eV for the surface configurations mentioned in ‘d2’ and ‘f2’. For specific structures where the atoms are placed adjacent, i.e., when the dopant atoms are at alternate sub-lattice positions, as in the ‘c2’ configuration, the band-gap is reduced to zero. Such effects are due to the introduction of symmetry by the dopants in the sub-lattices.

3.3. Adsorption on Boron-doped and Nitrogen-doped surfaces

Even though the adsorption of various gaseous species on the surface of graphene [18] doped with single boron and nitrogen has been investigated [27] previously, there have been no attempts to study the adsorption phenomena on graphene surfaces with various levels of

doping concentration and also with different patterns/configurations of doping. In addition to the adsorption on graphene with single boron (3.14%), we have investigated the adsorption characteristics on surfaces having dopant concentrations of 6.25% and 9.37%. Moreover, with each of these dopant concentrations, adsorption studies are carried out on various arrangements of the dopant atoms, making different patterns, as mentioned in Figure 3.1, and the results are presented below. The adsorption energy, the closest distance of the adsorbate gas molecule, and the band-gaps are shown in Table 3.2 for the adsorption on boron-doped systems. As mentioned previously, the configurations two boron doped b1 (6.25%) and three boron doped 'd1' and 'f1' (9.37%) show more band-gap opening compared to the other configurations because of sub-lattice symmetry breaking.

Table 3.2. The adsorption energy, the distance between adsorbate and adsorbent, and the band-gap of different concentrations for various configurations of boron atoms on graphene. The notation for the adsorption is adsorbate/adsorbent; for example, CO or NH_3/a1 implies that CO or NH_3 is adsorbed on a boron-doped graphene surface with the 'a1' configuration. Similar notations are also adopted for the other adsorptions. The band-gaps of free surfaces (BG, 'a1-f1') are also shown for comparison.

Configuration	**Adsorption energy $E_{ads.}$ (eV)**	**Distance (Å)**	**Band-gap (eV)**
BG	–	–	0.14
CO/BG	-0.105	3.42	0.18
NH_3/BG	-0.259	3.22	0.24
a1	–	–	0.21

CO/a1	-0.025	3.59	0.24
NH_3/a1	-0.561	1.67	0.54
b1	–	–	0.37
CO/b1	-0.031	3.75	0.39
NH_3/b1	-0.033	3.90	0.39
c1	–	–	0.16
CO/c1	-0.028	4.03	0.16
NH_3/c1	-1.021	1.646	0.26
d1	–	–	0.57
CO/d1	-0.309	3.06	0.64
NH_3/d1	-0.330	3.58	0.65
e1	–	–	0.16
CO/e1	-0.013	4.66	0.16
NH_3/e1	-0.079	3.35	0.15
f1	–	–	0.58
CO/f1	-0.291	3.14	0.63

NH_3/f1	-1.047	1.64	0.83

The results of the adsorption of CO on all the boron-doped surfaces show a similar trend. Though it is a fascinating molecule with both electron-donating and accepting centers in the different regions, as a whole, it acts like a p-acceptor. At the same time, the surface is already deficient in electrons with doped boron atoms. Due to this, the attraction towards the surface is less, resulting in negligible adsorption energies. All the distances with CO adsorption are found to be more than 3 Å, and low adsorption energies indicate that the adsorption falls in the range of physisorption. This physisorption does not influence the electronic properties, for example, it remains 0.57 eV for the bare surface of 'd1' and 0.64 eV after the adsorption of CO. There are no significant changes in the band-gaps, which remain almost the same as that of the doped, adsorbent surface. The total density of states of the adsorbate-adsorbent complex and the DOS of CO is given. The DOS corresponding to the CO shows the peaks at the same energy values for all three figures in Figure 3.7. This indicates that a p-acceptor like CO does not have any effect with respect to the electronic properties of extrinsic doping/ adsorption.

The 'b1' surface has an electronic band-gap of 0.37 eV, and CO/b1 shows a band-gap of 0.39 eV. The partial DOS of CO given in Figure 3.8 shows all the peaks unaltered implying only physisorption. To see the effect better, the DOS for the surface before and after adsorption in Figure 3.8. The DOS is almost unchanged after adsorption indicating CO is almost inert to the surface.

However, there are changes in the adsorption energy on the surface with a concentration of 9.37%, namely 'd1' and 'f1', where the symmetry breaking is already present without the adsorbate. Even though it is not adequate to classify it as chemisorption, and since it is difficult to classify the sharp dissimilarity between the intermediary cases of adsorption, one may classify the cases with favorable adsorption energy greater than 0.2 eV as a stronger

physisorption. For example, such cases are well known in the literature with the interactions in strong hydrogen bonds [11].

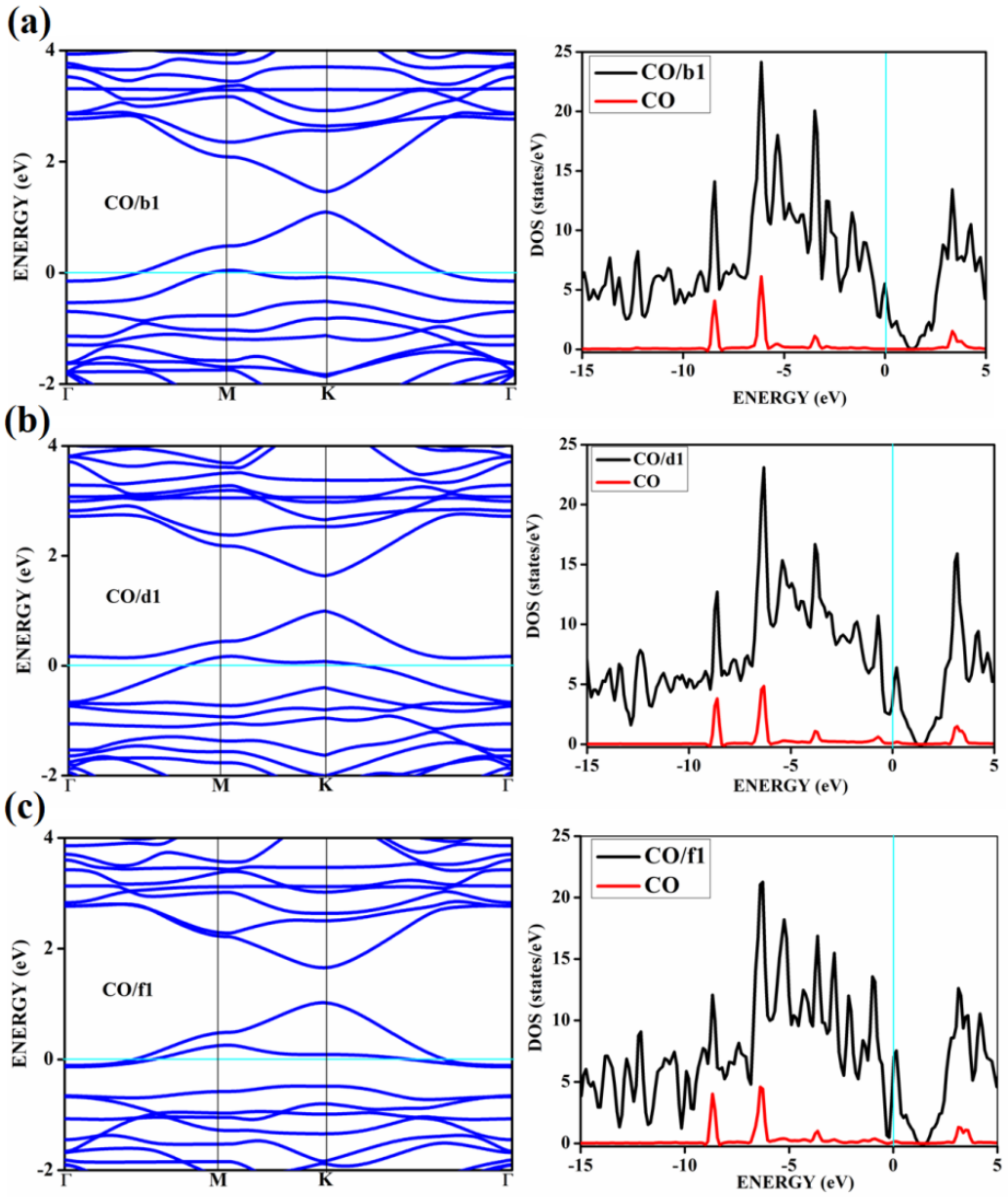

Fig. 3.7. The band structure and respective density of states (DOS) of CO adsorbed on B-doped surfaces with different concentrations and configurations (a) CO/b1 (b) CO/d1 and (c) CO/f1.

The somewhat stronger physisorptions mentioned here, CO/d1 and CO/f1, show closer distances to the surface of the order of about 3 Å compared to the adsorptions on other surfaces. We have found only negligible charge transfer of the order of 0.08e-0.11e for all these

physisorptions cases. However, this way of extrinsic doping by adsorption of gaseous species of the intrinsically doped surface further opens up the band-gap to a negligible extent of 0.05–0.07 eV and, therefore, is not promising. This shows that extrinsic doping with gaseous adsorbate fails when the adsorbate weakly interacts with the surface. In other instances, in which the adsorbent symmetry is not broken due to occupation of the dopant in different sites, like in CO/a1, CO/c1, CO/e1, etc., the band-gap remains unaltered concerning the adsorbent surface.

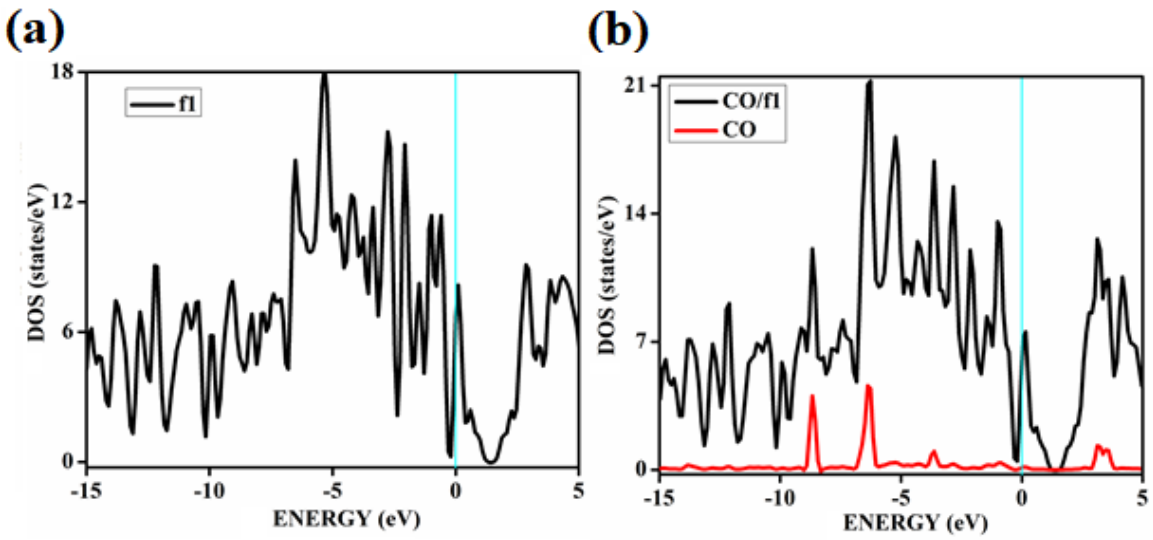

Fig. 3.8. The DOS of bare surface before and after adsorption of CO on the respective surface (a) 'f1' surface before adsorption of CO (b) After adsorption with CO. The red peaks represent the DOS of CO after adsorption.

On the other hand, ammonia showed drastically different behavior near the boron-doped surfaces. For example, the behavior of NH_3 near some of the adsorbent surfaces like 'b1', 'd1', and 'f1' shows a more substantial impact where apparent electronic changes result from extrinsic doping through adsorption. These are shown in Figure 3.9. Interestingly, considerable differences in adsorption energy and meaningful adsorption-adsorbent distances corresponding to the chemisorptive behavior are visible for adsorption on specific configurations. In addition, the effects are also visual as an appreciable band-gap opening on

adsorption. For example, for ammonia adsorption on the surface configuration labeled ‘a1’, the adsorption energy is -0.561 eV, with a distance of 1.67 Å, where the band-gap is also increased appreciably from 0.24 eV to 0.56 eV. The charge transfer is about -0.15e from ammonia to the surface, which is electron deficient due to boron doping. The appreciable opening of the gap from 0.24 to 0.54 eV is solely due to the adsorption phenomena where a bond is also formed between the nitrogen of ammonia and one of the boron atoms.

These significant changes are also reflected in the given density of states plot. In almost all cases, we see that the orbitals of NH_3 couple with that of the surface. For example, in NH_3/f1, some of the DOS peaks corresponding to NH_3 are absent near the Fermi level.

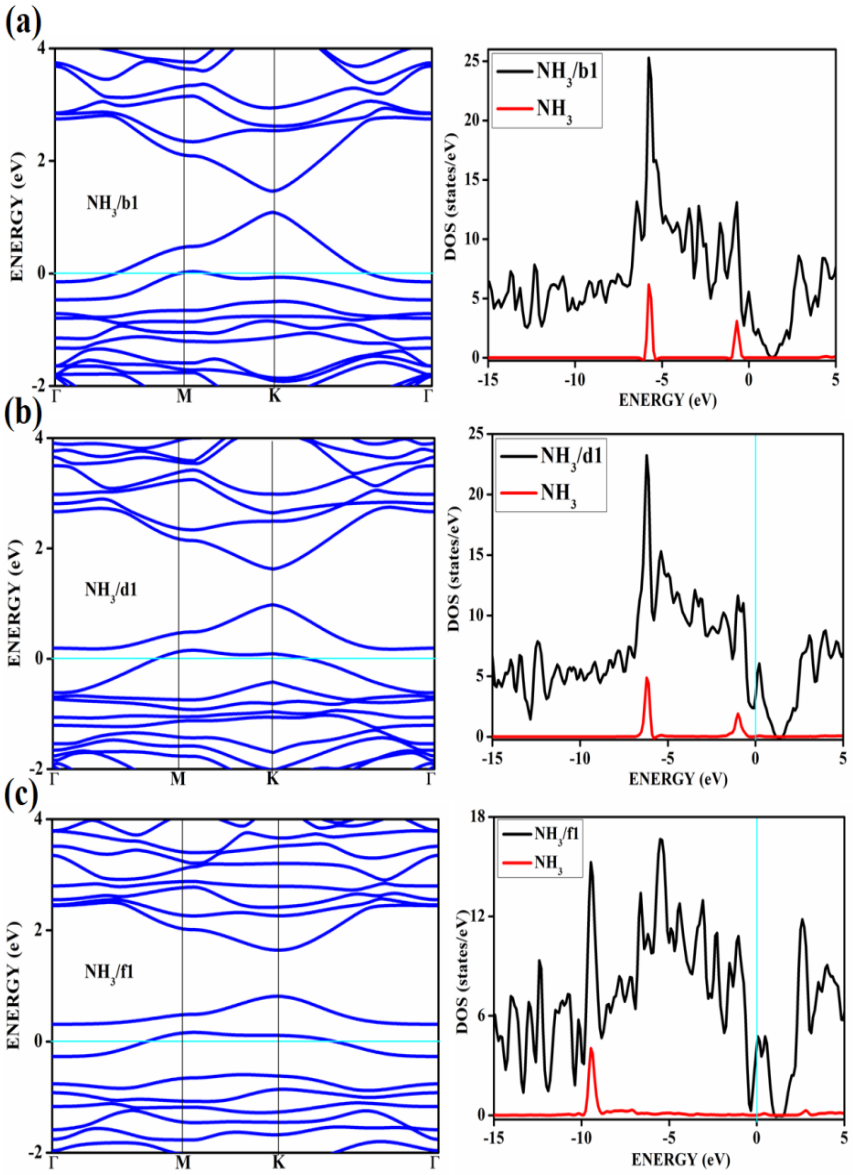

Fig. 3.9. The band structure and respective DOS of ammonia adsorbed on B-doped surfaces with different concentrations and configurations (a) NH_3/b1 (b) NH_3/d1 (c) NH_3/f1. The DOS of the gas molecule NH_3 is also given.

In the case of NH_3/a1, the band-gap is solely due to the symmetry breaking due to adsorption on one of the boron on the surface. Different perspectives of adsorption where the bond formation is visible are given in the optimized geometries in Figure 3.10.

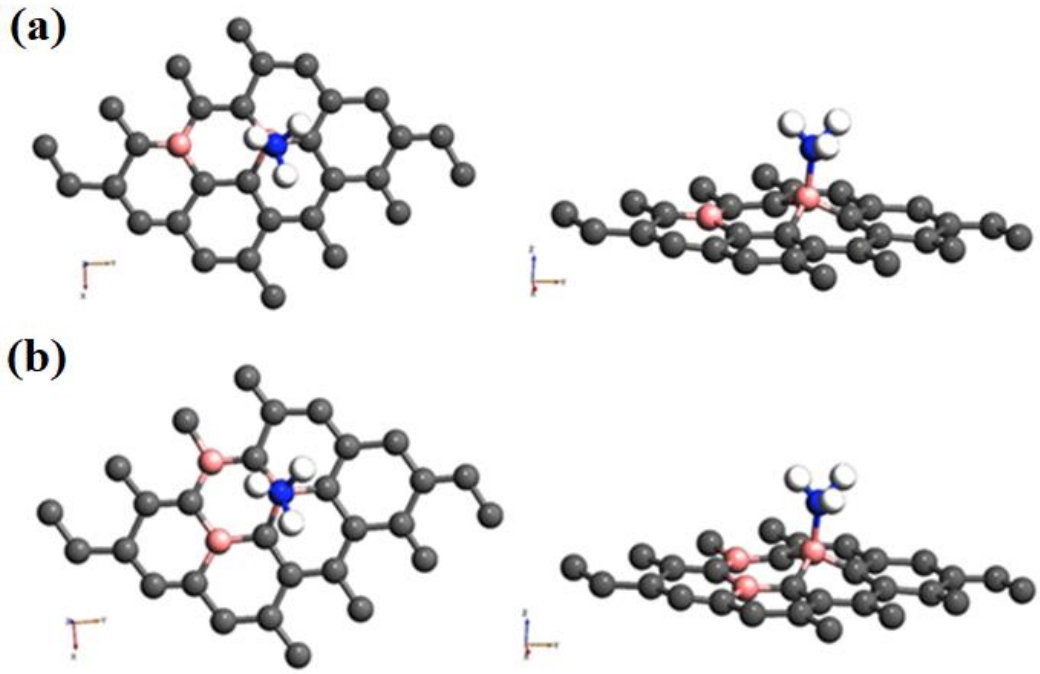

Fig. 3.10. The geometry-optimized structures of ammonia adsorption on the surfaces showing chemisorption (a) Top and side view of NH_3/a1 (b) Top and side view of NH_3/f1.

The band diagram corresponding to the adsorption of NH_3/a1, shown in Figure 3.11, shows a noticeable band-gap opening from 0.24 eV of the doped surface to 0.56 eV. The dispersion near the Dirac point is significantly affected due to the perturbations caused due to adsorption. Even though the bands show some unstable characteristics, the possibility of chemisorption cannot be neglected. Similar adsorption is also found on the NH_3 surface configuration specified by the surface ‘c1’. The surface ‘c1’ is one of the most undesirable adsorbent surfaces where the dopants are placed adjacently. While in the case of the ‘a1’

surface, the boron atoms are separated by two carbons, allowing a certain degree of electron deficiency distribution. Such a distribution is absent in the isomer 'c1', where it accumulates, forcing adsorption. The band-gap opening is also not palpable in this case, with a 0.1 eV difference with the adsorbate surface. Therefore, the adsorption is the sole effect that cannot induce any noticeable change in the band-gap, as seen in the case of NH_3/a1.

Interestingly, a similar effect is not seen in the case of CO/a1 or CO/c1 adsorptions. The reason is that the electron-donating capacity of CO from the slightly electron-rich carbon is negligible compared to that of the nitrogen holding a lone pair in the case of ammonia. This again shows that extrinsic doping is effective in causing the band-gap to open only with appropriate adsorbate molecules. It is also worthwhile to note that the band-gap opening can be used in its application for sensing the ammonia molecule with a surface where the dopants follow a specific pattern.

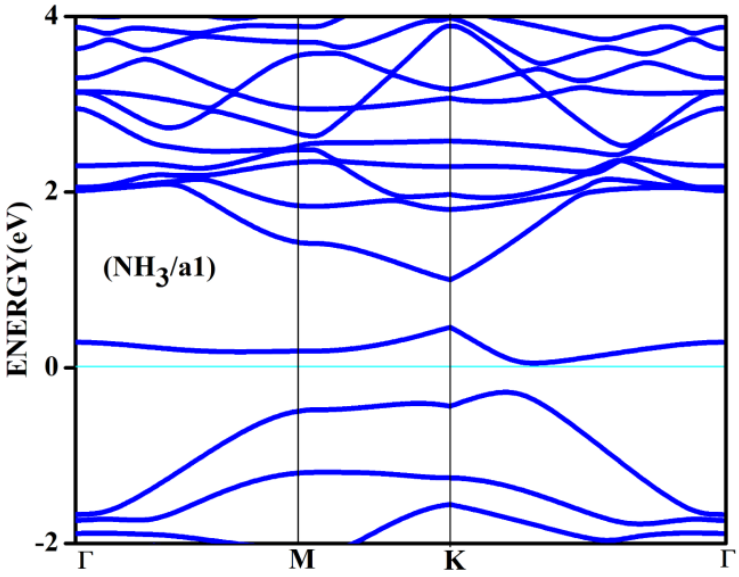

Fig. 3.11. The band structure for the adsorbed complex corresponding to ammonia adsorption on 'a1' surface.

Amongst the adsorptions on chemically/intrinsically modified graphene, the most prominent one is ammonia adsorption on the boron-doped surface with 9.37% dopant concentration and the boron atoms arranged in an alternate way as in NH_3/f1. The adsorption caused a favorable

energy of -1.047 eV with a distance of 1.64 Å between the nitrogen of NH_3 and the boron on the surface, corresponding to chemisorption. Compared with the stronger adsorptions on metal or transition metal doped surfaces, this moderate chemisorption is an added advantage for its prospective applications for sensing the gas molecule as it can also be desorbed under milder conditions. The electronic band-gap is found to be increased from the pure surface value of 0.58 to 0.83 eV. This surface configuration 'f1' is one where we can see symmetry breaking due to boron substitution on dissimilar sites. Therefore, the band-gap opening of an additional 0.25 eV can be attributed to additional symmetry breaking due to the formation of a favorable adsorption complex. The bond distances match the classical donor–acceptor (1.43 Å) B–N dative bonds. The charge transfer is found to be about 0.17e from nitrogen. The geometry-optimized structure is shown in Figure 3.9(b), and the band diagram for the surface, NH_3/f1, and the density of states are shown in Figure 3.12.

Figure 3.12 clearly shows a drastic change in the band-gap on adsorption, while the shifting of the Fermi level concerning the Dirac point is affected by an amount of about 0.25 eV. This shows the additional effects of the lone pair of electrons on the nitrogen of the adsorbate. The band-gap increase is also visible in the corresponding DOS plot.

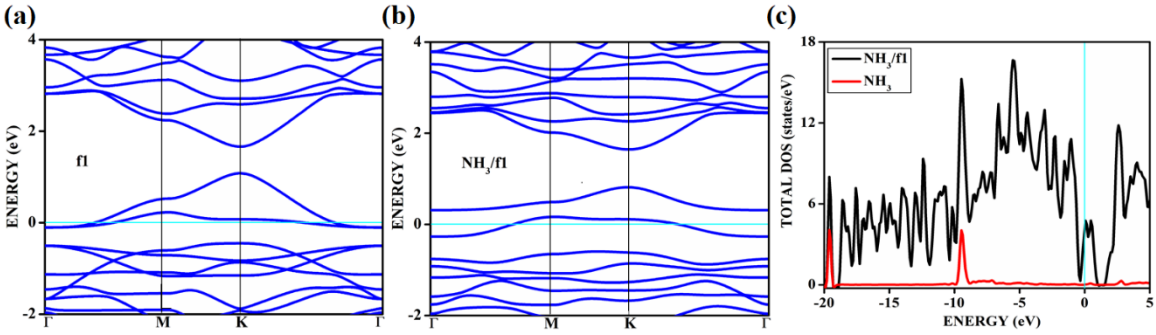

Fig. 3.12. The band diagram corresponding to NH_3 adsorption on the configuration 'f1' of three boron-doped graphenes and the corresponding density of states (a) Band structure of f1 (b) Band structure of NH_3/f1(c) DOS of NH_3/f1.

Similar to the bare boron doped systems, we have seen almost the same trend in band-

gaps in n-type doped surfaces with nitrogen, except that the Fermi level is shifted above the Dirac point because of the n-type doping. In similar systems where the doped atoms occupy the same sub-lattice positions, 'b2', 'd2', and 'f2' showed larger band-gap openings due to symmetry breaking of the sub-lattice. The band-gap results of these surfaces in Table 3.1 show an evident change from the semi-metal graphene to a semiconducting surface. The adsorption energy, distances, and band-gaps summarized in Table 3.3 show that CO and NH_3 have little or no impact on the n-type doped surfaces' electronic structure and are only feebly adsorbed onto the respective surfaces. On the other hand, favorable stronger physisorption for CO on the surfaces having dissimilar substitutions, namely, CO/d1 and CO/f1, and the chemisorption of NH_3 on specific configurations (NH_3/a1, NH_3/f1) are seen with the boron doped surfaces.

Table 3.3. The adsorption energy, the distance between adsorbate and adsorbent, and the band-gap for different concentrations and different patterned doped nitrogen atoms on the graphene surface. Notations used for adsorbate/adsorbent in the table are similar to that in Table 3.2.

Configuration	**Adsorption energy $E_{ads.}$ (eV)**	**Distance (Å)**	**Band-gap (eV)**
1NG	-	-	0.21
CO/1NG	-0.006	3.44	0.21
NH_3 /1NG	-0.077	3.80	0.21
a2	-	-	0.22
CO/a2	-0.140	3.66	0.20
NH_3/a2	-0.007	3.53	0.22

b2	-	-	0.40
CO/b2	-0.034	4.01	0.40
NH_3/b2	-0.018	4.58	0.40
c2	-	-	0.0
CO/c2	-0.021	3.73	0.0
NH_3/c2	-0.081	3.51	0.0
d2	-	-	0.57
CO/d2	-0.025	3.36	0.57
NH_3/d2	-0.092	3.27	0.57
e2	-	-	0.15
CO/e2	-0.015	3.34	0.16
NH_3/e2	-0.043	3.50	0.16
f2	-	-	0.59
CO/f2	-0.026	3.69	0.62
NH_3/f2	-0.105	3.25	0.61

Nevertheless, stronger physisorption and chemisorption are missing for these two adsorbates, CO and NH_3, on nitrogen-doped surfaces, as evident from its band structure in

Figure 3.13 and Figure 3.14. It is also worth noting that stronger physisorption, present for CO adsorption on specific p-type configurations, is also absent in CO adsorption on nitrogen-doped surfaces. This is due to the electron-rich surface in the case of n-doped cases. The reasons for the behavior in n-doped surfaces can be well explained based on the electron transport present in these systems in contrast to the hole transport in boron-doped systems. The pentavalent dopant makes three covalent bonds with the carbon atoms, leaving an electron free for transport.

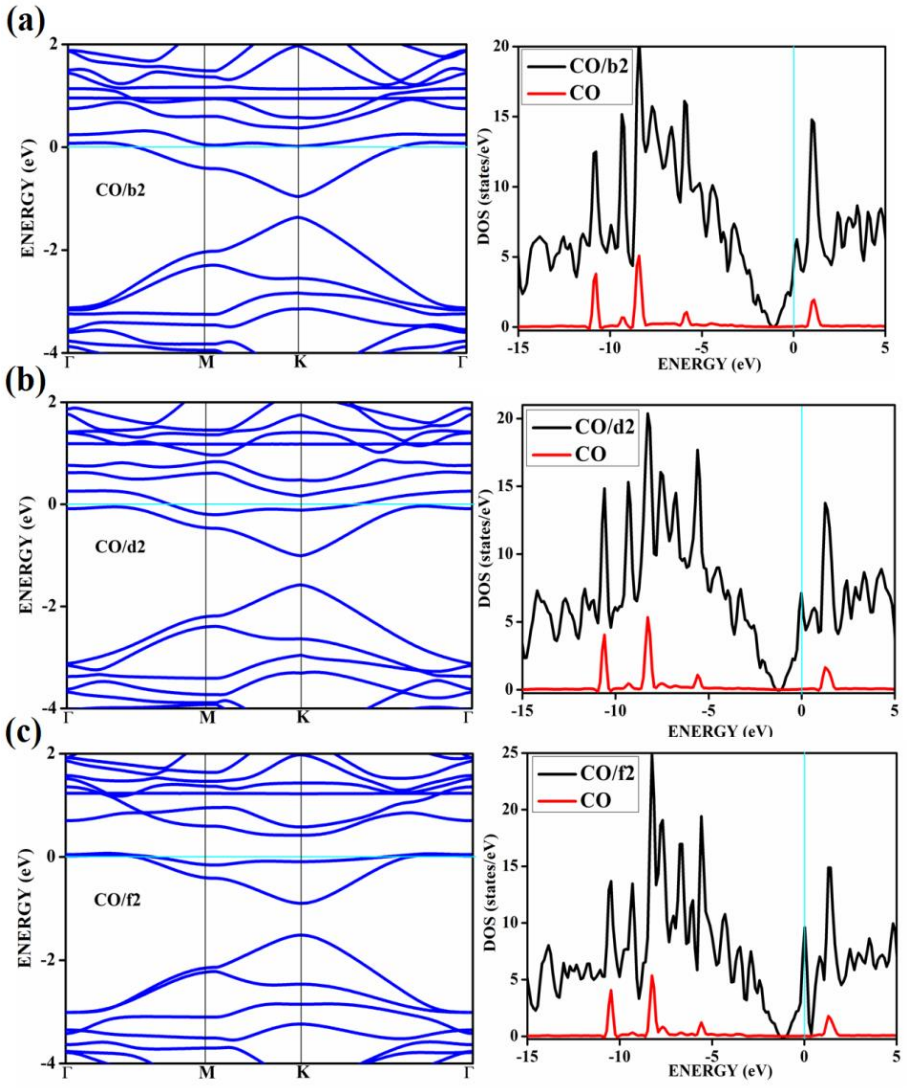

Fig. 3.13. The band structure and respective DOS of CO adsorbed on N-doped with different concentrations and configurations (a) CO/b2 (b) CO/d2 (c) CO/f2.

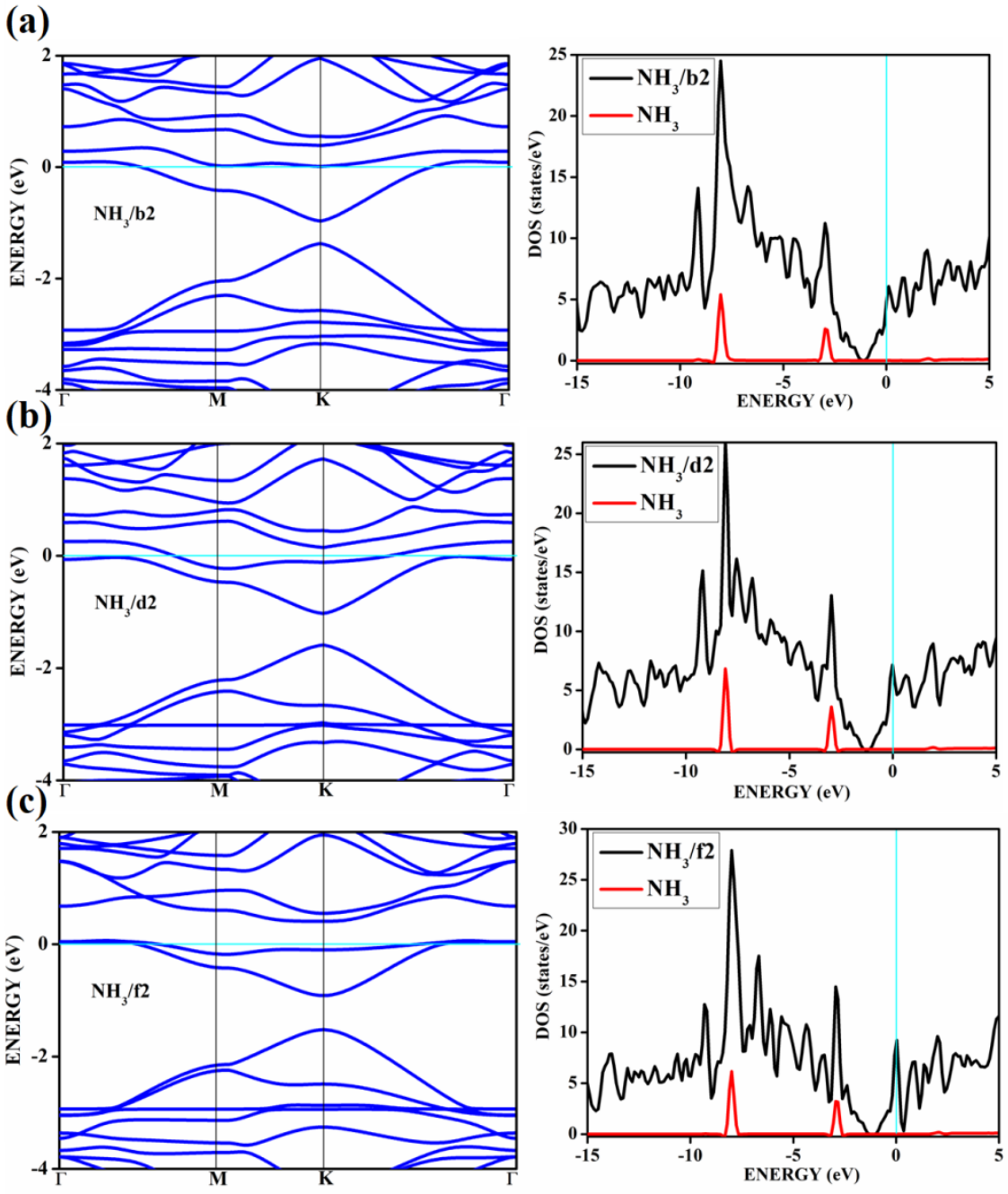

Fig. 3.14. The band structure and respective DOS of NH_3 adsorbed on N-doped graphene with different concentrations and configurations (a) NH_3 /b2 (b) NH_3 /d2 (c) NH_3 /f2.

The adsorbates CO and NH_3, with lone pairs of electrons, are not attracted to the electron-rich N-doped surfaces. Therefore, these molecules are only physisorbed weakly onto such surfaces with distances above 3.25 Å. In the case of adsorption on nitrogen-doped surfaces, all correspond to weak physisorption. For example, the band-gaps remain the same

for three nitrogens (9.37%) doped surface ‘f2’, i.e., 0.62 eV before and after adsorption. From the band structures provided in Figure 3.15, it is understood that the electronic structure has not changed with the adsorbate CO molecule for all configurations, unlike in the case of boron-doped systems. In the case of nitrogen-doped adsorbent surfaces, we have not encountered cases where the molecule CO or NH_3 binds chemically.

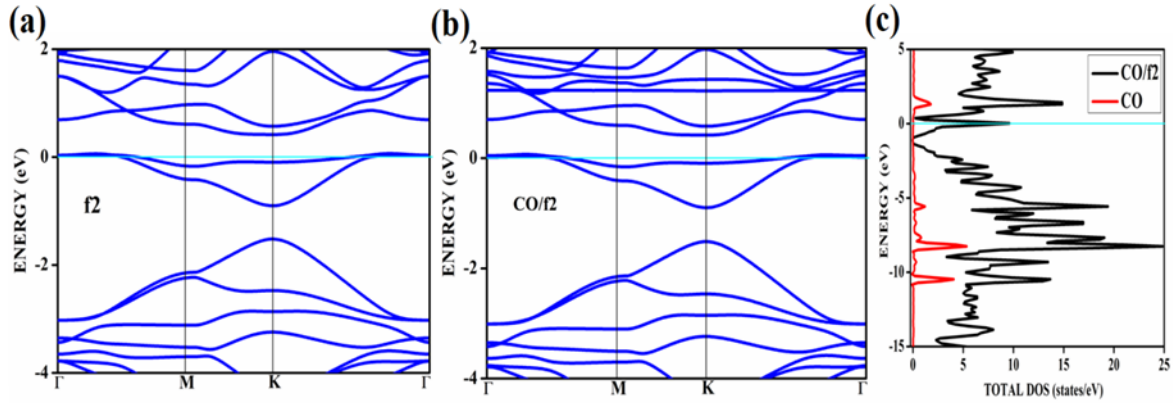

Fig. 3.15. The band structure of nitrogen-doped graphene surface before and after the physisorption of CO. The density of states of CO after the adsorption is also given (a) Band structure of f2 (b) Band structure of CO/f2 (c) DOS of CO/f2.

To confirm the category of adsorptions of CO and NH_3 on boron-doped and also on nitrogen-doped graphene surfaces, we have calculated the potential energy surfaces for a few relevant cases. For all the adsorption cases with low values of adsorption energy, the potential energy curves similar to that of physisorption are observed. For example, the potential energy curves for NH_3 on ‘d2’ and CO on ‘f1’ are drawn together in Figure 3.16. It shows characteristic curves for physisorption without any defined minima indicating weak interactions. It is evident from the potential energy curves in Figure 3.17 that the adsorption phenomena are purely physical and that when the single molecule of CO or NH_3 approaches the surface, it only has van der Waals weak interactions. The surfaces remain inert to the molecule, and the electronic structure remains unaffected.

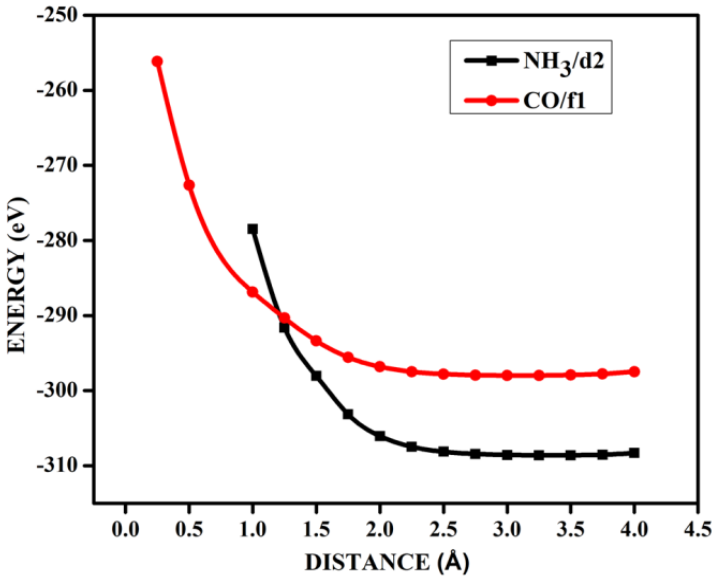

Fig. 3.16. The potential energy curves for NH_3 on d2 (NH_3/d2) and CO on f1 (CO/f1) surfaces show physisorption.

On the other hand, we have seen cases where ammonia is strongly adsorbed on some of the surfaces, thus causing perturbations in the electronic structure. For example, for the possibility of NH_3 adsorption on the 'f1' surface, in addition to the band diagrams provided in Figure 3.12, we can also visualize the effect of adsorption with the potential energy diagram mentioned in Figure 3.17, which shows the typical characteristics of chemisorption. Though the adsorption energy values are not very high and are about -1.04 eV, the tendency can be observed with a clear minimum at a distance of 1.64 Å in the potential energy diagram. The depth of the chemical well represents the intensity of adsorption. In contrast, the global minimum position at the horizontal axis equals the equilibrium bond distance for the adsorbed species on this surface, around 1.64 Å. For any potential sensing application, it is highly preferable to have surfaces with moderate adsorption energy values rather than extremely high ones. The cases we have observed, namely NH_3/a1, NH_3/c1, and NH_3/f1, fall into this category of moderate chemisorption. Therefore, such graphene adsorbent surfaces may find applications for sensors for ammonia molecules.

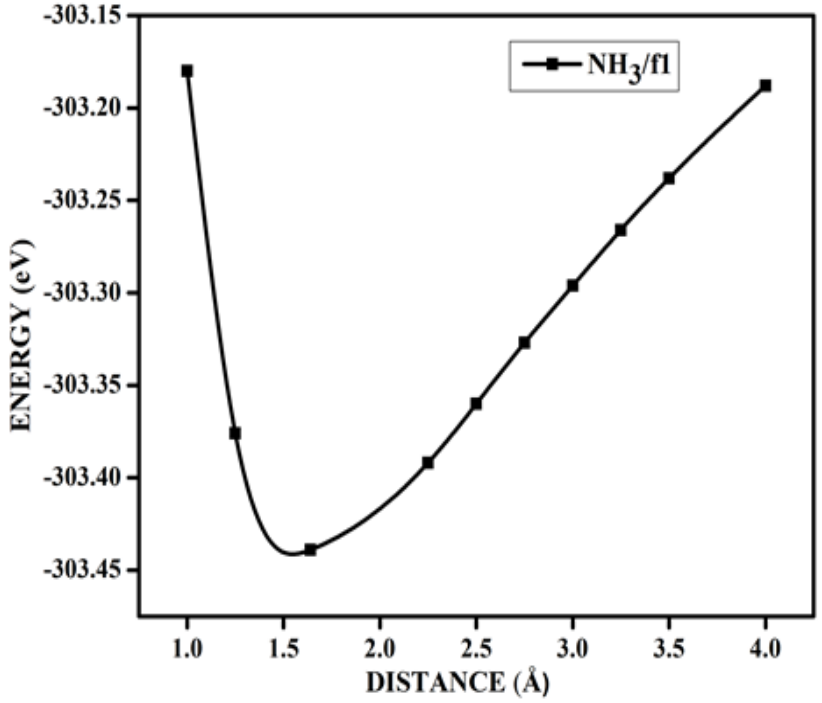

Fig. 3.17. The potential energy curves for NH_3 on the 'f1' (NH_3/f1) configuration showing chemisorption. The minimum of the curve corresponds to the B-N bond distance of 1.6 Å.

As chemisorption involves the bond formation between the gas molecule and the adsorbent surface, it requires energy corresponding to -1.05 eV. As is evident from Figures 3.11 and 3.12, the strong perturbation induced by the adsorbate influences the doped surface's electronic structure, leading to an increased band-gap in the case of ammonia on 'a1' and also on 'f1' types of surfaces. In the case of pure physisorption, such as CO/f1, weak van der Waals forces are the only attraction between the adsorbing molecule and the surface. As illustrated in Figure 3.16, the forces in the potential curve are negligible at a relatively wide distance from the top until a substantial rise in total energy is induced by strong repulsive forces resulting from overlaps in the electron density.

The minimum characterizes the potential energy curve at a shorter distance when chemical bond formation occurs, such as in NH_3/f1, indicating chemisorption. To further study the effects of adsorbed molecules on the electronic properties of graphene, charge density surfaces are calculated for a few systems with and without the adsorption, visualizing the

various interactions between the adsorbate and adsorbent. The sliced-up surfaces along lattice planes are done in VESTA to visualize the charge density and difference charge density iso-surfaces [32]. Figure 3.18 shows the charge density before and after adsorption of one of the essential cases, NH_3, on the 'f1' surface as (a) and (b), respectively. As can be seen, the colors indicate electron deficiency around the region where the doping is done. We constructed contour plots in the plane containing B–C–B bonds and the nitrogen of NH_3. The charge–density plots in Figure 3.18 show a dense mixture of charge density between the boron of the graphene plane and the N atom of NH_3, indicating a distinct degree of covalent bonding between B and N atoms. B–N bonds' bonding states lie on top of the valence bands. From Figure 3.18, we can see carbon with four electrons and boron with three electrons forms a covalent bond along the contour of *hkl* (110).

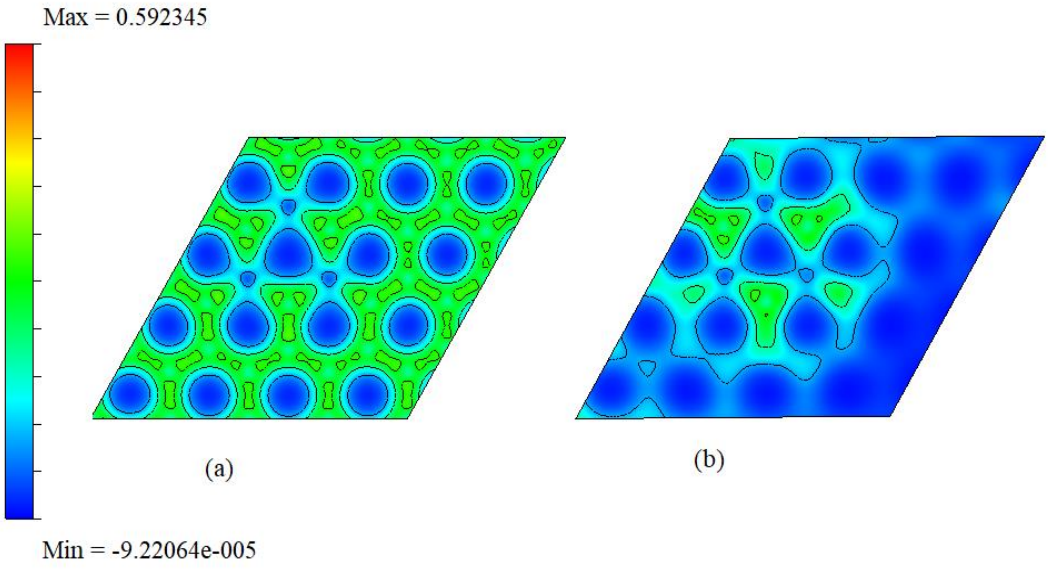

Fig. 3.18. The two-dimensional charge density surface for f1 (given before (a) and after (b)) adsorption of ammonia. The unit of isovalue is e/Å^3.

The charge concentration distributed among carbon atoms adjacent to borons involved in the bond formation is shown in Figure 3.19. The charge difference density is calculated according to the Eq 2.48 as,

$$\Delta\rho = \rho(NH_3/f1) - (\rho\ (f1) + \rho(NH_3)),$$

Where $\rho\ (NH_3/f1)$ denotes the charge density of the ammonia adsorbed on the surface 'f1'. In contrast, $\rho(f1)$ and $\rho(NH_3)$ represent the charge densities of the clean doped surface 'f1' and isolated molecule NH_3; therefore, the negative charge density regions correspond to areas where the electron density is lost. In contrast, the positive regions represent the areas where the electron density is accumulated. The difference between charge densities of the adsorbed complex and the surface and the gas molecule NH_3, according to Eq. 2.48, is plotted in Figure 3.19 in two different perspectives (a) and (b) to visualize the effect of perturbations due to adsorption. The difference density plot is to understand how the charge density redistribution occurs due to chemical bond formation and interactions.

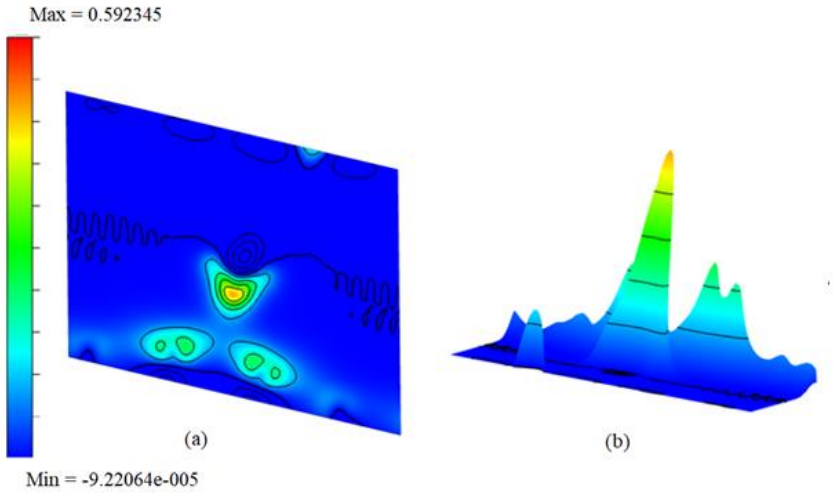

Fig. 3.19. The difference charge density contour surface of NH_3/f1 (a) Contour plot and (b) Bird-eye-view perspective. The unit of the isovalue is e/Å^3.

The effect of ammonia, which chemisorbs onto the surface, is clear from the charge density plot. The regions where the boron atoms are present still show areas of electron-deficient nature in the immediate vicinity compared to the rest of the surface. On the other hand, the physisorption on doped surfaces shows no appreciable change in the charge densities. The prominent charge accumulation occurs on the bond between the nitrogen atom of NH_3 and

the boron atom on the surface, indicating that a sizeable electronic pile is a deciding factor for forming a strong chemical bond in this adsorption process. Overall, it contributes to understanding the adsorption process and shows the electron distribution due to forming the bond between the adsorbate molecule and the doped surface.

3.4. Conclusions

We have investigated the adsorption of CO and NH_3 on a chemically modified graphene surface. The chemical modification and alteration of the electronic properties of the graphene layer are achieved by substitutional doping with boron and nitrogen. We have demonstrated that the band-gaps can be significantly opened up from a value of 0 eV up to 0.83 eV on molecular adsorption on doped surfaces. It is also interesting to see that the electronic properties are modified with various mole fractions of doping. However, it does not show a systematic increase with the increase in the dopant concentration. It is attributed to the sub-lattice-induced symmetry breaking for specific dopant configurations on the surface. Therefore, a high doping concentration cannot achieve an increased band-gap. More importantly, the dopant sites and configurational doping patterns are crucial. The adsorption of CO on specific isomers of the boron-doped surface is observed to fall in the more robust physisorption regime. The ammonia molecule adsorbs chemically on particular configurations of boron-doped surfaces with high adsorption energies ranging from -0.56 to -1.46 eV. The charge transfers of 0.17e to 0.20e are noticed upon ammonia adsorption on boron-doped surfaces.

In contrast, the interaction of both CO and NH_3 with nitrogen-doped surfaces falls in the physisorption range. Furthermore, this work also suggests that chemically modified graphene surfaces could be used as promising and valuable materials for possible sensing applications and their potential applications in new technologies in nanoscale optoelectronic devices as a direct band-gap semiconductor.

Chapter 4

Alteration of electronic properties upon adsorption of paramagnetic molecules on chemically doped graphene surface

4.1. Introduction

Oxides of nitrogen such as NO, NO_2, and N_2O are prevalent pollutants, posing a threat to the health of humans and animals as their prolonged exposure to nitrogen oxides is related to cardio-respiratory dysfunctions [1]. Among the many materials and techniques suggested for detecting nitrogen oxides, graphene-based materials are emerging for the sensing process with advantages, including low detection limits, operating at room temperature, fast sensing, and high recovery [2]. Even though the experimental investigation by Schedin *et al*. [3] has revealed graphene as a unique, two-dimensional material to attract gaseous moieties, surprisingly, at an individual level, it has been established now that pristine graphene is chemically inert to many of the gases and that its semi-metallic nature limits its device-based applications [4].

There is a broad demand for sensors derived from semiconductors, owing to their better sensitivity and selectivity, even with traces of gaseous species. As stated in the previous chapter 3, there have been many attempts, both theoretical [4] and experimental [5], to transform the zero band-gap graphene into a semiconductor. From our initial studies shown in Chapter 3 and some of the previous investigations [5-8,9-11], the band-gap of graphene can be engineered by substitutional doping, i.e., by replacing carbon atoms with boron or nitrogen, thus inducing p- or n-type semiconducting characteristics. Doped graphene has widespread importance in various applications, especially those related to the sensing of gaseous pollutants [7]. Such intrinsic doping with heteroatoms can open up the band-gap, making it a semiconductor, eventually enhancing the chemical sensing and, in some cases, favorably adsorbing them. There have also been many attempts to improve the chemical affinity of semi-metallic graphene surfaces through a combined effect of intrinsic and extrinsic doping in terms of molecular adsorption of external gaseous molecules [4,12-20]. It is also known in the literature that doped graphene and graphene

with defects [21] adsorb molecules better than the intrinsic surface.

Among all molecular adsorption studies on intrinsically doped graphene, comprising doping with the transition metals [22-24] are the most explored yet. The presence of abundant d-electron systems with empty orbitals makes them excellent candidates to bond with the gaseous molecules with ease. In the same direction, there are also investigations on noble-metal doped graphenes that show high sensitivity and affinity to gaseous molecules [25]. As expected, most of these gaseous species adsorb firmly on such surfaces, forming strong bonds with relatively high binding energies. This eventually makes the desorption of these gases difficult at ambient conditions, and the entire electronic structure may get altered during the process. Therefore, a semi-metal like graphene doped with metal or transition metal is not expected to yield beneficial optoelectronic properties.

Many investigations of gaseous molecules on doped surfaces [11-13, 15,16] have employed first-principles calculations. This chapter considers the adsorption of some NO, NO_2, and N_2O oxides on boron-doped surfaces. These oxides are atmospheric pollutants produced by burning fossil fuels in industrial combustion engines and naturally through combustion at high temperatures during lightning. Both NO and NO_2 exist in unison and are primarily considered to have the highest impact on the human respiratory system and the environment. These oxides have been investigated theoretically and experimentally on intrinsic graphene, graphene oxide, and doped graphene [19,26-28]. The room temperature sensitivity of these oxides to graphene surfaces [20] and the study of the adsorption of nitrogen oxides on graphene oxides [29] have also been investigated. Zhang and coworkers demonstrated [13] that the doped and defective graphene interacts with molecules like CO, NO, NO_2, and NH_3. Investigations to improve the gas-sensing properties of graphene by introducing defects [21] and dopants

[7,11,12,19] have been explored with small gas molecules. Ali *et al.* [21] have studied NO and NO_2 on defective and ozone-treated graphene and observed high sensitivity towards these surfaces. A recent investigation by Chaudhary *et al.* [18] looked at a few molecules on boron and nitrogen co-doped surfaces to check the sensitivity for increased concentration of dopants on the surface and found a systematic increase in band-gap with the concentration [18].

In the current study, the first-principles method based on DFT is employed to study the adsorption of NO, NO_2, and N_2O on graphene surfaces doped with boron, nitrogen and on surfaces co-doped with both boron and nitrogen, at various concentrations with dopants arranged in different patterns. Even though there are a few adsorption studies on singly doped surfaces, the aspect of adsorption on the surfaces with different concentrations of dopants and with varied configurations are not conclusively explored, except for a few investigations, making this study exceptionally important and distinctive. [11,18]. The study of adsorption of the potent gaseous molecules, N_2O, NO, and NO_2, on surfaces where the transport properties can be governed may find application as potential sensors for these molecules. The current study shows how the electronic structure can vary drastically, not only with increased dopant concentrations but also with the adsorption of these molecules. The 'flat dispersion-less bands' that arise due to the adsorption of paramagnetic oxides of nitrogen on boron and nitrogen-doped surfaces are also investigated. The study of electronic structure with this molecular adsorption of nitrogen oxides has never been explored previously and is expected to bring novel insights.

4.2. Results and Discussion

This section presents the result of the investigation of the adsorption of the gases N_2O, NO, and NO_2 on doped surfaces. A few crucial adsorptions on co-doped surfaces are also discussed. From the previous investigation [11], it is clear that the doping configurations on the surface or patterns of the dopants on the surface make a difference in the band-gaps

generated, correlated with the sub-lattice symmetry breaking in the supercell. This result contrasts with the systematic increase of band-gaps with doping concentration predicted by Chaudhary *et al.* [18] for up to 50% doping of a graphene surface where the band-gaps show an appreciable increase. Because of the doping of graphene with similarly sized boron, the two-dimensional structure is least affected, with only slight variations of bond lengths from 1.42 Å to 1.45- 1.48 Å. The doping patterns on which adsorptions are defined, except for the single boron-doped graphene (3.14% concentration, hereafter referred to as 1B), for 6.25 and 9.37% dopant concentrations of boron surfaces are shown in Figure 3.1. Similar concentrations are also considered for the nitrogen-doped systems, as shown in Figure 3.4.

To understand the effect of substitutional doping on graphene, the band structure is initially calculated for the systems discussed above. The electronic band structure diagrams for all boron-doped and nitrogen-doped systems corresponding to various configurations and different doping concentrations, from 'a' to 'f' are shown in the previous chapter as in Figures 3.3 and 3.5, respectively.

4.2.1. Adsorption of NO and NO_2 on doped graphene surfaces

This section discusses the adsorption of the paramagnetic molecules NO and NO_2 on boron-doped surfaces, their adsorption mechanisms, and the unusual electronic changes induced upon adsorption on doped surfaces. To understand both adsorption and the electronic changes, the calculated values of adsorption energy, the distances from the surface, and the charge transfer, along with the band-gaps of bare surface and for the gaseous molecules NO and NO_2 adsorbed on these surfaces, are presented in Table 4.1 and 4.2 respectively. NO adsorption on all surfaces other than 'b' and 'c' is strong physisorption with an appreciable adsorption energy of 0.4 - 0.9 eV and adsorbate - surface distances of 2-2.5 Å with typical charge transfers suitable for physisorptions.

Table 4.1. The adsorption energy, the distance of the adsorbate from the surface, the band-gap

of the bare surface, and charge transfers of NO gas molecules on graphene surfaces doped with boron with different concentrations forming various configurations. The positive sign in the charge transfer indicates charge transfer from NO to the graphene surfaces and vice versa. 1BG denotes 1boron doped graphene with 3.14% concentration.

Molecule/surface	**Adsorption Energy (eV)**	**Distance (Å)**	**Band-gap bare surface (eV)**	**Charge transfer (e)**
NO/G	-0.0291	3.36	0	+0.010
NO/1BG	-0.485	2.46	0.14	+0.014
NO/a	-0.600	2.05	0.21	+0.032
NO/b	-1.280	1.55 O-B 1.40 C-N	0.37	-0.880
NO/c	-1.521	1.52 O-B	0.15	-0.500
NO/d	-0.880	2.42	0.57	+0.017
NO/e	-0.456	2.38	0.16	+0.056
NO/f	-0.806	2.09	0.58	+0.069

NO adsorption on all surfaces other than 'b' and 'c' is strong physisorption with an appreciable adsorption energy of 0.4 - 0.9 eV and adsorbate - surface distances of 2-2.5 Å with typical charge transfers suitable for physisorptions. The geometry-optimized structures of the adsorption of NO on a few boron-doped surfaces with different mole fractions are shown in Figure 4.1. For adsorption on 'b' and 'c' type patterned surfaces (with both concentrations 6.28%), the molecule NO is chemisorbed as evident from the adsorption energy and the formation of bonds with the surface. Besides, both surfaces have appreciable charge transfer, confirming chemisorption. It is worth mentioning that the 'b' surface is where the equivalent

sites on the graphene supercell are occupied, leading to sub-lattice symmetry. The bond lengths for carbon to nitrogen are typical C-N single bond distances, and the boron to oxygen distances are typical tetra-coordinated boron. It is seen that the adsorption of NO, on most of the surfaces except for the intrinsic graphene, is strong physisorption or chemisorption with bond formation. In the case of NO on intrinsic graphene, the molecule is only weakly physisorbed, indicated by the low adsorption energy and negligible charge transfer. In all other cases, other than with the 'b' and 'c' type surface, stronger physisorptions can be seen through the higher energies and the distances to the surface lower than 2.5 Å. With distances less than 2.5 Å, one can classify them as similar to interactions in stronger hydrogen bonds.

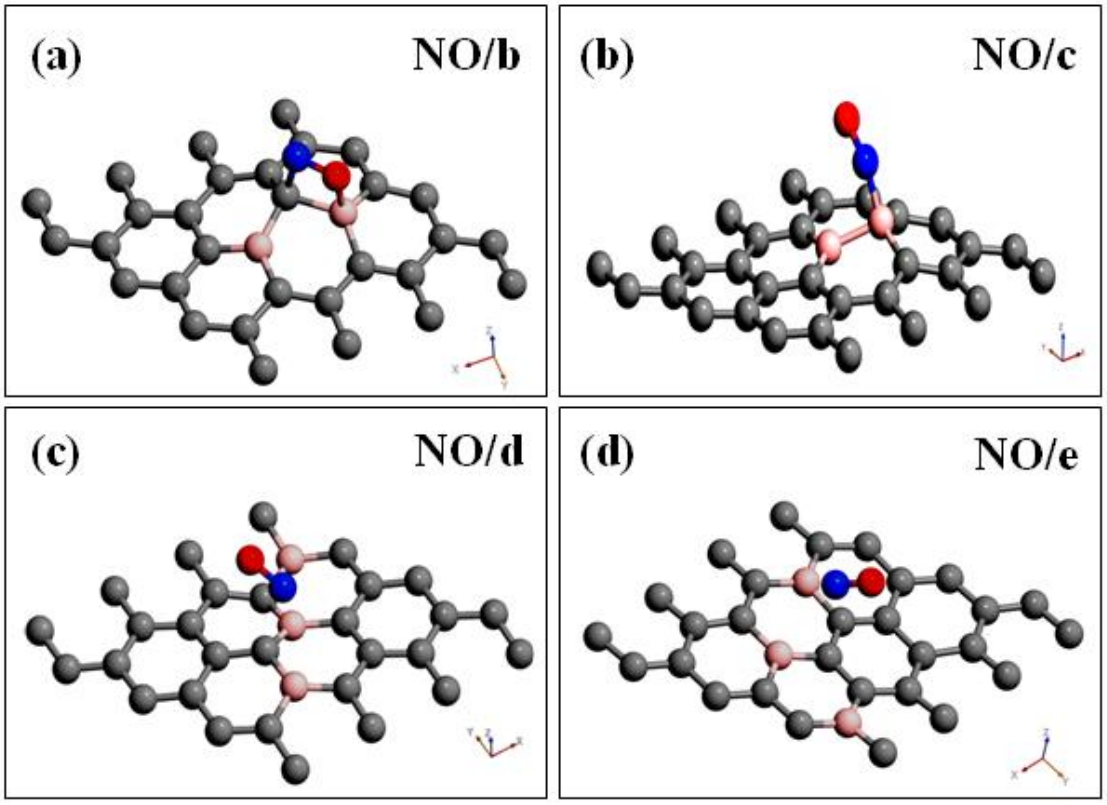

Fig. 4.1. The optimized geometry of boron-doped graphene (a) NO/a (b) NO/c (c) NO/d and (d) NO/e configurations.

Table 4.2. The adsorption energy, the distance of the adsorbate from the surface, the band-gap of the bare surface, and charge transfers of NO_2 molecule on graphene surfaces doped with boron, with different concentrations forming various configurations. The positive sign in the

charge transfer indicates charge transfer from the molecule to the surface and vice versa. 1BG denotes single boron-doped graphene with a 3.14% concentration of boron.

Molecule/surface	Adsorption Energy (eV)	Distance (Å)	Band-gap bare surface (eV)	Charge transfer (e)
NO_2/G	0.09256	3.50	0	-0.014
NO_2/1BG	-1.5097	1.64 B-O	0.14	-0.50
NO_2/a	-0.7359	1.60 B-O	0.21	-0.64
NO_2/b	-0.6272	1.68 B-O 1.63 C-O	0.37	-0.45
NO_2/c	-1.4704	1.47 B-O	0.15	-0.70
NO_2/d	-0.8783	1.61 B-O	0.57	-0.50
NO_2/e	-0.8381	1.60	0.16	-0.60
NO_2/f	-0.1655	2.98	0.58	-0.16

NO_2 adsorbs strongly on all surfaces except pristine graphene and the surface pattern 'f'. It shows chemical adsorption with the bond formation and appreciable charge transfer, in this case, to the electron-withdrawing molecule NO_2. As mentioned in the previous literature, these paramagnetic molecules are expected to produce significant doping effects [19]. The interaction of NO and NO_2 on intrinsic graphene is depicted in terms of the band structure and the density of states plot to understand the orbital interactions in Figure 4.2. The adsorption energy of NO on intrinsic graphene is very low, of the order of 0.01 eV, and the charge transfer to the surface is also low, 0.017e from NO to the graphene, and the molecule lies above 3.4 Å above the surface. NO is a donor molecule, and the HOMO (the LUMO) is degenerate and half-filled 2p-π molecular orbitals. The additional level seen in the band diagram originated

from the adsorbate and is only slightly below the Dirac point (less than 0.1 eV). At the distances of physisorption, there is no appreciable orbital overlap with the carbon at the p orbitals on graphene, as can be visualized from the DOS.

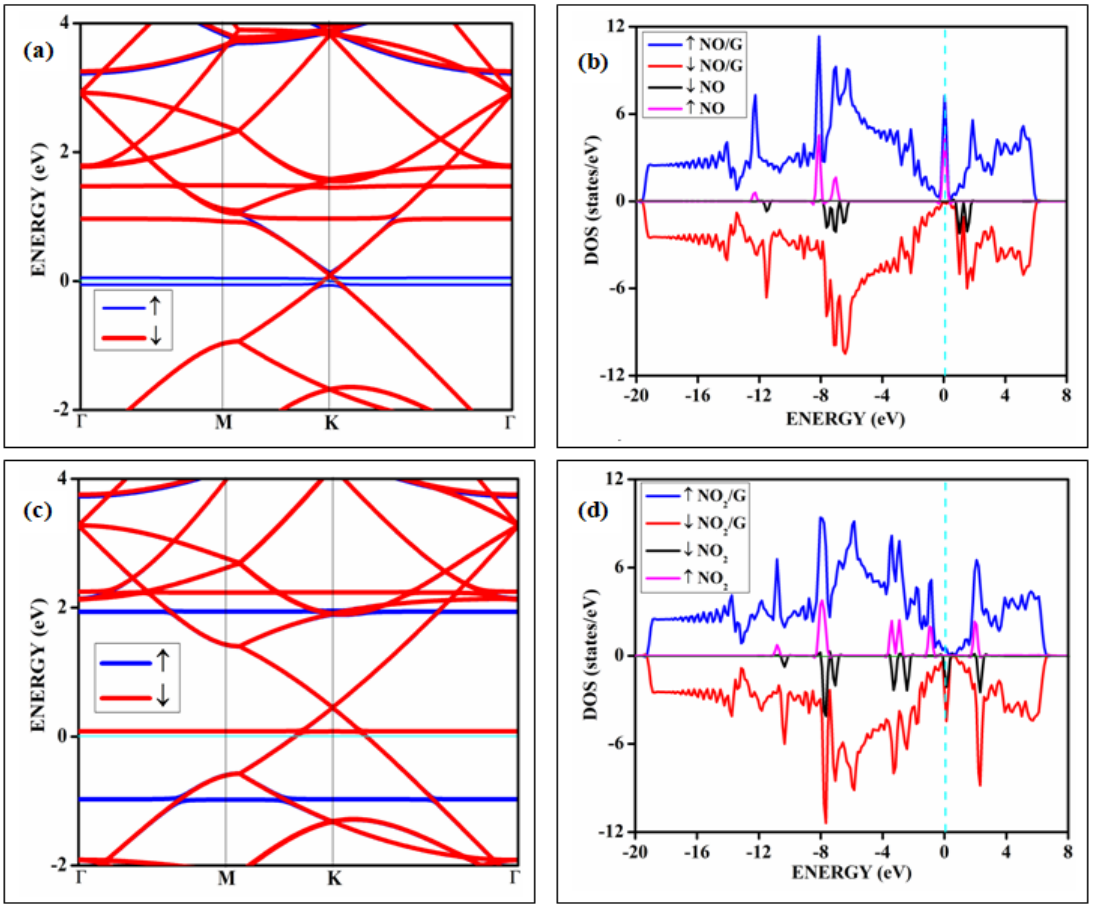

Fig. 4.2. The spin-resolved band structure (a) and the density of states (b) of NO on intrinsic graphene and that for NO_2 on intrinsic graphene ((c) and (d)).

Similarly, for the adsorption of the NO_2 molecule, we have found a charge transfer of 0.014e from graphene to the molecule. As noted for the adsorption of NO and NO_2 on pristine graphene by Leenaerts *et al*. [26], it is seen that the Fermi level is situated below the Dirac point by about 0.25 eV in the case of NO_2, which introduces slightly stronger doping effects compared to the NO, where the effects of doping are negligible. The peak in the down spin side of NO_2/G shows the HOMO orbital of NO_2 below the Fermi level.

The changes in the magnetic properties are visible as asymmetry in the molecule's partial

density of states (PDOS) of Figure 4.2. The band diagram and DOS of pure graphene are shown in Figure 4.3.

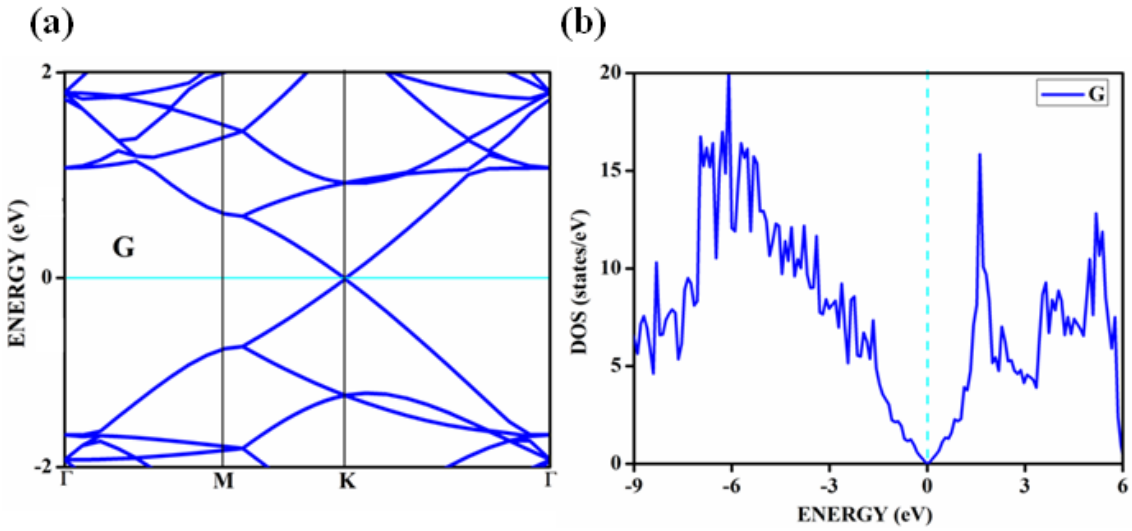

Fig. 4.3. (a) The band structure and (b) DOS of pristine graphene.

The introduction of states below the Fermi shows that states created below the Fermi lead to n-type doping with the adsorption of an electron donor like NO. While NO_2 is an electron-accepting species, similar states are formed slightly below the Dirac point. Similar to the prediction made by Leenaerts *et al.* [26], no significant doping effects with NO adsorption on intrinsic graphene are found in this study. The HOMO of NO, a paramagnetic species, is degenerate, half-filled, and lies slightly below the Dirac point. The small amount of charge transfer from NO is compensated for by the orbital mixing happening with carbon p-orbitals. Even though the band-gap is not opened with NO_2 adsorption on intrinsic graphene, the Dirac point is shifted above the Fermi level, indicating that the electronic structure of graphene is sensitive to the NO_2 molecule. The results on the intrinsic graphene compare with Leenaerts *et al*. [26] but contradict the claim by Wehling *et al*. [19] that the paramagnetic molecules are strong dopants found true only in the case of NO_2.

In the physisorption and chemisorption of NO and NO_2, adsorbate-absorbent interactions on the chemically doped surfaces show unusual and interesting electronic effects.

In almost all cases of adsorption of NO, chemisorption or strong physisorption occurs wherein adsorbate induces flattened-out bands with all the systems. The introduction of flat bands in the band structure can be attributed to the orbital contribution from the adsorbate molecules and the orbital mixing or hybridizations between the adsorbate and the adsorbent during the strong interplay with the surface. In this strongly bound limit, wherever strong physisorption or formations of bonds or chemisorption happen, the behavior of the adsorbate molecule is dominated by the potential energy. It implies that the band eigenvalues become independent of the k-vector, thus forming flat bands, as shown in Figures 4.4 for NO and 4.5 for NO_2. It leads to a band structure where the bands are almost horizontal and transform into levels similar to energy levels in isolated systems. It is observed that such dispersion-less flat bands occur when the adsorbate molecules are almost localized above the surface. The band structures obtained for the various adsorptions are shown in Figure 4.4 for the different NO/surface combinations. In this figure, the band structures of the doped surface without adsorption, for the adsorption complex, and the total and the projected density of states for the NO adsorbed on the corresponding surfaces are given, where NO/b and NO/c correspond to chemisorption and others to strong physisorption.

The effects of adsorbate-adsorbent interactions are very much visible, for example, in the dispersion-less band diagrams with flat bands and also from the density of states. The NO orbital interactions are highest in the cases of chemisorption (b) and (c), shown in Figure 4.4. It is interesting to see that the density peaks vanish from NO partial density of states in both NO/b and NO/c cases, meaning that the orbitals mix up via hybridization, resulting in bonding with the surface. In the case of (b) in Figure 4.4, the band-gap of the bare surface is 0.37 eV, and it vanishes after NO adsorption.

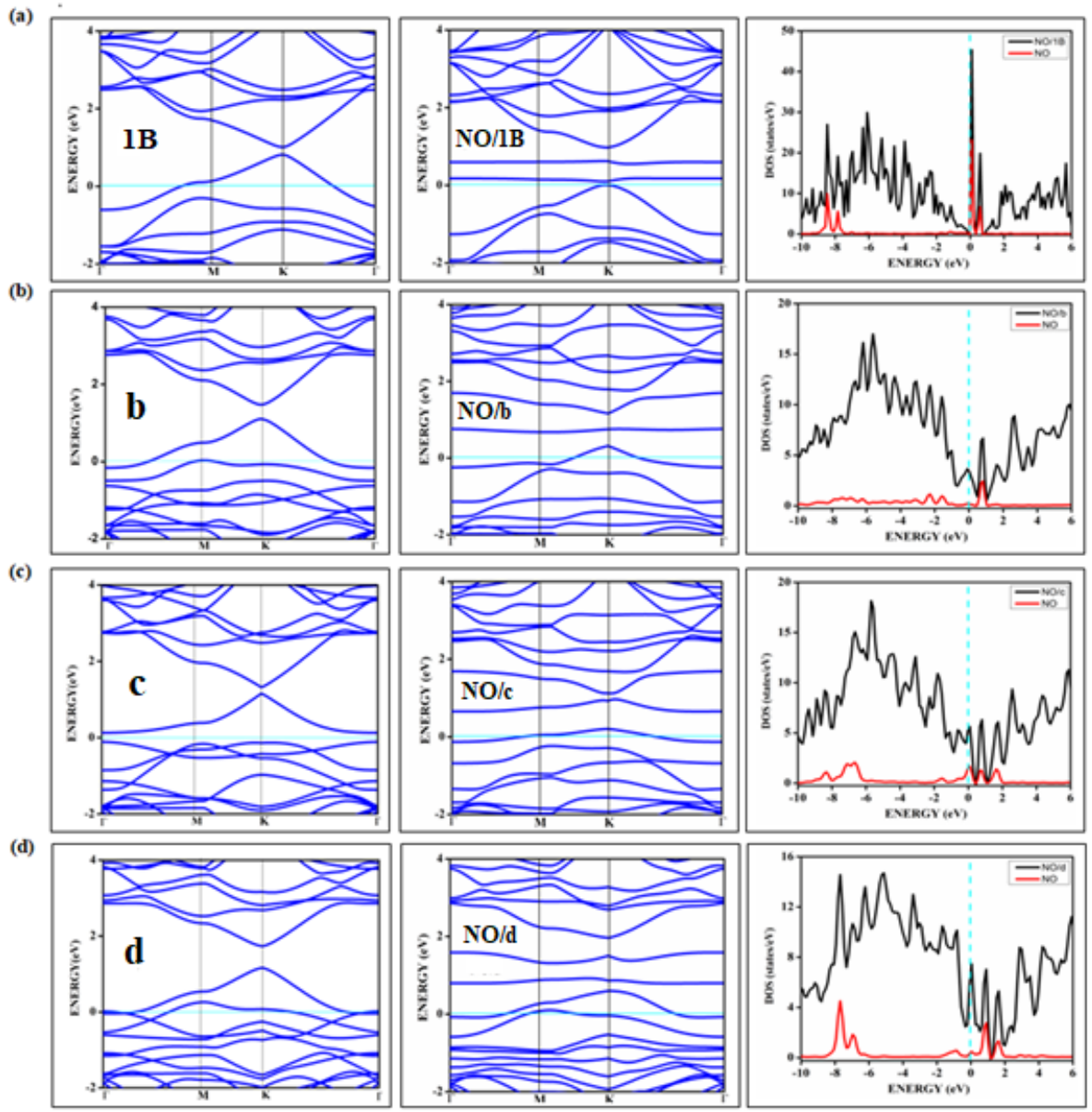

Fig. 4.4. The band structure and DOS of NO adsorbed on doped graphene surfaces, shown in each row (a), (b), (c), and (d) are the band structure of the surface, adsorbate surface complex, and the density of states. In the DOS plots, the states for the adsorbed molecules are also shown in addition to the total DOS (Total Density of States). 1B indicates single boron-doped graphene with a dopant concentration of 3.14%. The cyan line represents the Fermi level.

There is a complete loss of NO peaks from the lower energy region, and only a state is visible at around 0.6 eV above the Fermi level. In the other case of chemisorption, NO/c depicted in Figure 4.4 (c) also, the typical density of states of the pure NO vanishes, implying

that the molecule NO is not in its free state.

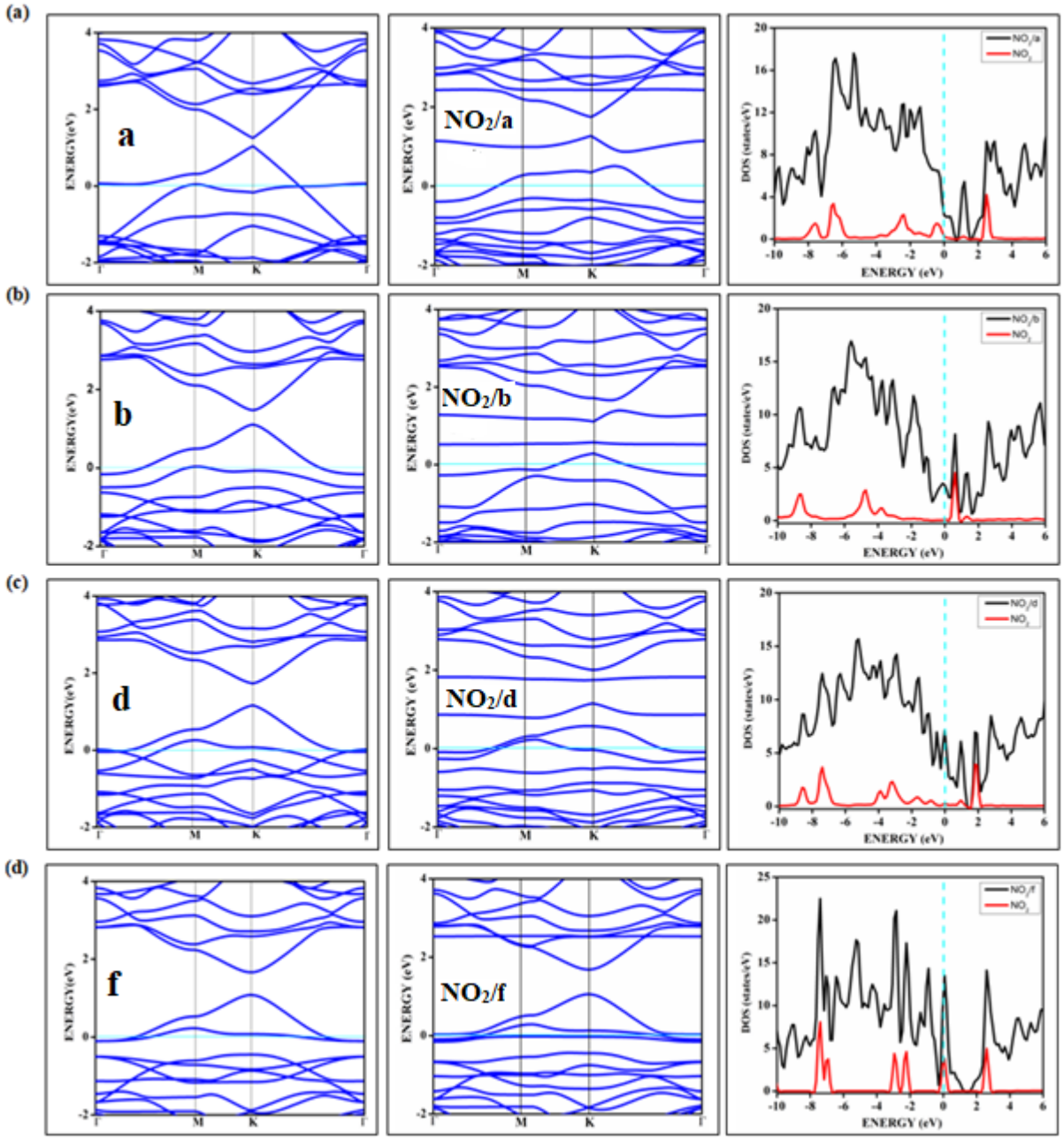

Fig. 4.5. The band structure and DOS of NO_2 adsorbed on doped graphene surfaces. The band structure of the surface, adsorbate surface complex, and the density of states are shown, respectively in (a), (b), (c), (d).

Additionally, it is to be noted that there are many states around the Femi due to the adsorbate NO, both for chemisorption and for physisorption. It indicates that the molecule is localized over the doped, adsorbent surface. In all the cases of NO/doped surface combinations, the

electronic structure deals with the complete loss of dispersion of bands, leading to a lack of special features as in intrinsic Dirac materials.

The spin-resolved band structure and total and partial densities of states are given in Figure 4.6 for a sample case of adsorption on the 'c' surface to understand the adsorption process further. The DOS plot for the adsorbed NO species has been changed compared to the bare NO, and the adsorbed complex NO/c shows a considerable difference from that of the plain surface, 'c'. In the adsorbed NO molecule, some of the typical peaks around the Fermi level, shown in Figure 4.6 (b), have disappeared or diminished compared to the bare molecule in Figure 4.3 (b). Above the Fermi, the clubbing of two or more states can be seen because of the flat bands, and therefore the system no longer behaves like a semiconductor or semi-metal and has transformed more into a metallic state. Compared to Figure 4.3 (b), the magnetic property is also expected to be reduced for the adsorbed molecule as the spin-up and down channels become less asymmetric than the adsorption on pristine graphene.

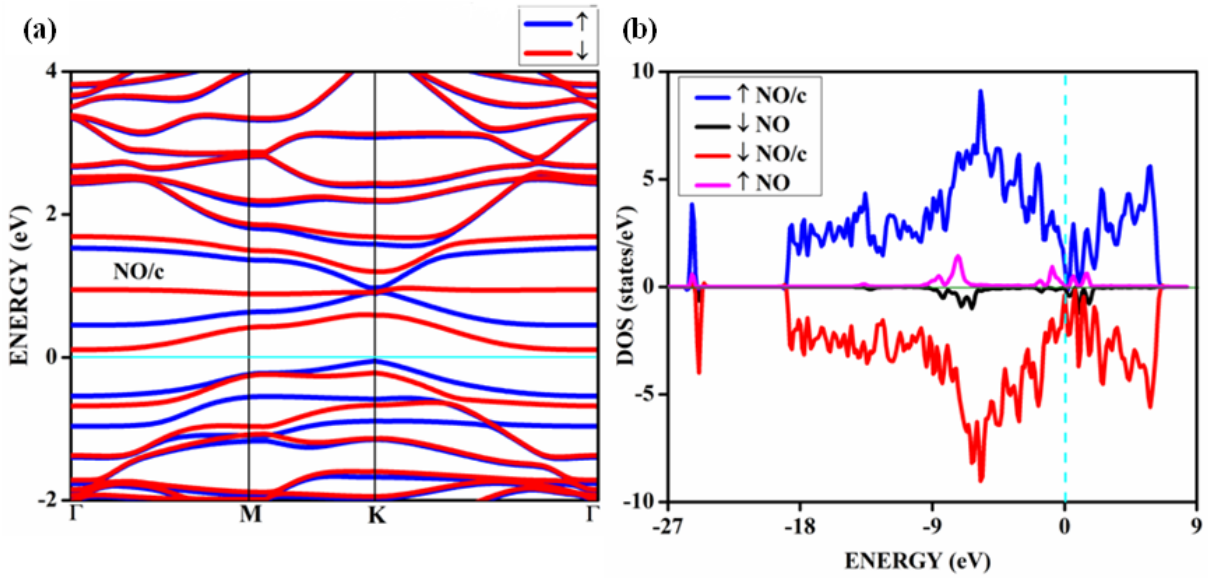

Fig. 4.6. The spin-polarized band structure (a) and DOS of NO/c system (b). The total DOS of the NO-surface (NO/c) complex and PDOS of NO are given.

Both NO/c and NO/b show appreciable charge transfer from the adsorbate, as shown in Tables 4.1 and 4.2, followed by considerable orbital overlaps. NO/b surface shows a significant

overlap of states, even those at lower eigenvalues, with possible hybridization with the carbon orbitals. The absence of the peak below -8 eV and other less intense peaks for NO/b supports this result. For both these cases, the charge transfers are of 0.88e for NO/c and 0.5e for NO/b surface.

In all cases of NO_2 except for adsorption on the 'f' surface, the adsorbate molecule interacts with the surface strongly leading to a dispersion-less band structure. It was observed that the states are induced in between the valence and the conduction bands of the original doped surface. Surprisingly, the NO_2/f system shows no such effect. The 'f' type doped surface of boron-doped graphene is of the concentration of about 9.4% dopants, and the borons are symmetrically substituted in the sub-lattice. The sub-lattice-induced based symmetry is responsible for the appreciable band-gap of 0.6 eV in the case of this surface. This surface remains unaffected by the NO_2 molecule, and this effect is visible in the DOS of Figure 4.5 (d), where the adsorbate molecule's states remain unchanged on the surface. The unreactive orbitals appear as flat lines at the Fermi level, much above the Dirac point in the conduction band at around 2.5 eV and below in the valence band below -2 eV.

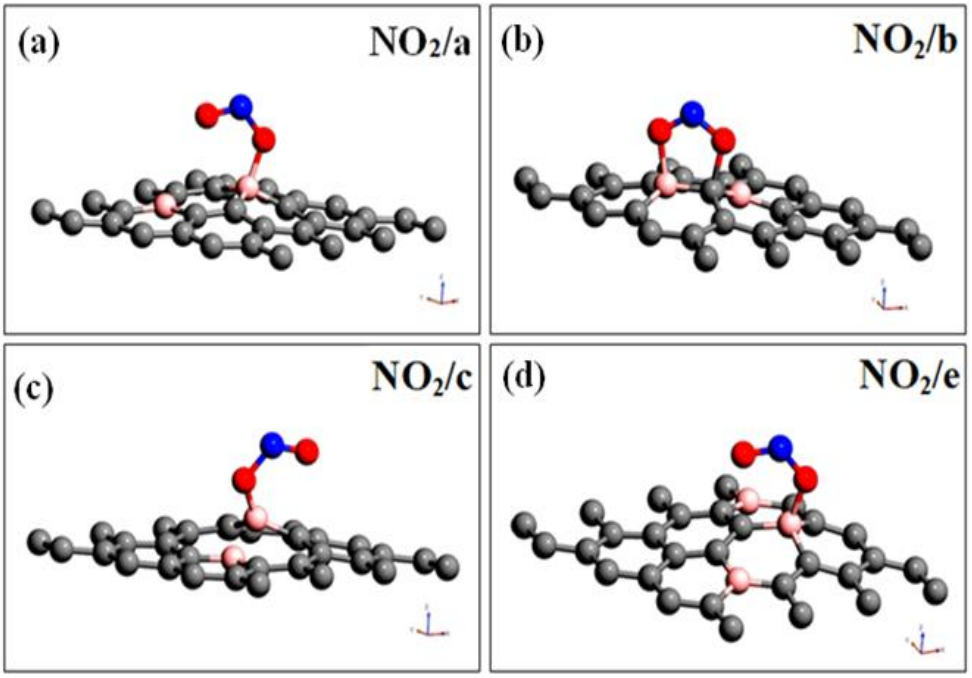

Fig. 4.7. The geometry optimized structures NO_2 on boron-doped graphene surfaces (a) NO_2/a (b) NO_2/b (c) NO_2/c and (d) NO_2/e configurations. All show chemisorption of NO_2.

The geometry-optimized structures for NO_2 chemisorbed on various boron-doped surfaces are shown in Figure 4.7. To better understand the orbital contributions, the spin-polarized density of states is drawn in Figure 4.8 only for NO on various substrates. Similar representative plots for NO_2 are shown in Figure 4.9.

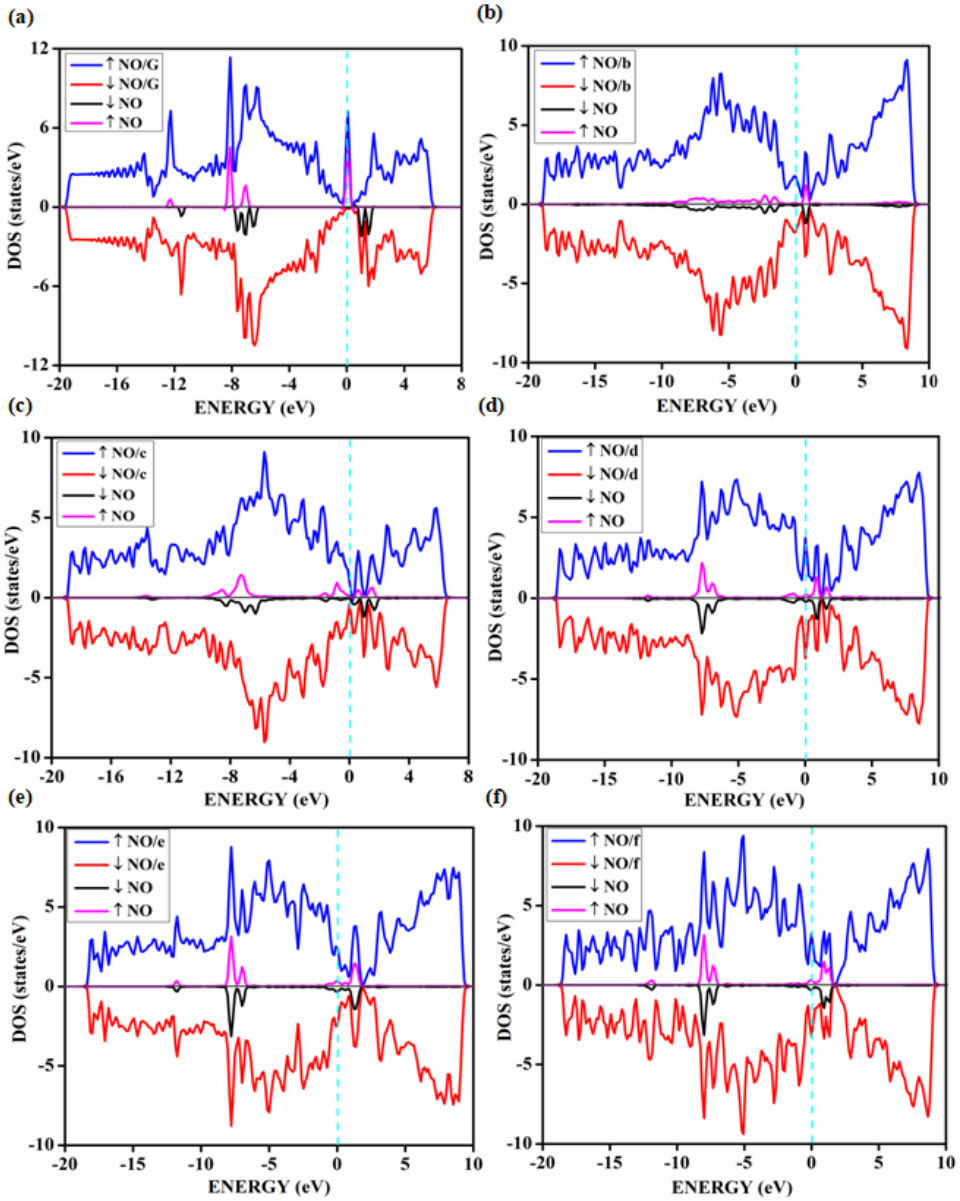

Fig. 4.8. The spin-polarized density of states for NO adsorption on various boron-doped adsorbents (a) NO/G (b) NO/b (c) NO/c (d) NO/d (e) NO/e (f) NO/f.

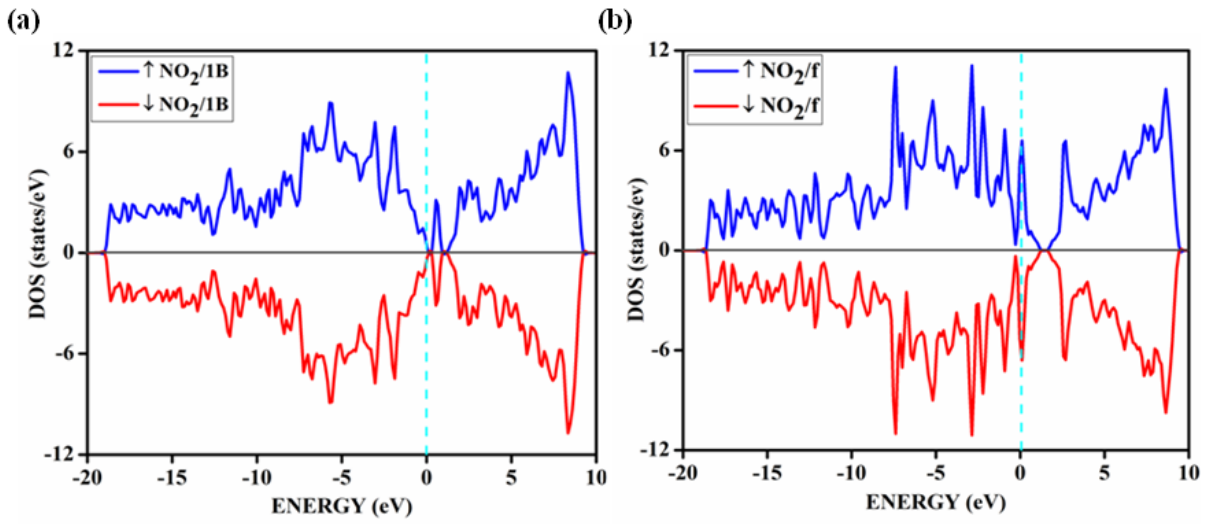

Fig. 4.9. The spin-polarized DOS showing up (↑) and down spin (↓) of (a) NO_2 on one boron doped noted as NO_2/1B and (b) NO_2 on 9.3% doped boron of configuration f noted as NO_2/f.

Due to the presence of the valence states near Fermi E_F, covalent adsorbate-adsorbent interactions facilitate the spontaneous formation of a bond. The spin-polarized DOS indicates a clustering of states near the Fermi level, meaning the valence and conduction bands and the adsorbed complex overlap have turned more into a metallic state.

Table 4.3. The adsorption energy, band-gap after adsorption of NO, band-gaps of surface without adsorbate, distance of adsorbate from the adsorbent for nitrogen-doped graphene of different concentrations and configurations, respectively.

System	Adsorption Energy (eV)	Band-gap (eV)	Pure surface band-gap (eV)	Distance (Å)
NO/1N	-0.05473	0.20	0.21	2.98
NO/a2	-0.184405	0.19	0.22	1.65 C-N
NO/b2	-0.445133	FLAT BAND	0.40	2.62
NO/c2	-0.07872	FLAT BAND	0.0	2.67

NO/d2	-0.461106	0.27	0.57	1.65 C-N
NO/e2	-0.170969	0.17	0.15	1.53 C-N
NO/f2	-0.752725	FLAT BAND	0.59	2.63

The NO adsorption calculations on nitrogen-doped surfaces have also been done, and their optimized geometries are shown in Figure 4.10. Their results are summarized in Table 4.3, and qualitatively similar effects with completely dispersion-less bands are observed and shown in Figure 4.11.

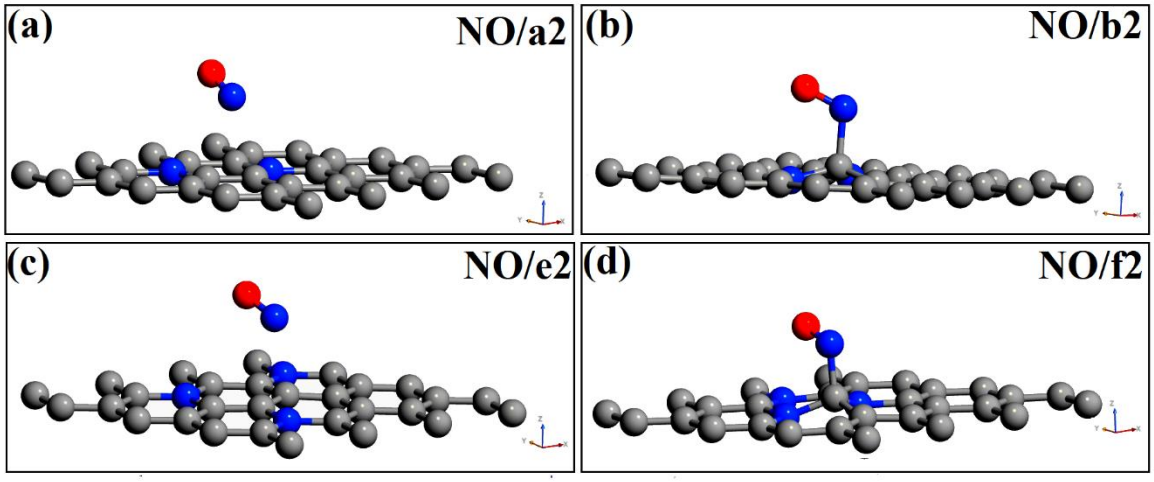

Fig. 4.10. The optimized structures of nitrogen-doped 4x4 supercell graphene (a) NO/a2 (b) NO/b2 (c) NO/e2 and (d) NO/f2 configurations.

On the other hand, with calculations with graphene surfaces co-doped with 3.14% boron and 9.37% nitrogen, the results agree with what is expected of an n-type doped surface discussed in our most recent work [11]. Here, the surface is co-doped with both boron and N-doped, and the n-type doping is more prominent with 3.14% boron and 9.37% nitrogen and forms an n-type semiconductor with a band-gap of 0.66 eV. The electron donor species NO does show appreciable interactions in terms of orbital mixing up with this electron-rich surface. On the other hand, NO_2 is found to be chemically adsorbed on the co-doped surface without disruption of the bands. The results are summarized in Figure 4.12; NO does not interact much

with the electron donor species in terms of orbital mixing up with this electron-rich surface.

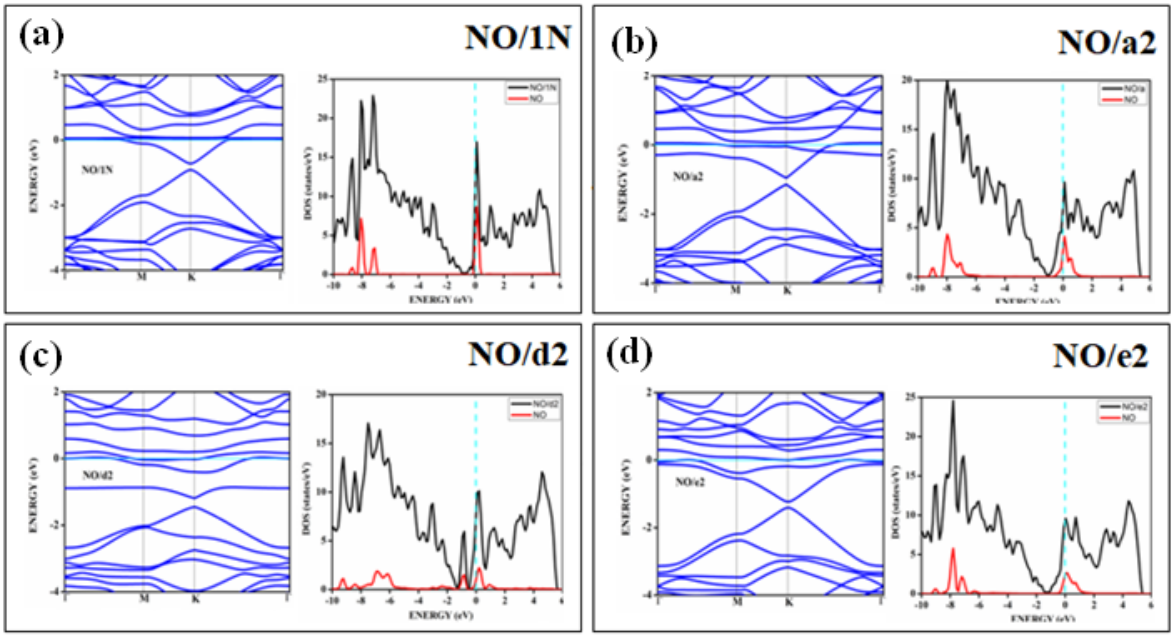

Fig. 4.11. The band structure and respective DOS of NO on (a) 1N, (b) a2, (c) d2, and (d) e2 of graphene surfaces.

NO_2 is found to be chemically adsorbed on the co-doped surface without disruption of the bands. The adsorption energy and bond distances are -1.92 eV and 1.53 Å. The additional levels about 0.5 eV above the Fermi level and those below the Fermi are from the adsorbate, which forms flat bands. In the adsorption of NO_2 on a co-doped surface, the interaction of the NO_2 acceptor molecule is predominant. Unsurprisingly, the electron-rich surface predominantly doped with n-type doping strongly adsorbs a molecular species, which is an electron acceptor. A recent investigation by Chaudhary *et al.* [18] claimed that co-doped surfaces are better sensors for nitrogen oxides. The question arises here as to why the adsorption on co-doped systems does not form flat bands that would have wholly disturbed the dispersion. Based on the earlier arguments based on the density of states, a clear explanation can be given that the complete disruption of the band dispersions happens only when the additional bands are created between the Dirac cones, i.e., between the valence and the conduction bands.

Regarding NO and NO_2 adsorptions on boron-doped surfaces, the interactions between the adsorbate and surface orbitals are highest near the Fermi level. It is also close to the Dirac region, creating additional flat bands due to the orbital couplings. In the case of co-doping, the orbital couplings happen at areas far away from the Dirac point.

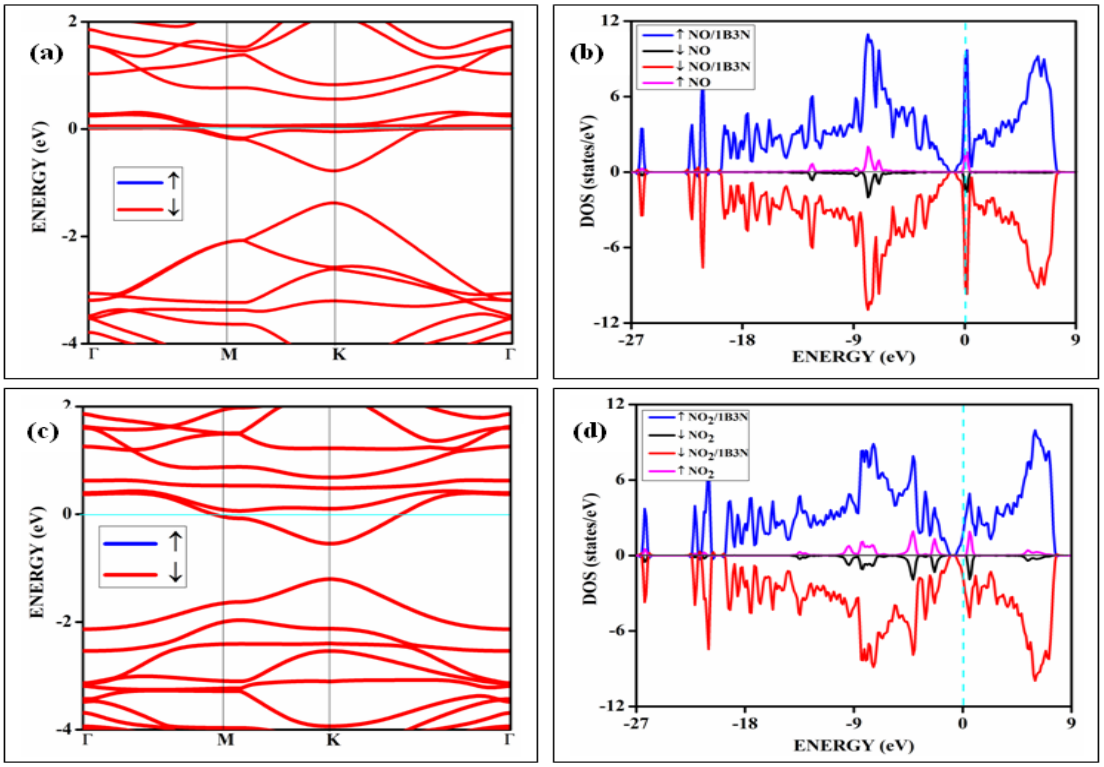

Fig. 4.12. The adsorption of NO and NO_2 on a co-doped graphene system is denoted as 1B3N, where 3.14% boron and 9.37% nitrogen are doped together. (a) and (b) are the band structure and respective DOS of NO/1B3N, (c) and (d) are the band structure and respective DOS of NO_2/1B3N.

To confirm the adsorption mechanism, the potential energy curves for a few representative cases are plotted in Figure 4.13 for physisorption and where there are strong chemical interactions and the formation of bonds.

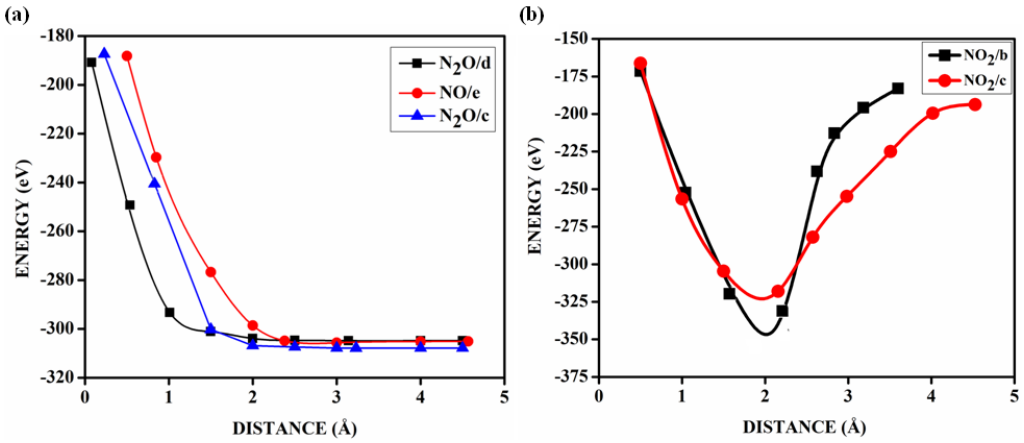

Fig. 4.13. Typical (a) physisorption and (b) chemisorption behaviors are represented as the potential energy diagram for representative cases of adsorptions of NO, NO_2, and N_2O.

It is possible to observe a clear minimum corresponding to the bond distances of the adsorbate gases with the doped surfaces in the case of chemical adsorption and typical curves for physisorption in the case of weaker adsorptions. The charge density difference plots are also made for some of the adsorptions, and the plots are available in Figure 4.14 and Figure 4.15. These plots are calculated based on Bader charge calculation using Eq. 2.48.

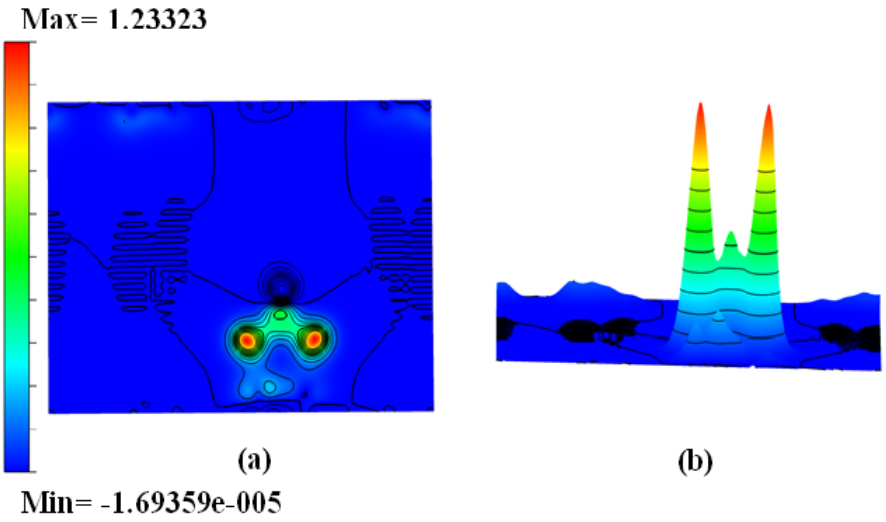

Fig. 4.14. The difference charge density contour surface of NO_2/b (a) Contour plot and (b) Bird-eye-view perspective. The unit of the isovalue is e/Å^3.

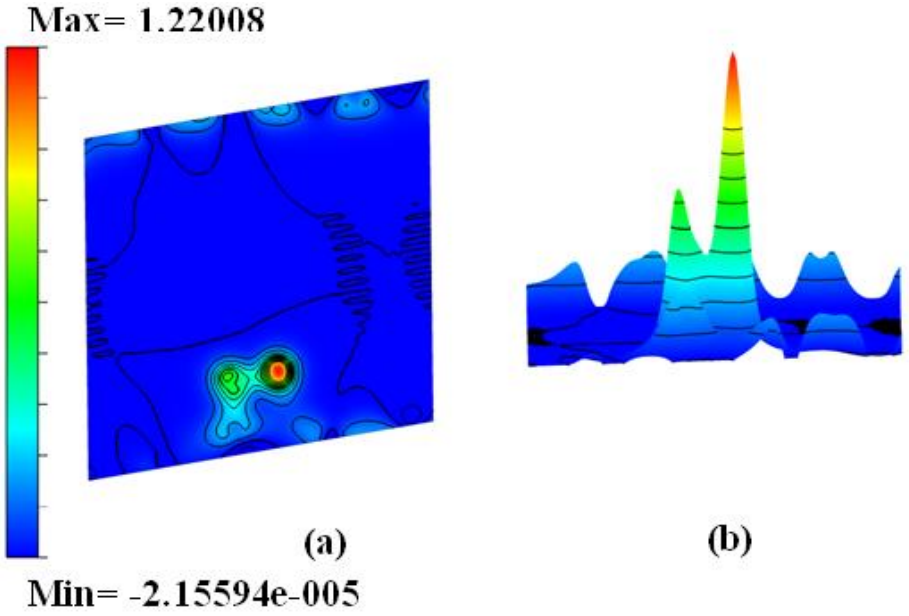

Fig. 4.15. The difference charge density contour surface of NO/b (a) Contour plot and (b) Bird-eye-view perspective. The unit of the isovalue is e/Å^3.

4.2.2. Adsorption of N_2O on doped surfaces

All cases of adsorption of N_2O on boron-doped graphene surfaces are physisorptions, as indicated by the low adsorption energy values and the adsorbate-adsorbent distances given in Table 4.4. A representative plot is given in Figure 4.16.

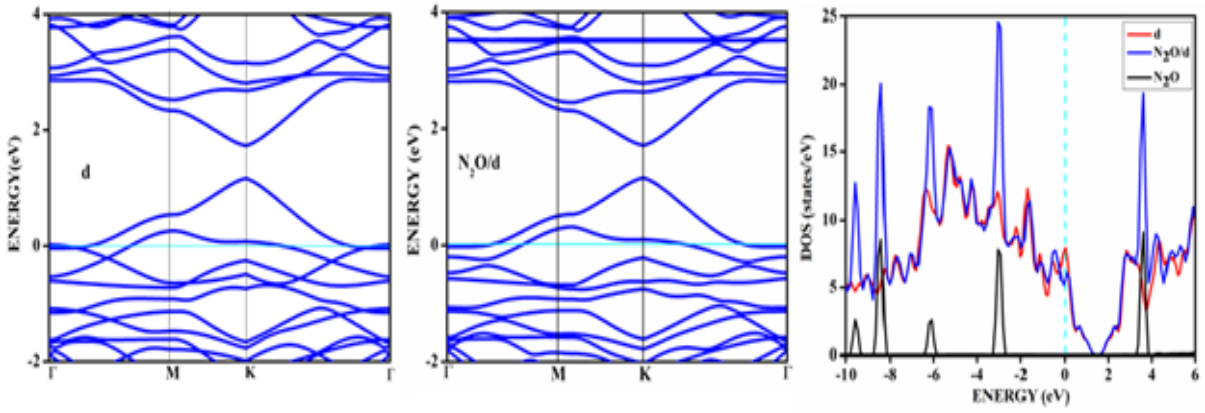

Fig. 4.16. The band structure and DOS of the surface 'd' and the adsorbed complex N_2O/d.

The adsorption energy values for the symmetrically doped surfaces, ‘b’, ‘d’, and ‘f’, are slightly higher. Still, the bare surfaces' band structure is unaffected by these negligible interactions, and the molecular orbitals of N_2O are the least affected. Similar to NO, NO_2

adsorption on a co-doped surface, for N_2O, we do not find any flat band near the Fermi level, but the localized states can be seen as a dispersion-less band near 1.8 eV as can be seen in Figure 4.17.

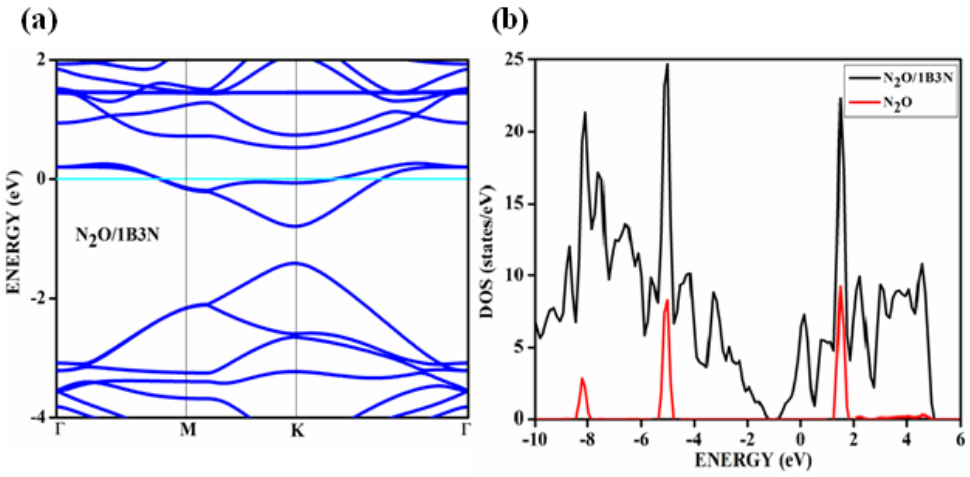

Fig. 4.17. The band structure and DOS of N_2O on 1B3N doped graphene (a) Band structure and (b) DOS.

Table 4.4. The adsorption energy, distance of adsorbate from the surface, the band-gap of the system, band-gap of the surface, sensing response, and charge transfers of N_2O gas molecules on different configurations and concentrations of boron-doped graphene surfaces.

Molecule/surface	**Adsorption Energy (eV)**	**Distance (Å)**	**Band-gap (eV)**	**Band-gap pure surface (eV)**	**Sensing Response**
N_2O/G	0.028	3.41	0	0	Nil
N_2O/1B	-0.005	3.44	0.20	0.14	0
N_2O/a	-0.003	3.32	0.14	0.21	1.55%
N_2O/b	0.088	3.34	0.38	0.37	1.5%
N_2O/c	-0.100	3.23	0.14	0.15	3.3%

N_2O/d	-0.123	3.14	0.56	0.57	3.04%
N_2O/e	-0.030	3.29	0.16	0.16	0
N_2O/f	-0.240	3.12	0.61	0.58	3.16%

As the surfaces labeled 1B, a, c, e, etc. show tiny band-gap opening before and after adsorption of N_2O, of the order of 0.14-0.2 eV, the formula is given in Eq. 4.1, based on Drude's formula [30], is applied to calculate the sensing response to the gas. Since Drude's procedure is valid for transport in metals, the same remains valid for graphene since it is a semi-metal with significant carrier mobility. The formula is rewritten in Eq. 4.2 in terms of the number of energy states near the Fermi level in terms of the density of states at the Fermi level with and without adsorbate gas [31,32]. Here, $N_F^{(g)}$ and $N_F^{(a)}$ are the DOS at the Fermi level with and without gas molecules, respectively.

$$S = \frac{|\sigma g - \sigma a|}{\sigma a} \times 100\ \% \qquad (4.1)$$

$$S = \frac{N_F^{(g)} - N_F^{(a)}}{N_F^{(a)}} \times 100\ \% \qquad (4.2)$$

The sensing responses for N_2O for various surfaces are calculated and presented in Figure 4.18. In cases where the electronic band-gaps for the surfaces remain small and are unaffected by the adsorbate N_2O, the sensing responses are low. In this case, where only physisorption happens, it is also worth assuming that the mobility of the adsorbent surface is independent of the concentration of the gas molecules.

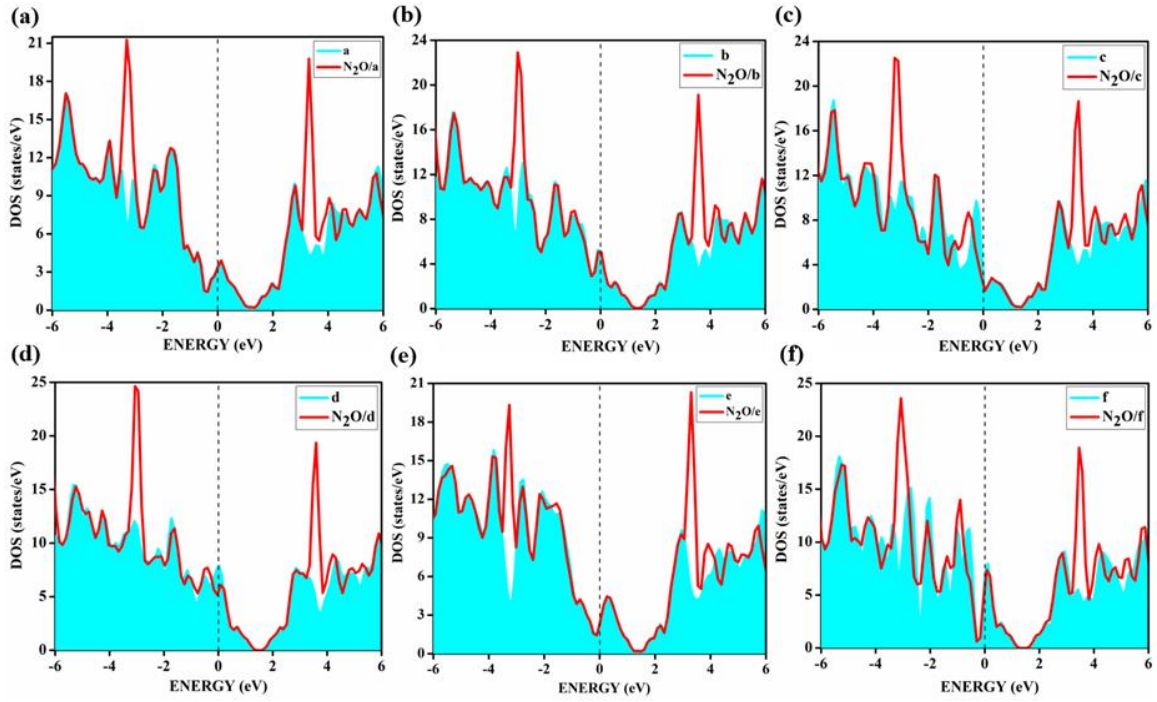

Fig. 4.18. The DOS of the system with adsorbate and in comparison with their respective surfaces (a) N_2O/a (b) N_2O/b (c) N_2O/c (d) N_2O/d (e) N_2O/e (f) N_2O/f. The sensing response is calculated based on Drude's formula for the weak adsorption of N_2O on doped graphene surfaces. The shaded region corresponds to the bare surface.

The adsorption scenarios where physisorption happens where the band-gaps are not changed much compared to the pristine graphene showed low sensitivity based on Drude's 5-10% formula. This value is very reasonable, considering there is only weak physisorption, even though the formula based on Drude's formula is inappropriate for describing a semi-metallic system. Also, the Bader charges show that there is only a negligible charge transfer of the order of 10^{-3} or less from or to the surface

4.3. Conclusion

In summary, the exotic effects in the electronic structure of graphene due to the molecular adsorption of paramagnetic oxides of nitrogen, NO, and NO_2 are discussed in this chapter. In both cases of adsorption, the creation of flat bands in the band structure, with the destruction of the Dirac cone dispersions, is observed. It is attributed to the intense coupling

of the adsorbate and adsorbent surface states near the Fermi level, where orbitals of both mixes lead to featureless bands. This kind of flat band offers many types of physical interpretations. In the case of strong physisorption or chemisorption, the behaviors of the adsorbate molecule are dominated by the potential energy. It implies that the band eigenvalues become independent of the k-vector, thus generating the flat bands that are almost horizontal and transform into the kind of energy levels in isolated systems. It is observed that such dispersion-less flat bands occur when the adsorbate molecules are almost localized above the surface. Also, in another way, in the momentum space, it can be viewed as the particle having infinite effective mass and, therefore, not dispersive.

Interestingly, complete disruption of the band dispersions happens only when the additional bands are created between the Dirac cones, i.e., between the valence and the conduction bands. In the case of NO and NO_2 adsorptions on boron-doped surfaces, it is seen that the interactions between the adsorbate and surface orbitals are highest near the Fermi level, which is also close to the Dirac region and due to the orbital couplings, additional flat bands are created. In the case of co-doping, the orbital couplings happen at regions far away from the Dirac point, and there are only a few states near the Fermi level. A recent paper by Haddadi *et al*. [33] discusses the generation of Moire flat bands in the case of twisted bilayer graphenes at magic angles. In this study, the flat band is induced by the chemical interactions between the adsorbent and adsorbate, which depends on the nature of adsorbate molecules near the doped graphene surface. The adsorption of paramagnetic oxides of nitrogen on chemically modified graphene surfaces thus gives an exciting insight into this new electronic feature of dispersion-less bands. In addition to the paramagnetic species discussed in this chapter, another important paramagnetic species, the triplet dioxygen molecule, along with the singlet dioxygen, are also investigated and are presented in Chapter 5.

Chapter 5

Adsorption of molecular oxygen in singlet and triplet states on chemically modified boron doped graphene

5.1. Introduction

The effects of oxygen adsorption on carbon nanomaterials have been the focus of a great deal of research [1-3]. Oxygen detection and assessing sensors are in great demand and have widespread applications. Numerous industries, from the cement and steel sectors to the biological and food-processing sectors, chemical facilities, and even vehicles, have found uses for oxygen sensors [1]. Most commercial oxygen sensors fall into three categories: potentiometric, amperometric, and semiconducting metal oxide sensors [2]. Amperometric sensors have a challenging design, whereas potentiometric and metal oxide sensors need operating temperatures of 300–1000°C [2]. The medical, food industrial, and waste management sectors all need continuous monitoring of oxygen levels in the ambient environment [2]. Optical sensors are the only available sensors in the market that can function in ambient circumstances. Still, they have a slower reaction time (about 40 seconds) and need a lot of energy to run [3]. There have been theoretical and experimental studies to demonstrate that graphene has the potential to function as a susceptible gas sensor by exhibiting changes in transport properties upon exposure to gases such as NO_2 and NH_3 at atmospheric temperatures.

It is seen that the electrical and optical properties of graphene and other similar 2D materials show deviations upon exposure to gases [4-7]. Understanding the adsorption characteristics of gases on the surface is extremely important to envisage two-dimensional-based sensor devices. Following the experimental investigation [4] with individual molecules, the adsorption of small molecules like O_2, CO, H_2O, NO_2, NO, NH_3, etc., has been explored [8-12] to understand their influence on the electronic structure properties of pristine graphene.

Nonetheless, most gas molecules can only weakly physisorb on pristine graphene [13,14,15]. Such physisorptions cannot improve the semiconducting properties of graphene and, therefore, forbid its potential use in gas sensors and other electronic devices. To enhance the sensitivity of gases towards the intrinsic graphene, doping the surface with either n- or p-

type dopants is common. It is expected to alter the electronic and transport properties [5,13]. Regular practice is replacing one or more carbon atoms with metal, transition metals, and non-metals [16,17] or decorating the surface extrinsically with atoms [18]. It is already established that B- or N-doped and B- and N- co-doped graphene can significantly improve the sensing of gases like NO, NO_2, NH_3, and CO [13,17,19-21]. Metal and transition metal doped [22,23] graphene are found to alter the electronic structure drastically and, therefore, cannot be employed in semiconductor devices. On the experimental front, several non-metals doped graphene-based materials were synthesized successfully with boron, nitrogen, etc. [24,25].

This section discusses an overview of oxygen adsorption on intrinsic and B-doped graphene. Using the computational first-principles technique, Nakamura *et al.* [26] found that oxygen atoms selectively adsorb on intrinsic graphene, forming epoxide rings and modifying structural and electrical characteristics. There have been a few experimental [5,27-29] and theoretical attempts [13,16,30-37] to explore the sensing of molecular dioxygen, O_2, on pristine and doped graphene monolayers. Some earlier literature reveals attempts to make oxygen sensors [27,28] with monolayer graphene. Such oxygen sensors were made at room temperature by chemical vapor deposition, and rapid changes in the current were shown when the sensors were exposed to different oxygen concentrations at room temperature [27]. Bagsican *et al.* [29] employed temperatures programmed terahertz (THz) emission microscopy (TPTEM) to explore the local O_2 adsorption and desorption dynamics on graphene and tungsten disulfide (WS_2). They have found an adsorption energy of about -0.15 eV for oxygen molecules on pristine graphene.

All the theoretical investigations predict only weak adsorptions with molecular oxygen [16,30-37], and some studies indicate increased oxygen sensitivity after doping with silicon [30,33]. It is also suggested that Si-doped surfaces can be a metal-free catalyst for oxygen reduction reactions (ORRs) [33]. Diffusion Monte Carlo (DMC) calculations were also

performed for O_2 adsorption on single-layer graphene [31] to accurately describe the adsorption's nature. They have obtained adsorption energy of −0.142 eV, close to the experimental value of -0.15 eV [29]. The adsorption of O_2 is also facilitated by topological defects and compressive mechanical strain [36].

With their pioneering work, Dai and colleagues found that dioxygen adsorbs weakly onto B-doped and N-doped (each with a single dopant atom). In contrast, it is more robust with transition metal doped surfaces [13,16]. The adsorption of singlet oxygen molecules onto aromatic hydrocarbon molecules like benzene, naphthalene, and pyrene, employing ab initio MO calculations, was also done previously [38]. They have found dioxetane-like metastable structures on adsorption of singlet O_2 onto hydrocarbons. Even though it is clear that the theoretical studies on triplet dioxygen, which is O_2 in its natural state, $^3\Sigma_g$, were conducted on graphene and singly B-doped graphene, the investigations on the adsorption of singlet dioxygen, $^1\Delta_g$, is hardly discussed irrespective of its importance. Additionally, the information on the electronic structure in terms of band structures and density of states (DOS) is not discussed previously in the literature for both triplet and singlet oxygen.

All previous investigations show that triplet O_2 is unreactive to the surface. This theoretical investigation is the first to discuss the differences between singlet and triplet dioxygen adsorption and electronic characteristics. Additionally, this work involves adsorption on graphene with various dopant concentrations and surfaces with different doping patterns. Therefore, it is vital to understand the scope of using boron-doped graphene to capture singlet oxygen for its potential uses as nano-catalysts, sensor platforms, and medical-related applications. Moreover, a boron-doped graphene surface exposed to singlet dioxygen may limit its use as a sensor for various other gaseous molecules.

5.2. Results and discussion

The results of the electronic structure calculation of adsorption dioxygen, O_2, on graphene

chemically doped surfaces, are discussed in this section. The adsorption studies explore oxygen in the paramagnetic triplet ($^3\Sigma_g$) ground state and the diamagnetic singlet ($^1\Delta_g$) state on various B-doped graphene. The effect of the surface doping concentrations, as well as configurations or the patterns made by the dopants on the electronic band-gaps, has been discussed in our previous investigations [17,19]. It has been reported that the doping concentrations and the configurations lead to appreciable variations in the electronic band-gaps of the graphene, even without the adsorption of gaseous molecules. Based on the sub-lattice symmetry breaking, some configurations show improved electronic aspects. This study considers doping with boron atoms as it causes the slightest deformity to the two-dimensional planar surface on substitutional doping. The dopant concentrations studied are 3.12, 6.25, and 9.37%. The pristine graphene is indicated as PG, and the singly doped graphene with 3.12% boron is represented as BG. For 6.25% of dopant concentration, the doped graphene surfaces are designated as a1, b1, c1, whereas for 9.37%, there are three patterns of doped surfaces, denoted as d1, e1, f1 as in Chapter 3. A few doped surfaces show increased band-gaps with 6.25%, and all 9.37% doping concentrations are shown in Figure 5.1. The remaining patterns of 6.25% dopant concentration, i.e., B-C-C-B, are named a1 and –C-B-B-C- as c1 and shown in Figure 5.2.

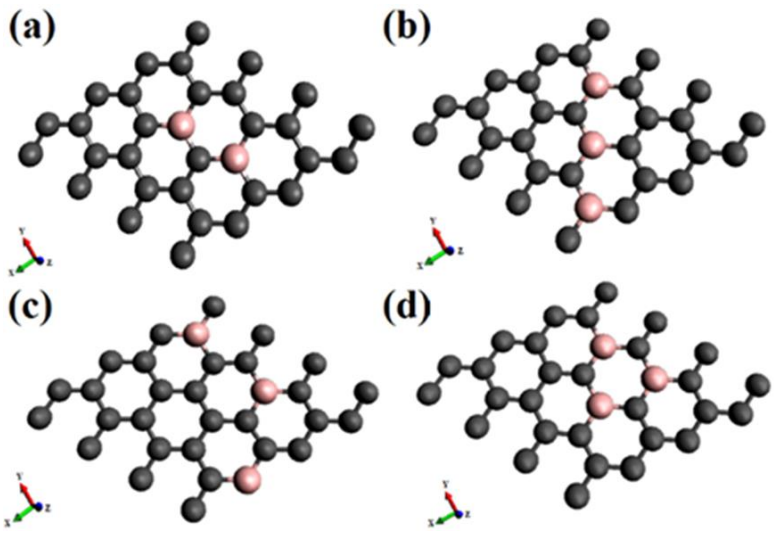

Fig. 5.1. The different patterns of doping on 6.25 % and 9.37 % boron-doped 4 × 4 supercell

of graphene in four different patterns indicated by the names, (a) b1 (b) d1 (c) e1 (d) f1. The grey color represents the carbon atoms, and the pink represents the boron atoms.

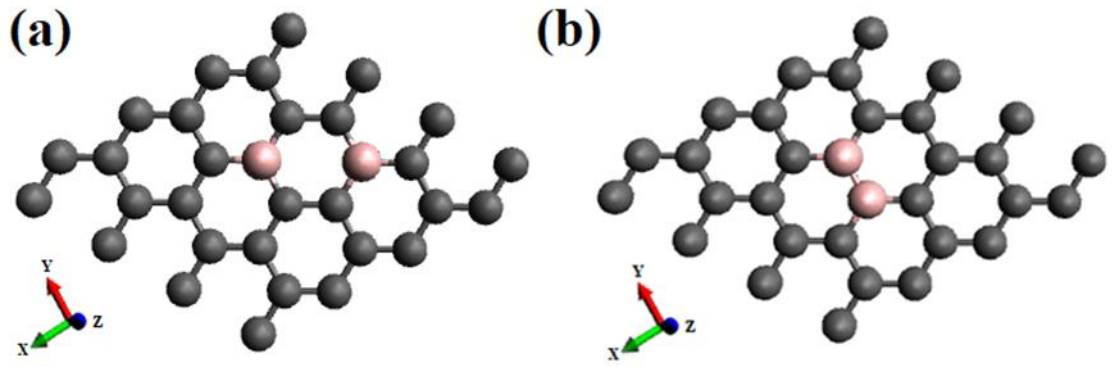

Fig. 5.2. The 4×4 boron-doped graphene supercell configurations with different concentrations of 6.25% boron, (a) and (b) denoted as a1 and c1 respectively.

To further confirm the possibility of interactions of -B-C-C-B- (a1)/ -B-C-B- (b1) pairs with their periodic images, we have carried out calculations of adsorption of singlet and triplet oxygen on the patterns specified, namely -B-C-B-/ -B-C-C-B- on a 5×5 graphene supercell. The doping patterns on the 5×5 supercell are considered a1/5×5 and b1/5×5 and are shown in Figure 5.3. The respective band-gaps are shown in Figure 5.4.

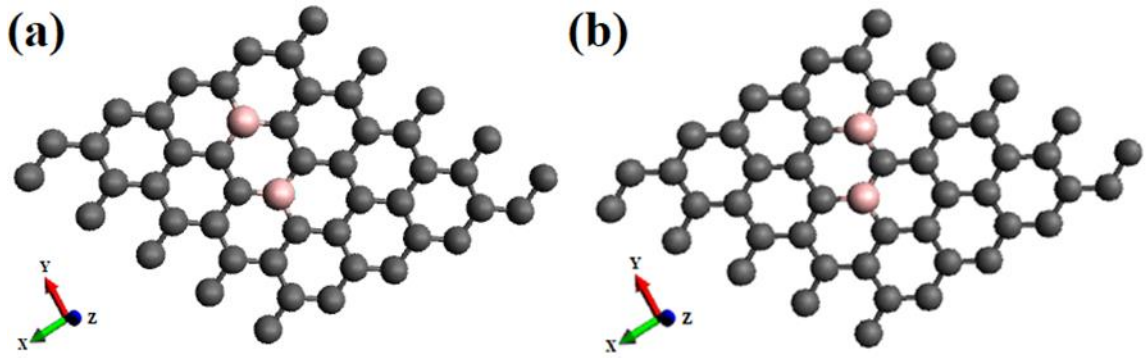

Fig. 5.3. The optimized 5×5 boron-doped graphene supercell with a concentration of 4% with different configurations from (a) and (b) denoted as a1/5×5 and b1/5×5.

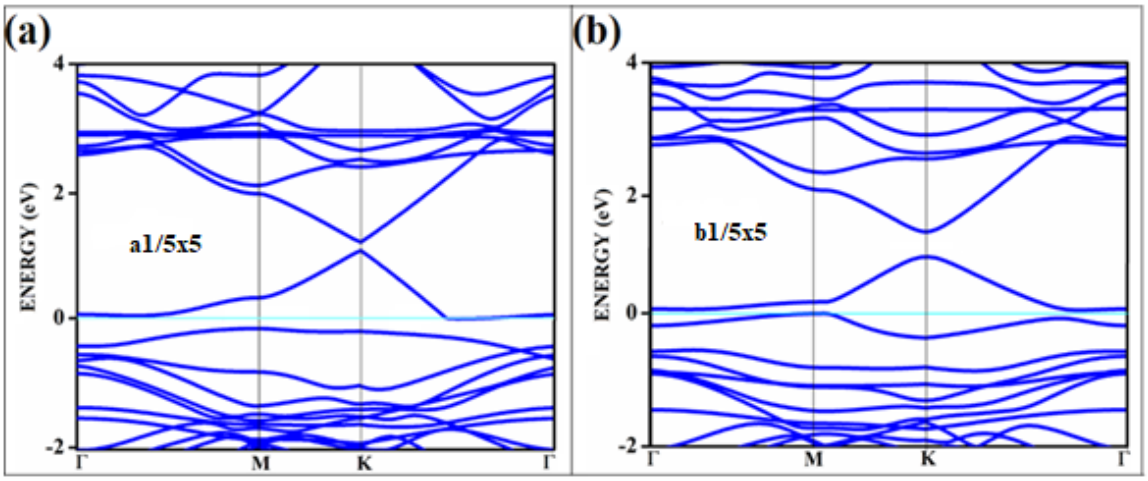

Fig. 5.4. The band structures of boron doped graphene supercell of configurations with doping percent of 4% as shown in Figure 5.3 (a) a1/5 × 5 (b) b1/5 × 5.

We have observed that the supercell size that we have done previously is sufficient to overcome the image interactions, as the results on 4 × 4 and 5 × 5 supercells showed almost the same results. The slight variations are due to the minor variations in dopant mole fractions. The change in band-gap or adsorption energies is not that appreciable. This indicates that our study with 4 × 4 supercell is sufficient to discuss the adsorption and electronic properties of the doped systems considered in this study.

5.2.1. Adsorption of dioxygen

Although there are few studies on oxygen adsorption [13,16,36], the effect of the spin nature of the molecule on the electronic structure and the adsorption characteristics still need to be considered. The majority of the previous studies deal with adsorption on pristine graphene surfaces, and other graphene-based materials [14], and a few on transition metal doped [23,30] and on defective graphene [34,39]. In this chapter, we discuss the results of the adsorption of dioxygen in both triplet and singlet states. The adsorption studies are conducted for various dopant concentrations and patterns. A few geometries-optimized configurations are given in Figure 5.1. The results of the calculations, the adsorption energies, optimized distances, band-gaps wherever necessary, and charge transfers for the triplet ground state and singlet are

summarized in Tables 5.1 and 5.2, respectively.

Table 5.1. Represents the adsorption energy in eV, distance of oxygen from the surface, and the band-gap and charge transfer for triplet oxygen adsorbed on various graphene surfaces are given. Band gaps for the bare surface is given in parenthesis.

System $^3\Sigma_g$ on	Adsorption energy (eV)	Distance (Å)	Band-gap (eV)	Charge transfer (e)
PG	-0.147	3.0	0	0.06
BG	-0.265	2.93	0.20 (0.14)	0.03
a1	-0.144	2.86	Flat line (0.21)	0.02
b1	-0.138	2.9	0.41 (0.37)	0.04
c1	-0.127	2.97	0.16 (0.15)	0.01
d1	-0.374	2.9	0.64 (0.57)	0.07
e1	-0.186	2.9	0.15 (0.16)	0.014
f1	-0.367	2.78	0.63 (0.58)	0.05

Adsorption of the oxygen molecule in both its spin states on the graphene surface is expected to improve the adsorption properties and electronic characteristics. It thus may contribute to exceptional applications of graphene. Both triplet and singlet oxygen are physisorbed onto the intrinsic graphene surface at a distance of about 3Å, as shown in Tables 5.1 and 5.2. The adsorption energy for triplet oxygen on intrinsic graphene is found to be -0.147 eV, confirming weak physisorption. This result agrees with the previous experimental result [29] of -0.15 eV and the earlier calculations of -0.142 eV [35].

Table 5.2. The adsorption energy, equilibrium distance from the surface, and charge transfer of singlet dioxygen adsorbed on various graphene surfaces are given. The length of the B-O

bond formed during chemisorption is also given.

System $^1\Delta_g$ on	Adsorption energy (eV)	Distance (Å)	Charge transfer (e)
PG	-0.396	2.96	0.08
BG	-0.718	2.20	0.22
a1	-0.664	1.9	0.06
b1	-1.222	1.53	0.32
c1	-0.932	1.9	0.04
d1	-1.747	1.52	0.55
e1	-0.176	2.97	0.03
f1	-1.504	1.54	0.63

Therefore, the DFT-D3 method, including the dispersion correction, can be conveniently used to investigate adsorption on boron-doped systems. In Table 5.1, the electronic band-gaps caused by triplet oxygen adsorption are also given. The corresponding doped, bare adsorbent band-gaps are shown in parenthesis. With the triplet oxygen, the physisorptions are not strong enough to cause appreciable changes in the electronic band-gaps. However, with surfaces 'd1' and 'f1', the band-gaps are slightly more than the bare doped surface, as seen in Table 5.1. The equilibrium distances are around 2.9-3 Å with negligible charge transfers, suggesting physisorptions. On doping with boron, the adsorption energies are improved for certain surfaces by 0.05-0.07 eV for the following reasons.

First, p-type doping makes it easier for the oxygen molecule to have the lone pair of electrons get attracted to the surface, irrespective of the spin nature of the molecule. The adsorption energies of triplet oxygen on various surfaces are slightly higher in the case of triplet

adsorption on the doped surface configurations 'd1' and 'f1' than the other surface configurations. After doping with boron, the unpaired p-orbitals on the surface are the most reliable sources of radical spins. The radical spin nature contributes to intermolecular interactions between graphene and oxygen molecules because of the high reactivity of unpaired electrons on triplet oxygen. It leads to a slightly larger band-gap opening. The higher adsorption energies of triplet oxygen in these two cases, i.e., d1 and f1 systems with higher band-gaps than other systems, are attributed to equivalent site doping, resulting in sub-lattice symmetry breaking. The optimized geometries of triplet oxygen on various doped surfaces are shown in Figure 5.5. All of them exhibit physisorption at a distance of around 3Å.

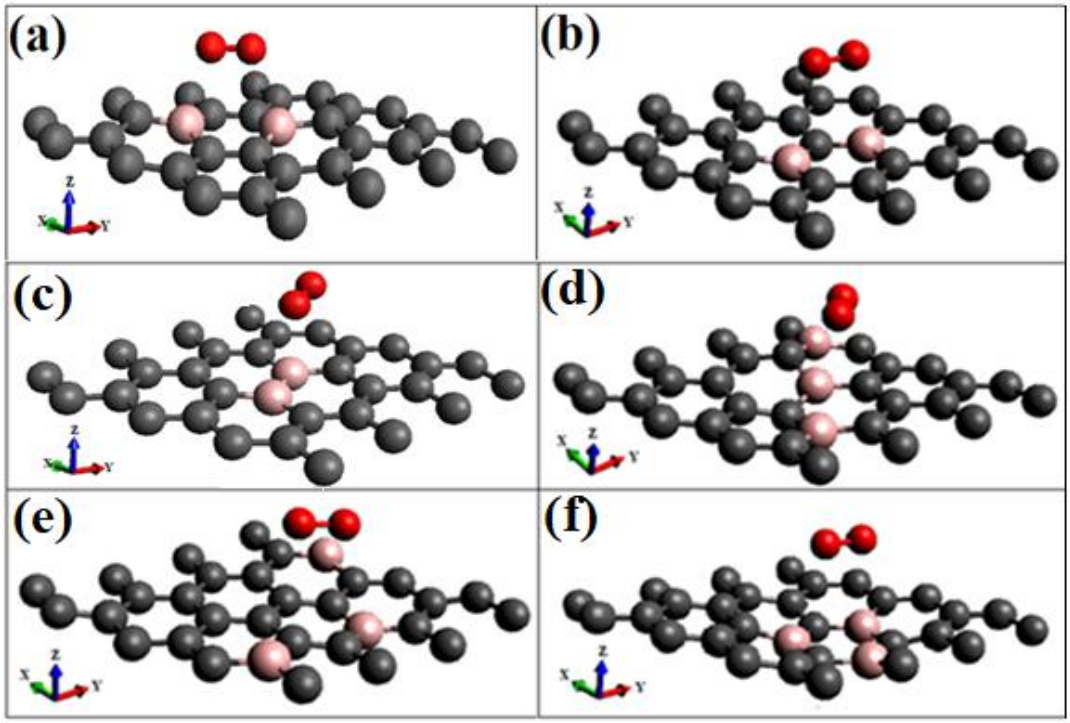

Fig. 5.5. The optimized geometries of respective triplet O_2 adsorption on different modified graphene surfaces (a) O_2(t)/a1 (b) O_2(t)/b1 (c) O_2(t)/c1 (d) O_2(t)/d1 (e) O_2(t)/e1 (f) O_2(t)/f1 ((t)-triplet states).

The adsorption of triplet oxygen on surfaces specified by a1 and b1 with a 5×5 supercell is also investigated in order to check for any supercell size effect due to image interaction. The optimized geometries of triplet oxygen adsorption on these surfaces are shown in Figure 5.6,

and the respective spin-polarized band structure is shown in Figure 5.7. the adsorption energy, the distance between adsorbate and adsorbent, the band-gaps, and the charge transfers of these systems are given in Table 5.3. By comparing Tables 5.2 and 5.3, it is seen that the adsorption energies, band-gaps, charge transfers, etc, remain the same for both cases.

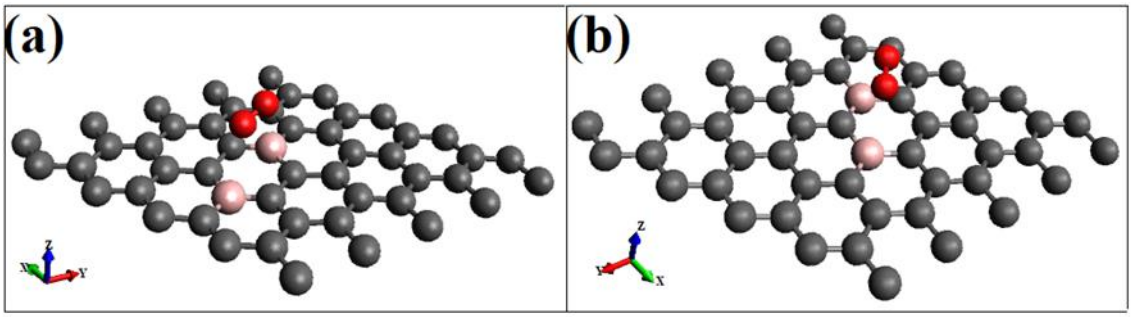

Fig. 5.6. The optimized geometries of triplet O_2 adsorption on modified graphene surfaces (a) O_2(t)/a1/5 × 5 (b) O_2(t)/b1/5 × 5.

Table 5.3. The adsorption energy, distance of adsorbate from the adsorbent, band-gaps, and the Bader charge transfers of oxygen in triplet state adsorption on 5 × 5 supercell boron-doped graphene, respectively. The values in the bracket show oxygen adsorption on 4 × 4 supercell.

System $^3\Sigma_g$ on 5 × 5	**Adsorption energy (eV)**	**Distance (Å)**	**Band-gap (eV)**	**Charge transfer (e)**
a1 (B-C-C-B)	-0.154 (-0.144)	2.80 (2.86)	-	0.02 (0.02)
b1 (B-C-B)	-0.146(-0.138)	2.85(2.9)	0.39 (0.41)	0.04(0.04)

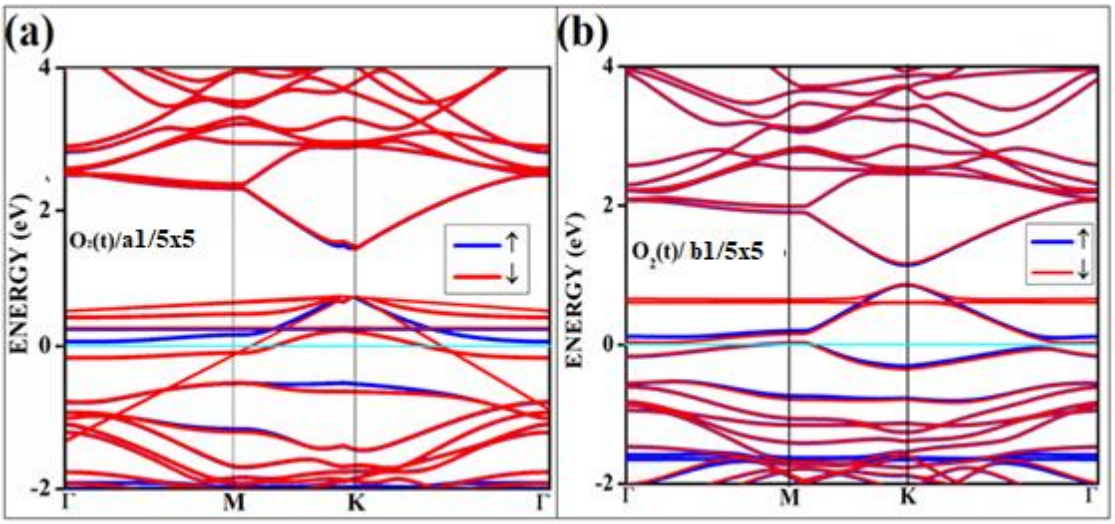

Fig. 5.7. The band structure of oxygen in triplet state adsorbed on surfaces (a) O_2(t)/a1/5 × 5 (b) O_2(t)/b1/5 × 5 ((t); triplet state of oxygen).

Comparing the adsorption energies of triplet and singlet oxygen on the same type of surfaces in Tables 5.1 and 5.2, we see that the singlet adsorptions are more stabilized. It leads to chemisorption on the doped graphene surface except for the pristine graphene (PG) and singly doped graphene (BG). By analyzing the adsorption energies, it is found that the magnitude of the adsorption energies of singlet oxygen is appreciable compared to that of triplet oxygen adsorption, even on the pristine graphene surface. The adsorption energy value is -0.39 eV for singlet oxygen adsorption on pristine graphene compared to -0.147 for triplet. The reason for this is easy to understand. The oxygen molecule in the triplet ground state is more stable than the singlet by 1eV (experiment value is 0.97 eV), and the bond distance is smaller than in singlet oxygen. As the triplet oxygen is already in the lowest energy state, like other diatomic species near bare graphene surface, it is only weakly physisorbed [29,35]. On the other hand, singlet oxygen is reactive, remains excited at higher energy, and therefore gets more attracted towards the bare surface to get stabilized. The charge transfer also indicates that there is stronger adsorption than in the case of triplet oxygen.

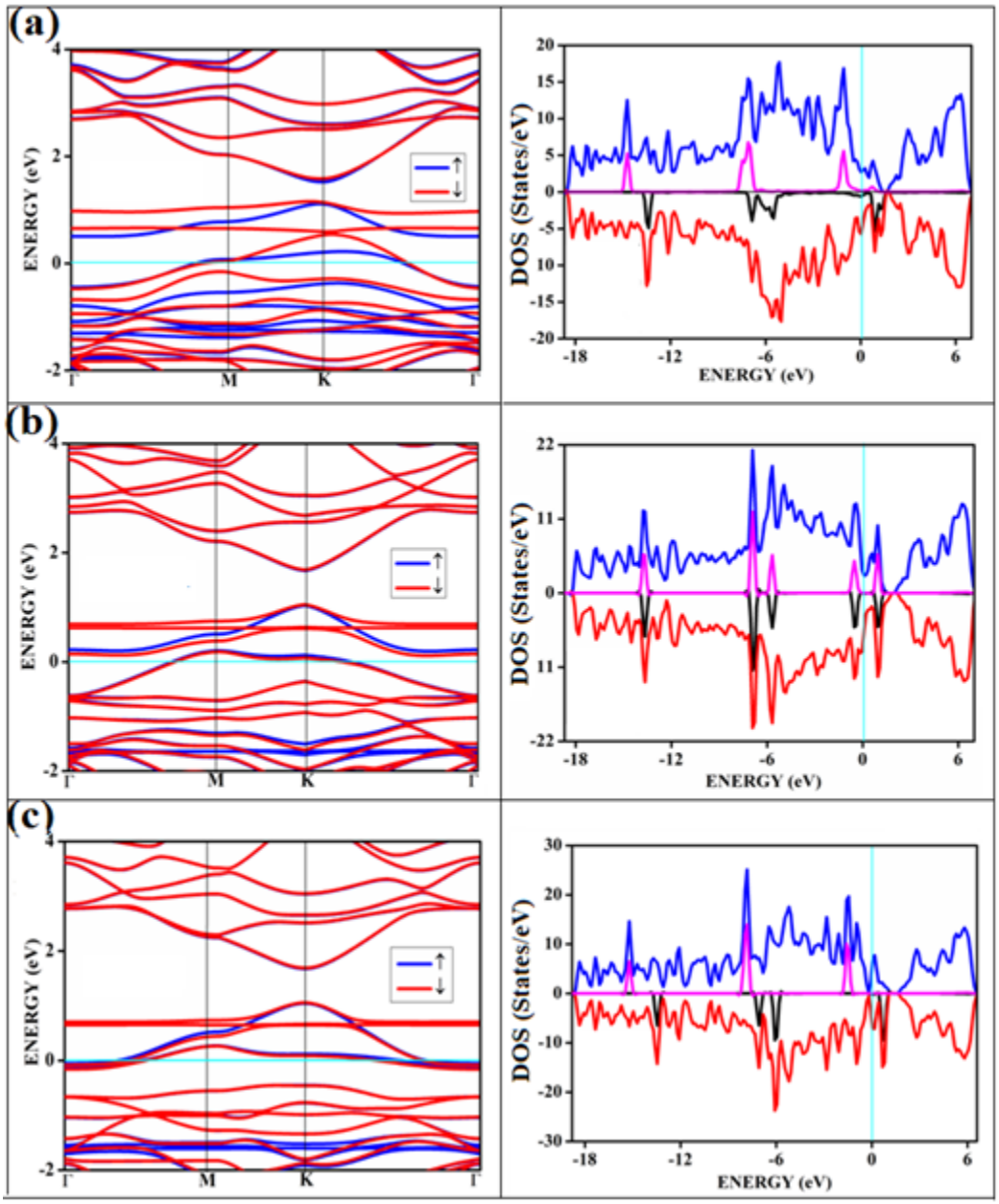

Fig. 5.8. The band structure and respective DOS of oxygen in triplet state adsorbed on surfaces (a) O_2(t)/b1 (b) O_2(t)/d1 (c) O_2(t)/f1 ((t)-triplet state of oxygen). The purple and black correspond to the PDOS of oxygen.

The band structures and the corresponding density of states of the relevant cases of triplet oxygen adsorption are shown in Figure 5.8. The effect of dopant concentration on the band-gap is discussed elaborately in our previous publications [17]. The triplet oxygen adsorption on configurations like a1, c1, and e1 with dopant concentrations of 6.25% and 9.37%, respectively, do not show an appreciable change in band-gap after adsorption of the

adsorbate. The band structures and respective density of states (DOS) are shown in Figure 5.9.

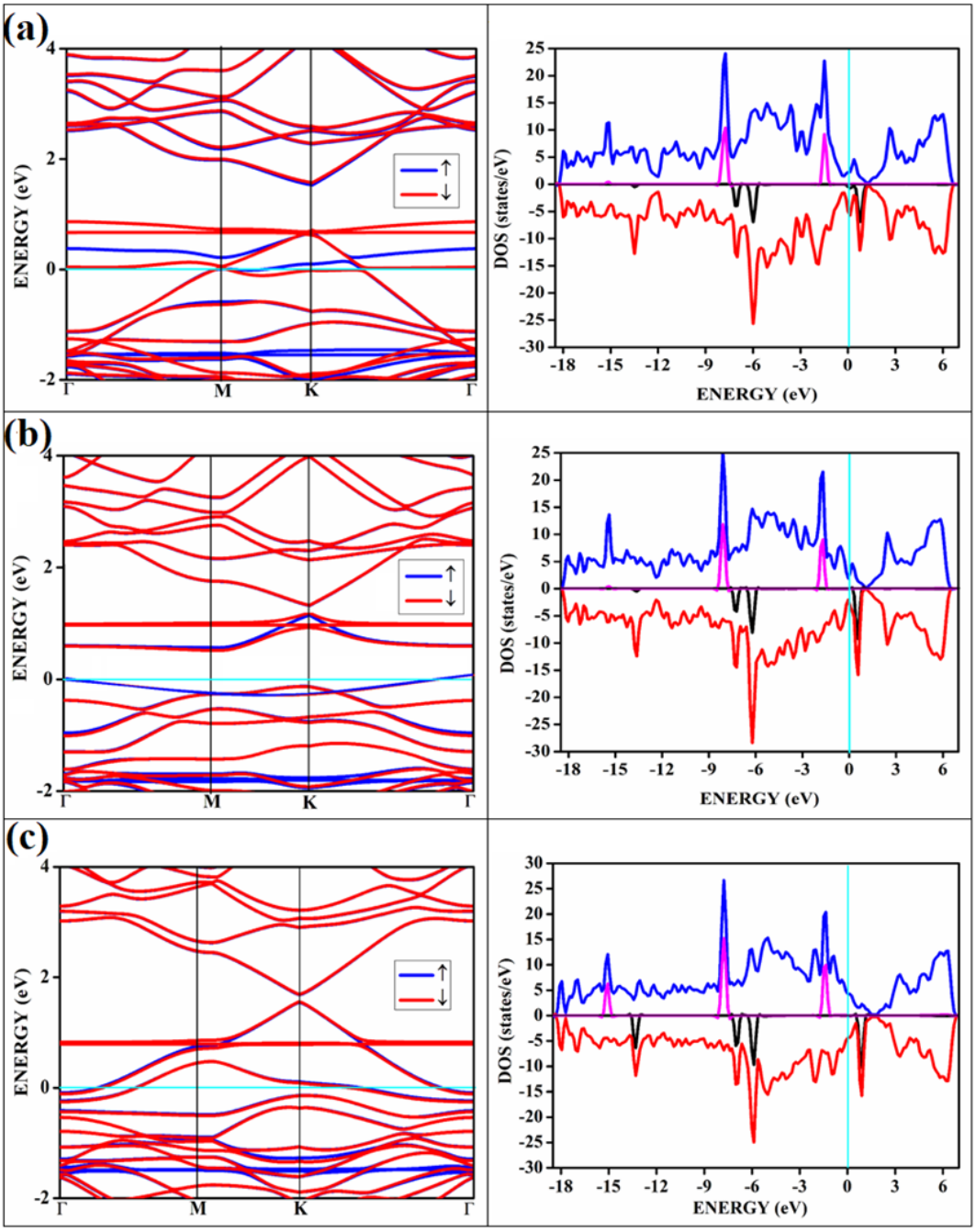

Fig. 5.9. The band structure and corresponding DOS of oxygen in triplet state adsorbed on surfaces (a) O_2(t)/a1 (b) O_2(t)/c1 (c) O_2(t)/e1 ((t); triplet state of oxygen). The magenta and black correspond to the PDOS of oxygen.

However, we do not see a one-to-one correspondence of the band-gap with the dopant concentration, and the band-gap does not necessarily vary linearly with the dopant

concentration. The band-gap of O_2(t)/b1 is 0.41 eV, close to the bare surface value of 0.37 eV. Similar behavior for the other two cases, O_2(t)/d1 and O_2(t)/f1, is shown in Figure 5.8. Though the band-gaps for the bare surfaces d1 and f1 show an increase in band-gaps, changes during the adsorption of triplet oxygen are minimal, without any appreciable differences in the band structure. The π* orbitals do not participate in any bond formation except for a weak mixing with the p-orbitals on the surface. The flat bands near the Fermi indicate the contribution from P_z orbitals of the oxygen atoms, creating bands above the Fermi, indicating a p-type nature. The band-gaps (in Table 5.1) are unaffected and remain similar to the bare surface.

It shows physical adsorption and is confirmed by the density of states (DOS). The partial density of states (PDOS) for triplet oxygen is drawn together with the total DOS. The state not participating in bond formation appears as peaks slightly above the Fermi. It is also possible to see slight mixing and contribution from both π* orbitals and carbon and boron P_z in Figure 5.10. The oxygen P_z orbitals remain without much mixing, with a small contribution from boron, and it appears as a straight band near 1 eV.

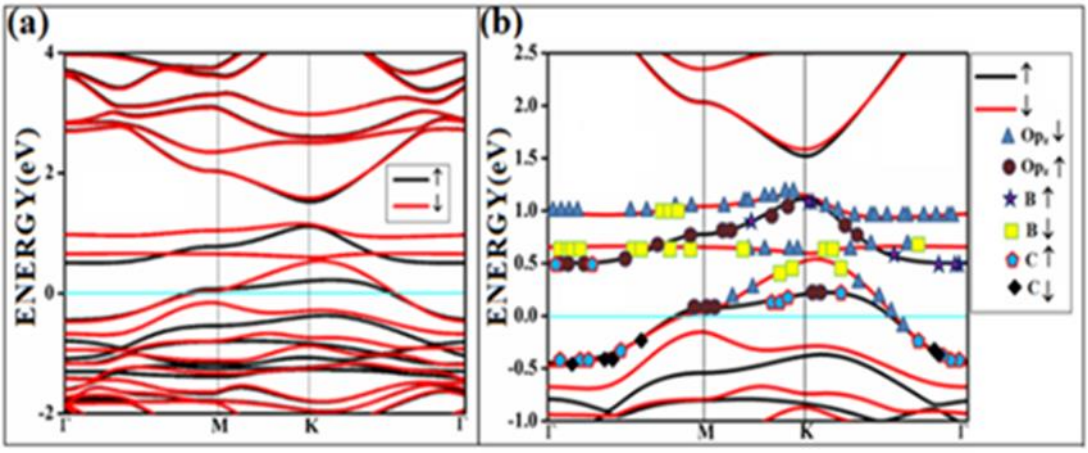

Fig. 5.10. The band structure of triplet with the orbital contribution (a) O_2(t)/b1 (b) O_2(t)/b1 mixed orbitals. The line above 0.5 eV indicates oxygen P_z and boron p-orbitals.

Three effects are to be considered while understanding the difference in the adsorptive behavior of triplet and singlet oxygen: repulsive, attractive, and spin-spin interactions. The triplet oxygen has two electrons occupying two π* antibonding molecular orbitals with parallel

spins and is a biradical. The exact spin directions make it more repulsive. Attractive forces emerge from the tendency of the kinetic energy between the parallel spins to move apart. In the case of triplet oxygen, the repulsive forces between the biradical oxygen and the doped surface overcome the attractive interactions with the boron-doped graphene surface.

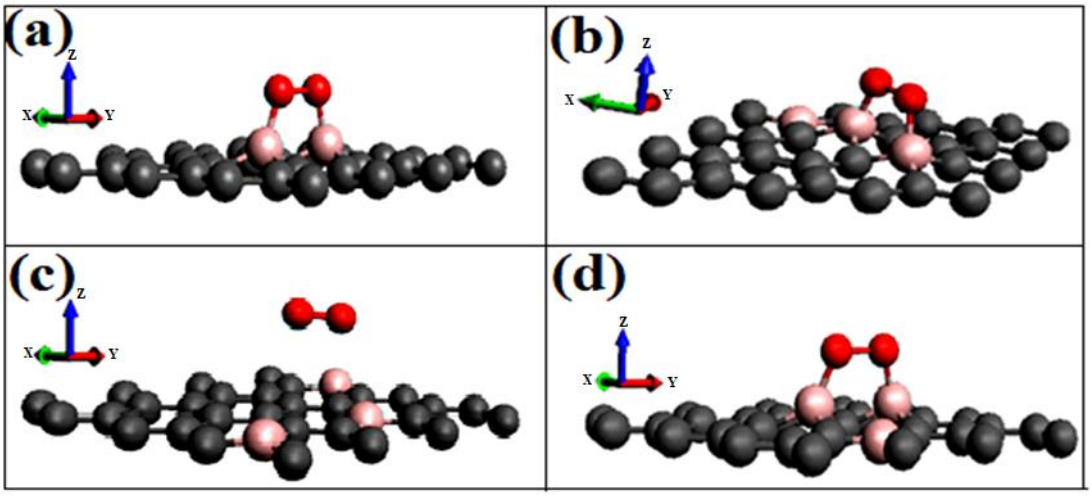

Fig. 5.11. The optimized geometries of respective singlet O_2 adsorption on modified graphene surfaces (a) O_2(s)/b1 (b) O_2(s)/d1 (c) O_2(s)/e1 (d) O_2(s)/f1 ((s)- singlet).

Most singlet oxygen adsorptions proceed through a dioxetane-like (with B-O bonds) ring formation except for the d1 configuration, where two carbon atoms separate the dopant borons. The B-O distances in the dioxetane-type ring ranged from 1.52 to 1.54 Å. The geometry of the optimized structure is shown in Figure 5.11, and a detailed figure of the dioxetane-type ring formed on one of the patterns (f1) is shown in Figure 5.12. Some unfavorable patterns do not show oxetane ring formation even on singlet oxygen adsorption at 6.25% doping concentration. An example is shown in Figure 5.13, where it only physisorb.

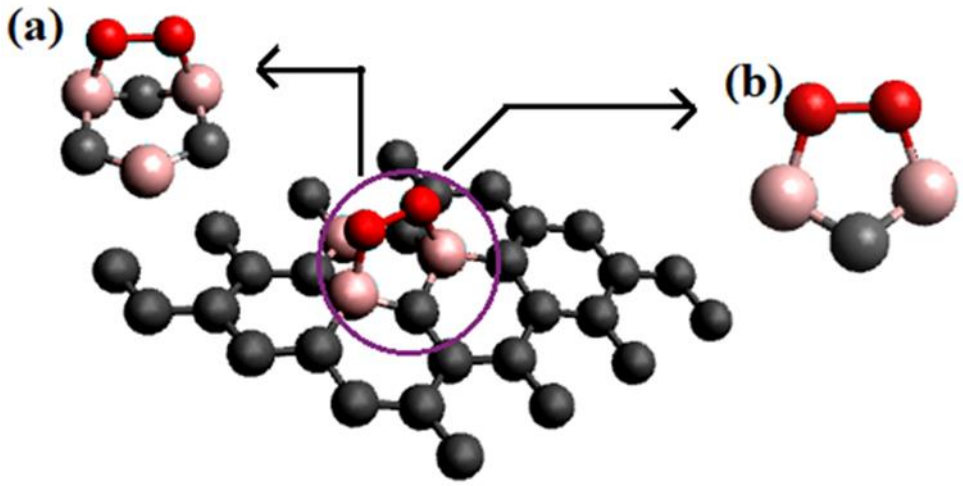

Fig. 5.12. Represents the dioxetane-type ring formed by O_2(s)/f1 (a) Rear view (b) Side view (pink color represents boron, red for oxygen, and grey represents carbon atoms of graphene).

A study of adsorption of singlet oxygen onto aromatic hydrocarbon molecules [38] found that singlet oxygen has the potential to chemisorb onto simple hydrocarbons. This attribute can be compared with the reaction of singlet oxygen with ethylene, where the dioxetane-type transition state is identified [40]. A similar reaction path cannot be located for dioxetane-type for the triplet state of oxygen. In other words, the singlet oxygen does tend to oxidize the corresponding surfaces. The singlet oxygen is chemisorbed onto all surfaces except on intrinsic graphene and 'e1' with the formation of dioxetane-type rings.

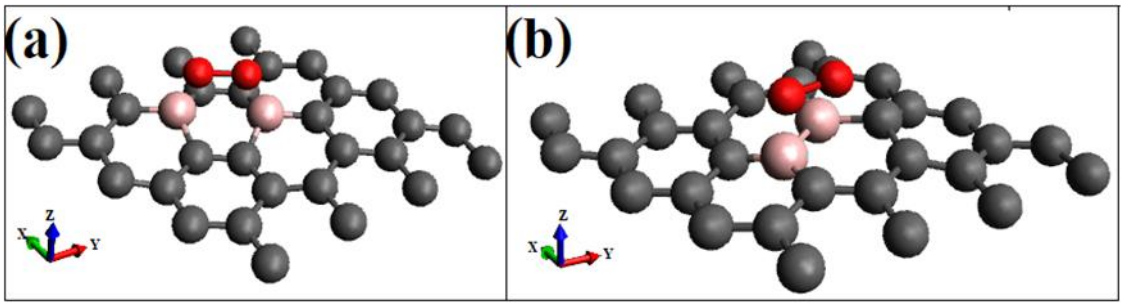

Fig. 5.13. The optimized geometries of singlet O_2 adsorption on modified graphene surfaces (a) O_2(s)/a1 (b) O_2(s)/c1.

The adsorption of singlet oxygen on a1 and b1, with 4% doping concentration on non-equivalent and equivalent sites, respectively, on a 5×5 supercell, are also investigated to see

the supercell effect. The 4 × 4 and 5 × 5 supercells showed the same properties, validating no supercell size effect. The optimized geometries of singlet oxygen adsorption on these surfaces is shown in Figure 5.14, and the respective band structure is shown in Figure 5.15. From Table 5.4, we can see that there is no difference in the case of singlet oxygen adsorption on supercell size.

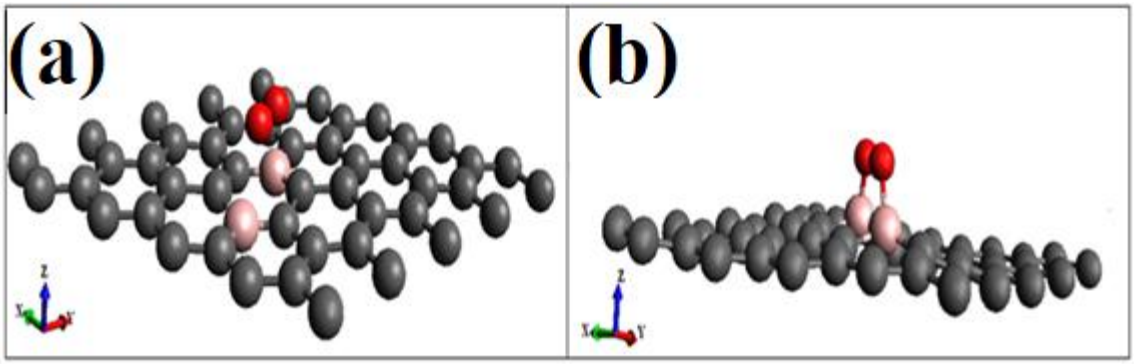

Fig. 5.14. The optimized geometries of respective singlet O_2 adsorption on modified graphene surfaces (a) O_2(s)/a1/5 × 5 (b) O_2(s)/b1 /5 × 5.

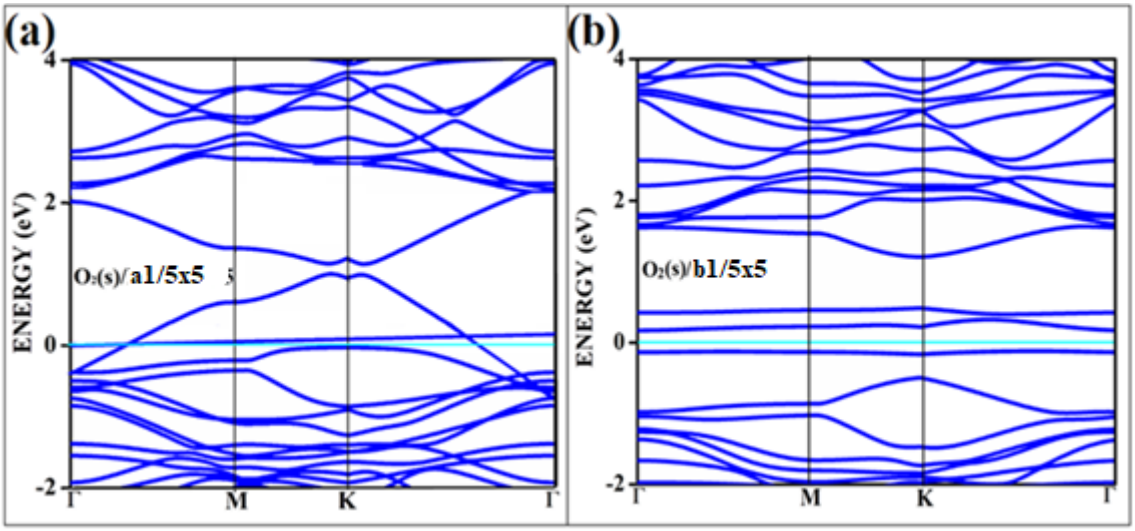

Fig. 5.15. The band structure of oxygen in singlet state adsorbed on surfaces (a) O_2(s)/a1 /5 × 5 (b) O_2(s)/ b1/5 × 5 ((s); singlet state of oxygen).

Table 5.4. The adsorption energy, distance of adsorbate from the adsorbent, band-gaps, and the Bader charge transfers of oxygen in singlet state adsorption on 5 × 5 supercell, 4% boron-doped graphene are given. The values obtained for 6.25% boron concentration on 4 × 4

supercell are shown in parenthesis.

System $^1\Delta_g$ on 5×5	**Adsorption energy (eV)**	**Distance (Å)**	**Charge transfer (e)**
a1 (B-C-C-B)	-0.752 (-0.664)	2.0 (1.9)	0.06(0.06)
b1 (B-C-B)	-1.152 (-1.222)	1.53 (1.53)	0.34 (0.32)

All the band structures for singlet O_2 adsorptions are primarily featureless bands with ill-defined band-gaps; a few are shown in Figure 5.16, along with the corresponding DOS. The unremarkable bands result from the intense mixing of p-orbitals of boron, carbon, and molecular π^* orbital of dioxygen formed from p-orbitals. The mixing is depicted in Figure 5.17 for singlet oxygen adsorption on the surface d1. The density of states shows that the adsorbate orbitals are undergoing appreciable orbital mixing with that of the surface, especially with the vertical P_z orbitals on boron, as can be seen from Figure 5.17 due to chemical bond formation.

The flat lines at around 0.59-0.85eV correspond to the P_z orbital of oxygen. In this model, the p-orbitals of boron, carbons, and π^*-orbital of oxygen molecule interact for bonding. The electrons are arranged according to the Pauli exclusion principle in the singlet oxygen adsorption. Therefore, it is more attracted to borons on the surface, resulting in strong physisorption or chemisorption. The 'e1' configured surface observed strong physisorption rather than chemisorption. In this surface pattern, the borons are separated by two carbons. Compared to the other configurations with a 9.37% dopant configuration, the lower band-gap is due to the non-equivalent site doping in the e1 surface configuration. The band structures' respective DOS of the singlet oxygen adsorption on the remaining surface patterns of doping,

a1, c1, and e1, are shown in Figure 5.18.

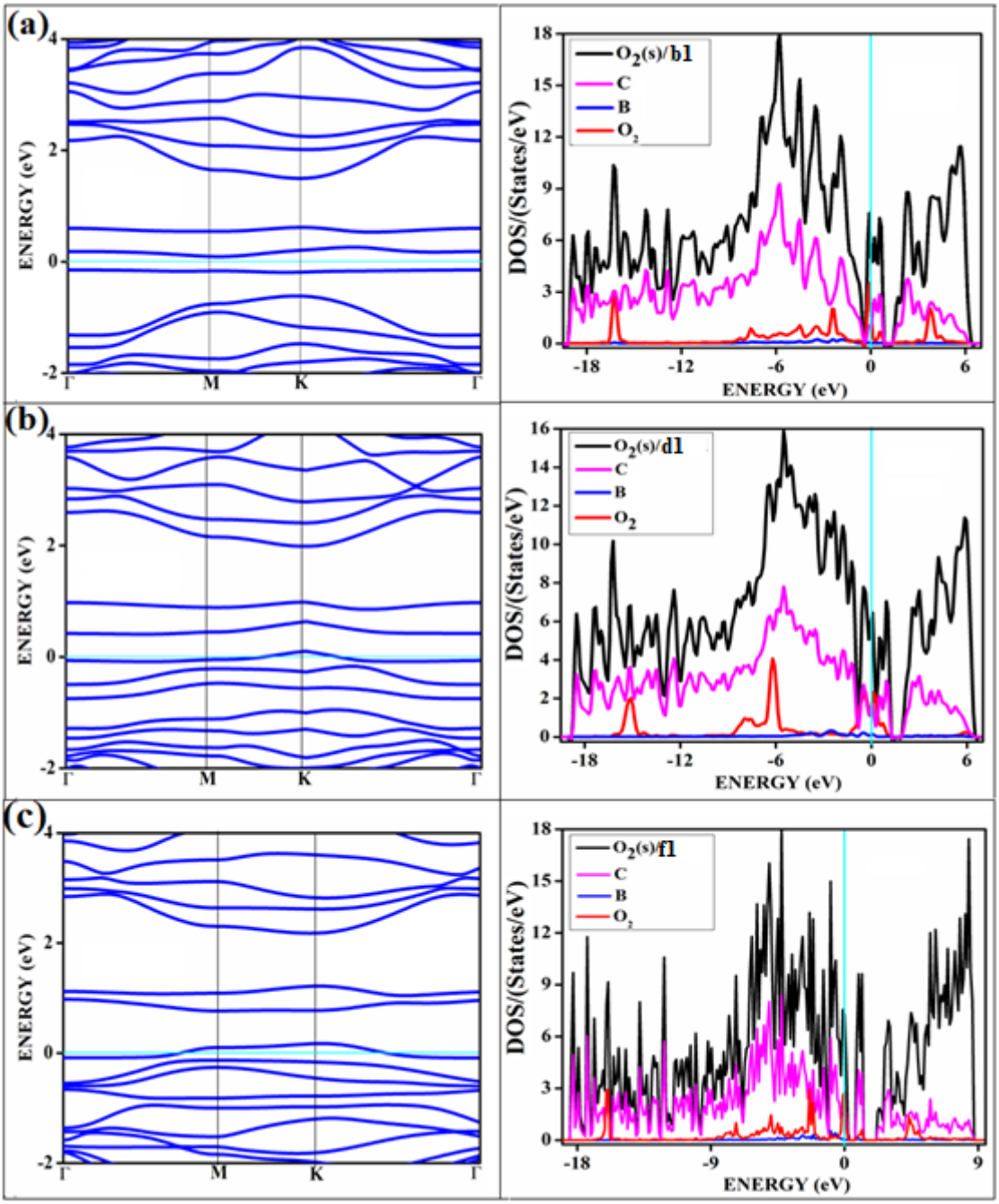

Fig. 5.16. The band structure and corresponding DOS of oxygen in singlet state adsorbed on surfaces (a) O_2(s)/b1 (b) O_2(s)/d1 (c) O_2(s)/f1 ((s); singlet state of oxygen).

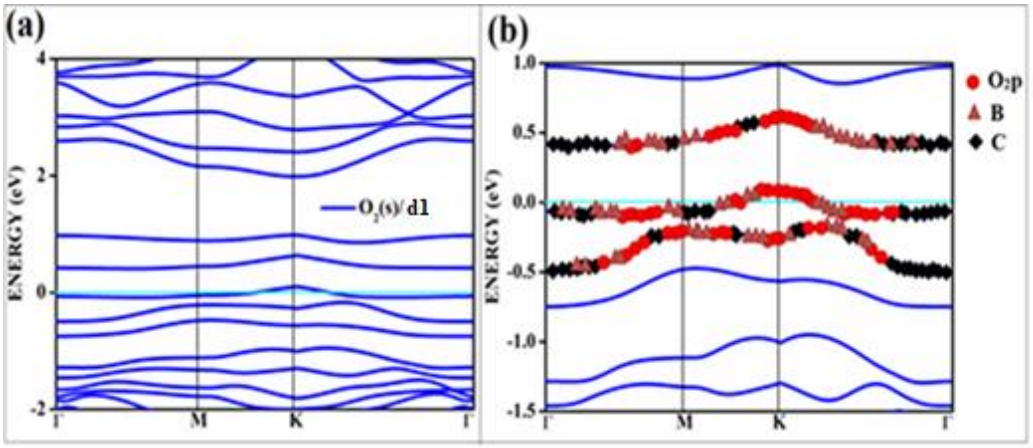

Fig. 5.17. The band structure of triplet with the orbital contribution (a) O_2(s)/f1 (b) O_2(s)/f1 mixed orbitals. The line above -0.5 eV indicates oxygen P_z and boron p orbitals.

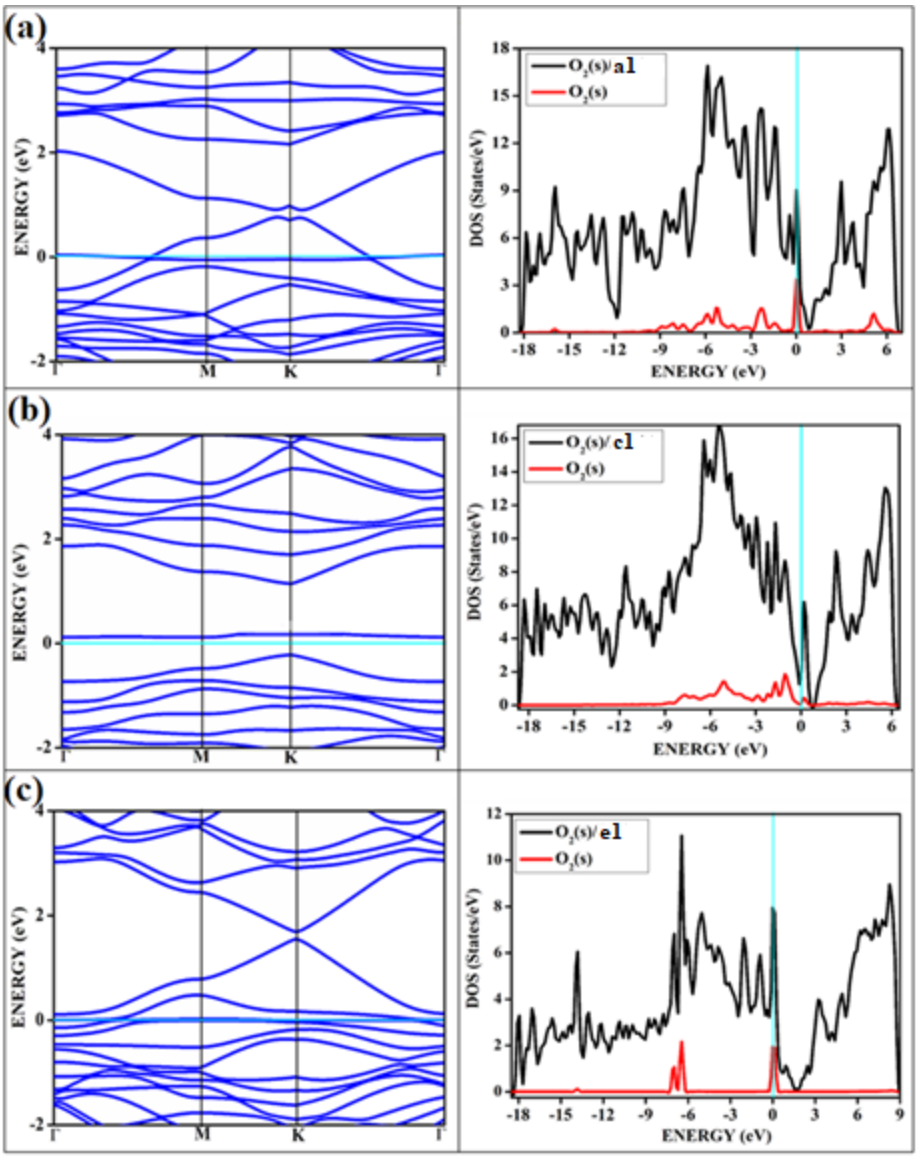

Fig. 5.18. The band structure and corresponding DOS of oxygen in singlet state adsorbed on surfaces (a) O_2(s)/a1 (b) O_2(s)/c1 (c) O_2(s)/e1 ((s); singlet state of oxygen). The red represent the PDOS of oxygen.

On intrinsic graphene, attractive forces are insufficient to form a dioxetane-type intermediate, even though such systems are predicted to form on aromatic hydrocarbons without doping [38]. The effect of singlet oxygen adsorption on one of the surfaces is shown in Figure 5.19. The total DOS of the f1 surface before and after singlet oxygen adsorption is shown. The states near Fermi are magnified to show the intense orbital mixings due to chemisorption.

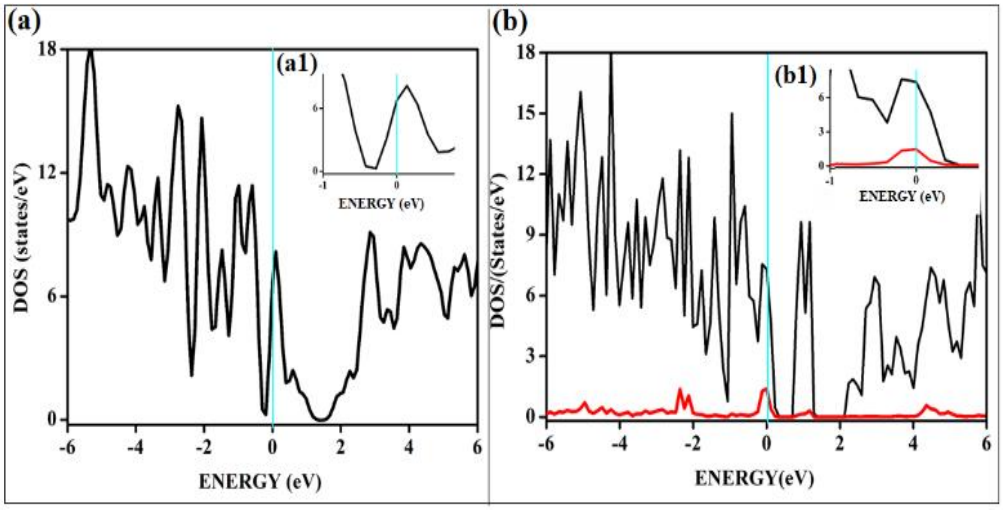

Fig. 5.19. The total DOS corresponding to the f1 surface before and after adsorption of singlet O_2. (a1) Magnified image of DOS near Fermi of f1 surface (b1) Magnified image of f1 near Fermi after O_2 adsorption.

To confirm the adsorption mechanism of adsorption of singlet and triplet oxygen on these graphene surfaces, the potential energy curves for a few representative cases are plotted in Figure 5.20, along with the total local potential for triplet and singlet oxygen. From the average potential curves shown in Figure 5.20(b) and 5.21(b), the stable equilibrium of adsorbate and adsorbent is confirmed to be 1.9 and 2.9 eV, respectively. It is possible to observe a clear minimum corresponding to the bond distances of the adsorbate gases with the

doped surfaces in the case of chemical adsorption of singlet oxygen and typical curves for physisorption in the case of weaker adsorptions for triplet oxygen.

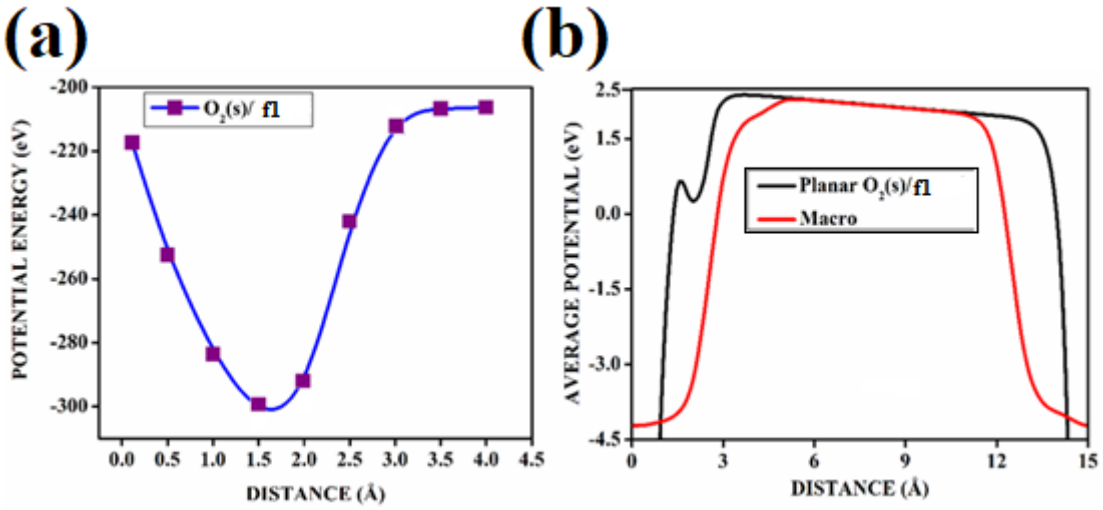

Fig. 5.20. The typical chemisorption behavior of singlet O_2 is represented as (a) The potential energy diagram O_2(s)/f1 (b) Total Local Potential.

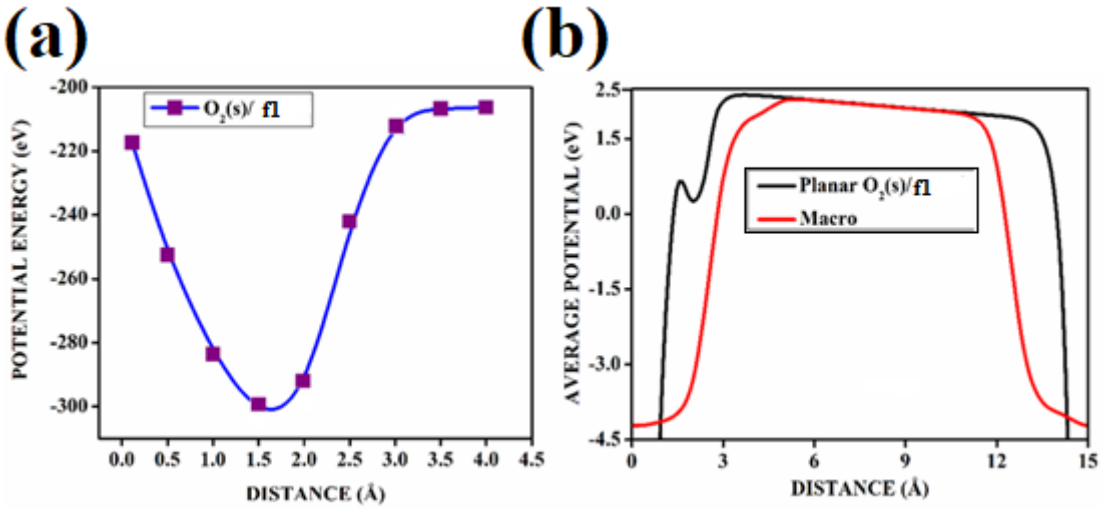

Fig. 5.21. The typical physisorption behaviors of triplet O_2 are represented as (a) The potential energy diagram O_2(t)/f1 (b) Total Local Potential.

To visualize the difference in the charge transfers on adsorption, the VESTA (Visualization for electronic and structure analysis) software is used [41]. The charge density and the difference density plots with color coding shown in Figures 5.22 and 5.23, respectively, explain both the physisorption of triplet oxygen and chemisorption with dioxetane-type ring

formation in the case of singlet oxygen with the surface d1.

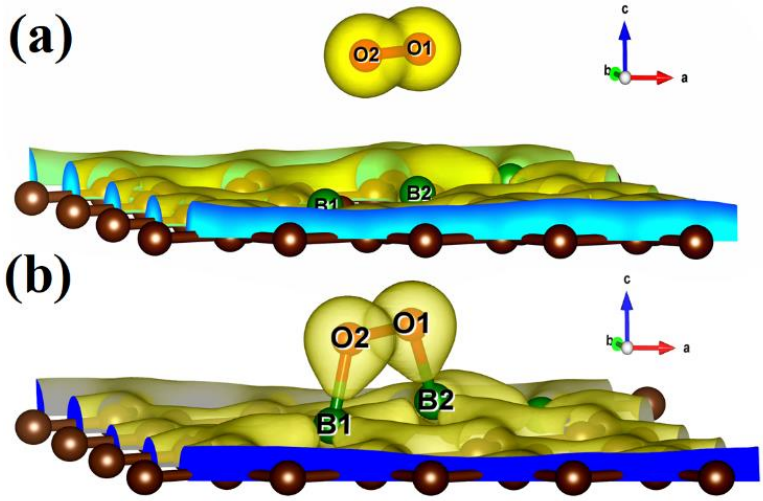

Fig. 5.22. The charge density surfaces of (a) O_2(t)/d1 contour plot and (b) O_2(s)/d1. Yellow represents charge/electrons accumulation, while blue represent charge/electrons depletion.

For various partitions of electronic charge densities of O_2(s)/d1, the plane *hkl* (110) containing O-O-B bonds is employed. The charge density difference between the adsorbed complex, the surface, and the gas molecule O_2 is computed using Eq. 2.48. Charge density rearrangement can be seen in the case of chemisorptive adsorption. Electron-deficient patches may be seen near boron atoms than the rest of the surface. The red color reflects high charge density oxygen, the green iso-charge surfaces represent 8.95e-06 e/Å^3 charge buildup, and the bottom cyan color represents 0.55 e/Å^3 charge depletion on the graphene surface.

Furthermore, the charge collected around the oxygen attracts it to the charge-deficient area (cyan iso-surface, i.e., boron of graphene iso-surface), contributing to the energy preference of oxygen to connect with the specific borons doped in graphene. In this case, the valence charge (cyan) around the boron atoms is drawn to the oxygen atom (from the cyan toward the green iso-charge surface), leading to the covalent bond formation (dioxetane-type ring). O-O-B bonds with bonding states on top of the valence bands.

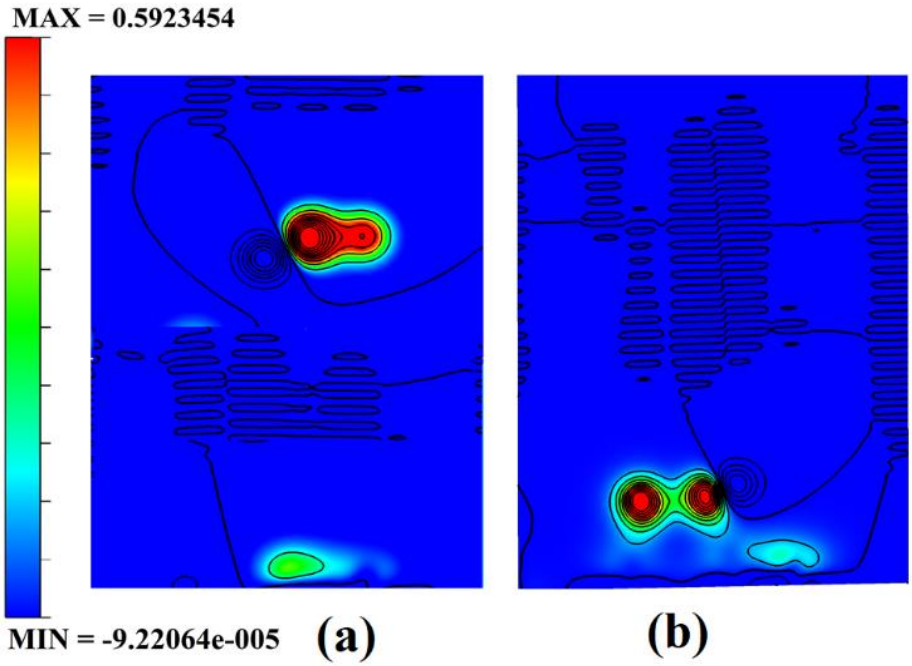

Fig. 5.23. The difference charge density contour surface of (a) O_2(t)/d1 and (b) O_2(s)/d1. The unit of the isovalue is e/Å^3.

The graphic depicts the charge concentration spread among carbon atoms near the bond formation site with boron. In Figure 5.22, the charge transfers between triplet oxygen and boron are minimal, showing physisorption on the graphene surface of configuration d1. In the case of triplet oxygen, the contour red color depicts the charge on oxygen. However, the charge accumulation is much lower than in the case of singlet oxygen, i.e., at 1.16e-05 of green color and bottom cyan color at 0.037, depicting charge depletion on graphene due to boron atoms.

5.3. Conclusions

The spin-polarized calculations reveal that the results vary drastically upon considering triplet and singlet oxygen adsorption on doped surfaces. With the intrinsic graphene surface, both types of oxygen show weak attractions, as is evident from the previous investigations [38]. The triplet oxygen is only physically adsorbed on all chemically doped surfaces, whereas singlet oxygen undergoes chemisorption. Chemisorption of the singlet follows with the dioxetane-type intermediate formation on the doped surface. This result can be best understood from the orbital structures of doped graphene and oxygen and the various possible interactions.

A considerable amount of orbital mixing of the orbitals of singlet dioxygen and the orbitals of boron and carbons in the vicinity of bond formation is seen. The charge transfer is also appreciable, with charge density accumulation near the surface confirming the bond formations. It is interesting to know the different adsorption behavior with the different spin states of the adsorbate molecule. Though there is theoretical evidence to support the spin states and their occupancy on adsorption [15], the experimental evidence to suggest the spin states' importance is still premature. Though there is little research on the effect of spin states on the catalytic activity of transition metal oxides [42], the experimental strategies to follow up the spin states are still under study. Whether the change of spin states changes the adsorption configuration and reaction path is still unclear.

Chapter 6

Adsorption of ammonia on bilayer graphene doped with boron

6.1. Introduction

The ability to detect ammonia has several important applications, including pollution monitoring and factory checks. In addition, there are promising applications for ammonia detection in medical diagnosis. Exhaled ammonia measurements, for instance, may help distinguish among bacterial and viral infections in lung disorders, which might help support the administration of antibiotics [1], and the gas ammonia monitoring may be utilized as a substitute for urea levels in the monitoring of renal disease [2]. Detecting such transmission of signals metabolic products (disease indicators) and detecting them in trace amounts is difficult. The minute levels of analyte molecules and their sensitivity to a given analyte are significant challenges. Low-dimensional materials have recently been prominent for gas detection [3, 4], and in particular, it has been observed that graphene may be utilized as a sensor for gases with excellent sensitivity, along with superior reliability for the detection of ammonia groups [5, 6]. Bilayer graphene (BLG) devices may exhibit distinct electronic characteristics compared to monolayer graphene (MG) devices [7,8].

Multi-layered graphene, particularly bilayer graphene, has also attracted great attention as, surprisingly, it shows different electronic properties from monolayer graphene while retaining much of the physical features of the monolayer [9]. It has also been observed that multi-layered graphene shows unique properties at room temperature, such as ballistic transport [10]. Graphene is additionally susceptible to the adsorption of gas molecules [11,12]. The use of graphene and doped-graphene-based systems for developing sensors and other nanoelectronic devices has been extensively reported [13-17]. This study aims to investigate the adsorption of ammonia on chemically altered bilayer graphene. To summarize the state of the art in this area, some recent investigations on the interaction of small gas molecules on bilayer and doped bilayer graphene are also reviewed. Here, the emphasis is on how small gas molecules (H_2, NO_2, NO, CO, F_2, NH_3, H_2O) adsorb onto bilayer graphene structures and how

such interactions affect the electronic properties. Some of the adsorbed gases' potential applications on graphene are also discussed [18].

6.2. Bilayer Graphene

Bilayer Graphene (BLG) is a two-layered structure where a graphene layer is stacked on top of another graphene layer. The layers are usually stacked in two ways - AA Stacking and AB stacking (also known as Bernal stacking). In AA stacking, the second layer is directly above the first layer. In AB stacking, the second layer is slightly displaced, such that one of the two inequivalent carbon atoms lies above the hollow of the lower layer. DFT studies on bilayer graphene by Alattas *et al.* [9] showed that the interlayer distance after optimization for AA was 3.6 Å and that for AB was 3.4 Å. The preferred bilayer stacking configuration has also been empirically observed as Bernal stacking.

Alattas *et al.* [9] and Fujimoto *et al.* [19] have investigated the electronic architectures of BLGs with AA and AB stacking. The Dirac point is observed to be divided into two points that were situated slightly off the K point in AA stacking. In AB stacking, the valence and conduction bands overlap at the K point, with the dispersion around the K point being parabolic as opposed to linear in monolayer graphene. BLG showed a semi-metallic nature in both the AB and AA stacking, as shown in Figure 6.1.

The impact of dopants on the structures and electrical characteristics of BLG has been further investigated [9,19]. As would be predicted given the size disparities, the relaxed systems in both cases exhibited little to no structural deformation, with the bond length of the B-C bond being more extended than that of the N-C bond. The band structures demonstrated that B-doped BLG exhibited p-type characteristics while N-doped BLG exhibited n-type characteristics. Additionally, there was an opening of the band-gap in both cases, with similar band-gap values.

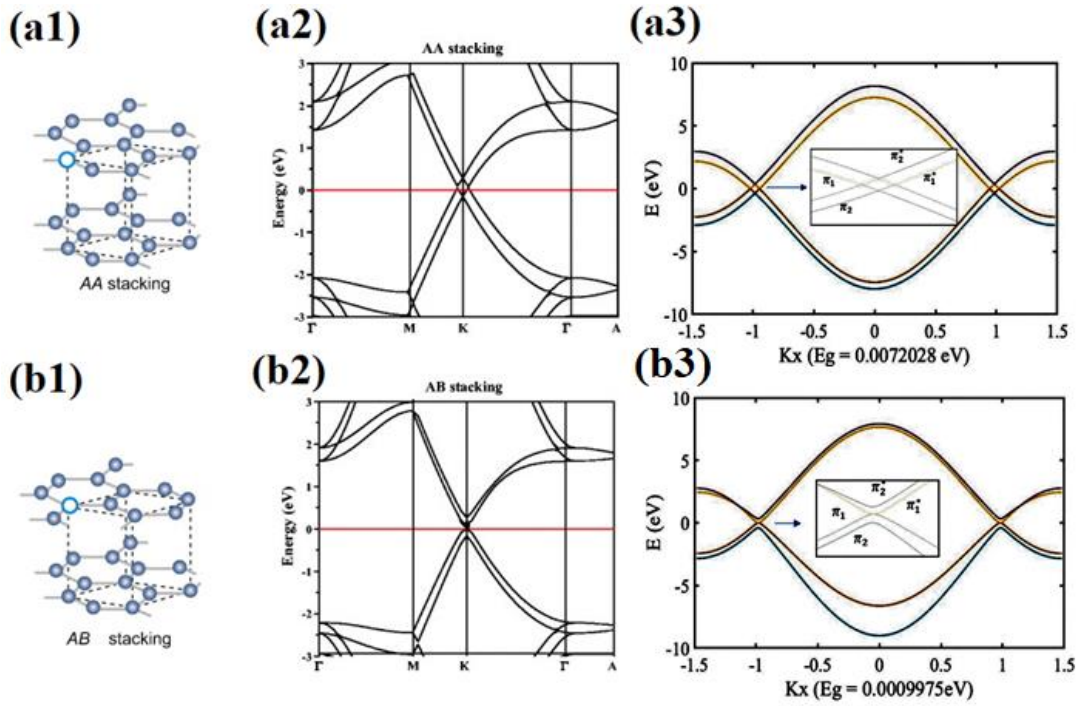

Fig. 6.1. The two dimensional of both AA- and AB-stacked bilayer graphene layer in (a1) and (b1), (a2) and (b2) represents the respective band structures, (a3) The energy band structure AA-stacked bilayer Graphene, under 0 eV electric field, (b3) The energy band structure AB-stacked bilayer Graphene, under 0 eV electric field. The zero represents the Fermi level. (These images are adapted from [20-22].

By swapping the dopant atom in each of the inequivalent locations of the higher layer, Fujimoto *et al.* [19] also investigated the impact of dopant position in the AB stacking. It was found that the band-gap opening was around half the value achieved when the dopant atom was above the hollow of the bottom layer. Based on charge transfer studies [19], charge transfer occurs from the lower to the top layer when the dopant atom is above the carbon atom. It reduced the charge difference between the layers, decreasing the band-gap. When the dopant atom was on top of a hollow of the benzene ring, the charge transfers predominantly occurred within the layer, increasing the charge differential between the layers, which led to a more significant band-gap opening.

6.3. Adsorption of Small Gas Molecules

6.3.1. Undoped Bilayer Graphene

There have been studies on the adsorption of small molecules on a few bilayer graphene. Shayeganfar [12] employed density functional calculations to investigate the F_2 adsorption on the characteristics of bilayer graphene. For each point, the parallel and perpendicular orientations of the F-F bond to the graphene layers are considered at different places of the F_2 molecule between the layers. According to the computational findings, the perpendicular orientation of F-F bonds was more stable than its parallel orientation due to the effect of the atoms' closer distances to the layers. The adsorption energies at different places ranged from -1.3 eV to -2.45 eV. In addition, band-gap opening was observed for both perpendicular and parallel arrangements of fluorine molecule. The band-gap opening ranged from 0.083 eV at the lowest to 0.313 eV at the highest. It was also found that an internal electric field was generated between the layers due to the effect of the dipole moment of the F-F bond. Further, it was seen that both the electric field and the band-gap varied with the strength of the dipole, suggesting that the geometry of the F_2 adsorption could tune the induced band-gap in BLG [12].

Santos *et al.* [23] investigated the binding energies and electronic properties of F_2 adsorption on bilayer graphene. It was found that the binding energies of adsorption of F_2 depend on the sub-lattice of the carbon atoms bonded with the fluorine. When carbon atoms of different sub-lattices were involved in the C-F bonds, the binding energy was higher than for the case with a single sub-lattice. It was found that the binding energy for bilayers was slightly lesser than that for monolayers, with the same qualitative features regarding sub-lattices. Additionally, the fluorination of bilayer graphene is accompanied by the de-coupling of the two graphene layers, attributed to the partial sp^3 nature of the C-F bonds in only one layer and the resulting lesser interaction between the graphene layers. From the electronic band

structure calculations, the de-coupling could be clearly observed as the band structure is akin to the sum of a pristine graphene monolayer and a fluorinated monolayer. At higher fluorine content, the fluorinated monolayer has a metallic nature for single sub-lattice binding and a semiconducting nature for multiple sub-lattice binding, which could also be seen in bilayer fluorinated graphene. This de-coupling could be an exciting method to create an electronically single-layer graphene sandwiched between a fluorinated graphene layer and a substrate through F_2 adsorption.

Ribeiro *et al.* [24] studied the effect of water and ammonia molecules on bilayer graphene using DFT with local density approximations (LDA). Their calculations found that the binding energies of both ammonia and water on one of the layers of the bilayer graphene were lesser than those of monolayer graphene. This drop in binding energy is due to sharing electrons with the bottom layer, thus resulting in a lesser number of electrons that can be transferred to the adsorbed molecule. The band structures were calculated, and a band-gap opening was observed for both molecules, with band-gaps of 0.03 eV for water and 0.042 eV for ammonia. It is commonly known that LDA underestimates band-gaps, implying that the actual band-gaps due to adsorption could be higher than those obtained from the calculations. The band-gap for the bilayer is more significant than that of a monolayer, which is expected to be due to an electric field generated between the two layers. The electric field is caused due to the dipole moment of the molecules polarizing the carbon atoms of the bound layer, which is higher for ammonia and is reflected in the band-gaps. This opening of band-gaps using gaseous adsorbates could be a more feasible method of band-gap opening than straining the structure or edge functionalization.

Sun *et al.* [25] fabricated a device using bilayer graphene to experimentally study the sensing properties of CO_2 gas at room temperature. It was found that the electronic transport in BLG is strongly affected by the physisorption of CO_2 gas molecules onto the surface.

Applying a back-gate voltage to the BLG could further control the adsorption rate. DFT and molecular dynamics (MD) simulations were performed to understand the mechanisms for enhanced adsorption rate theoretically and changed electronic properties. In the absence of an electric field, the CO_2 molecule bounced off the surface easily due to high kinetic energy at room temperatures [25]. In the presence of an electric field, the dipoles of the molecule are attracted toward high-intensity field regions, and the subsequent van der Waals interactions are strong enough to overcome the molecule's kinetic energy. The charge density difference between CO_2 and BLG was obtained from DFT simulations [25]. Even with negligible charge transfer from CO_2 due to physisorption, Coulomb scattering of charged impurities creates a potential energy barrier that is strong enough to block carrier diffusion, thus increasing the resistance of the BLG. This increased resistance could be used as an indicator to detect the presence of CO_2, allowing for its use in gas sensing.

The adsorption of hydrogen adatoms on bilayer graphene was studied by Mapasha *et al.* [26], where it was found that multiple competing stable configurations depended on the arrangement of the hydrogen atoms. In configurations where an H_2 dimer was physisorbed between the layers, de-coupling of the layers was observed, suggesting hydrogen intercalation as a means of graphene exfoliation. Chemisorption of hydrogen atoms at indirect sites led to various configurations with reduced interlayer distances, bringing the direct carbon atoms into close contact. Electronic band structure calculations of the multiple configurations showed that the relatively more stable configurations exhibit semi-metallic or insulating properties, whereas the unstable arrangements are metallic. Systems with physisorbed H_2 molecules retained the original band structure of graphene, with two new bands due to the adsorbed atom.

The interaction of NO_2 molecules with bilayer graphene, both free-standing and on a SiC (0001) substrate, was examined by Caffrey *et al.* [27]. Adsorption of NO_2 was considered only on one side of the bilayer. The binding energy values with and without substrate being

considered are similar, with the free-standing bilayer having a higher binding energy of -114 meV. The free-standing BLG band structures after NO_2 adsorption showed p-doping character, with the Dirac point shifting above the Fermi level by 0.18 eV. A small band-gap of 0.08 eV is seen due to the asymmetric doping of BLG by NO_2 molecules. The charge transfer from BLG to NO_2 is also uneven, with the top layer contributing almost 80% of the charge transfer. It also leads to generating an electric field, which contributes to the band-gap opening. Graphene layers on silicon carbide (SiC) substrates are found to be heavily *n*-doped [27]. While the adsorption of NO_2 is seen to shift the Dirac point closer to the Fermi level by 0.19 eV, a transition from n-p character is not seen for lower NO_2 concentrations. The band structures show a large band-gap opening of 0.24 eV due to the asymmetry induced by the SiC substrate and the adsorbed NO_2. It can be seen that the substrate plays a vital role in the electronic properties, and therefore can be considered for applications involving the sensing of gases using BLGs.

6.3.2. Doped Bilayer Graphene

To study the effects of boron and nitrogen doping of the bilayer on the adsorption of toxic gases (CO, CO_2, NO, NO_2), Fujimoto *et al.* [20] have done DFT calculations. From the binding energies, it is seen that all 4 gas molecules are physically adsorbed for N-doped BLG. For B-doped BLG, CO, and CO_2 are physisorbed, whereas NO and NO_2 molecules are chemically bound to the B atom in the bilayer. These results are due to the presence of unpaired electrons in the gas molecules and depend on the nature of the dopant atom. B-doped BLG shows a p-type character, and the presence of unpaired electrons in NO and NO_2 leads to the chemisorption of the molecules.

In contrast, CO and CO_2 lack unpaired electrons and weakly bind to the boron dopant. Additionally, N-doped BLG shows an n-type character, with excess electrons of nitrogen preventing any chemical bond formation with the gas molecules. Electronic band structures of

NO and NO_2 adsorbed B-doped BLG revealed a p-type nature for the adsorbed systems, with a band-gap opening present only in the NO_2 adsorption case. Charge transfer calculations showed that in the case of NO, some charge is transferred from NO to B-doped BLG, whereas in the case of NO_2, a more considerable amount of charge is transferred from B-doped BLG to NO_2. It leads to a change in the conduction properties of B-doped BLG upon NO and NO_2 adsorption, which could be useful for sensing NO and NO_2 molecules.

Tang *et al.* [28] studied the adsorption characteristics of Fe-doped bilayer graphene towards gases such as NO, CO, HCN, and SO_2. All the gas molecules were chemically adsorbed onto the Fe-BLG with a charge transfer from the Fe atom to the gas molecule and the graphene layer. NO showed the highest binding energy among all the molecules and produced a net magnetic moment. The presence of a platinum substrate below the BLG reduced the BE of all the molecules; however, it gave rise to clear magnetic moments for the system. The density of states (DOS) calculations revealed the strong interactions between the 3d states of the Fe atom with the local density of states (LDOS) of the gas molecules. The adsorbed NO on Fe-BLG showed a semimetallic nature, while CO adsorbed on Fe-BLG showed a semiconducting nature. These differences could be exploited to use Fe-BLG in gas sensor devices. Additionally, the change in the magnetic properties due to the addition of substrate could potentially have applications in electronic and spintronic devices.

6.4. Results and Discussions

We have considered adsorption on doped AB stacked bilayer graphene surface, where different doping patterns and mole fractions are investigated. AB stacking is preferred for all calculations due its stability compared to AA stacking. To check the validity of the simulations, proper referencing is made with the previous results of un-doped bilayer and single boron atom doped bilayers and compared the results with the existing results [7,9,19]. The calculations match the results with the previous studies [9,19], and the calculated band structure for the

single atom doped bilayer with the mole fraction of 1.56% is comparable to that made by Schwingenschlögl *et al.* [9]. The results, the band structures, and the corresponding density of states on un-doped BLG and singly doped BLG are given together in Figure 6.2. We study three different concentrations of doping, 1.56, 3.12, and 4.68%, and with different doping patterns. These patterns are defined as 1B-AB for 1.56%, b-AB for 3.12%, and d-AB, e-AB, f-AB for 4.68% dopant concentrations of boron.

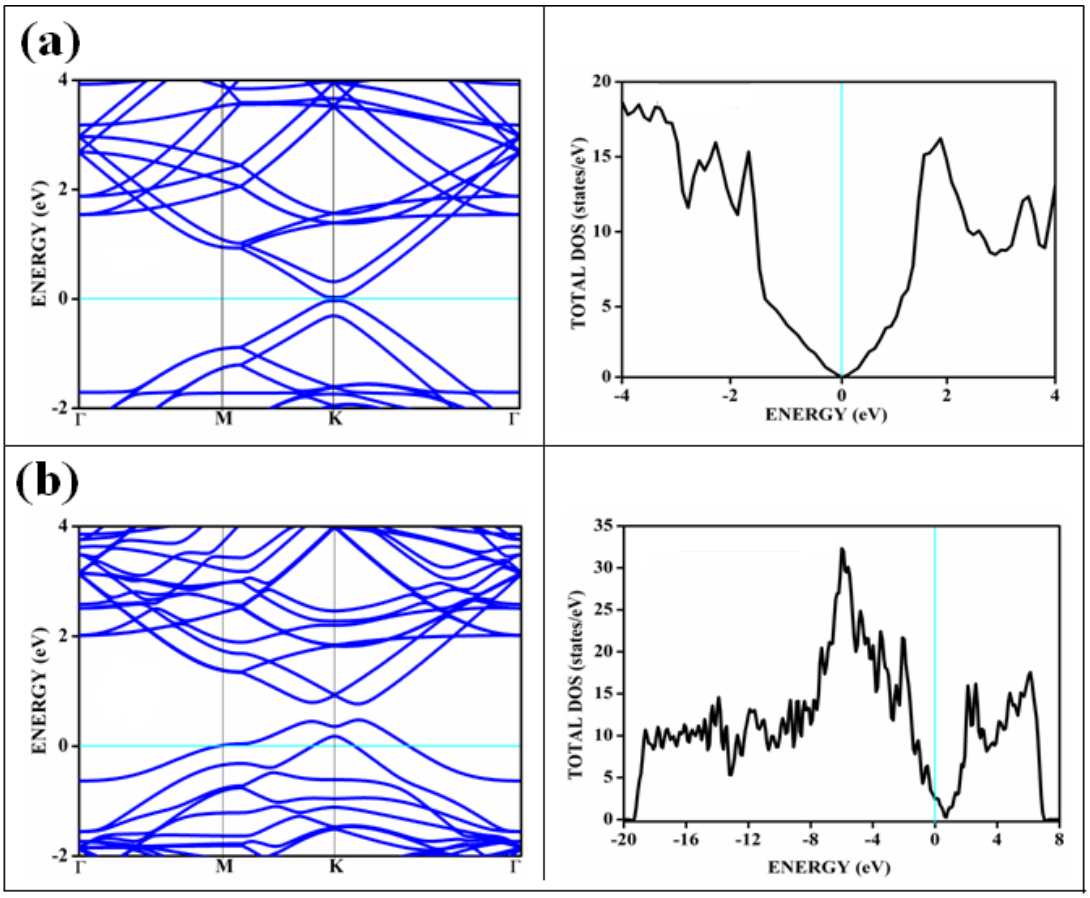

Fig. 6.2. The calculated band structure and the corresponding density of states of (a) intrinsic bilayer and (b) doped bilayer graphene in AB stacking with 1.56% boron (depicted as 1B-AB).

The interlayer distance for the intrinsic bilayer is found to be 3.4 Å for AB stacking, which is in agreement with the experimental observations [29]. These values are modified by the presence of dopant atoms for the concentrations considered in this study, and an in-plane lattice parameter of ~ 2.5 Å is observed for all the doped surfaces. The different configurations studied with two different mole fractions of doping, 3.12% and 4.68%, are shown in Figure

6.3.

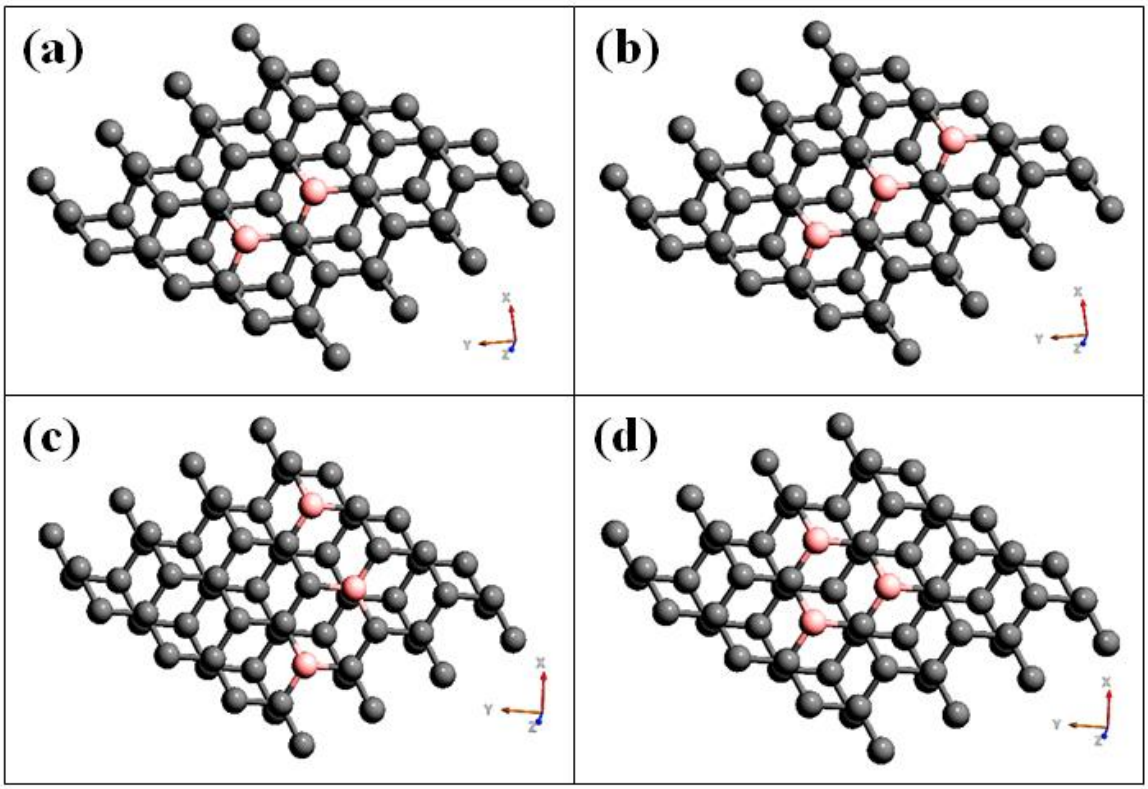

Fig. 6.3. The optimized geometries of doped bilayer structures, depicted with the notations (a) b-AB, (b) d-AB, (c) e-AB, and (d) f-AB. b-AB corresponds to the dopant concentration of 3.12%, and all other configurations (b)-(d) correspond to 4.68%.

Two concealed Dirac cones can be seen at the K-point in Figure 6.2 (b), which can be attributed to the layers doped with B (unoccupied cone) and the bare graphene layer, and a band-gap of 0.28eV is observed. Such buried cones are also visible for the other configurations in the band structures in Figure 6.4 and for the surfaces with doping concentrations mentioned in Figure 6.2. The energetically favourable distance of ~ 2.5 Å indicates favourable π-π interactions between the layers. The electronic band structure of the minimum energy configurations shown in Figure 6.4 suggests that the occupation of the various sub-lattice positions has no influence on the band-gap observed, unlike doping in the case of single-layered graphene [13]. The parabolic bands can be seen in the vicinity of the Fermi energy, as expected for AB stacked bilayer graphene for all the cases. The band-gaps and the optimized distance

between the layers corresponding to these different configurations of BLG are given in Table 6.1. It is seen that the band dispersions are not very much affected, except in the case of specific configurations, and doping in moderate concentrations leads to a band-gap of about 350 meV.

Table 6.1. The band-gap and the optimized interlayer distanced for graphene bilayer surface with different dopant concentrations and patterns. D is the interlayer distance after optimization.

System	Band-gap (eV)	D (Å)
1B-AB	0.28	2.68
b-AB	0.34	2.65
d-AB	0.35	2.71
e-AB	0.38	2.71
f-AB	0.12	2.37

The B-doped graphene systems possess holes in the valence bands and are p-type materials on which ammonia, with its lone pair of electrons, adsorbs strongly. The results of ammonia adsorption on these surfaces are summarized in Table 6.2. It is interesting to note that the adsorption energies of NH_3 on some of the boron-doped bilayer graphene, for example, on the ‘d-AB’ and the ‘e-AB' surface are strong, and the adsorption energies and charge transfers correspond to that of typical chemisorption. On the other hand, in all different configurations, it is only physisorbed with negligible charge transfer and adsorption energies. The difference in the adsorptions can be explained in terms of charge differences occurring in various substrates.

The computed electronic band structures of 'd-AB' and 'e-AB' show a significant variation in band-gaps before and after ammonia adsorption. The origin of band-gap opening comes

from the redistribution of surface charge due to the B atoms that break the local symmetry of the BLG. The redistribution of the charge density of the B-doped BLG gives rise to the separation of the valence band and conduction band at the Dirac point. A narrowing of the band-gap in BLG is also induced by interlayer interaction. The computed band-gaps of the 'd-AB' and 'e-AB' are 0.35 and 0.38 before the adsorption of ammonia and 0.28 eV and 0.16 eV after the ammonia adsorption, respectively. Interestingly, the band-gaps of the 'd-AB' and 'e-AB' with the repulsive interaction between the doped layer and bottom layer are relatively larger than those of the other configurations with the attractive interaction between the layers. It has been confirmed that the repulsive interaction between the layers forms a direct and large band-gap, while an attractive interaction induces a small band-gap. With this increase in repulsion forces between layers of 'd-AB' and 'e-AB' configurations, it is more electron deficient, attracted towards the lone pairs electrons of ammonia establishing chemical bonds between boron and nitrogen. In the configurations where it is chemisorbed, the boron atom is much more electron deficient than in the other patterns and therefore forms a bond with the nitrogen of ammonia. In this case, the B–N distance is of the order of 1.66Å, which falls in the typical range of B-N single bond distance. Similar adsorption has also been observed for ammonia adsorption on doped carbon nanotubes [30].

The electronic band structure of these adsorption studies is summarized in Figure 6.5, where the optimized structures are shown alongside the electronic band diagram and the corresponding density of states. Interestingly, the electronic band-gaps change by a few meV for the cases of strong chemisorption and remain unaltered for the physisorptions. Though these are not appreciable, these changes are expected to cause changes in the transport properties. The adsorption energies are appreciable for the NH_3/d-AB and NH_3/e-AB and are of -1 eV. The DOS of ammonia, shown in red, indicates that there is a shift to lower energy for two of the bands. To understand the chemisorptive behavior, this is further analyzed.

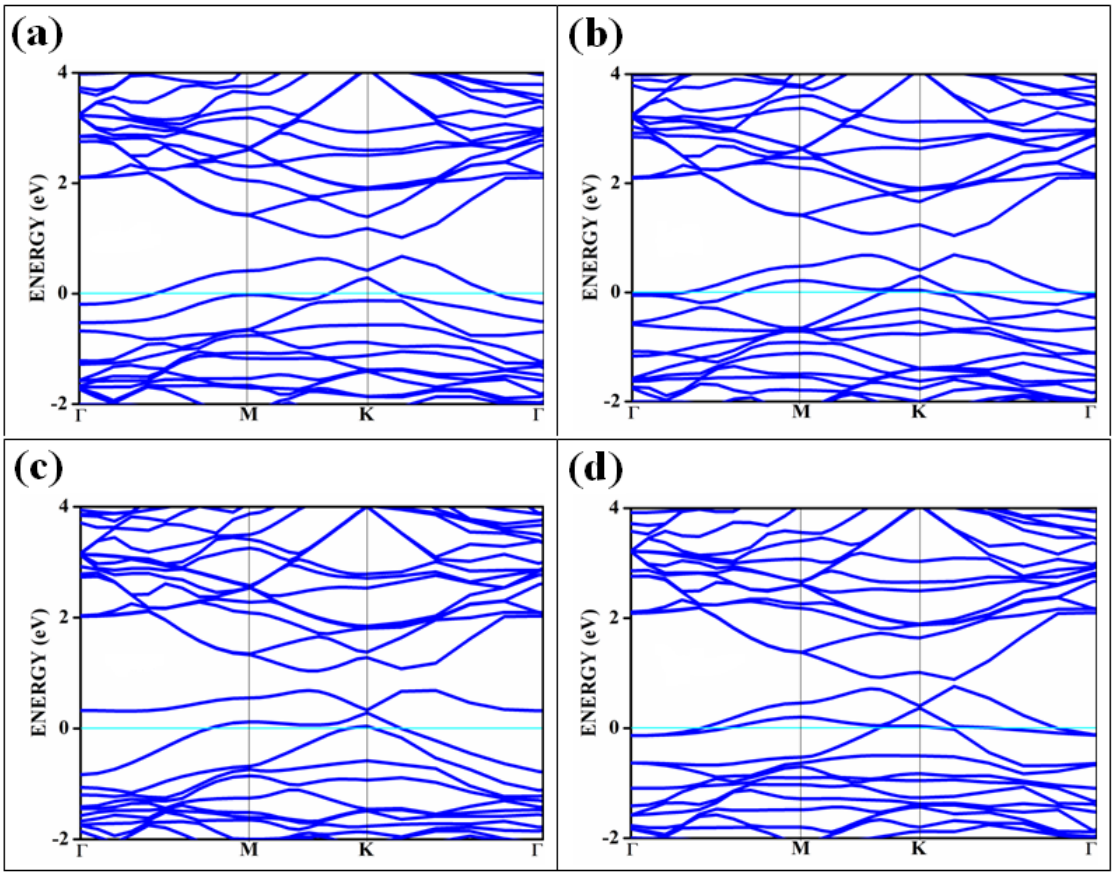

Fig. 6.4. Band Structures of stable BLG structures (a) b-AB (b) d-AB (c) e-AB and (d) f-AB

Table 6.2. The adsorption energy (E_a), the distance between two layers after optimization (D1), the distance between adsorbate and adsorbent (D2), and the band-gaps after adsorption of ammonia on most stable configurations.

System	**(E_a) (eV)**	**D1 (Å)**	**D2 (Å)**	**Band-gap (eV)**
NH_3/1B-AB	-0.046	2.59	3.2	0.26
NH_3/b-AB	-0.222	2.59	3.4	0.31
NH_3/d-AB	-0.989	2.9	1.66	0.28

NH_3/e-AB	-1.012	2.95	1.66	0.16
NH_3/f-AB	-0.284	2.62	3	0.12

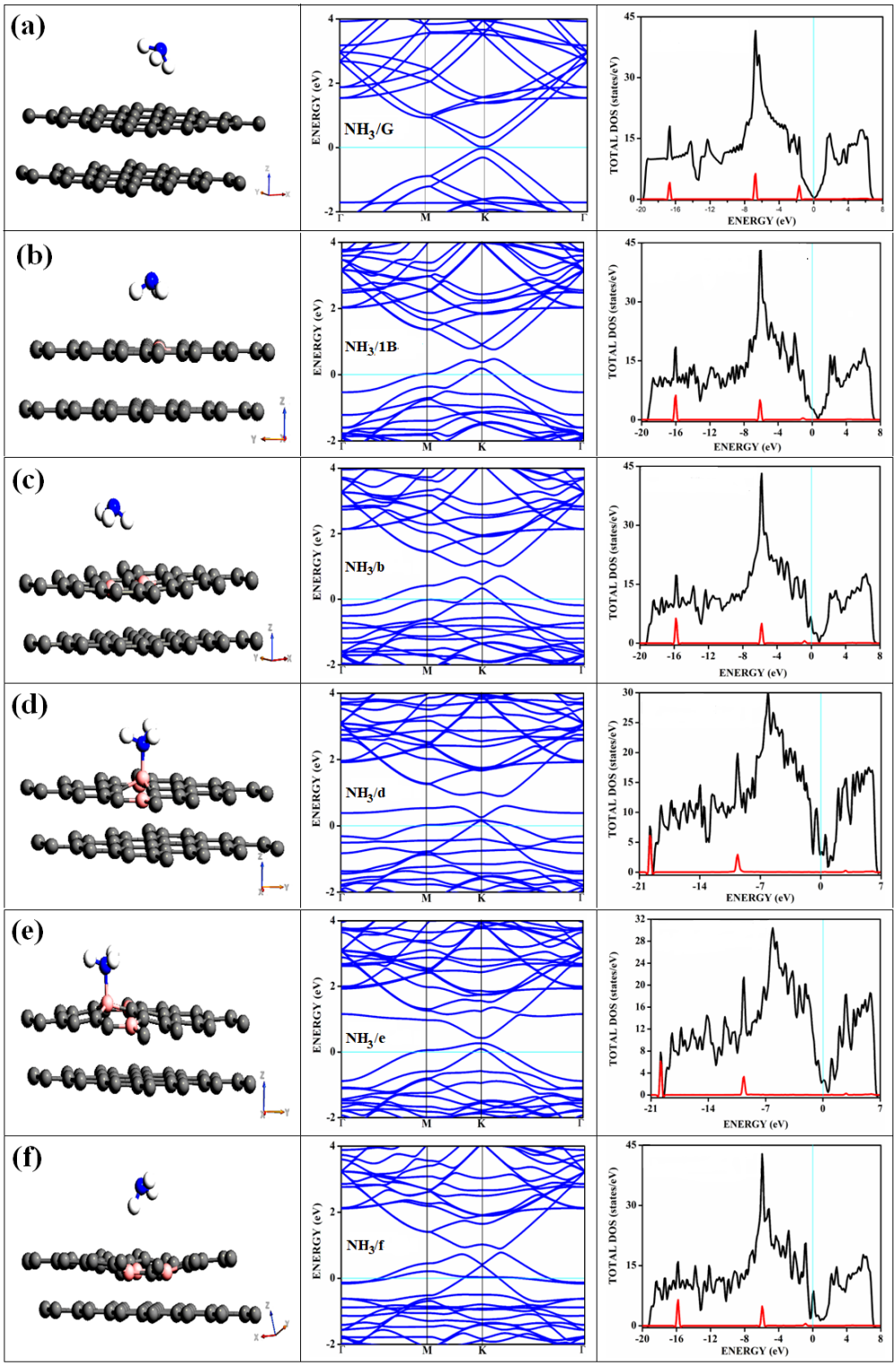

Fig. 6.5. The band structures and respective density of states for different bilayer systems studied with ammonia as adsorbate (a) NH_3/G-AB (ammonia on un-doped, AB stacked BLG) (b) NH_3/1B-AB (c) NH_3/b-AB (d) NH_3/d-AB (e) NH_3/e-AB (f) NH_3/f-AB. The partial density of states for ammonia for these adsorption processes is shown in red.

Analyzing the density of states corresponding to the case where chemisorption is observed in the case of surfaces d-AB and e-AB, orbital hybridization happens between the '2a1' orbital, which is a non-bonding p-orbital on the nitrogen of ammonia and the p-orbital on boron. Figure 6.6 shows the density of states corresponding to ammonia before and after the adsorption on the surface type 'd-AB.' Before adsorption (represented by the black line), it shows three peaks corresponding to the three molecular orbitals of ammonia. After the adsorption (blue line), the peak near the Fermi disappears. The peak near the Fermi corresponds to the '2a1' orbital, the HOMO, non-bonding p orbital of nitrogen, and is occupied. The absence of this peak corresponding to '2a1' in (d) and (e) in Figure 6.5 shows that the chemisorption takes place with the mixing of this non-bonding orbital and the orbitals of the electron-deficient boron to form the bond. For comparison, the electronic structure corresponding to the un-doped bilayer, doped bilayer, and ammonia adsorption are drawn together in Figure 6.7. The changes in the band-gap are visible from this plot, and there is a dispersion loss after the adsorption.

To extract and visualize helpful information on the valence charge transfer contours from the first-principles calculations, the VESTA (Visualization for electronic and structure analysis) software package [31] is used. Contour plots of the electronic charge density associated with the valence and conduction bands of NH_3/d-AB are shown in Figure 6.8. We have constructed the electron density contour plots to investigate the chemical bonding behavior of B-N bonds in-depth. The plane *hkl* (110) containing N-B-C bonds for various partitions of electronic charge densities of NH_3/d-AB is used for this purpose.

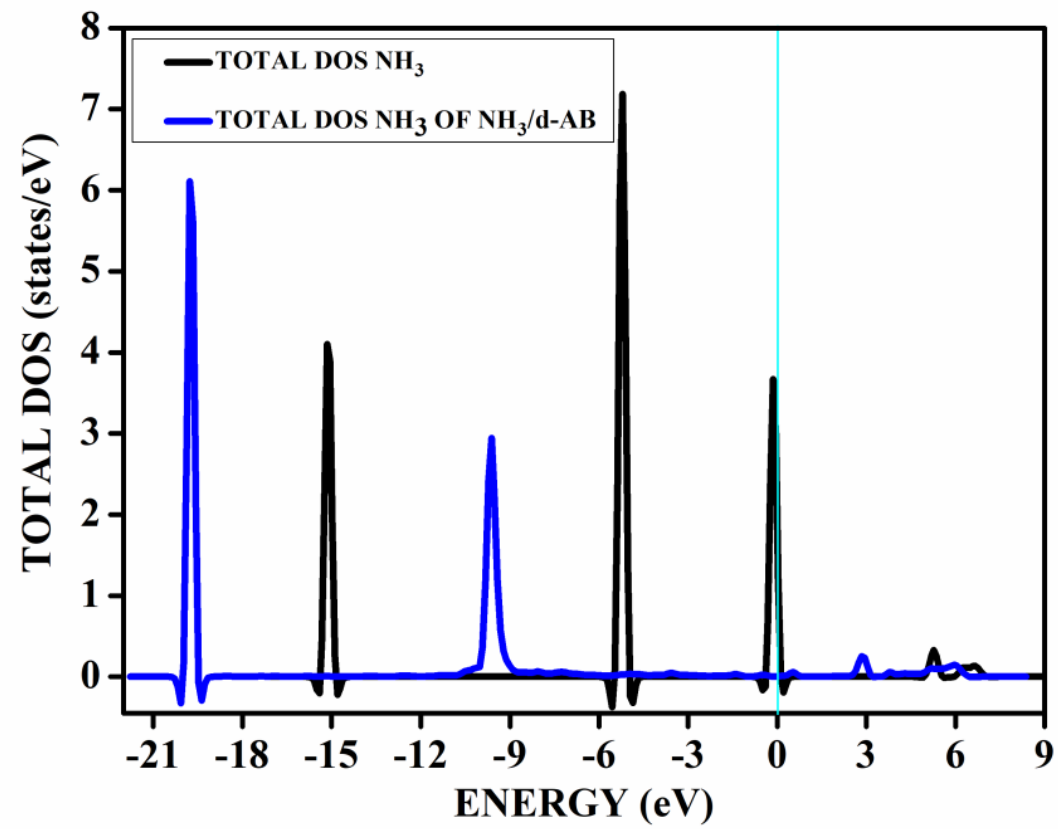

Fig. 6.6. The total DOS of ammonia before and after adsorption on surface d-AB of bilayer graphene. The absence of the blue peak near the Fermi corresponds to the orbital hybridization.

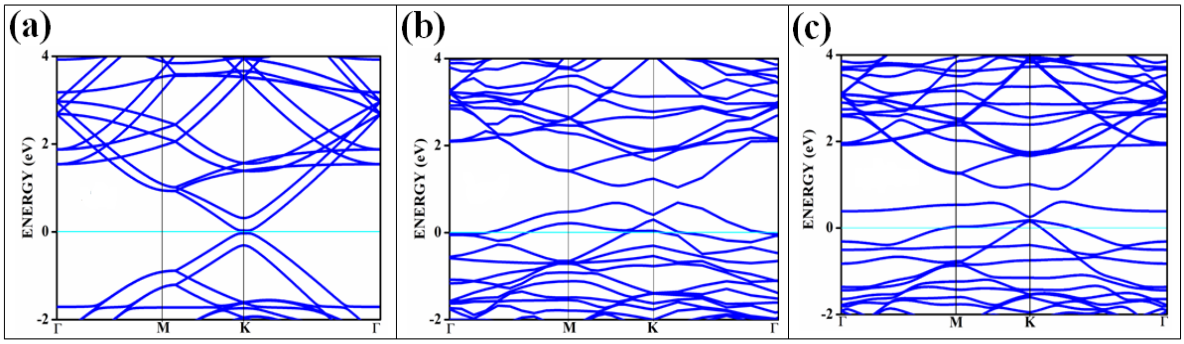

Fig. 6.7. The band Structures of geometry with doped monolayer, doped and ammonia as adsorbate respectively (a) G-AB (b) d-AB (c) NH_3/d-AB.

The difference between charge densities of the adsorbed complex and the surface and the gas molecule NH_3, according to Eq. 2.48, is plotted in Figure 6.8 in two different perspectives, (a) and (b), to visualize the effect of perturbations due to adsorption. The difference density plot is to understand how the charge density redistribution occurs due to

chemical bond formation or interaction. The impact of ammonia adsorption is evident from this. The regions where the boron atoms are present still show areas of electron-deficient nature in the immediate vicinity compared to the rest of the surface. The red color from the figure represents nitrogen with high charge density, yellow iso-charge surfaces represent 2.24e-05 e/Å^3 of charge accumulation, and the bottom cyan color shows 0.023 e/Å^3 charge depletion on the graphene surface.

Furthermore, the valence charge accumulated around the nitrogen is attracted towards the charge-depleted region (cyan iso-surface, i.e., boron of graphene bilayer iso-surface), contributing to the energetic preference of nitrogen to bond with that particular boron, which is AB stacked to the bottom layer. Here, the valence charge (cyan) around boron atoms was attracted towards the nitrogen atom (from the cyan toward the yellow iso-charge surface), contributing to the energetic preference of forming a covalent bond. The bonding states of B–N bonds lie on top of the valence bands. Figure 6.8 shows the concentration of charge that has been distributed among carbon atoms that are adjacent to borons or have formed bonds with borons.

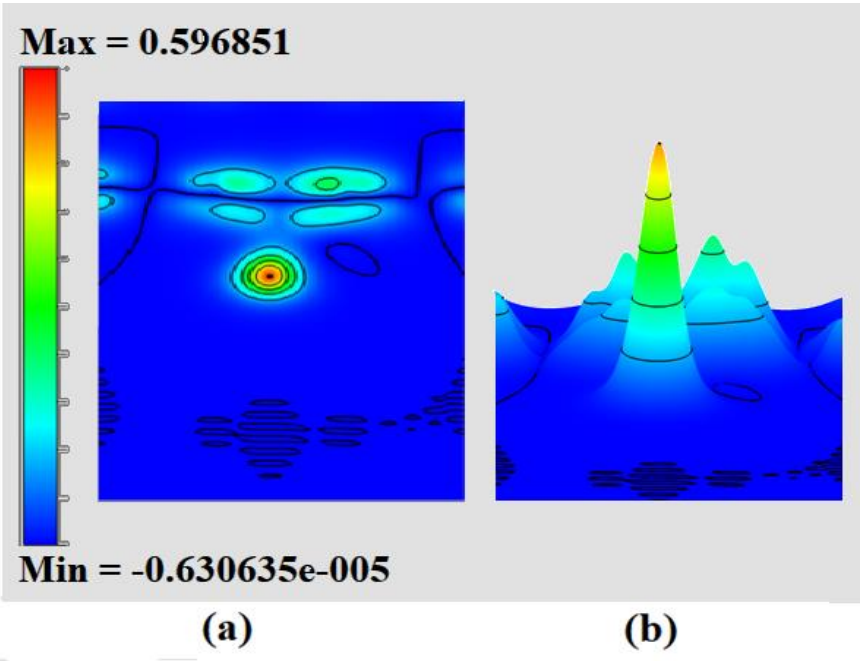

Fig. 6.8. The electron charge density contour map of ammonia adsorption on the surface d-

AB (NH_3/d-AB) (a) contour plot and (b) the bird-eye-view perspective. The unit of the isovalue is e/Å^3.

6.5. Conclusion

Graphene bilayer and its doped derivatives clearly show favorable properties towards the adsorption of gases and, correspondingly, show potential for developing gas sensor devices. As discussed, doping with moderate concentrations and ammonia adsorption on BLG show specific changes in the electronic properties. The electronic structure for doped systems indicates a band-gap opening for the semi-metallic bilayer, and adsorption is favored on some of the surface patterns. It could lead to unique dopant combinations for sensing various specific gases. Controlling adsorption parameters by use of dopant concentrations and varied configurations is observed and can be a key factor in developing devices to improve gas sensing performance.

Overall, the future of bilayer graphene and its derivatives in gas adsorption and sensing seems promising and could also potentially extend to the storage and capture of gases. Much effort remains to be made in understanding the effect of dopants on the adsorption of various non-toxic gases such as NH_3, CH_4, H_2O, H_2, and O_2. Advancements for the practical applications of these chemically modified bilayers include their prospective potential application in sensing pollutants like ammonia.

Chapter 7

A first-principles study on adsorption of hydrogen cyanide and hydrogen isocyanide on substituted phosphorene

7.1. Introduction

There has been a lot of interest in the recent past in the atomic-layer thick two-dimensional (2D) materials and combinations of such 2D layers as van der Waals heterostructures after the discovery of graphene. Silicene, boron nitride, transition metal chalcogenides, etc., are a few such materials, owing to their unique properties compared to the bulk and their numerous potential applications in nanoelectronic devices have gathered a considerable amount of interest in recent years [1].

The gaseous pollutants hydrogen cyanide (HCN) and hydrogen isocyanides (HNC), which are produced as byproducts of industrial operations, are well recognized for their toxicity and significant risks to human health [2]. Driven by those results, this investigation focuses on exploring phosphorene's potential as a sensing material for detecting hydrogen cyanide and hydrogen isocyanide gases. The effectiveness of chemical modification, namely impurity atom doping, in altering the characteristics of black phosphorous (BP) or phosphorene has been proven in previous studies [3–5]. We have conducted theoretical studies to enhance the efficacy of phosphorene gas sensors, including introducing p-type and n-type impurity atoms for doping purposes. Based on the information presented in Chapter 1, significant research has been conducted on gas sensors based on 2D materials for commonly found gases in the environment and some industrial gases, such as SO_2 and CH_4. However, it is essential to note that a limited number of studies have specifically focused on investigating the gas-sensing capabilities of hydrogen cyanide and hydrogen isocyanide molecules [5,6]. It is worth noting that there is a lack of ab initio calculations on the characteristics of hydrogen cyanide and hydrogen isocyanides when adsorbed on phosphorene surfaces.

Black phosphorene (BP) is an emerging two-dimensional (2D) material with a honeycomb lattice where each phosphorous is covalently bonded to three other atoms. The band-gap of the BP is layer-dependent. Compared to the low band-gap (~0.3 eV) bulk

phosphorene, the single layer direct band-gap is about 0.80 eV, making it an excellent direct band-gap semiconducting material. As we add up the layers, the band-gap ranges from 1.51 eV to 0.59 eV. Mechanical exfoliation of black phosphorus crystals has effectively isolated a novel 2D semiconducting material called few-layer black phosphorus or phosphorene [7,8]. Phosphorene's direct band-gap is large and unusual compared to other 2D materials; it ranges from 1.51 eV for a monolayer to 0.59 eV for a five-layer structure [9]. Phosphorene has high on/off ratios, up to 104 mobility [10] and the phosphorene-based field-effect transistor (FET) has high mobility of 286 cm^2/Vs. Phosphorene is a wonderful 2D material for electrical and optical applications [11], and it has attracted a lot of attention from researchers [12–14] due to its valuable properties, such as its anisotropic electric conductance and optical responses.

In addition to its direct semiconducting [15] and ultrahigh mobility at room temperature [9], mechanical flexibility[16], and high thermoelectric performance [17,18] in phosphorene properties, it has several other exciting features [7,8]. Its unique set of characteristics makes it a promising candidate for use in many different fields, including field-effect transistors [15,19], lithium and sodium ion batteries [20], solar cells [21], photocatalysts [22], spintronics [23], and gas sensors [24,25].

The primary challenges for phosphorene research are its scarcity and tendency to degrade quickly. More significant investments for mass manufacture of the material are needed to address the former, which will be spurred by the gradual discovery of the material's potential benefits. The rapid deterioration when exposed to environmental conditions is a second challenge, although there are techniques to overcome that. Encapsulation, modeled after conventional procedure in the organic light-emitting diode sector, is the first practical and reliable method. Monolayer and few-layer BP have been successfully encapsulated using every currently-known technique, including atomic layer deposition (ALD) of alumina, polymethylmethacrylate (PMMA) encapsulation, and encapsulation in 2D stacked

heterostructures. Secondly, this capacity for deterioration may be used to one's advantage in some contexts, such as trace oxygen molecule sensing. Theoretical simulations suggest that a wide variety of magnetic moments may be produced in Ag-, Au-, Ti-, V-, Cr-, Mn-, Fe-, and Co-doped phosphorene in all forms of black phosphorene predicted by Kulish *et al.* [26]. However, simulations using the generalized gradient approximation (GGA) and those adding the Hubbard U factor (GGA-U) [27,28] show that this doping causes magnetic moments with DMS (dilute magnetic semiconductor) features [29], and leads to a half-metallic state.

Furthermore, the characteristics of different charge carriers may be adjusted by adsorbing various atoms on phosphorene. The structural, electrical, and magnetic characteristics of atoms adsorbed on phosphorene were comprehensively investigated by Ding and Wang [30] using the first-principles computations. The capacity of a semiconductor to be both p-doped and n-doped is necessary for many electrical devices, including the p-n junctions and complementary metal oxide semiconductors (CMOS), as is well known. To make this novel 2D valuable material for various fields, it is essential to utilize certain techniques to alter its electronic structure. Molecular doping is a promising, simple, and effective technique to adjust the electronic properties of 2D materials through their interactions with the molecules.

The 3.08 Å inter-sheet spacing in phosphorene allows it to accommodate ions like B, C, N, O, S, and Si [31]. It is well known that substitutional dopants maintain the semiconducting property with an odd number of valence electrons, such as those in group IIIA (B) [32]. It is predicted that such doped systems would have high thermodynamic stability [32,33]. Since the n-type dopant and neighboring phosphorus atoms have a strong electron pairing and hybridization of s-p orbitals [32–34]. Doping boron into black phosphorene does not result in the emergence of magnetism. However, p-doped BP monolayers might undergo a ferromagnetic-to-antiferromagnetic phase shift when holes or electrons are introduced through a potential gate [35]. Black phosphorus's semiconducting and anisotropic transport properties

are maintained by isovalence doping with nitrogen from group VA [32]. Since the valence electrons of the dopant couple up with electrons from the surrounding phosphorus atoms, no magnetism is generated [33]. As can be observed from earlier studies [32], the Si- and S-doping not only confers metallic features on BP, but also gives highly anisotropic transport properties. Instead of the simpler substitution geometries observed in tetrahedral semiconductors, these impurities follow the 8-N coordination rule, typical of amorphous semiconducting materials [36]. As a result of creating a non-bonding 3p electron of the nearby phosphorus atom, the ground states of Si- and S-doped systems are magnetic and half-metallic, but the charged dopants Si^+ and S^+ induced no magnetism [33,34]. Primary anionic species like sulfur have high binding energy, which makes their existence in black phosphorene more stable [5]. However, it may cause the natural phosphorene's space inversion symmetry to be broken, resulting in a C_s symmetry.

After considering the current status of adsorption on doped black phosphorus, the adsorption of HCN and HNC on N-doped phosphorene monolayer using first-principles calculations is considered. A hypothetical free-standing two-dimensional phosphorene structure is taken for the study to elucidate this behavior. Binding energies, electronic structural properties, and charge transfers were calculated to explore the characteristics of phosphorene as a potential adsorbent material for gas-sensing applications.

7.2. Results and discussions

In order to study the electronic configurations of the doped phosphorene, we initially considered a 3×3 supercell, wherein a dopant substituted a solitary phosphorus atom to consider a doping concentration of 2.7%, as depicted in Figure 7.1. The supercell is extended into z in the conventional direction from the surface with a lattice parameter of 20 Å along the z-axis to avoid an image interaction between neighboring layers.

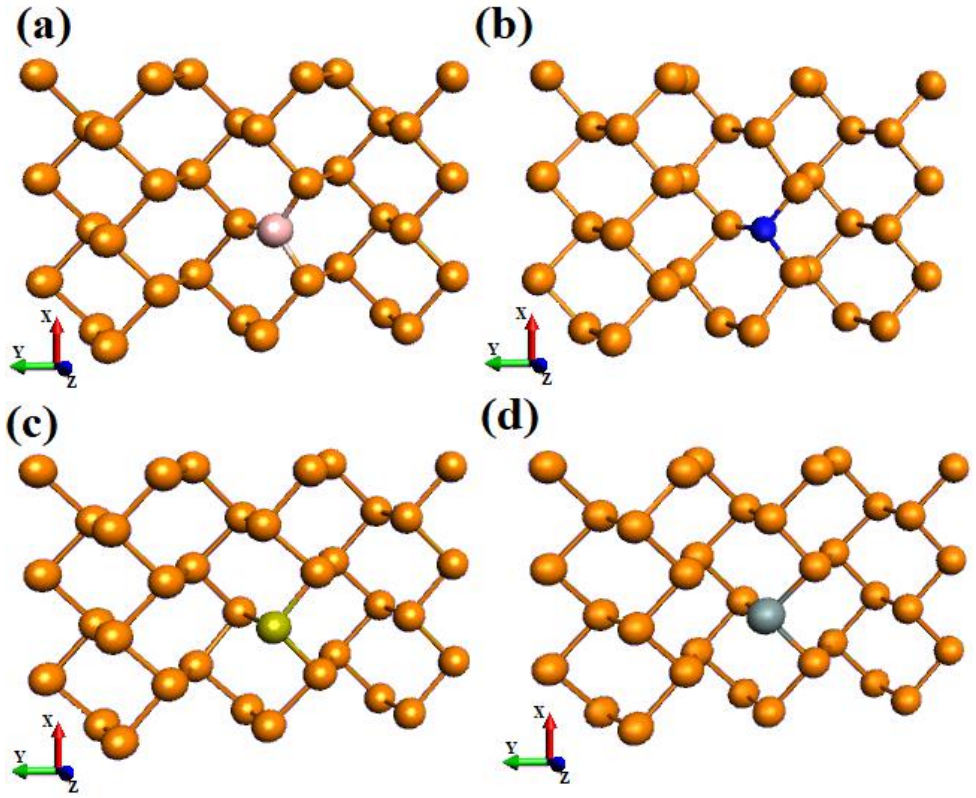

Fig. 7.1. The ball and stick model of 2.7% (a) boron, (b) nitrogen, (c) sulphur and (d) silicon doped phosphorene surfaces. Pink represents the boron atom, blue nitrogen, green sulphur, and grey silicon; golden represents phosphorous atoms.

The band structures of pristine phosphorene and phosphorene doped with B, N, Si, and S are computed and shown in Figure 7.2. Calculations in the case of pristine phosphorene shows a direct band-gap of approximately 0.80 electron volts, consistent with the earlier findings [31]. Upon analyzing the doped systems, it is evident that the Fermi levels in phosphorene doped with silicon and nitrogen exhibit a downward shift towards the valence band. Conversely, as expected, in S-doped phosphorene, the Fermi levels display an upward shift towards the conduction band, as represented in Figure 7.2.

Since the n-type dopant and neighboring phosphorus atoms have a strong electron pairing and hybridization of s-p orbitals [32,33], doping boron into black phosphorene does not result in the emergence of magnetism. The B-doped system shows an n-type semiconducting nature. On the other hand, as illustrated in Figure 7.2b, it exhibited an indirect band-gap and

high anisotropy for optical devices [31]. Figure 7.2c shows that the band-gap of nitrogen-doped black phosphorene can be made to be 0.90 eV, which agrees with the previous studies[32]. It is found that the Si and S doping not only confers metallic features on BP but also gives highly anisotropic transport properties [33]. Band-gaps for the 3×3 supercell are shown in Figure 7.2b to be 0.84 (indirect) eV for B-doped phosphorene and 0.90 eV for N-doped phosphorene, whereas pure phosphorene has a band-gap of 0.80 eV, in agreement with the findings of Goulant *et al.* [31]. The band-gap is shown to vary depending upon the valence electron count of even and odd in dopant atoms. There is a substantial correlation between the hybridization of p- orbitals between dopants and phosphorene and the decrease or enhancement of gap opening in doped phosphorene, as shown below.

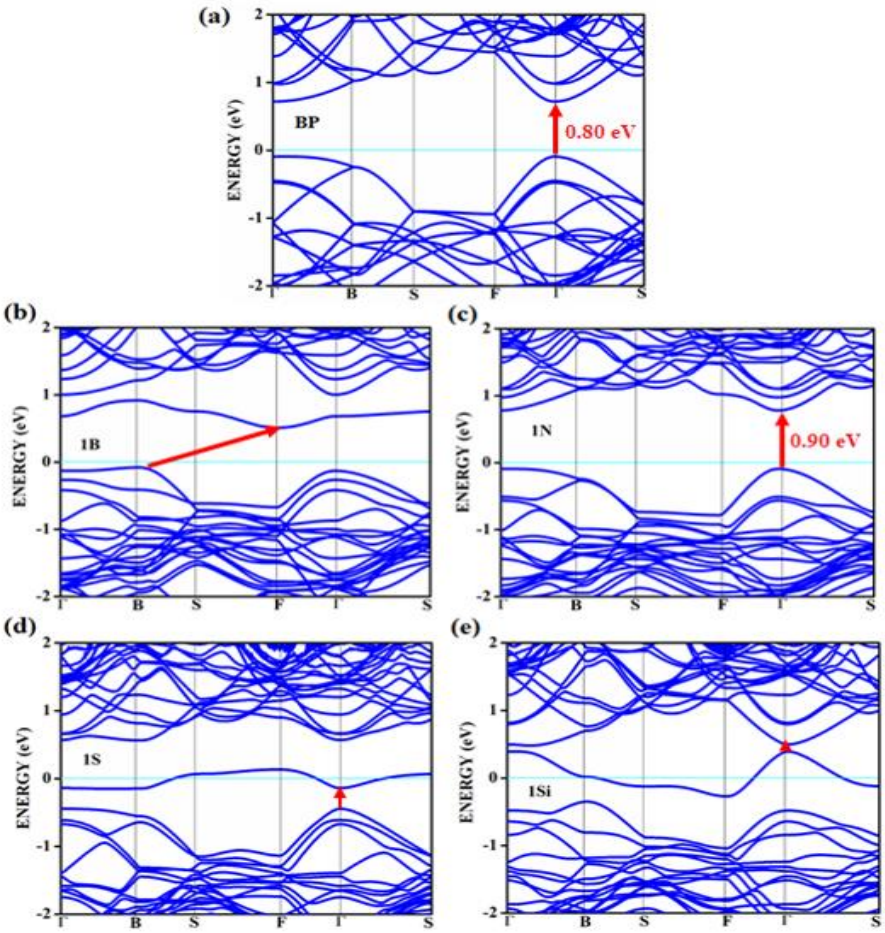

Fig. 7.2. The band structures corresponding to pristine and doped phosphorene surfaces, (a) pristine phosphorene, whereas (b)-(e) refers to band structures for boron, nitrogen, sulphur, and

silicon doped phosphorene surfaces. Fermi level is shown by the cyan line.

Each phosphorus atom in phosphorene (with valence electron configuration $3s^2\ 3p^3$) form sp^3 bonds with a lone pair of valence electrons of the dopants, thus explaining their metallic and semiconducting characteristics in doped phosphorene. As can be seen in Figure 7.2, the valence-electron states of dopant atoms readily tune the non-bonding lone-pair electronic states of pure phosphorene, resulting in the semiconducting or metallic electronic states at the Fermi level. N-doped phosphorene retains the same semiconducting characteristics as pure phosphorene because three of the electrons in nitrogen are engaged in bonding with surrounding phosphorus atoms, leaving one lone pair of electrons on each atom. In contrast, B-doped phosphorene retains its semiconducting characteristics despite the absence of lone pairs on boron atoms due to the bonding of all three valence electrons to surrounding phosphorus atoms. In the case of C-doped phosphorene, the metallic property is because of the lack of only one electron results in a delocalized energy band that is only half full [32].

In contrast, O-doped phosphorene exhibits metallic characteristics in its half-filled state due to three non-bonding electrons. When compared to the traditional doping effect in group IV semiconductors, where n- and p-type dopants cause certain localized doping-induced states in the band-gap, our results on the metal-semiconductor oscillatory behaviors in doped phosphorene systems stand out. Total and partial density of states (PDOS) for B-, Si-, N-, and S-doped phosphorenes are shown in Figure 7.3, which helps to elucidate the underlying bonding process between the dopants and the phosphorus atoms. Strong hybridization of s-p orbitals between dopants and phosphorene is shown by the fact that the computed partial density of states (PDOS) projected onto the 2p-orbitals of each dopant atom exhibits a comparable pattern and peak locations to that for the phosphorus atom (see Figure 7.3a/b/c/d). The partial DOS for dopants is widened due to this intense hybridization. In particular, S/Si-doped phosphorene exhibits metallic behavior because the 2p partial DOS peaks for the S/Si

dopant and the phosphorus atom are located near the Fermi level. Therefore, this abovementioned work on doping provides a novel method for controlling electrical characteristics using dopants.

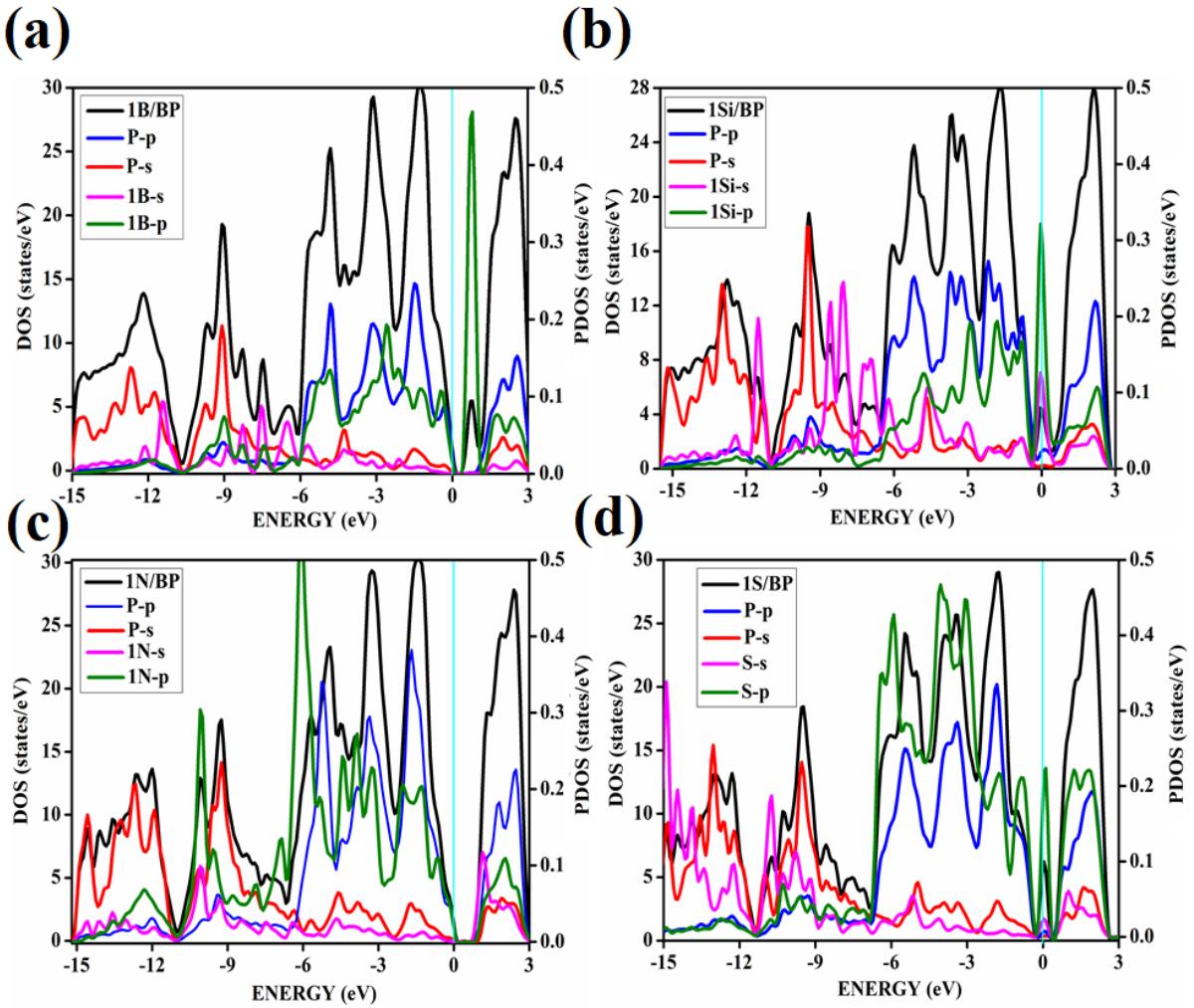

Fig. 7.3. The total and partial density of states (PDOS) of B, Si, N, and S-doped phosphorene (a) 1B/BP (b) 1Si/BP (c) 1N/BP (d) 1S/BP. The blue represents phosphorous p orbital, red represents phosphorous s orbital, magenta is for respective dopants s orbital, and green represents dopants p orbitals.

1B/BP represents 2.7% doped boron phosphorene and similar nomenclature for 1Si/BP, 1N/BP, and 1S/BP given for phosphorene doped with silicon, nitrogen, and sulphur, respectively. To investigate whether the above metallic–semiconducting oscillation with a number of the valence electrons is general, we calculate the band structures of various dopants

of different concentrations and configurations using a relatively 3×3 supercell. The different concentrations are 5.5%, where two phosphorus atoms are replaced by dopants in the structure in a 3×3 supercell, and another concentration of 8.3%, where dopants replace three phosphorus atoms. The different configurations of dopants are shown in Figure 7.4. We have considered the same concentration and configurations for dopants B, N, S, and Si. In systems doped with boron and nitrogen, the dopant forms connections with three phosphorus atoms. The bond lengths in these systems (dopant-phosphorus) are always lower than 2.22 Å and the the phosphorus atoms around the impurity have one lone pair of electrons. Consequently, these atoms continue to form sp^3 bonds, similar to the structure of pristine phosphorene. The N-doped system exhibits the highest stability and the greatest binding energy compared to the B, S, and Si systems. N-doped systems are used because nitrogen (N) has the same valence electron distribution as phosphorus (P). The N-doped system exhibits the shortest bond length between the dopant and phosphorene among all systems, which may be attributed to the dopant's highest electronegativity.

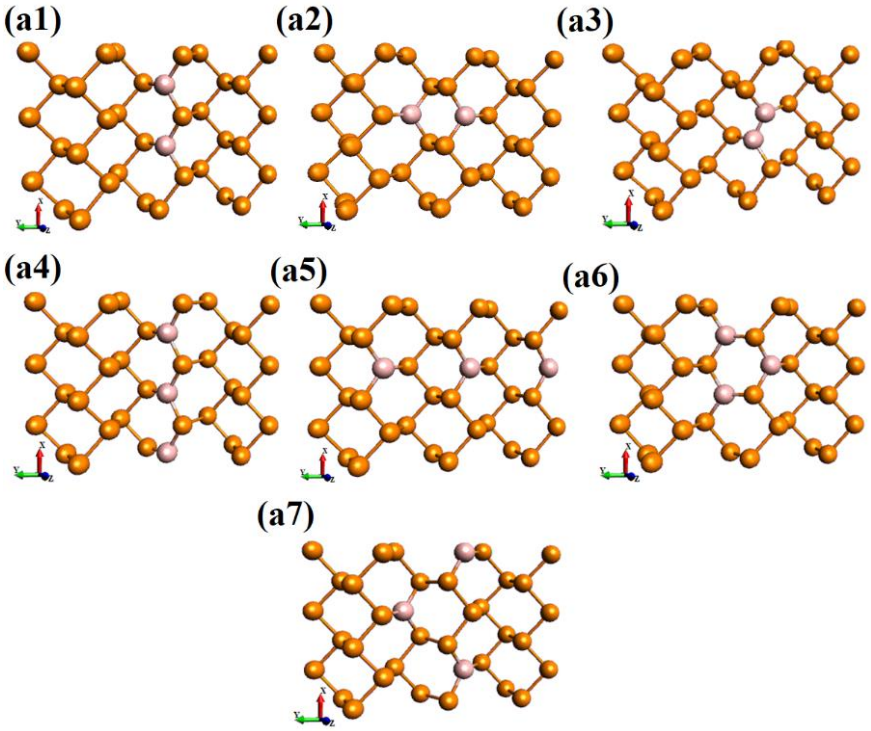

Fig. 7.4.1. The optimized geometries of different concentrations and configurations of dopants

(a1)-(a3) 5.5% dopant concentration of boron, (a4)-(a7) 8.3% boron doping concentration. Similar patterns of doping and concentrations are followed for silicon, nitrogen, and sulphur dopants. Here below the optimized geometries of these dopants that show metallic nature in the case of nitrogen dopant and semiconducting nature in the case of silicon and sulfur after optimization are shown as follows,

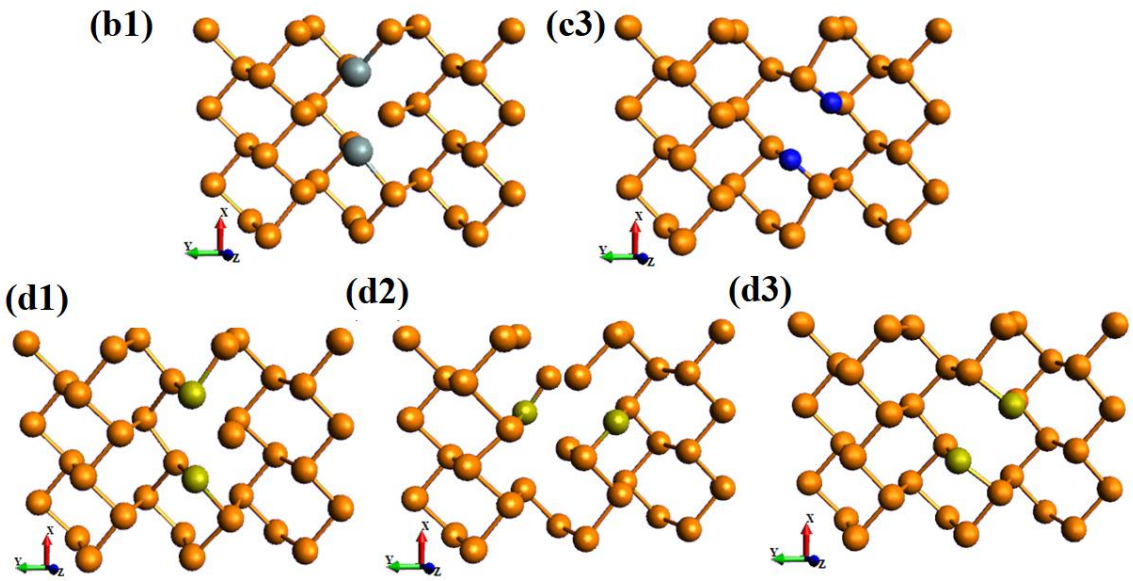

Fig. 7.4.2. The optimized structures of (b1) 5.5% dopant concentration of silicon, (c3) 5.5% concentration of nitrogen, (d1)-(d3) 5.5% dopant concentration of sulphur. Orange color represents phosphorous atoms; nitrogen is shown in blue. Pink represents boron, grey represents silicon, and green is shown for sulphur.

The different patterns of boron doping are considered, and they are nomenclature as 2BADJ, 2BOPP, 2BSIDE from (a1)-(a3) represents 5.5% of doping as shown in Figure 7.4.1 respectively, and 3BADJ, 3BOPP, 3BV, and 3BEACH from (a4)-(a7) shown for 8.3% of doping concentration. Similar terminology is followed for nitrogen, sulphur, and silicon doping as 2NADJ, 2NOPP, 2NSIDE, 3NADJ, 3NOPP, 3NV, and 3NEACH; 2SADJ, 2SOPP, 2SSIDE, 3SADJ, 3SOPP, 3SV, and 3SEACH; 2SiADJ, 2SiOPP, 2SiSIDE, 3SiADJ, 3SiOPP, 3SiV and 3SiEACH respectively. Figure 7.4.2 shows the bond break after optimization of

geometries, i.e., 2NADJ, 2SiSIDE, 2SADJ, 2SOPP, 2SSIDE are observed. In the case of the 2NSIDE configuration, the nitrogen impurity causes the compression of the phosphorene lattice along -P-N-N-P-. It leads to the break of the bond between nitrogen atoms. In the case of sulphur doping, all the configurations show the bond break because of the increased size in the geometries with concentrations. The atomic size of sulfur is 180 pm, and that of phosphorus is 195 pm, and the puckered structure makes it challenging to accommodate these dopants. Though the single-atom dopant is a stable geometry upon increasing doping concentration, few configurations show bond cleavage, making the optimized geometries unstable.

Dopant like boron and nitrogen, which consists of an odd number of valence initially with 2.7% of doping, shows semiconducting nature. As the concentration increases with different types of configuration, this nature changes. The configuration where the dopants are arranged in the pattern -P-X-P-X-P- and -P-X-P-P-X-P- (X = N, B) shows a semiconducting character as the phosphorus atom is connected to an odd valence dopant. For dopants like boron, the band-gap is indirect with different concentrations and configurations as the p-orbital of boron affects the electron valances of the structure near Fermi, as shown in Figure 7.5. In the case of nitrogen dopant, the 2.7% dopant shows 0.90 eV of the band-gap, whereas with different concentrations and configurations, this band-gap varies from 0.41- 0.89 eV as shown in Figure 7.6, and the band-gaps are shown in Table 7.1. (a1)-(a3) of Figure 7.6, represents the 5.5% dopant concentration of boron and (a4)-(a7) represents for 8.3% boron doping concentration and nomenclature as 2BADJ, 2BOPP, 2BSIDE, 3BADJ, 3BEACH, 3BOPP and 3BV respectively.

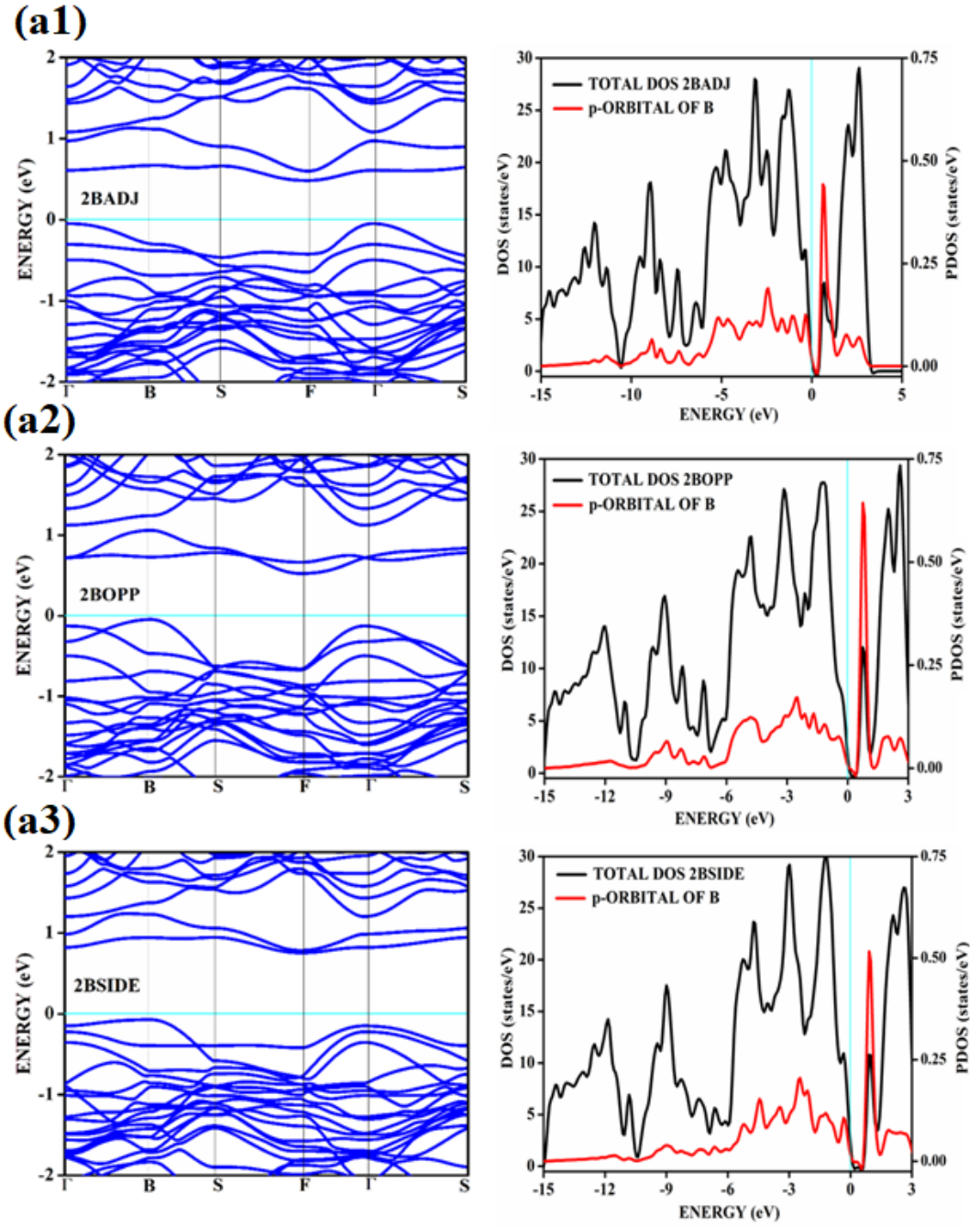
(a1)
2BADJ
ENERGY (eV)
Γ
B
S
F
Γ
S
TOTAL DOS 2BADJ
p-ORBITAL OF B
DOS (states/eV)
PDOS (states/eV)
ENERGY (eV)
(a2)
2BOPP
TOTAL DOS 2BOPP
p-ORBITAL OF B
(a3)
2BSIDE
TOTAL DOS 2BSIDE
p-ORBITAL OF B

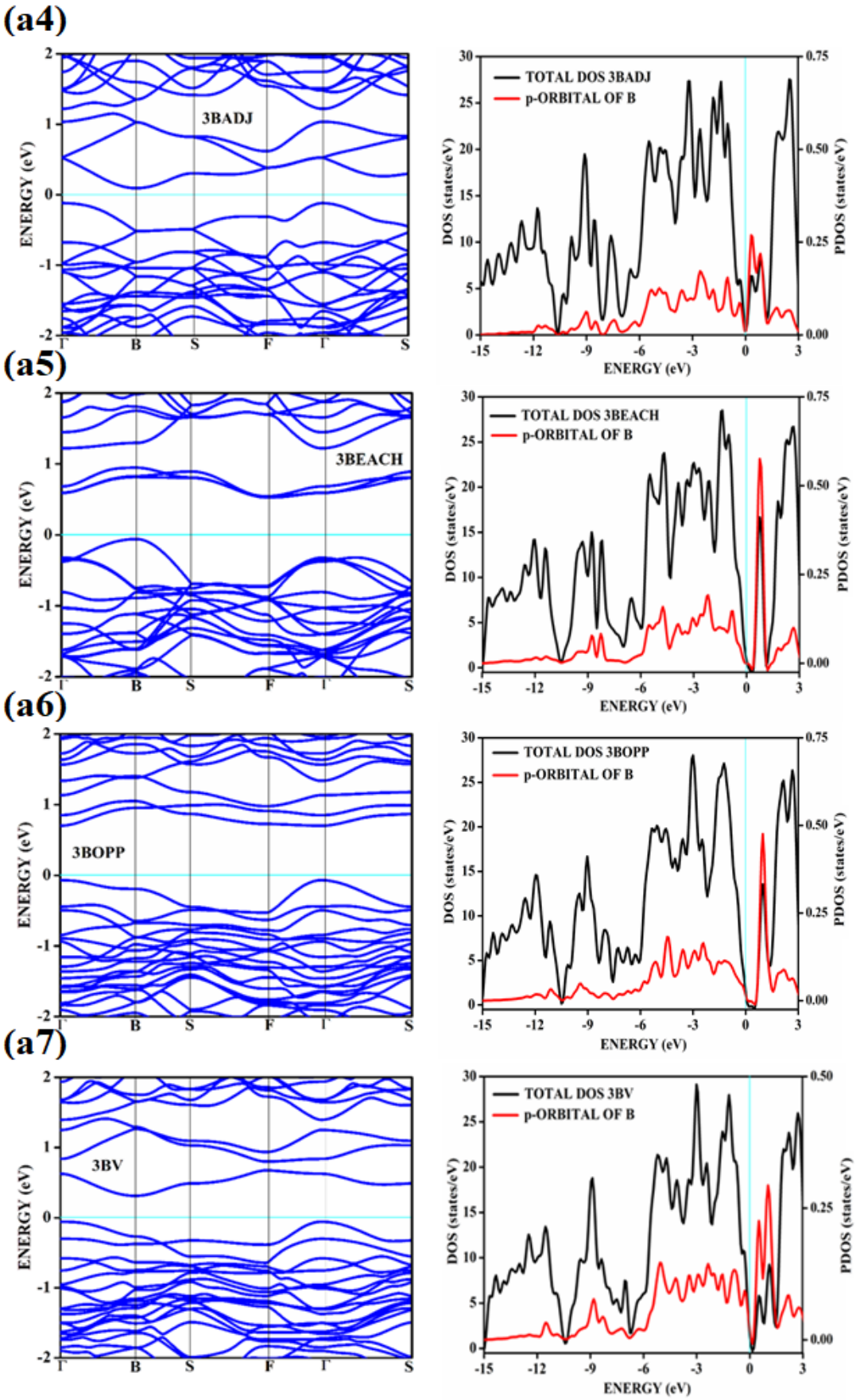

Fig. 7.5. The band structure and respective density of states of boron-doped phosphorene (a1)

2BADJ (a2) 2BOPP (a3) 2BSIDE (a4) 3BADJ (a5) 3BEACH (a6) 3BOPP (a7) 3BV. The cyan color represents the Fermi level; the red color represents the PDOS of the dopant.

Table 7.1. The band-gap for different concentrations and patterned doped nitrogen atoms on various phosphorene surfaces.

Configuration	Band-gap (eV)
1N	0.90
2NADJ	0.87
2NOPP	0.79
2NSIDE	0.66
3NADJ	0.53
3NOPP	0.54
3NV	0.41
3NEACH	0.89

In all the configurations of nitrogen dopant, the structure deformation can be observed because nitrogen size is 65 pm, which is much smaller than that of phosphorus at 195 pm. In configuration 2Nside, we see the bond breakage between nitrogens, as dinitrogen tends to form pπ-pπ interactions, which is impossible in this case as nitrogen forms sigma bonds with adjacent phosphorus atoms. The configuration, like P-N-N-P, shows a metallic nature, as shown in Figure 7.6(c). This is observed because when two nitrogens are placed side by side, there is a bond breakage between nitrogen atoms, creating a vacancy with a free electron pair on nitrogen together, making the total valence even and resulting in a metallic nature of the surface. This change of metal and semiconducting behavior is absent with 8.3% doping as, here, all the dopants concentration leads to an odd number of electrons, and here, the

semiconducting nature is preserved.

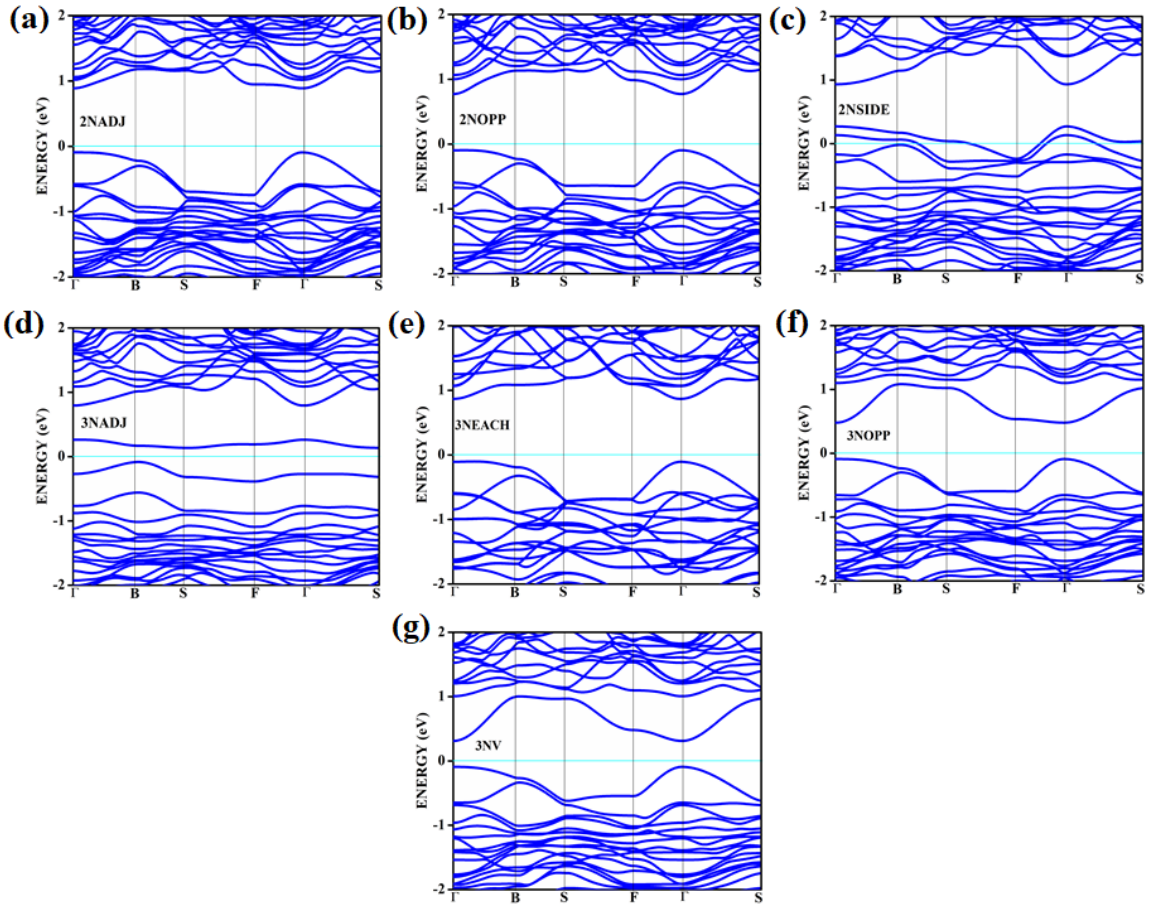

Fig. 7.6. The band structures corresponding to nitrogen-doped phosphorene surfaces of 5.5% from (a) to (c), designated as 2NADJ, 2NOPP, 2NSIDE, and 8.3% from (d) to (g), defined as 3NADJ, 3NEACH, 3NOPP AND 3NV respectively. The cyan line represents the Fermi level.

The 2.7% nitrogen dopant shows the direct semiconducting band-gap increase among the boron and nitrogen dopants. In the case of Si, all the configurations and concentrations show a metallic nature with an indirect band-gap, as shown in Figure 7.7. In the case of sulphur 5.5% doping concentrations show semiconducting nature. In all the configurations of 5.5% Sulphur dopant bond breakage between phosphorous and in configuration like -P-S-S-P-, we can observe bond breakage between S-S as shown in Figure 7.4(d3).

(b1)

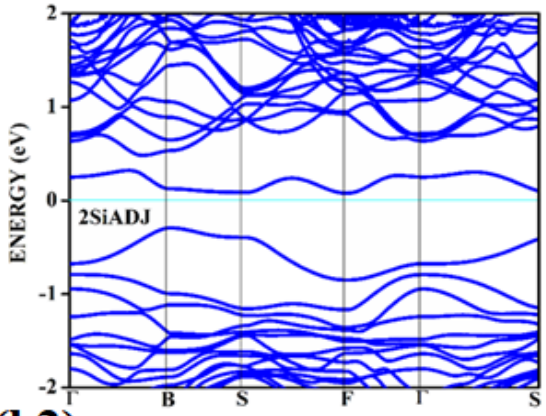
ENERGY (eV)
2SiADJ
Γ
B
S
F
Γ
S

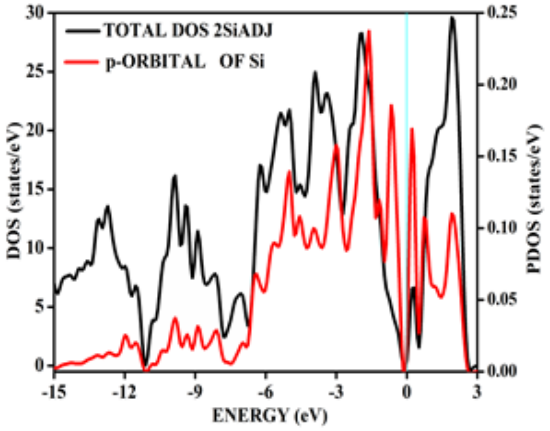
TOTAL DOS 2SiADJ
p-ORBITAL OF Si
DOS (states/eV)
PDOS (states/eV)
ENERGY (eV)

(b2)

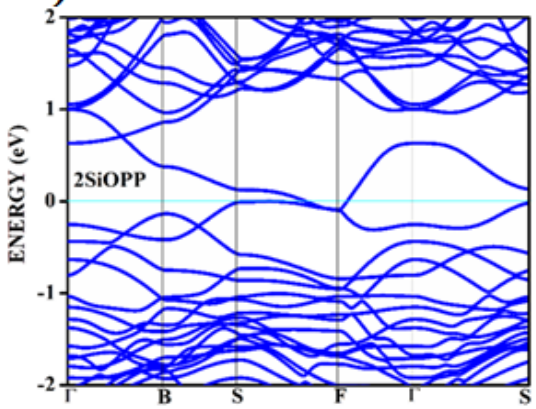
ENERGY (eV)
2SiOPP
Γ
B
S
F
Γ
S

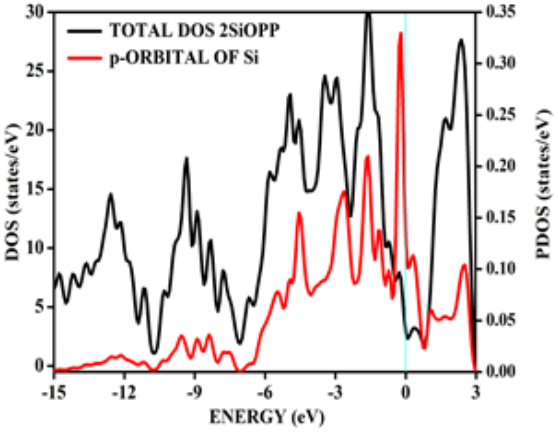
TOTAL DOS 2SiOPP
p-ORBITAL OF Si
DOS (states/eV)
PDOS (states/eV)
ENERGY (eV)

(b3)

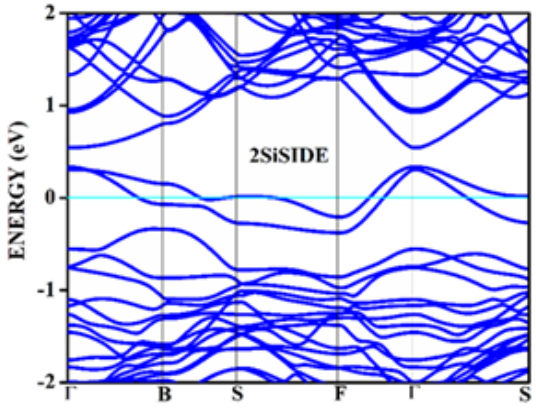
ENERGY (eV)
2SiSIDE
Γ
B
S
F
Γ
S

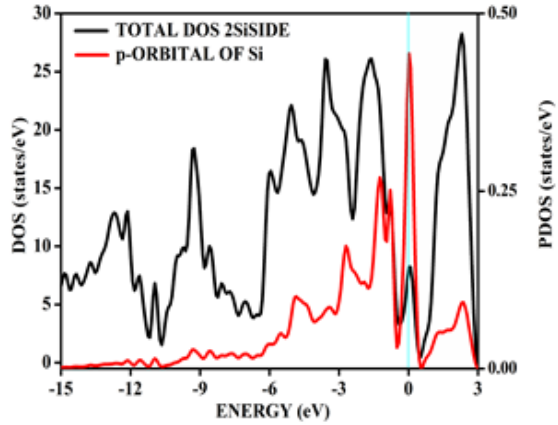
TOTAL DOS 2SiSIDE
p-ORBITAL OF Si
DOS (states/eV)
PDOS (states/eV)
ENERGY (eV)

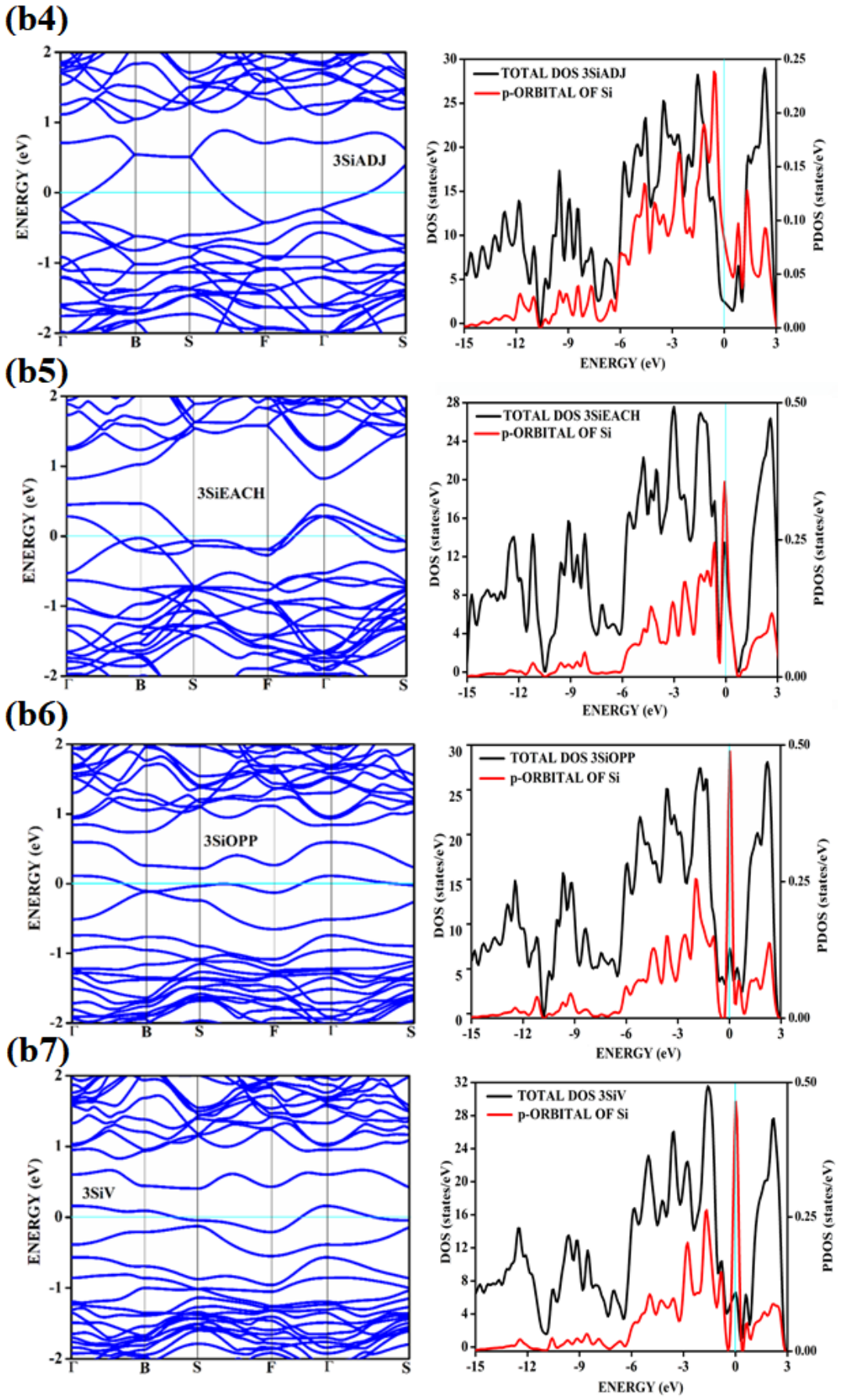

Fig. 7.7. The band structure and the corresponding density of states of silicon-doped

phosphorene (b1) 2SiADJ (b2) 2SiOPP (b3) 2SiSIDE (b4) 3SiADJ (b5) 3SiEACH (b6) 3SiOPP (b7) 3SiV. The cyan color represents the Fermi level, and the PDOS of the dopant is shown in red.

Phosphorene doped with sulphur causes metallic behavior which is evident from the Figure 7.8. Upon doping with sulphur the band-gap from pristine phosphorene 0.80 eV is reduced to 0.35 eV and further increase of dopant concentration the surface shows metallic nature, where valence band and conduction band overlaps as seen in Figure 7.9c. These bond breakages create vacancies in the structure. For configuration where sulfur atoms are doped side by side designated as 2SSIDE, we can observe the band-gap of 0.60 eV. For all the remaining configurations, the flat bands are seen, represented in Figure 7.9. With the calculated information above, we have found that phosphorene with 2.7% nitrogen dopant shows the best results with an increased band-gap. Therefore, N-doped systems are used for our further study for the adsorption of hydrogen cyanide and hydrogen isocyanide because it is having direct band gap and nitrogen has the same valence electron distribution as phosphorus.

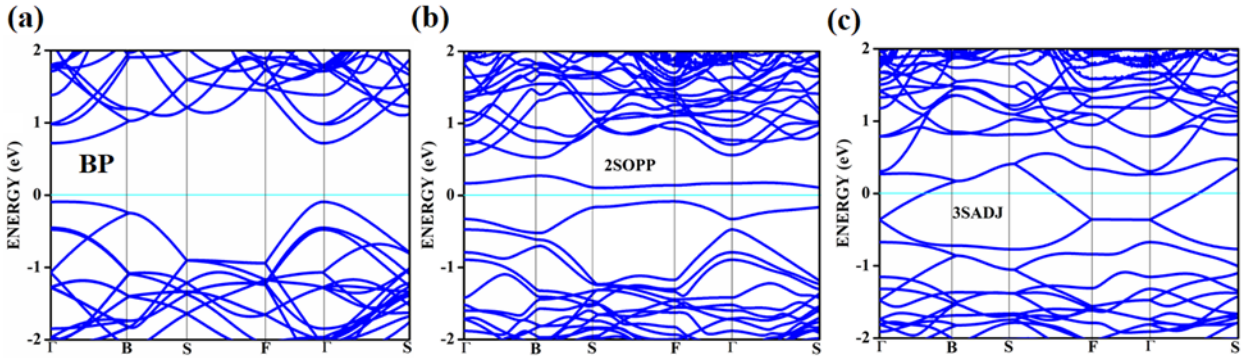

Fig. 7.8. The band structure of sulphur-doped phosphorene in comparison with pristine phosphorene. (a) Band structure of pristine phosphorene; (b) Band structure of 2SOPP sulphur doped phosphorene; (c) Band structure of 3SADJ sulphur doped phosphorene. The cyan color represents the Fermi level.

(d1)

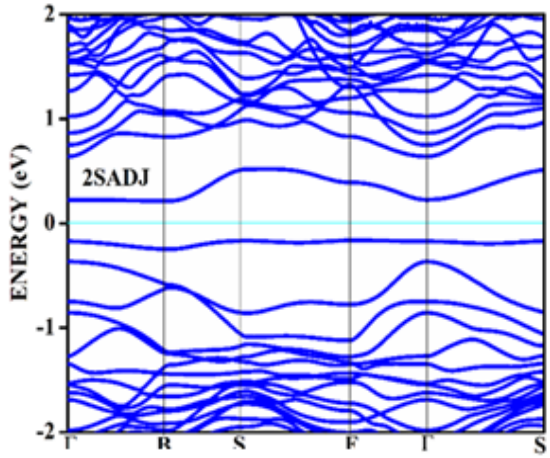
2SADJ
ENERGY (eV)
Γ B S F Γ S

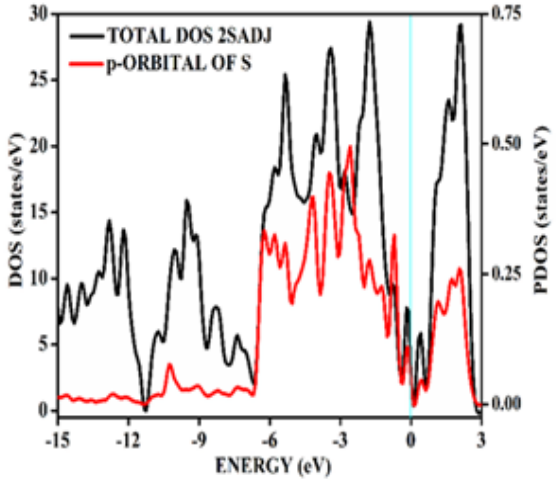
TOTAL DOS 2SADJ
p-ORBITAL OF S
DOS (states/eV)
PDOS (states/eV)
ENERGY (eV)

(d2)

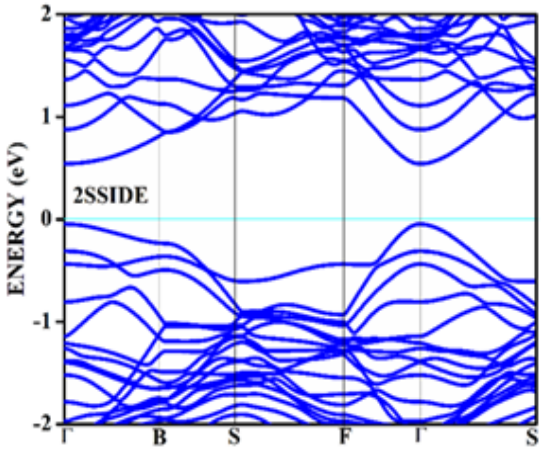
2SSIDE
ENERGY (eV)
Γ B S F Γ S

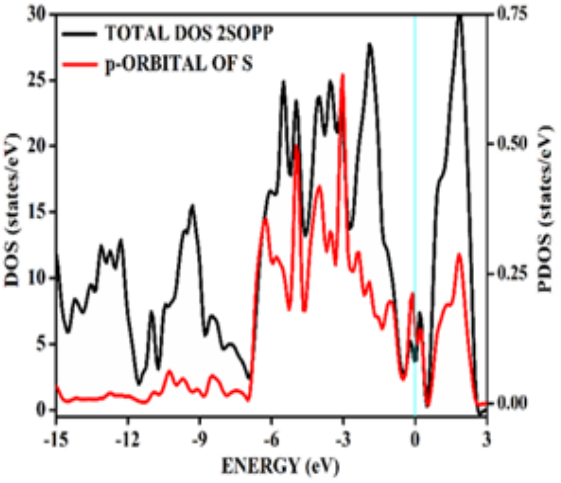
TOTAL DOS 2SOPP
p-ORBITAL OF S
DOS (states/eV)
PDOS (states/eV)
ENERGY (eV)

(d3)

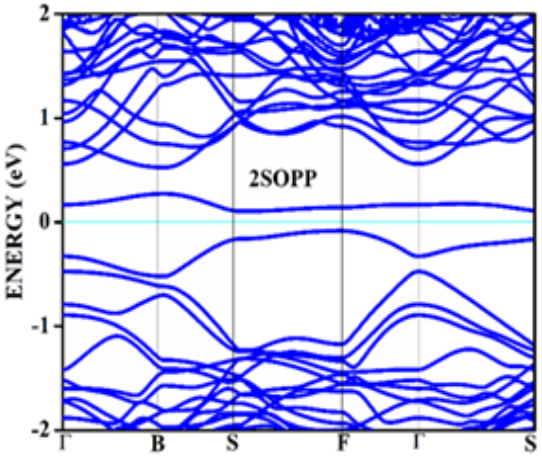
2SOPP
ENERGY (eV)
Γ B S F Γ S

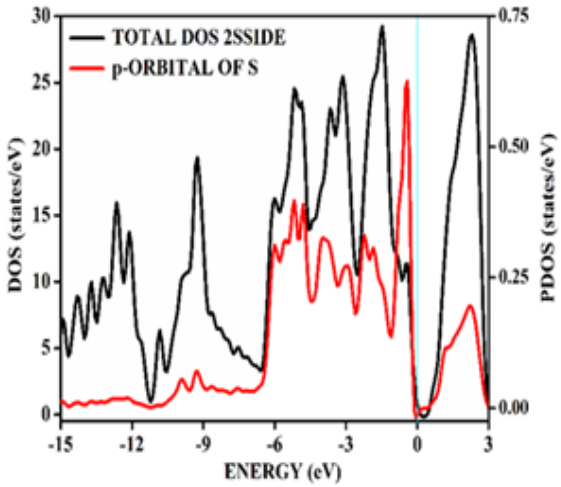
TOTAL DOS 2SSIDE
p-ORBITAL OF S
DOS (states/eV)
PDOS (states/eV)
ENERGY (eV)

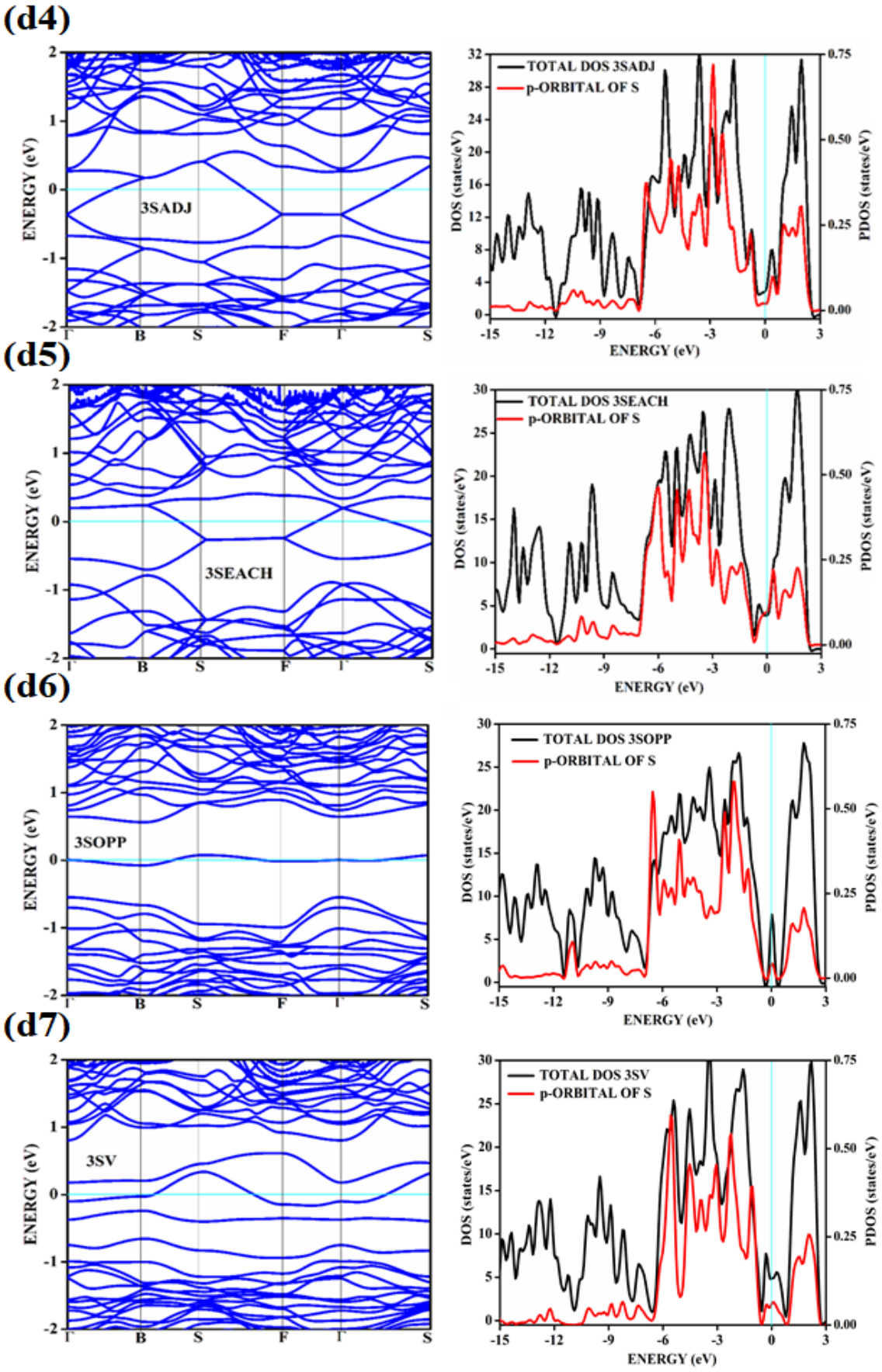

Fig. 7.9. The band structure and the corresponding density of states of sulphur-doped

phosphorene (d1) 2SADJ (d2) 2SSIDE (d3) 2SOPP (d4) 3DADJ (d5) 3SEACH (d6) 3SOPP (d7) 3SV. The cyan color represents the Fermi level; the red color represents the PDOS of the dopant.

7.2.1. Hydrogen cyanide adsorption

The relaxed lattice constants of pure phosphorene are determined to be a = 13.35 Å and b = 9.95 Å, which is in excellent accord with earlier studies [37], using a 3×3 supercell of the phosphorene layer. First, the HCN molecule is simulated in a variety of positions and orientations above the phosphorene to find the most energetically stable adsorption arrangements. To find the optimal orientation for the HCN gas molecule, we tested two perpendicular (with the H atom facing up or down) orientations and one parallel to the substrate. Figure 7.10(a)-(f) shows the energetically preferred adsorption configurations of HCN molecules adsorbed on undoped and N-doped phosphorene substrates, respectively.

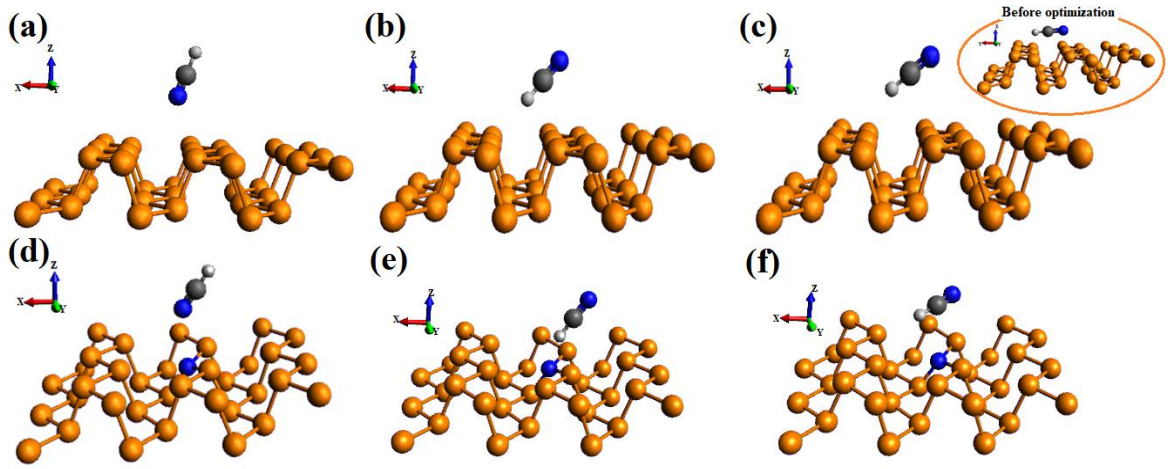

Fig. 7.10. The optimized geometries upon HCN adsorption on the phosphorene surface with different orientations (a) HCN/BP/N (b) HCN/BP/H (c) HCN/BP/C (d) HCN1N/N (e) HCN/1N/H (f) HCN/1N/C. The dopant nitrogen is shown in blue color.

Figure 7.10 shows different optimized geometries for different orientations of HCN for adsorption on pristine and N-doped phosphorene. The orientation HCN with H-atom near the surface is designated as HCN/BP/H. Similarly, nitrogen or carbon near the phosphorene

surface are defined as HCN/BP/N and HCN/BP/C, respectively. As such, the designation for N-doped phosphorene for different orientations of HCN on the surface is named accordingly as HCN/1N/H (H near to the surface), HCN/1N/N (N near to the surface) and HCN/1N/C (C near to the surface). To obtain a quantitative description of the interaction strength of gas molecules on phosphorene sheets, we calculate the adsorption energy (E_{ad}) with the help of Eq. 2.47, and the 'd' indicates the minimum distance between the gas molecule and substrate. In addition, we also calculate the Bader charge transfer (ρ) with the help of Eq. 2.48 between the gas molecule and substrate. The results obtained are summarized in Table. 7.2.

Table 7.2. The adsorption energy, band-gap, and distance between adsorbate and adsorbent for different orientations of HCN on phosphorene and nitrogen-doped surface. The distances, 'd' given in the table denote the minimum distance between the adsorbate and the surface.

Orientation	**Adsorption energy (eV)**	**Distance (Å)**	**Band-gap (eV)**	**Charge transfer (e)**
HCN/BP/H	-0.269	1.8	0.84	-0.19
HCN/BP/C	-0.270	2.6	0.83	-0.17
HCN/BP/N	-0.198	2.6	0.80	-0.15
HCN/1N/H	-0.276	1.8	0.86	0.23
HCN/1N/C	-0.259	2.1	0.85	0.22
HCN/1N/N	-0.180	2.6	0.84	0.20

A.E = adsorption energy, d = distance between adsorbate and adsorbent, B.G. = band-gap

Adsorption of a single HCN molecule onto pure phosphorene is seen in Figure 7.10(a), where the molecule is about in the middle of the puckered honeycomb with the H atom pointing to the surface. Distance (d) between hydrogen and phosphorene (1.8 Å) is greater than the sum of covalent radii of hydrogen and phosphorus (1.43 Å) in an earlier study [38]. Additionally, the charge transfers between HCN and pure phosphorene is -0.19 e, which is moderate and

therefore advantageous for any detection. For the HCN molecule and phosphorene, the E_{ad} is determined to be -0.269 eV, which is large enough to create a strong hydrogen bond, substantially greater than typical physisorption conditions [39]. The E_{ad} (-0.276 eV) and (0.23 e) in the N-doped phosphorene system are in striking contrast to those of impurity-doped phosphorene. Furthermore, as shown in Figure 7.10(d), after structural optimization, the hydrogen atom relocates to the top of the doped N atom with the shortest distance of 1.8 Å, which is close to the sum of the covalent atomic radii of H-N (1.07 Å). We find that the obtained adsorption energies of HCN molecule on pristine and N-doped phosphorene are large enough that they are similar to the situation of HCN on a graphene substrate, as shown in Figure 7.11, suggesting a great level of sensitivity for the HCN detection [40].

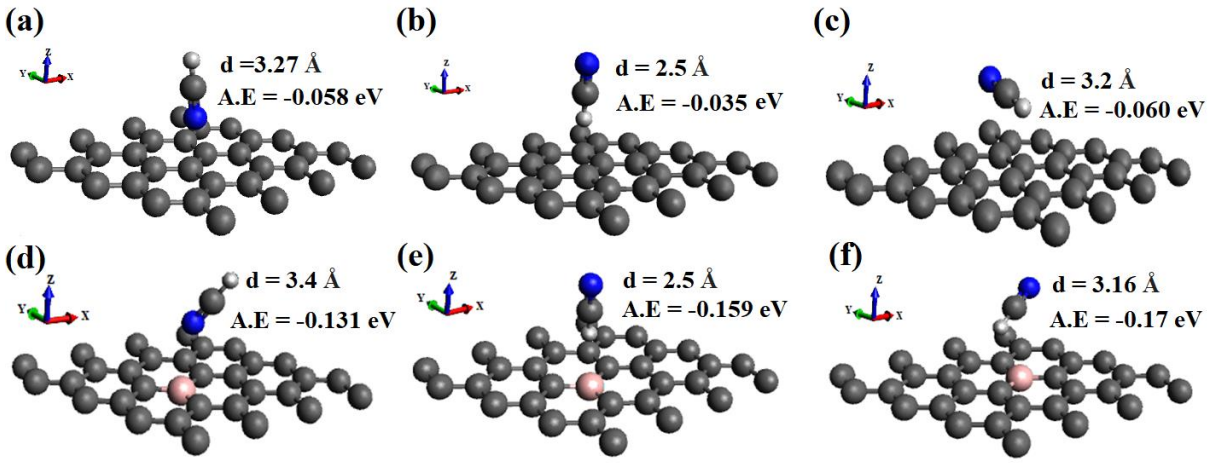

Fig. 7.11. The optimized geometries upon HCN adsorption on graphene surface with different orientations (a) HCN/G/N (b) HCN/G/H (c) HCN/G/C (d) HCN/1B/N (e) HCN/1B/H (f) HCN/1B/C. The dopant boron is shown in pink color, and blue color represents nitrogen.

Figure 7.11 shows the adsorption of HCN on graphene and boron-doped graphene with different orientations of HCN. Here, the adsorption of HCN on pristine graphene with the orientation of the N-atom of HCN close to the surface is designated as HCN/G/N, similarly, the orientation of HCN with H- or C-atom close to the surface is defined as HCN/G/H and HCN/G/C respectively. A similar designation is followed for different orientations of HCN on

boron-doped graphene as HCN/1B/N (N-atom of HCN is near to the surface), HCN/1B/H (H-atom of HCN is near to the surface) and HCN/1B/C (C-atoms of HCN is near to the surface). By comparing the band structures of phosphorene substrates with and without HCN gas molecule adsorption, as illustrated in Figure 7.12(a)-(c), we have investigated the impact of HCN orientations adsorption on the substrates' electronic characteristics. The 0.80 eV value for the band-gap of pure phosphorene is in agreement with previous DFT simulations of pristine phosphorene [31]. As seen in Figure 7.12(a), the band-gap after HCN adsorption is only slightly more significant than the band-gap value of free phosphorene at 0.84 eV, depending on the orientation of HCN. Moreover, as plotted in Figure 7.12(c), in sharp contrast with the DOS of pristine phosphorene, the adsorption of HCN on phosphorene can trigger an evident DOS peak in the energy range of -3 to -5 eV. The prominent electronic properties changes of phosphorene after HCN adsorption indicate that the pristine phosphorene has good sensitivity to HCN gas molecules.

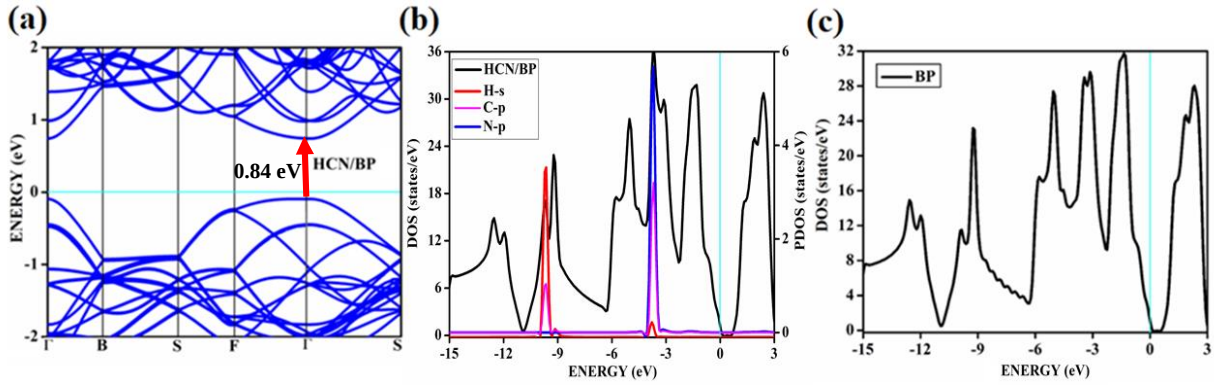

Fig.7.12. The band structures and DOS of phosphorene before and after adsorption of HCN. (a) Band structure of HCN/BP (BP – Black Phosphorene) (b) Total Density of States (DOS) of HCN/BP (c) DOS of BP. The cyan color represents the Fermi level.

In addition, to get a deeper insight into the interaction mechanism between HCN molecules and substrates, we also calculate the Bader charger difference analysis, computed using Eq. 2.48. As shown in the inset of Figure 7.13, the golden yellow spots and green region represent the charge accumulation and depletion, respectively. It is clear to see that there is a

charge accumulation close to the phosphorus atom between the gas molecule and phosphorene. However, it also shows a slight charge depletion around the H atom of the gas molecule. Besides, the Bader charge transfer of the H, C, and N atoms are 0.023 e, -0.018 e, and -0.197 e, respectively. The positive value of 0.023 e indicates that the charge of the H atom is decreased after the HCN gas adsorbs on the pristine phosphorene.

The electronic properties of N-doped phosphorene surfaces are explored to gain insight into the bonding between the HCN molecule and N-doped phosphorene. Of all the orientations of HCN on N-phosphorene, the case where the hydrogen atom of HCN is near to nitrogen dopant (Figure 7.10(d)) shows the best results among the three, as HCN being acidic, tends to react with base nitrogen dopant to form cyanide ions. Figure 7.14 displays the band structure, DOS, and PDOS calculations for the HCN on the N-doped phosphorene system. Between -3 and -5 eV, there is abundant evidence of orbital hybridization between H-1s and N-2p orbitals. The discussion of the charge density differential helps to elucidate the mechanism of interaction between the HCN molecule and the N-doped phosphorene. Because of the charge transfer (0.23 e) between N-doped phosphorene and the HCN molecule, the charges are redistributed across the molecule, as illustrated in the top inset of Figure 7.15. The range of redistribution is also substantially broader in contrast to pure phosphorene. Thus, we foresee HCN and N-doped phosphorene interacting more favorably than pristine phosphorene. The resistivity of the substrates ought to be modified due to the charge transfer generated by the HCN adsorption. The change of resistance is a critical factor in determining the sensing performance of the substrate materials. Herein, we mainly focus on the nitrogen-doped phosphorene with and without HCN gas molecule adsorption. The above analysis shows that the nitrogen-doped phosphorene may be a potential candidate for HCN sensing.

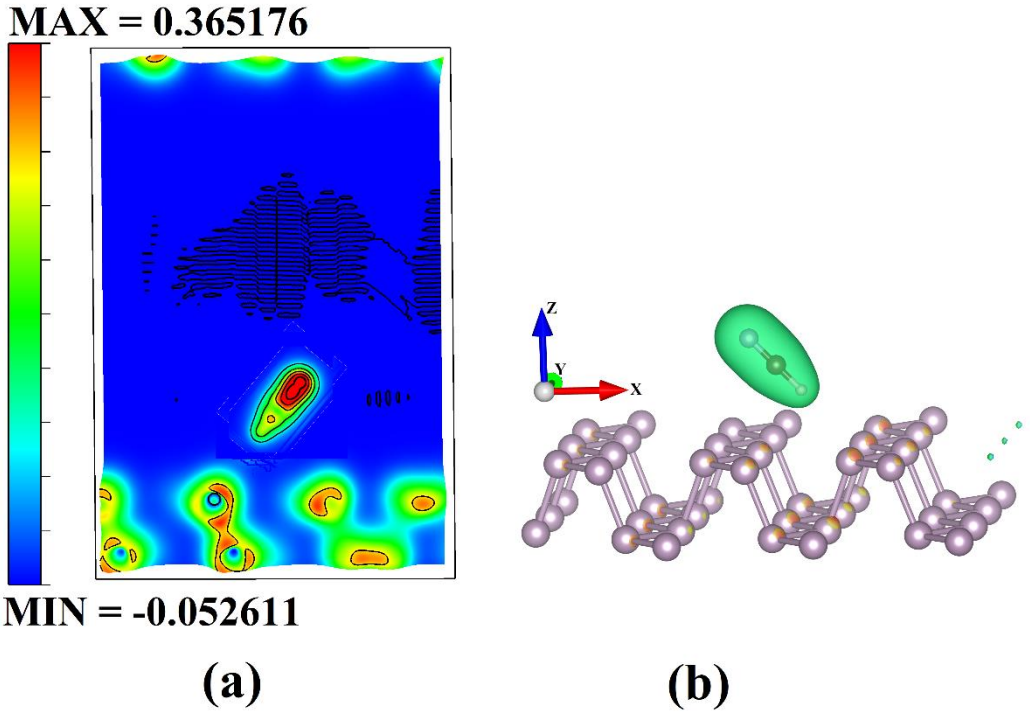

Fig. 7.13. The difference charge density plots of HCN on pristine phosphorene (a) Contour plot (b) 3D representation. The unit of the isovalue is e/Å^3.

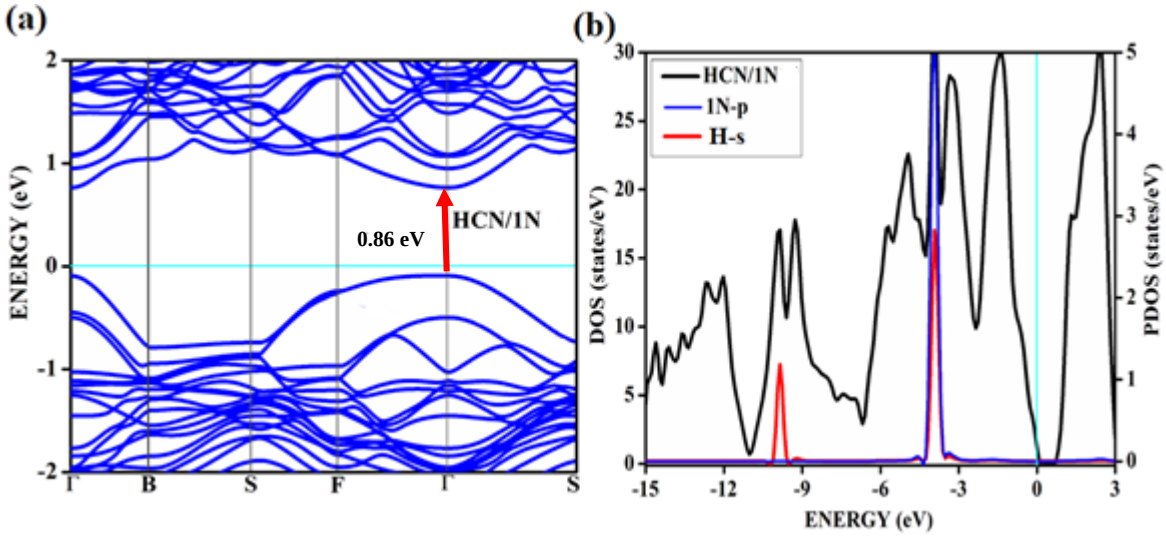

Fig. 7.14. The band structure and density of states along with the partial density of states (PDOS) upon adsorption of HCN on N-doped phosphorene (a) Band structure of HCN adsorbed on N-phosphorene (b) DOS of HCN/1N, the red line shows the PDOS of HCN's H-atom s-orbital and blue line represents p-orbital of nitrogen.

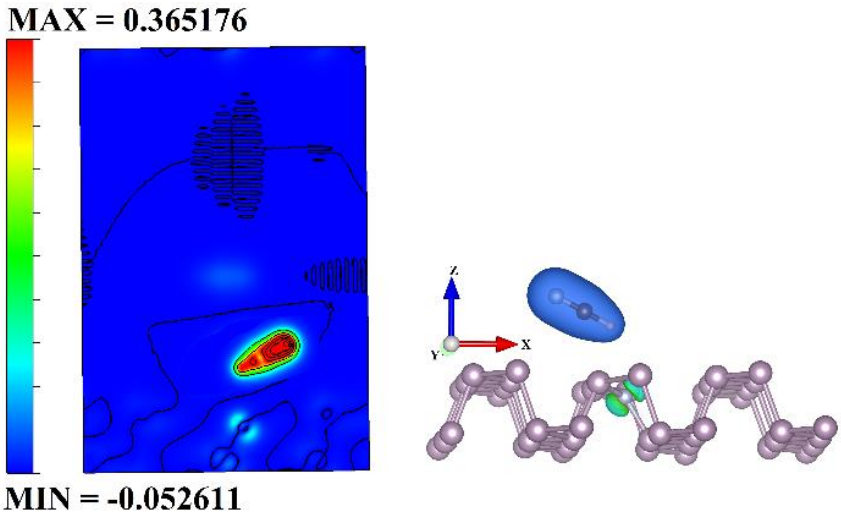

Fig. 7.15. The difference charge density plots of HCN on nitrogen-doped phosphorene (a) Contour plot (b) 3D representation. The unit of the isovalue is e/Å^3.

The study indicates that the adsorption of HCN gas molecules significantly impacts the transport efficiency of the N-doped phosphorene. Charge transfer from the phosphorene to the HCN gas molecules under study is evidence of substrate oxidation and target gas reduction, as mentioned above. Also, N-doped phosphorene is a p-type semiconductor. Therefore, hole carriers predominate. While the band-gap does fall from 0.90 eV before the adsorption of HCN to 0.86 eV after the adsorption of HCN, the concentration of hole carriers is considerably increased, suggesting changes in transport properties. Because of the charge transfer between the HCN gas molecule and the phosphorene substrate, the conductivity of the HCN/N-phosphorene system changes at a considerably faster pace than that of HCN/pristine phosphorene. Based on our findings, we infer that N-phosphorene is a promising material for HCN detection due to its high sensitivity.

7.2.2. Hydrogen isocyanide adsorption

Our study also includes a simulation of the HNC molecule, an isomer of the HCN molecule, adsorbed on the phosphorene substrates to investigate its adsorption on N-doped phosphorene. Figure 7.16 displays the adsorption configurations of HNC molecules that are most

energetically advantageous for adsorption on both undoped and N-doped phosphorene substrates. Table 7.3 shows the results of the computations for E_{ad}, d, and Q.

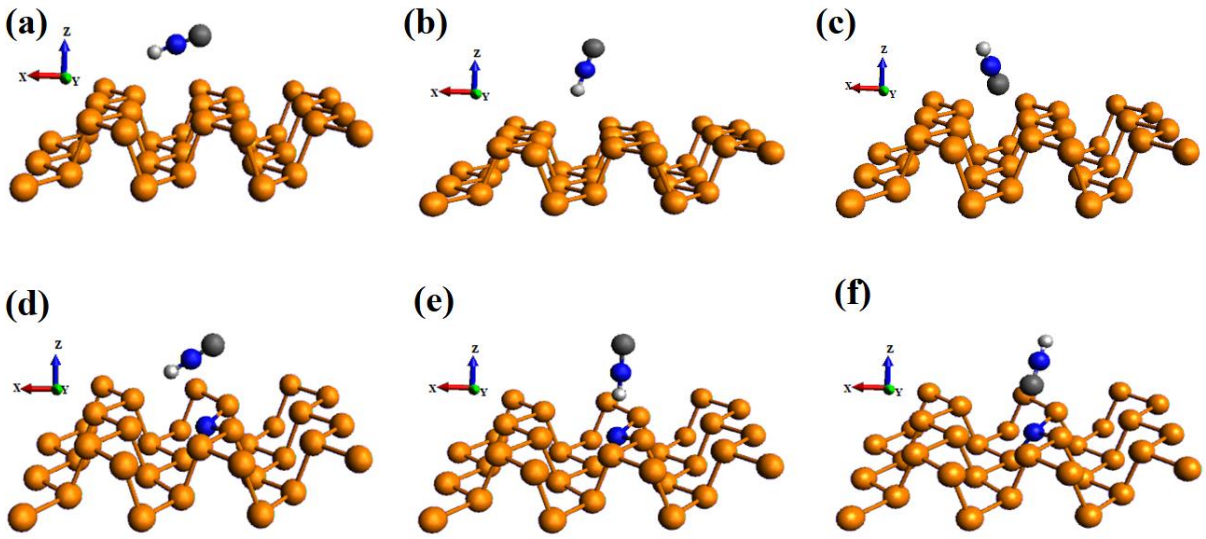

Fig. 7.16. The optimized geometries upon HNC adsorption on the phosphorene surface with different orientations (a) HNC/BP/N (b) HNC/BP/H (c) HNC/BP/C (d) HNC/1N/N (e) HNC/1N/H (f) HNC/1N/C. The dopant nitrogen is shown in blue color.

In Figure 7.16, different optimized geometries for different orientations of HNC for adsorption on pristine and N-doped phosphorene are shown. The orientation HNC with the H-atom near the surface is designated as HNC/BP/H. Similarly, N or C near the phosphorene surface are defined as HNC/BP/N and HNC/BP/C, respectively. As such, the designation for N-doped phosphorene for different orientations of HNC on the surface is named accordingly as HNC/1N/H (H near to the surface), HNC/1N/N (N near to the surface) and HNC/1N/C (C near to the surface).

Table 7.3. The adsorption energy, band-gap, and distance between adsorbate and adsorbent for different orientations of HNC on pristine phosphorene and nitrogen-doped phosphorene.

Orientation	**Adsorption energy (eV)**	**Distance (Å)**	**Band-gap (eV)**	**Charge transfer (e)**

HNC/BP/H	-0.503	2.0	0.84	-0.20
HNC/BP/C	-0.455	2.4	0.82	-0.19
HNC/BP/N	-0.355	2.6	0.82	-0.19
HNC/1N/H	-0.359	2.1	0.83	0.242
HNC/1N/C	-0.352	3.3	0.81	0.236
HNC/1N/N	-0.363	2.6	0.81	0.217

As shown in Figure 7.16(a), the HNC molecule occupies a central position in the hexagonal honeycomb structure of the pristine phosphorene surface. The diagonal orientation of HNC to the surface with H towards down gives the best results with an E_{ad} of -0.503 eV, a distance (d) of 2.0 Å, and a band-gap of 0.84 eV, as shown in Figure 7.17. The obtained distance is larger than the sum of the covalent radii of the hydrogen and phosphorus atoms (1.43 Å). Strong hydrogen bond formation between the HNC molecule and phosphorene is seen as the E_{ad} is high enough and exceeds the criteria for various types of physisorption. In addition, a charge transfer of -0.20 e is noted between phosphorene and HNC molecule. The significant adsorption energy of -0.359 eV shows strong adsorption between HNC molecule and N-doped phosphorene. A charge transfer of 0.24e between HNC (orientation with hydrogen atoms near to the surface) and doped phosphorene surface is observed. As shown in Figure 7.18, adsorption of HNC in all the surface orientations reduces the band-gap of N-phosphorene. These numerical findings demonstrate that the N-doped phosphorene substrate physisorps the HNC molecule and could be a promising metal-free catalyst for HNC degradation.

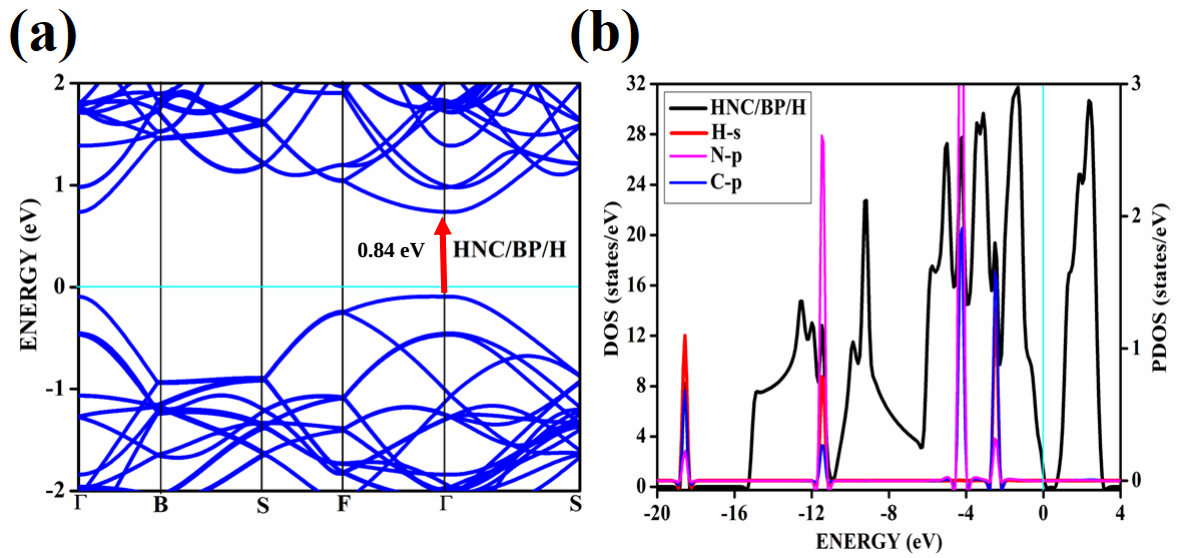

Fig. 7.17. The band structure and density of states along with the partial density of states (PDOS) upon adsorption of HNC on phosphorene (a) Band structure of HNC adsorbed on phosphorene (b) DOS of HNC/BP, the red line shows the PDOS of H-atom s-orbital and the blue line represents p-orbital of carbon and magenta represents p-orbitals of nitrogen.

The band structure of the HNC molecule on the N-phosphorene system, together with the corresponding DOS, is calculated and shown in Figure 7.18. By comparing the band structures of N-doped phosphorene surface with and without HNC gas molecule adsorption, as illustrated in Figure 7.18(a)-(c), we have investigated the impact of HNC orientations adsorption on the N-doped phosphorene surface electronic characteristics. As can be seen in Figure 7.18(a), after the adsorption of the HNC gas molecule on the N-phosphorene substrate, the band-gap of the HNC/N-phosphorene system is calculated to be 0.83 eV, which is only 0.07 eV smaller than that of the band-gap of nitrogen-doped phosphorene (0.90 eV). Moreover, as plotted in Figure 7.18(b), it demonstrates that the HNC gas molecule adsorption has a slight effect on the DOS of N-phosphorene, with minor DOS enhancement in the energy range of 0 to -2 and -3 to -6 eV. These slightly enhanced peaks show the interaction of H-1s on the N-doped phosphorene surface. The prominent electronic properties changes of N-doped phosphorene after HNC adsorption indicate that the N-doped phosphorene has good sensitivity

to HCN gas molecules.

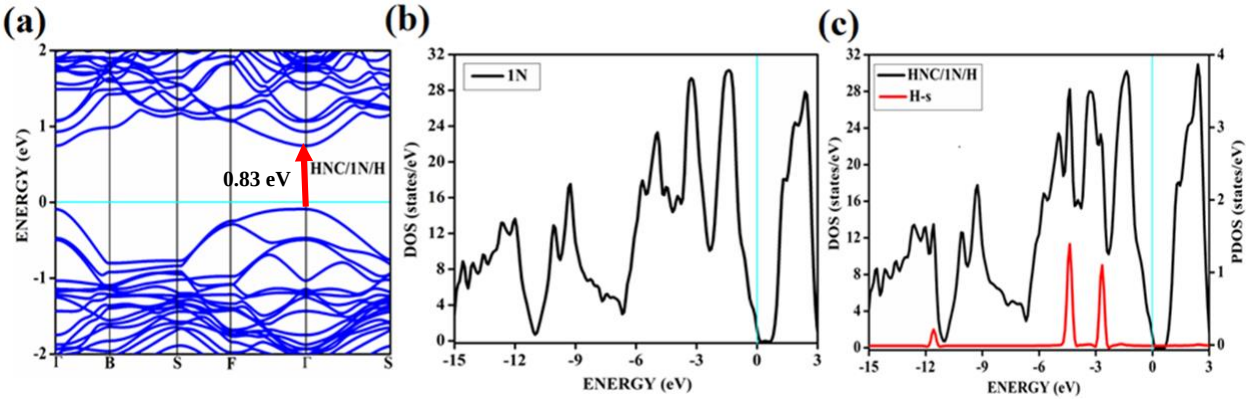

Fig. 7.18. The band structure and DOS of HNC on adsorption of N-phosphorene (a) Band structure of HNC on N-doped phosphorene (b) DOS of N-doped phosphorene (c) DOS and PDOS of HNC on N-doped phosphorene. The red line represents the hydrogen atom's orbital. The cyan line represents the Fermi level.

We compute the charge density difference of pure phosphorene with HNC adsorption and HCN on N-phosphorene to investigate the interaction mechanism between the two molecules. After the adsorption of the HNC molecule on the N-phosphorene substrate, the charges are relocated, as illustrated in the inset of Figure 7.19, establishing that the HNC molecule is adsorbed on the N-phosphorene substrate. However, it does not show any bond formation.

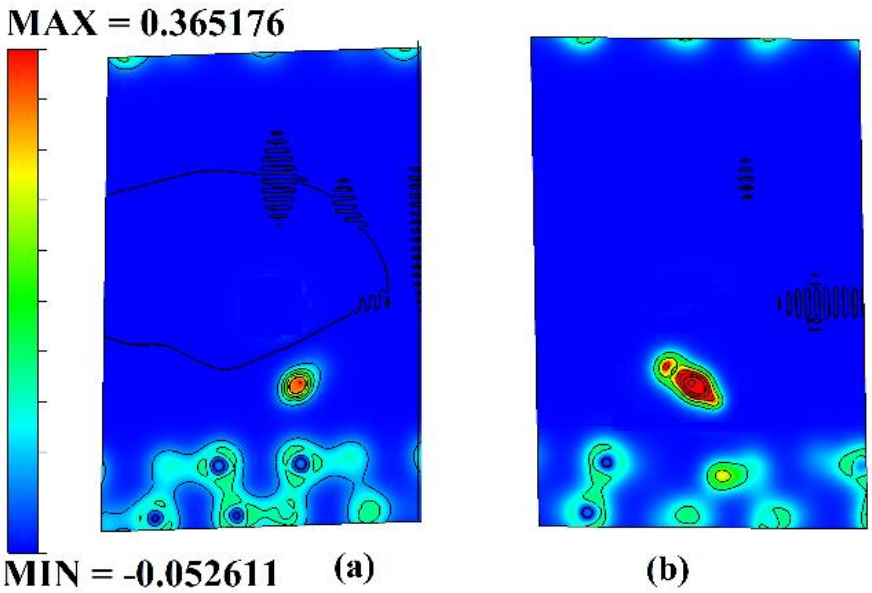

Fig. 7.19. The difference charge density plots of HNC on pristine and nitrogen-doped phosphorene (a) Contour plot of HNC on pristine phosphorene (b) Contour plot of HNC on N-phosphorene. The unit of the isovalue is e/Å^3.

As mentioned above, HCN and HNC gas molecules adsorb on pristine phosphorene systems and nitrogen-doped phosphorene with distinct physisorption properties. The resulting material, N-phosphorene, exhibits better properties than pristine phosphorene in sensing HCN and HNC, as discussed above (the band-gap shifts by 0.04 and 0.07 eV, respectively, upon adsorption of HCN and HNC).

7.3. Conclusion

The present study employs ab initio density functional calculations to investigate the electronic characteristics of phosphorene that has substitutionally doped with group B, N, S, and Si elements. Our research has revealed that dopants belonging to group of S and Si, possessing an even number of valence electrons, exhibit metallic properties. Conversely, dopants belonging to group boron and nitrogen, having an odd number of valence electrons, retain their semiconducting properties. The manifestation of distinct electronic properties in doped phosphorene based on equality is attributed to the robust s-p orbital hybridization between the dopants and the phosphorene. In continuation of our investigation into the metallic-semiconducting conflict, as determined by valence electrons, we have analyzed various doping patterns with total concentrations of 2.7%, 5.5%, and 8.3%.

Among the dopants mentioned above, it has been observed that nitrogen at a concentration of 2.7% yields optimal outcomes, characterized by an augmented band-gap of 0.90 electron volts and a semiconductive disposition. Subsequently, a thorough examination of the adsorption of HCN and HNC gases on intrinsic phosphorene and nitrogen-doped phosphorene are conducted through first principles DFT computations. The outcomes of our study reveal that the phosphorene doped with nitrogen impurities manifests distinct sensing

traits towards HCN or HNC gases. Among the various orientations of HCN and HNC, it has been established that the adsorbate exhibiting favorable adsorption characteristics with both pristine phosphorene and nitrogen-doped phosphorene is the one positioned perpendicular to the surface, with the hydrogen atom oriented downwards. In its unadulterated state, Phosphorene exhibits a visible susceptibility to HCN and HNC gases, demonstrating a moderate degree of adsorption energy and adsorption distance. Of crucial significance, the band structure elucidates that the electronic conductivity of unadulterated phosphorene has been considerably augmented after the adsorption of HCN or HNC gas, thereby developing the increased reactivity of the phosphorene sensor to HCN and HNC gas molecules.

The outstanding phosphorene material showcases commendable efficacy and remarkable sensitivity and selectivity, positioning it as a promising contender for distribution as a sensor for HCN and HNC gases. The introduction of nitrogen atoms into phosphorene results in a marked reduction in its reactivity towards HCN and HNC gases, with the formation of physical bonds. As such, N-doped phosphorene may be a metal-free catalyst for HCN or HNC adsorbate activation and catalysis. Doping phosphorene with nitrogen of high concentrations and configurations is only helpful in improving HCN or HNC sensing performance as the surface is unstable. Additionally, doping phosphorene with B, S, or Si is unnecessary since it does not improve the stability of the surface performance, although these elements are semiconducting and metallic, respectively. In light of our computation, the unadulterated phosphorene exhibits considerable promise as a gas sensor, particularly in detecting hazardous gases such as HCN or HNC.

Chapter 8

Conclusions and future scope

8.1. Summary and conclusions

Gas detection technology is now gaining recognition as a significant use for smart devices and is attracting growing interest from both business and academia. The detection and monitoring of gaseous species released during industrial and greenhouse processes have become increasingly important due to environmental concerns. These activities are crucial in various fields, such as environmental monitoring, industrial chemical processing, public safety, food production, agriculture, medicine, and indoor air quality control. The current gas sensors based on metal oxide semiconductors often face challenges such as extended recovery times, limited selectivity, and high operating temperatures. These limitations have hindered their use in dynamic gaseous environments with quickly changing conditions. Therefore, there is a growing need for materials that can detect toxic gaseous species with high sensitivity and selectivity.

Graphene, an ultra-thin layer of carbon atoms organized in a hexagonal crystal lattice, has shown significant potential in gas sensing due to its exceptional structural and electrical characteristics. Graphene derivatives, including graphene oxide and reduced graphene oxide, possess notable features such as a large surface area, chemically reactive sites, and adjustable chemical and electronic properties. These attributes have been shown to offer enhanced gas sensing capabilities compared to pristine nanostructured metal oxide, carbon nanotubes (CNTs), and conductive polymers. Although both carbon-based nanomaterials, such as CNTs and graphene, exhibit unique electronic properties that make them suitable for potential gas sensing applications, the observed higher sensitivity of graphene-based materials compared to CNTs can be attributed to their larger surface area per unit volume. This increased sensing area is due to the two-dimensional structure of graphene, in contrast to the one-dimensional structure of CNTs.

Additionally, the planar configuration of graphene renders it more conducive for use in

conventional microlithography techniques, facilitating the integration of graphene devices compared to CNTs. Through more progress, it has been discovered that the alteration of the surface of graphene has shown to be very effective in attaining heightened sensitivity and offering selectivity towards a specific gas. Some previous studies show that incorporating dopants on the surface of graphene improved the detection limit and reaction time at ambient temperatures. These are crucial for enhancing the performance of gas adsorption systems.

The investigation of graphene-gas molecule adsorption systems has shown the presence of weak physisorption between gas molecules and intrinsic graphene. This discovery presents a significant obstacle to using graphene-based gas sensors for future applications. Both practical and theoretical investigations have shown that the efficacy of graphene's interactions with gas molecules may be enhanced via heteroatom doping. Computational quantum mechanical calculations can be employed for studying gas adsorption on intrinsic and hetero-atom doped graphene. This approach enhances our understanding of the fundamental processes governing sensing mechanisms and assists in pinpointing optimal doping strategies for graphene, thereby facilitating the further advancement of gas sensors.

This thesis aimed to examine the impact of gas molecule adsorption on intrinsic and heteroatom-doped graphene's structural and electronic properties. The objective is to analyze how doping affects the susceptibility of graphene towards gas molecules and to explore the potential of graphene's unique characteristics in developing susceptible gas sensors for practical applications in gas detection.

The structural properties of B- and N-doped graphene are first analyzed using DFT-based methods. The analysis considered different doping mole fractions and configurations. The results revealed that the planar hexagonal structure of the graphene sheet remained unaffected following B- and N-doping, but significant alterations were observed in the bond lengths. The cohesive energies of the doped graphene systems tend to increase as the doping concentration

increases, resulting in a reduction in the energetic stabilities of the doped systems with higher doping levels. The stability of N-doped graphene structures is greater than that of their B-doped counterparts. The cohesive energies of graphene structures with dopant atoms positioned at alternating sublattices are the lowest across all doping concentrations. Consequently, these structures exhibit the highest level of stability. The arrangement of dopant atoms on various sites on the surface determines the stability and band-gap opening.

The investigation of the electronic configurations of graphene supercells containing several B- or N-atoms has shown the presence of non-zero band gaps near the Dirac point. The calculations indicate that all graphene systems doped with B and N have shown both p-type and n-type semiconducting characteristics, regardless of the presence or absence of band gaps. Graphene is doped with boron and nitrogen of 3.12, 6.25, and 9.37% of doping concentrations and different patterns of doping configurations. These observations are based on the specific doping concentrations and configurations. The highest band gap is seen when the dopant atoms occupy the same sublattice, whereas a minimal band gap is observed when the dopants are situated on alternating sublattice positions. The band structures of graphene supercells with B and N co-doping do not drastically change the band gap and doping configurations. The findings derived from the first-principles simulations demonstrate that the band gap of graphene can be carefully modified by incorporating B- and N-dopants.

This study investigates the adsorption behavior of several small gas molecules (NH_3, CO, NO, NO_2, N_2O, O_2, HCN, and HNC) on intrinsic and chemically modified graphene surfaces with B- and N- doping, bilayer, and phosphorene surfaces. DFT calculations are used to analyze the adsorption properties to explore the possible application of these materials as effective adsorbents for harmful gases. The addition of 6.25% boron doping did not exhibit significant improvement in CO adsorption, and it has been reported that the 'd1' configuration doped with 9.37% boron demonstrates the ability to adsorb CO molecules. Consequently,

increasing graphene's doping concentration with boron may serve as a CO sensor. Among several configurations, we find that a few configurations with 9.37% have shown the most favorable outcomes in N-doped graphene. The adsorption of ammonia is most effectively seen on a boron-doped graphene system, as well as on nitrogen-doped graphene in a few patterns. These configurations have resulted in an enhanced band gap and improved adsorption capabilities. The adsorption of NO and NO_2 significantly impacts B-doped graphene's structural and electronic characteristics, mainly owing to the strong interactions between the molecules and the graphene material. Therefore, it is plausible to consider using B-doped graphene as an effective gas sensor for detecting NO and NO_2 molecules. The significant adsorption energies and close binding distances observed for NO_2 and NO on B-doped graphene suggest the occurrence of chemisorption with chemically modified graphene. The Bader charge analysis, examination of electronic band structures, and evaluation of the density of states for CO-, NH_3-, NO-, and NO_2-adsorbed-doped graphene systems have provided evidence that the electronic characteristics of B- and N-doped graphene are influenced by the presence of CO, NH_3, NO, and NO_2 molecules. The flat band phenomenon occurs in B-doped graphene configurations when paramagnetic gas molecules, such as NO and NO_2, adsorb. DFT calculations were conducted to examine the adsorption of N_2O on graphene sheets with different dopants (intrinsic, heteroatom-doped with boron, nitrogen, and boron-nitrogen co-doping). These calculations aimed to evaluate the impact of these dopants on the gas-sensing capabilities of graphene towards N_2O.

The calculations revealed weak interactions between N_2O and the intrinsic, boron-doped, nitrogen-doped, and boron-nitrogen co-doped graphenes. The findings indicate that intrinsic graphene and graphene doped with B, N, and co-doped with both B and N exhibit a lack of sensitivity towards the N_2O molecule. The inclusion of an N-dopant in the graphene structure was seen to enhance the interaction between graphene and N_2O significantly. Reasonable

values for the sensitivity of N_2O on B-doped graphene have been obtained from calculations using Drude's formula. Although there is a slight change in the band gap after the adsorption of these molecules onto chemically treated graphene surfaces, the examination of charge distribution, band structure, and density of states (DOS) plots for B-doped graphene, reveals that the adsorption of individual NO, NO_2, and N_2O molecules significantly influences the electronic characteristics of B-doped graphenes. The findings further suggest that B-doped graphene exhibits optimal characteristics as sensing materials for detecting N_2O gas.

The present study used spin-polarized density functional calculations to investigate the adsorption behavior of O_2 on B-doped graphene in both singlet and triplet states. The primary objective was to assess the susceptibility of B-doped graphene to O_2 molecules present in the ambient air. The singlet oxygen has shown the chemisorption of O_2 on B-doped graphene with oxetane-like ring formation where triplet is physisorbed on all configurations of B-doped graphene. The dramatic change of atomic and electronic structures of B-doped graphene by the adsorbed O_2 molecule reveals the sensitivity of B-doped graphene to O_2, which affects its sensing towards other harmful gases and thus the potential usage of B-doped graphene as toxic gas sensors. From this analysis, we can clearly distinguish between O_2 in singlet and triplet states with the help of B-doped graphene.

To investigate the effect of ammonia on layered graphene, we have chosen bilayer AB stacked graphene over AA stacking, as AA bilayer is less stable and known to exhibit metallic properties. With the help of first principle calculations, we have followed the doping patterns of boron similar to that in the monolayer studies. The results show that the boron and nitrogen doped monolayer graphene shows high band gaps and acts better for the adsorption of gas molecules compared to bilayers. The advantage of bilayer graphene over monolayer graphene is that they have less formation energy.

We have investigated other 2D materials for gas adsorption, which is in the subsequent

advance to graphene, i.e., phosphorene. Though the research on phosphorene has yet to be in progress, our findings show that phosphorene is also a potential surface for gas adsorption. The doping effects of phosphorene with different heteroatoms show anomalous features. Doping with odd valence electrons preserves semiconducting nature; even electron dopant causes metallic nature. We have studied other heteroatom dopants with different concentrations and patterns and inferred that single-doped nitrogen shows the best results. We have used single-doped phosphorene to study the adsorption of HCN and HNC and found that phosphorene is an excellent sensor for these molecules.

8.3. Gaps covered in our research

Despite the potential of pristine graphene, graphene oxide, and reduced graphene oxide as gas sensing platforms for detecting gases at room temperature, they are significantly influenced by various gas species and exhibit slow recovery and inadequate electrical stability in diverse environmental conditions. One potential approach to address this issue involves chemically modifying graphene or reducing graphene oxide by introducing defects, dopants, metal or metal oxide nanoparticles, and polymers. These modifications have demonstrated promising results in enhancing the sensing capabilities of these materials, including increased specificity, improved sensitivity, and lowered detection limits.

Various methods for band gap engineering have been examined in the existing body of literature. These methods include intrinsic approaches, such as substitutional doping, and extrinsic approaches, including the adsorption of different species onto 2D nanomaterials like graphene. However, most prior research has focused chiefly on using metals or transition metals for doping. Furthermore, the investigation of electronic modifications induced by adsorption necessitates the thorough examination of metal-free doping. In this regard, a comprehensive investigation explores methods for opening band gaps while minimizing disruption to the two-dimensional surface structure and the band structure around the Fermi

level.

Furthermore, the investigation of the dispersion of the band structure in the vicinity of the Fermi energy still needs to be explored. Further research is required to investigate the alterations in electronic structure and its dependence on the number of layers and doping of the layers. This aspect has been addressed in our ongoing research endeavors.

Despite few contributions, there has been a need for comprehensive investigations covering several adsorption sites, varying concentrations of dopants, and diverse surface patterns. The investigation of doping with different mole fractions and its influence on the adsorption properties of these surfaces has yet to be undertaken. Our research endeavors to examine the adsorption of these gases on different concentrations and geometries, marking it as a pioneering study in this field. Further investigation is required to understand the impact of changes in electronic structure on the sensitivity of the material to variations in layer count and doping. We have effectively addressed this knowledge gap by introducing boron and nitrogen doping at various concentrations and patterns to address this knowledge gap. Quantum mechanical calculations and atomic scale simulation tools have shown their efficacy in determining the appropriate functionalization of graphene for specific target analytes. This approach may be further applied to developing and simulating graphene-based sensing systems with increased capabilities.

Enhanced gas sensing capabilities in graphene may be accomplished by introducing certain heteroatoms, leading to a stronger affinity between the gas molecules and the graphene surface. Exposure to gases would lead to discernible alterations in the electronic conductivity of doped graphenes. Enhancing the selectivity of adsorption for gas molecule sensing is of utmost importance in several domains, such as environmental monitoring, chemical process control, agriculture, and medicinal applications. The investigation of transport features, such as conductivity changes resulting from adsorption, provides valuable insights into the nature

of the adatom. This aspect is thoroughly examined in our research. A limited body of research focused on examining the van der Waals effect in 2D heterolayers. Concerning this matter, an extensive examination is conducted to explore the electronic characteristics of the varying distances between the layers.

8.2. Future scope of work

The current significance of modeling nano-sensing devices using 2D materials is essential, as it offers the potential to investigate the fundamental sensing principles and evaluate sensor performance before costly experimental attempts. Investigating the electronic structure and quantum transport properties of electronic sensors based on 2D materials, both before and during their contact with gas molecules, has significance in advancing and producing innovative nano-sensors.

The primary advancement in materials science has been the recent application of the exciting properties of exfoliated 2D materials, including graphene, which distinguish them from their 3D counterparts. Two-dimensional (2D) materials can significantly impact various fields, such as electronics, optoelectronics, energy conversion and storage, and chemical and biological sensing, owing to their distinctive physical, electrical, and chemical characteristics. In addition to their helpful electrical properties for gas adsorption, gas sensors based on 2D materials have demonstrated high sensitivity in detecting a wide variety of gas molecules at low concentrations. This is due to their maximum sensor surface area per unit volume, low noise, and superior ability to screen charge fluctuations compared to 0D and 1D systems.

Despite significant progress in the domain of graphene-based gas sensors over the last decade, several enormous challenges must be addressed to satisfy the industry's growing need to develop high-performance gas sensors. Additionally, theoretical research must be expanded to comprehend the interaction mechanism between functional nano-hybrids based on graphene and various gases. This understanding will facilitate the experimental and device fabrication

processes crucial for developing improved sensors. Although there are investigations into doped and defective graphene systems, the literature on oxide–graphene and polymer–graphene hybrid systems are either scarce or nonexistent.

In addition, it is essential to research novel dopants, functional molecules, and manufacturing processes, considering sensitivity and selectivity as crucial performance measures. It is necessary to compare current sensing technologies based on graphene with other gas-sensing materials to identify superior ways. Therefore, it is probable that future research in gas sensor technology using graphene would prioritize the integration of graphene with other functional materials to enhance its activity.

It is seen that gases interact with 2D materials like rGO, MoS_2, phosphorene, and others very strongly. This makes the desorption process take a long time. Usually, UV light or high-temperature annealing is needed to help the materials release the gases. This problem with 2D material-based gas monitors needs to be fixed. It makes them less useful because it lowers their sensitivity, detection limit, and accuracy. Though the use of 2D materials to sense gases has already been used in the existing few studies, most had to be done in a controlled setting because other gases in the real world changed the sensitivity values. So, future research should focus on making ultra-high selective gas sense devices that can be used in real life with 2D materials. It was possible to apply the functionalization method to phosphorene, which had already worked very well for materials made from graphene.

Another problem is that it is not possible to make a lot of 2D things that are good quality and cover a lot of space. Because 2D materials have such good dynamic attributes, they could be used to make flexible electronics that work better with the device manufacturing process. Some of the studies discussed in the previous chapters show that the electronic properties can be altered by molecular adsorption on graphene. However, only a few reports are available on similar adsorption studies on phosphorene.

The discovery of 2D materials has started a new era of materials science. The calculations of properties of 2D infinite systems are state-of-the-art in computational materials science and condensed matter physics. Besides the obvious challenges such as the inclusion of structural and stoichiometric defects and doping of the surfaces, where electronic and optical properties depend on the lateral size of the 2D structures, another important problem is the interaction of the 2D materials with gas molecules present in their environment. The enormous progress in the field of 2D materials suggests that many of those challenges will be tackled near future. After addressing the above problems, and fully understanding the properties of 2D materials and their sensing mechanisms, with continued research efforts directed toward resolving these issues and attaining a comprehensive understanding of the properties of 2D materials and their sensing mechanisms, gas sensors based on 2D materials are poised to realize their full potential, offering unprecedented sensitivity, selectivity, and versatility in gas detection applications.

Annexures

Chapter 1

[1] G. Fiori, F. Bonaccorso, G. Iannaccone, T. Palacios, D. Neumaier, A. Seabaugh, S. K. Banerjee, L. Colombo, Electronics based on two-dimensional materials, Nat. Nanotechnol. 9 (2014) 768–779.

[2] Q. H. Wang, K. Kalantar-Zadeh, A. Kis, J. N. Coleman, M. S. Strano, Electronics and optoelectronics of two-dimensional transition metal dichalcogenides, Nat. Nanotechnol. 7 (2012) 699–712.

[3] K. S. Novoselov, A. K. Geim, S. V. Morozov, D. Jiang, Y. Zhang, S. V. Dubonos, I. V. Grigorieva, A. A. Firsov, A. A. F. K. S. Novoselov, A. K. Geim, S. V. Morozov, D. Jiang, Y. Zhang, S. V. Dubonos, I. V. Grigorieva, K. S. Novoselov, A. K. Geim, S. V. Morozov, D. Jiang, Y. Zhang, S. V. Dubonos, I. V. Grigorieva, A. A. Firsov, Electric Field Effect in Atomically Thin Carbon Films, Science. 306 (2004) 666–669.

[4] F. Schedin, A. K. Geim, S. V. Morozov, E. W. Hill, P. Blake, M. I. Katsnelson, K. S. Novoselov, Detection of individual gas molecules adsorbed on graphene, Nat. Mater. 6 (2007) 652–655.

[5] L. Kong, A. Enders, T. S. Rahman, P. A. Dowben, Molecular adsorption on graphene, J. Phys. Condens. Matter. 26 (2014) 443001.

[6] S. Prezioso, F. Perrozzi, L. Giancaterini, C. Cantalini, E. Treossi, V. Palermo, M. Nardone, S. Santucci, L. Ottaviano, Graphene oxide as a practical solution to high sensitivity gas sensing, J. Phys. Chem. C. 117 (2013) 10683–10690.

[7] J. T. Robinson, F. K. Perkins, E. S. Snow, Z. Wei, P. E. Sheehan, Reduced Graphene Oxide Molecular Sensors, Nano Lett. 8 (2008) 3137–3140.

[8] P. Miró, M. Audiffred, T. Heine, An atlas of two-dimensional materials, Chem. Soc. Rev. 43 (2014) 6537–6554.

[9] S. Z. Butler, S. M. Hollen, L. Cao, Y. Cui, J.A. Gupta, H. R. Gutiérrez, T. F. Heinz, S.

S. Hong, J. Huang, A.F. Ismach, E. Johnston-Halperin, M. Kuno, V. V. Plashnitsa, R. D. Robinson, R. S. Ruoff, S. Salahuddin, J. Shan, L. Shi, M. G. Spencer, M. Terrones, W. Windl, J.E. Goldberger, Progress, challenges, and opportunities in two-dimensional materials beyond graphene, ACS Nano. 7 (2013) 2898–2926.

[10] A. K. Geim, K. S. Novoselov, The rise of graphene, Nat. Mater. 6 (2007) 183–191.

[11] H. Liu, Y. Liu, D. Zhu, Chemical doping of graphene, J. Mater. Chem. 21 (2011) 3335–3345.

[12] N. Joshi, T. Hayasaka, Y. Liu, H. Liu, O. N. Oliveira, L. Lin, A review on chemiresistive room temperature gas sensors based on metal oxide nanostructures, graphene and 2D transition metal dichalcogenides, Microchim. Acta. 213 (2018) 185-189.

[13] G. Lu, L. E. Ocola, J. Chen, Reduced graphene oxide for room-temperature gas sensors, Nanotechnol. 20 (2009) 445502.

[14] Y. Dan, Y. Lu, N. J. Kybert, Z. Luo, A. T. C. Johnson, Intrinsic response of graphene vapor sensors, Nano Lett. 9 (2009) 1472–1475.

[15] Y. H. H. Zhang, Y. B. Bin Chen, K. G. G. Zhou, C. H. H. Liu, J. Zeng, H. L. L. Zhang, Y. Peng, Improving gas sensing properties of graphene by introducing dopants and defects: A first-principles study, Nanotechnology. 20 (2009) 185504.

[16] K. S. Novoselov, D. Jiang, F. Schedin, T. J. Booth, V. V. Khotkevich, S. V. Morozov, A. K. Geim, Two-dimensional atomic crystals, Proc. Natl. Acad. Sci. 102 (2005) 10451–10453.

[17] F. Yavari, N. Koratkar, Graphene-based chemical sensors, J. Phys. Chem. Lett. 3 (2012) 1746–1753.

[18] S. S. Varghese, S. H. Varghese, S. Swaminathan, K. K. Singh, V. Mittal, Two-dimensional materials for sensing: Graphene and beyond, Electron. 4 (2015) 651–687.

[19] L. Kou, T. Frauenheim, C. Chen, Phosphorene as a superior gas sensor: Selective

adsorption and distinct I – V response, J. Phys. Chem. Lett. 5 (2014) 2675–2681.

[20] K. S. Novoselov, V. I. Fal'Ko, L. Colombo, P.R. Gellert, M. G. Schwab, K. Kim, V. I. Fal′ko, L. Colombo, P. R. Gellert, M. G. Schwab, K. Kim, V. I. Fal'Ko, L. Colombo, P. R. Gellert, M. G. Schwab, K. Kim, V. I. Fal′ko, L. Colombo, P. R. Gellert, M. G. Schwab, K. Kim, A roadmap for graphene, Nature. 490 (2012) 192–200.

[21] N. O. Weiss, H. Zhou, L. Liao, Y. Liu, S. Jiang, Y. Huang, X. Duan, Graphene: An emerging electronic material, Adv. Mater. 24 (2012) 5782–5825.

[22] A. K. Geim, I. V. Grigorieva, Van der Waals heterostructures, Nature. 499 (2013) 419–425.

[23] H. Zhang, Ultrathin two-dimensional nanomaterials, ACS Nano. 9 (2015) 9451–9469.

[24] F. Schwierz, Graphene transistors, Nat. Nanotechnol. 5 (2010) 487–496.

[25] K. Nakada, A. Ishii, DFT calculation for adatom adsorption on graphene, Graphene Simul. (2011).

[26] Y. Zhu, S. Murali, W. Cai, X. Li, J.W. Suk, J. R. Potts, R. S. Ruoff, Graphene and graphene oxide: Synthesis, properties, and applications, Adv. Mater. 22 (2010) 3906–3924.

[27] C. Geesthacht, Micromechanical modelling of damage and fracture, Fatigue Fract Eng Mater Struct. 21 (1998) 1175–1188.

[28] K. J. Lee, S. J. Kim, Theoretical investigation of CO_2 adsorption on graphene, Bull. Korean Chem. Soc. 34 (2013) 3022–3026.

[29] M. Darvish Ganji, S. M. Hosseini-khah, Z. Amini-Tabar, Theoretical insight into hydrogen adsorption onto graphene: A first-principles B3LYP-D3 study, Phys. Chem. Chem. Phys. 17 (2015) 2504–2511.

[30] Z. Chen, P. Darancet, L. Wang, A. C. Crowther, Y. Gao, C. R. Dean, T. Taniguchi, K. Watanabe, J. Hone, C. A. Marianetti, L. E. Brus, Physical adsorption and charge transfer

of molecular Br_2 on graphene, ACS Nano. 8 (2014) 2943–2950.

[31] A. Salmankhani, Z. Karami, A. H. Mashhadzadeh, M. R. Ganjali, V. Vatanpour, A. Esmaeili, S. Habibzadeh, M. R. Saeb, V. Fierro, A. Celzard, New insights into H_2S adsorption on graphene and graphene-like structures: A comparative DFT study, C. 6 (2020) 74-82.

[32] C. Thierfelder, M. Witte, S. Blankenburg, E. Rauls, W. G. Schmidt, Methane adsorption on graphene from first principles including dispersion interaction, Surf. Sci. 605 (2011) 746–749.

[33] A. Z. Alzahrani, First-principles study on the structural and electronic properties of graphene upon benzene and naphthalene adsorption, Appl. Surf. Sci. 257 (2010) 807–810.

[34] X. Lin, J. Ni, C. Fang, Adsorption capacity of H_2O, NH_3, CO, and NO_2 on the pristine graphene, J. Appl. Phys. 113 (2013) 034306.

[35] O. Leenaerts, B. Partoens, F. M. Peeters, Adsorption of H_2O, NH_3, CO, NO_2, and NO on graphene: A first-principles study, Phys. Rev. B - Condens. Matter Mater. Phys. 77 (2008) 125416.

[36] D. J. Buckley, N. C. G. Black, E. G. Castanon, C. Melios, M. Hardman, O. Kazakova, Frontiers of graphene and 2D material-based gas sensors for environmental monitoring, 2D Mater. 7 (2020) 032002.

[37] T. Wang, D. Huang, Z. Yang, S. Xu, G. He, X. Li, N. Hu, G. Yin, D. He, L. Zhang, A review on graphene-based gas/vapor sensors with unique properties and potential applications, Nano-Micro Lett. 8 (2016) 95–119.

[38] G. Ko, H. Y. Y. Kim, J. Ahn, Y. M. M. Park, K. Y. Y. Lee, J. Kim, Graphene-based nitrogen dioxide gas sensors, Curr. Appl. Phys. 10 (2010) 1002–1004.

[39] T. O. Wehling, K. S. Novoselov, S. V. Morozov, E. E. Vdovin, M. I. Katsnelson, A. K.

Geim, A. I. Lichtenstein, Molecular Doping of Graphene, Nano Lett. 8 (2008) 173–177.

[40] P. Rani, V. K. Jindal, Designing band gap of graphene by B and N dopant atoms, RSC Adv. 3 (2013) 802–812.

[41] L. Miao, R. Jia, Y. Wang, C. P. Kong, J. Wang, R. I. Eglitis, H. X. Zhang, Certain doping concentrations caused half-metallic graphene, J. Saudi Chem. Soc. 21 (2017) 111–117.

[42] X. Zhang, Z. Shao, X. Zhang, Y. He, J. Jie, Surface Charge Transfer Doping of Low-Dimensional Nanostructures toward High-Performance Nanodevices, Adv. Mater. 28 (2016) 10409–10442.

[43] V. Georgakilas, M. Otyepka, A. B. Bourlinos, V. Chandra, N. Kim, K. C. Kemp, P. Hobza, R. Zboril, K. S. Kim, Functionalization of graphene : covalent and non-covalent approaches , derivatives and applications, chem. Rev. 11 (2012) 6156–6214.

[44] D. Wei, Y. Liu, Y. Wang, H. Zhang, L. Huang, G. Yu, Synthesis of N-Doped Graphene by Chemical Vapor Deposition and Its Electrical Properties, Nano Lett. 9 (2009) 1752–1758.

[45] L. Shao, G. Chen, H. Ye, Y. Wu, Z. Qiao, Y. Zhu, H. Niu, Sulfur dioxide adsorbed on graphene and heteroatom-doped graphene: A first-principles study, Eur. Phys. J. B. 86 (2013) 2–6.

[46] F. Li, Y. H. H. Zhang, L. F. F. Han, Y. H. H. Xiao, D. Z. Z. Jia, Z. H. H. Guo, F. Li, Understanding dopant and defect effect on H_2S sensing performances of graphene: A first-principles study, Comput. Mater. Sci. 69 (2013) 222–228.

[47] F. Nasehnia, M. Seifi, Adsorption of molecular oxygen on VIIIB transition metal-doped graphene: A DFT study, Mod. Phys. Lett. B. 28 (2014) 1450237.

[48] H. P. Zhang, X. G. Luo, X. Y. Lin, X. Lu, Y. Leng, H. T. Song, Density functional theory calculations on the adsorption of formaldehyde and other harmful gases on pure, Ti-doped, or N-doped graphene sheets, Appl. Surf. Sci. 283 (2013) 559–565.

[49] T. Lin, F. Huang, J. Liang, Y. Wang, A facile preparation route for boron-doped graphene, and its CdTe solar cell application, Energy Environ. Sci. 4 (2011) 862–865.

[50] D. Geng, Y. Chen, Y. Chen, Y. Li, R. Li, X. Sun, S. Ye, S. Knights, High oxygen-reduction activity and durability of nitrogen-doped graphene, Energy Environ. Sci. 4 (2011) 760–764.

[51] Q. Zhou, L. Yuan, X. Yang, Z. Fu, Y. Tang, C. Wang, H. Zhang, DFT study of formaldehyde adsorption on vacancy defected graphene doped with B, N, and S, Chem. Phys. 440 (2014) 80–86.

[52] J. Dai, J. Yuan, P. Giannozzi, Gas adsorption on graphene doped with B, N, Al, and S: A theoretical study, Appl. Phys. Lett. 95 (2009) 232105.

[53] J. Rafiee, X. Mi, H. Gullapalli, A. V. Thomas, F. Yavari, Y. Shi, P. M. Ajayan, N. A. Koratkar, Wetting transparency of graphene, Nat. Mater. 11 (2012) 217–222.

[54] H. Search, C. Journals, A. Contact, M. Iopscience, N. J. Phys, Graphene hydrate: theoretical prediction of a new insulating form of graphene, New J. Phys. 12 (2010) 125012.

[55] J. S. Bunch, S. S. Verbridge, J. S. Alden, A. M. van der Zande, J. M. Parpia, H. G. Craighead, P. L. McEuen, Impermeable atomic membranes from graphene sheets, Nano Lett. 8 (2008) 2458–2462.

[56] A. S. Rad, V. P. Foukolaei, A. Shokuhi Rad, V. Pouralijan Foukolaei, Density functional study of Al-doped graphene nanostructure towards adsorption of CO, CO_2 and H_2O, Synth. Met. 210 (2015) 171–178.

[57] X. Wang, X. Li, L. Zhang, Y. Yoon, P. K. Weber, H. Wang, J. Guo, H. Dai, N-doping of graphene through electrothermal reactions with ammonia, Science. 324 (2009) 768–771.

[58] I. V. Antonova, S. V. Mutilin, V. A. Seleznev, R. A. Soots, V. A. Volodin, V. Y. Prinz,

Extremely high response of electrostatically exfoliated few layer graphene to ammonia adsorption, Nat. Nanotechnol. 22 (2011) 285502.

[59] M. Zhou, Y. H. H. Lu, Y. Q. Q. Cai, C. Zhang, Y. P. P. Feng, Adsorption of gas molecules on transition metal embedded graphene: A search for high-performance graphene-based catalysts and gas sensors, Nanotechnol. 22 (2011) 385502.

[60] A. Sahithi, K. Sumithra, Adsorption and sensing of CO and NH_3 on chemically modified graphene surfaces, RSC Adv. 10 (2020) 42318–42326.

[61] D. Cortés-Arriagada, N. Villegas-Escobar, D. E. Ortega, Fe-doped graphene nanosheet as an adsorption platform of harmful gas molecules (CO, CO_2, SO_2 and H_2S), and the co-adsorption in O_2 environments, Appl. Surf. Sci. 427 (2018) 227–236.

[62] X. Yang, H. Chi, Y. Tian, T. Li, Y. Wang, Research progress of graphene and its derivatives towards exhaled breath analysis, Biosensors. 12 (2022) 48–49.

[63] Y. Peng, J. Li, Ammonia adsorption on graphene and graphene oxide: A first-principles study, Front. Environ. Sci. Eng. 7 (2013) 403–411.

[64] S. Novikov, N. Lebedeva, A. Satrapinski, J. Walden, V. Davydov, A. Lebedev, Graphene based sensor for environmental monitoring of NO_2, Sens. Actuators B: Chem. 236 (2016) 1054–1060.

[65] Z. Bo, X. Guo, X. Wei, H. Yang, J. Yan, K. Cen, Density functional theory calculations of NO_2 and H_2S adsorption on the group 10 transition metal (Ni, Pd and Pt) decorated graphene, Phys. E Low-Dimensional Syst. Nanostructures. 109 (2019) 156–163.

[66] Q. Li, Y. Liu, D. Chen, J. Miao, X. Zhi, S. Deng, S. Lin, H. Jin, D. Cui, Nitrogen dioxide gas sensor based on Ag-doped graphene : A first-principle study, Chemosensors. 9 (2021) 227–237.

[67] A. Sahithi, K. Sumithra, New insights in the electronic structure of doped graphene on adsorption with oxides of nitrogen, Mater. Today Commun. 27 (2021) 102417.

[68] J. Dai, P. Giannozzi, J. Yuan, Adsorption of pairs of NO_x molecules on single-walled carbon nanotubes and formation of $NO+NO_3$ from NO_2, Surf. Sci. 603 (2009) 3234–3238.

[69] A. Bussmann-holder, H. Keller, Superconductivity and the Jahn – Teller Polaron, Condens. Matter. 7 (2022) 1–17.

[70] X. Zhu, K. Liu, Z. Lu, Y. Xu, S. Qi, G. Zhang, Effect of oxygen atoms on graphene: Adsorption and doping, Phys. E: Low-Dimens. Syst. Nanostructures. 117 (2020) 113827.

[71] F. R. Bagsican, A. Winchester, S. Ghosh, X. Zhang, L. Ma, M. Wang, H. Murakami, S. Talapatra, R. Vajtai, P. M. Ajayan, J. Kono, M. Tonouchi, I. Kawayama, Adsorption energy of oxygen molecules on graphene and two-dimensional tungsten disulfide, Sci. Rep. 7 (2017) 1774-1781.

[72] F. Mehmood, R. Pachter, W. Lu, J. J. Boeckl, Adsorption and diffusion of oxygen on single-layer graphene with topological defects, J. Phys. Chem. C. 117 (2013) 10366–10374.

[73] E. V. Castro, K. S. Novoselov, S. V. Morozov, N. M. R. Peres, J. M. B. Lopes Santos, J. Nilsson, F. Guinea, A.K. Geim, A.H. Castro Neto, Electronic properties of a biased graphene bilayer, J. Phys. Condens. Matter. 22 (2010) 175503.

[74] S. M. Mousavi, M. T. Ahmadi, J. F. Webb, H. Sadeghi, A. Nilghaz, A. Amin, Z. Johari, R. Ismail, Bilayer graphene nanoribbon carrier statistics in the degenerate regime, in: AIP Conf. Proc. (2011) 180–183.

[75] J. Lin, W. Fang, W. Zhou, A. R. Lupini, J. C. Idrobo, J. Kong, S. J. Pennycook, S. T. Pantelides, AC/AB stacking boundaries in bilayer graphene, Nano Lett. 13 (2013) 3262–3268.

[76] M. Aoki, H. Amawashi, Dependence of band structures on stacking and field in layered

graphene, Solid State Commun. 142 (2007) 123–127.

[77] Y. Zhang, T. T. T. Tang, C. Girit, Z. Hao, M. C. Martin, A. Zettl, M. F. Crommie, Y. R. Shen, F. Wang, Direct observation of a widely tunable bandgap in bilayer graphene, Nature. 459 (2009) 820–823.

[78] Z. Liu, K. Suenaga, P. J. F. Harris, S. Iijima, Open and closed edges of graphene layers, Phys. Rev. Lett. 102 (2009) 015501.

[79] L. Liu, H. Zhou, R. Cheng, W. J. Yu, Y. Liu, Y. Chen, J. Shaw, X. Zhong, Y. Huang, X. Duan, High-yield chemical vapor deposition growth of high-quality large-area AB-stacked bilayer graphene, ACS Nano. 6 (2012) 8241–8249.

[80] T. Yu, E. K. Lee, B. Briggs, B. Nagabhirava, B. Yu, Reliability study of bilayer graphene - Material for future transistor and interconnect, in: IEEE Int. Reliab. Phys. Symp. Proc., IEEE, (2010) 80–83.

[81] Y. Fujimoto, S. Saito, Electronic structures and stabilities of bilayer graphene doped with boron and nitrogen, Surf. Sci. 634 (2015) 57–61.

[82] A. H. Castro Neto, F. Guinea, N. M. R. R. Peres, K. S. Novoselov, A. K. Geim, The electronic properties of graphene, Rev. Mod. Phys. 81 (2009) 109–162.

[83] C. R. Dean, A. F. Young, I. Meric, C. Lee, L. Wang, S. Sorgenfrei, K. Watanabe, T. Taniguchi, P. Kim, K. L. Shepard, J. Hone, Boron nitride substrates for high-quality graphene electronics, Nat. Nanotechnol. 5 (2010) 722–726.

[84] K. S. Novoselov, E. McCann, S. V. Morozov, V. I. Fal'ko, M. I. Katsnelson, U. Zeitler, D. Jiang, F. Schedin, A. K. Geim, Unconventional quantum Hall effect and Berry's phase of 2π in bilayer graphene, Nat. Phys. 2 (2006) 177–180.

[85] S. Ghosh, W. Bao, D. L. Nika, S. Subrina, E. P. Pokatilov, C. N. Lau, A. A. Balandin, Dimensional crossover of thermal transport in few-layer graphene, Nat. Mater. 9 (2010) 555–558.

[86] Y. Y. Zhang, C. M. Wang, Y. Cheng, Y. Xiang, Mechanical properties of bilayer graphene sheets coupled by sp^3 bonding, Carbon N. Y. 49 (2011) 4511–4517.

[87] R. R. Nair, P. Blake, A. N. Grigorenko, K. S. Novoselov, T. J. Booth, T. Stauber, N. M. R. Peres, A. K. Geim, Fine structure constant defines visual transparency of graphene, Science. 320 (2008) 1308-1315.

[88] D. C. Elias, R. R. Nair, T. M. G. Mohiuddin, S. V. Morozov, P. Blake, M. P. Halsall, A. C. Ferrari, D. W. Boukhvalov, M. I. Katsnelson, A. K. Geim, K. S. Novoselov, Control of graphene's properties by reversible hydrogenation: Evidence for graphane, Science. 323 (2009) 610–613.

[89] J. Yan, M. H. Kim, J. A. Elle, A. B. Sushkov, G. S. Jenkins, H. M. Milchberg, M. S. Fuhrer, H. D. Drew, Dual-gated bilayer graphene hot-electron bolometer, Nat. Nanotechnol. 7 (2012) 472–478.

[90] E. McCann, V. I. Fal'ko, Landau-level degeneracy and quantum hall effect in a graphite bilayer, Phys. Rev. Lett. 96 (2006) 086805.

[91] K. Sugawara, K. Kanetani, T. Sato, T. Takahashi, Fabrication of Li-intercalated bilayer graphene, AIP Adv. 1 (2011) 022103.

[92] E. V. Castro, K. S. Novoselov, S. V. Morozov, N. M. R. Peres, J. M. B. L. Dos Santos, J. Nilsson, F. Guinea, A. K. Geim, A. H. C. Neto, Biased bilayer graphene: Semiconductor with a gap tunable by the electric field effect, Phys. Rev. Lett. 99 (2007) 216802.

[93] R. J. Young, I. A. Kinloch, L. Gong, K. S. Novoselov, The mechanics of graphene nanocomposites: A review, Compos. Sci. Technol. 72 (2012) 1459–1476.

[94] S. Peng, K. Cho, Ab Initio study of doped carbon nanotube sensors, Nano Lett. 3 (2003) 513–517.

[95] Y. Fujimoto, S. Saito, Interlayer distances and band-gap tuning of hexagonal boron-

nitride bilayers, J. Ceram. Soc. Japan. 124 (2016) 584–586.

[96] S. O. Guillaume, B. Zheng, J. C. Charlier, L. Henrard, Electronic properties and STM images of doped bilayer graphene, Phys. Rev. B. 85 (2012) 035444.

[97] Y. Fujimoto, Formation, energetics, and electronic properties of graphene monolayer and bilayer doped with heteroatoms, Adv. Condens. Matter Phys. 2015 (2015) 1–14.

[98] L. S. Panchakarla, K. S. Subrahmanyam, S. K. Saha, A. Govindaraj, H. R. Krishnamurthy, U. V. Waghmare, C. N. R. Rao, Synthesis, Structure and properties of boron- and nitrogen-doped graphene, Adv. Mater. 21 (2009) 4726-4730.

[99] P. Rani, V. K. Jindal, Stability and electronic properties of isomers of B/N co-doped graphene, Appl. Nanosci. 4 (2014) 989–996.

[100] M. Alattas, U. Schwingenschlögl, Band Gap Control in Bilayer Graphene by Co-Doping with B-N Pairs, Sci. Rep. 8 (2018) 17689.

[101] L. Bai, Z. Zhou, Computational study of B- or N-doped single-walled carbon nanotubes as NH_3 and NO_2 sensors, Carbon N. Y. 45 (2007) 2105–2110.

[102] Y. Fujimoto, S. Saito, Gas adsorption, energetics and electronic properties of boron- and nitrogen-doped bilayer graphenes, Chem. Phys. 478 (2016) 55–61.

[103] A. Carvalho, M. Wang, X. Zhu, A. S. Rodin, H. Su, A. H. Castro Neto, Phosphorene: From theory to applications, Nat. Rev. Mater. 1 (2016) 16061.

[104] A. Devi, A. Singh, Study thermal properties of black phosphorene and doped phosphorene (C, N & O): A DFT Study, AIP Conf Proc. 090042 (2018) 1–5.

[105] H. Liu, A. T. Neal, Z. Zhu, Z. Luo, X. Xu, D. Tománek, P. D. Ye, Phosphorene: An unexplored 2D semiconductor with a high hole mobility, ACS Nano. 8 (2014) 4033–4041.

[106] F. Xia, H. Wang, Y. Jia, Rediscovering black phosphorus as an anisotropic layered material for optoelectronics and electronics, Nat. Commun. 5 (2014) 4458-4467.

[107] A. S. Rodin, A. Carvalho, A. H. Castro Neto, Strain-induced gap modification in black phosphorus, Phys. Rev. Lett. 112 (2014) 176801.

[108] H. Zheng, J. Zhang, B. Yang, X. Du, Y. Yan, A first-principles study on the magnetic properties of nonmetal atom doped phosphorene monolayers, Phys. Chem. Chem. Phys. 17 (2015) 16341–16350.

[109] D. W. Boukhvalov, A. N. Rudenko, D. A. Prishchenko, V. G. Mazurenko, M. I. Katsnelson, Chemical modifications and stability of phosphorene with impurities: A first principles study, Phys. Chem. Chem. Phys. 17 (2015) 15209–15217.

[110] M. Lalitha, Y. Nataraj, S. Lakshmipathi, Calcium decorated and doped phosphorene for gas adsorption, Appl. Surf. Sci. 377 (2016) 311–323.

[111] W. Yu, Z. Zhu, C.Y. Niu, C. Li, J.H. Cho, Y. Jia, Anomalous doping effect in black phosphorene using first-principles calculations, Phys. Chem. Chem. Phys. 17 (2015) 16351–16358.

[112] D. W. Boukhvalov, The atomic and electronic structure of nitrogen- and boron-doped phosphorene, Phys. Chem. Chem. Phys. 17 (2015) 27210–27216.

[113] L. Yang, W. Mi, X. Wang, Tailoring magnetism of black phosphorene doped with B, C, N, O, F, S and Se atom: A DFT calculation, J. Alloys Compd. 662 (2016) 528–533.

[114] Q. Yang, R. S. Meng, J. K. Jiang, Q. H. Liang, C. J. Tan, M. Cai, X. Sun, D. G. Yang, T. L. Ren, X. P. Chen, First-Principles Study of sulfur dioxide sensor based on phosphorenes, IEEE Electron Device Lett. 37 (2016) 660–662.

[115] Z. F. Wu, P. F. Gao, L. Guo, J. Kang, D. Q. Fang, Y. Zhang, M. G. Xia, S. L. Zhang, Y. H. Wen, Robust indirect band gap and anisotropy of optical absorption in B-doped phosphorene, Phys. Chem. Chem. Phys. 19 (2017) 31796–31803.

[116] T. Low, A.S. Rodin, A. Carvalho, Y. Jiang, H. Wang, F. Xia, A.H.C. Neto, Tunable optical properties of multilayer black phosphorus thin films, 075434 (2014) 3–7.

[117] A. H. Woomer, T. W. Farnsworth, J. Hu, R.A. Wells, C.L. Donley, S. C. Warren, Phosphorene : Synthesis , scale-up , and quantitative optical spectroscopy, ACS Nano. 9 (2015) 8869–888.

[118] O. F. Samples, The Electrical Properties of Black Phosphorus,Phys. Rev. 92 (1988) 580-584.

[119] N. Suvansinpan, F. Hussain, G. Zhang, C. H. Chiu, Y. Cai, Y. W. W. Zhang, Substitutionally doped phosphorene: electronic properties and gas sensing, Nanotechnology. 27 (2016) 065708.

[120] A. N. Abbas, B. Liu, L. Chen, Y. Ma, S. Cong, N. Aroonyadet, M. Ko, M. Köpf, T. Nilges, C. Zhou, Black phosphorus gas sensors, ACS Nano. 9 (2015) 5618–5624.

[121] Y. Maruyama, S. Suzuki, K. Kobayashi, S. Tanuma, Synthesis and some properties of black phosphorus single crystals, Phys. B+C. 105 (1981) 99–102.

[122] R. Zhang, B. Li, J. Yang, A First-principles study on electron donor and acceptor molecules adsorbed on phosphorene, J. Phys. Chem. C. 119 (2015) 2871–2878.

[123] Q. Yang, Y. Huang, R. Meng, X. Chen, Adsorption of CO_2 and CO gas on impurity-decorated phosphorenes: A first-principles study, in: 2016 17th Int. Conf. Electron. Packag. Technol. ICEPT 2016, IEEE, (2016) 749–752.

[124] H. ping Zhang, A. Du, Q. bin Shi, Y. Zhou, Y. Zhang, Y. Tang, Adsorption behavior of CO_2 on pristine and doped phosphorenes: A dispersion corrected DFT study, J. CO_2 Util. 24 (2018) 463–470.

[125] D. Liu, Y. Shi, L. Tao, D. Yan, R. Chen, S. Wang, First-principles study of methanol adsorption on heteroatom-doped phosphorene, Chinese Chem. Lett. 30 (2019) 207–210.

[126] L. Britnell, R. V. Gorbachev, R. Jalil, B. D. Belle, F. Schedin, A. Mishchenko, T. Georgiou, M. I. Katsnelson, L. Eaves, S. V. Morozov, N. M. R. Peres, J. Leist, A. K. Geim, K. S. Novoselov, L. A. Ponomarenko, Field-effect tunneling transistor based on

vertical graphene heterostructures, Science. 335 (2012) 947–950.

Chapter 2

[1] P. Hohenberg, W. Kohn, Inhomogeneous electron gas, Phys. Rev. 136 (1964) B864–B871.

[2] A. J. Cohen, P. Mori-Sánchez, W. Yang, Challenges for density functional theory, Chem. Rev. 112 (2012) 289–320.

[3] P. Singh, Density-functional theory of material design: fundamentals and applications-I, Oxford Open Mater. Sci. 1 (2021) 1–44.

[4] W. Kohn, L. J. Sham, Self-consistent equations including exchange and correlation effects, Phys. Rev. 140 (1965) A1133–A1138.

[5] D. Cremer, Møller-Plesset perturbation theory: From small molecule methods to methods for thousands of atoms, Wiley Interdiscip. Rev. Comput. Mol. Sci. 1 (2011) 509–530.

[6] I. Y. Zhang, A. Grüneis, Coupled cluster theory in materials science, Front. Mater. 6 (2019).

[7] E. Runge, E. K. U. Gross, Density-functional theory for time-dependent systems, Phys. Rev. Lett. 52 (1984) 997–1000.

[8] M. Petersilka, U. J. Gossmann, E. K. U. Gross, Excitation energies from time-dependent density-functional theory, Phys. Rev. Lett. 76 (1996) 0–3.

[9] E. Fermi, Un metodo statistic per la determinazione di alcune paioriete dell' atome, Rend. Dell Accad. Del Lincei. 6 (1927) 602–607.

[10] P. A. M. M. Dirac, Note on exchange phenomena in the thomas atom, Math. Proc. Cambridge Philos. Soc. 26 (1930) 376–385.

[11] M. Born, R. Oppenheimer, Zur quantentheorie der molekeln, Ann. Phys. 389 (1927) 457–484.

[12] K. Capelle, A bird's-eye view of density-functional theory, Brazilian J. Phys. 36 (2006) 1318–1341.

[13] G. X. Zhang, A. M. Reilly, A. Tkatchenko, M. Scheffler, Performance of various density-functional approximations for cohesive properties of 64 bulk solids, New J. Phys. 20 (2018) 063020.

[14] S. Lany, Semiconducting transition metal oxides, J. Phys. Condens. Matter. 27 (2015) 283203.

[15] J. P. Perdew, Density-functional approximation for the correlation energy of the inhomogeneous electron gas, Phys. Rev. B. 33 (1986) 8822–8824.

[16] J. P. Perdew, Y. Wang, Erratum: Accurate and simple analytic representation of the electron-gas correlation energy, Phys. Rev. B. 98 (2018) 244–249.

[17] A. D. Becke, Density-functional exchange-energy approximation with correct asymptotic behavior, Phys. Rev. A. 38 (1988) 3098–3100.

[18] J. P. Perdew, K. Burke, M. Ernzerhof, Generalized gradient approximation made simple, Phys. Rev. Lett. 77 (1996) 3865–3868.

[19] J. M. Pérez-Jordá, A. D. Becke, A density-functional study of van der Waals forces: rare gas diatomics, Chem. Phys. Lett. 233 (1995) 134–137.

[20] J. Šponer, J. Leszczynski, P. Hobza, Base stacking in cytosine dimer. A comparison of correlated ab initio calculations with three empirical potential models and density functional theory calculations, J. Comput. Chem. 17 (1996) 841–850.

[21] F. London, Zur theorie und systematik der molekularkräfte, Zeitschrift Für Phys. 63 (1930) 245–279.

[22] S. Grimme, J. Antony, S. Ehrlich, H. Krieg, A consistent and accurate ab initio parametrization of density functional dispersion correction (DFT-D) for the 94 elements H-Pu, J. Chem. Phys. 132 (2010) 154104.

[23] S. Grimme, Accurate description of van der Waals complexes by density functional theory including empirical corrections, J. Comput. Chem. 25 (2004) 1463–1473.

[24] S. Grimme, Semiempirical GGA-type density functional constructed with a long-range dispersion correction, J. Comput. Chem. 27 (2006) 1787–1799.

[25] Refer, e.g., Thomson Reuter's Web of Science Core Collection,

[26] S. Grimme, Density functional theory with London dispersion corrections, Wiley Interdiscip. Rev. Comput. Mol. Sci. 1 (2011) 211–228.

[27] S. Grimme, J. Antony, T. Schwabe, M. Christian, Density functional theory with dispersion corrections for supramolecular structures , aggregates , and complexes of (bio) organic molecules, Org. Biomol. Chem. 5 (2007) 741–758.

[28] A. Stone, The theory of intermolecular forces, Oxford University Press, 2013.

[29] P. Pyykkö, M. Atsumi, Molecular single-bond covalent radii for elements 1-118, Chem. - A Eur. J. 15 (2009) 186–197.

[30] E. R. Johnson, A. D. Becke, A post-Hartree-Fock model of intermolecular interactions: Inclusion of higher-order corrections, J. Chem. Phys. 124 (2006) 174104.

[31] L. Goerigk, A comprehensive overview of the DFT-D3 London-dispersion correction, 1st ed., Elsevier Inc., 2017.

[32] M. C. Payne, M. P. Teter, D.C. Allan, T. A. Arias, J. D. Joannopoulos, Iterative minimization techniques for ab initio total-energy calculations: Molecular dynamics and conjugate gradients, Rev. Mod. Phys. 64 (1992) 1045–1097.

[33] H. Hellmann, A new approximation method in the problem of many electrons, 61 (1935) 8–9.

[34] V. Heine, D. Weaire, Pseudopotential theory of cohesion and structure, in solid state Phys. Adv. Res. Appl., (1970) 249–463.

[35] D. R. Hamann, M. Schlüter, C. Chiang, Norm-conserving pseudopotentials, Phys. Rev.

Lett. 43 (1979) 1494–1497.

[36] P. E. Blöchl, Projector augmented-wave method, Phys. Rev. B. 50 (1994) 17953–17979.

[37] F. Bloch, Über die quantenmechanik der elektronen in kristallgittern, Zeitschrift Für Phys. 52 (1929) 555–600.

[38] L. Brillouin, L. B. Les, D. B. J. Phys, E. T. Le, R. Des, R. D. E. Bragg, Les électrons libres dans les métaux et le role des réflexions de Bragg To cite this version : HAL Id : jpa-00233038, (1930).

[39] A. Beiser. Concepts of Modern Physics 6th edition, p. 371-373 (ISBN 007-123460-8).

[40] C. Rule, The physics of the hume-rothery electron concentration rule, Crystals. 7 (2017) 9-12.

[41] M. N. Huda, Epitaxial growth of lateral graphene / hexagonal boron nitride heterostructures, Phys. Adv Mater. (2018) 42-46.

[42] M. Abedin, A self-adjusting lin-log active pixel for wide dynamic range cmos image sensor, Department of Electrical and Electronic Engineering Chittagong University of Engineering and Science, (2016).

[43] R. F. W. Bader, A Quantum Theory of Molecular Structure and Its Applications, Chem. Rev. 91 (1991) 893–928.

[44] MedeA®, Materials Exploration and Design Analysis, Software Package, Ver. 2.22, Materials Design, Inc., San Diego, CA, USA, 2019.

[45] F. Abild-pedersen, F. Studt, T. Bligaard, Density functional theory in surface chemistry and catalysis, 108 (2011) 937–943.

Chapter 3

[1] V. B. Mohan, K. tak Lau, D. Hui, D. Bhattacharyya, Graphene-based materials and their composites: A review on production, applications and product limitations, Compos. Part B Eng. 142 (2018) 200–220.

[2] A. Nag, A. Mitra, S. C. Mukhopadhyay, Graphene and its sensor-based applications: A review, Sensors Actuators, A Phys. 270 (2018) 177–194.

[3] M. Coroş, S. Pruneanu, R. I. Stefan-van Staden, Review recent progress in the graphene-based electrochemical sensors and biosensors, J. Electrochem. Soc. 167 (2020) 037528.

[4] C. I. L. Justino, A .R. Gomes, A. C. Freitas, A. C. Duarte, T. A. P. Rocha-Santos, Graphene based sensors and biosensors, TrAC Trends Anal. Chem. 91 (2017) 53–66.

[5] D. R. Cooper, B. D'Anjou, N. Ghattamaneni, B. Harack, M. Hilke, A. Horth, N. Majlis, M. Massicotte, L. Vandsburger, E. Whiteway, V. Yu, Experimental review of graphene, ISRN Condens. Matter Phys. 2012 (2012) 1–56.

[6] R. Garg, N. Dutta, N. Choudhury, Work function engineering of graphene, Nanomaterials. 4 (2014) 267–300.

[7] P. Rani, V. K. Jindal, Designing band gap of graphene by B and N dopant atoms, RSC Adv. 3 (2013) 802–812.

[8] M. Alattas, U. Schwingenschlögl, Band Gap Control in Bilayer Graphene by Co-Doping with B-N Pairs, Sci. Rep. 8 (2018) 17689.

[9] S. Ullah, A. Hussain, F. Sato, Rectangular and hexagonal doping of graphene with B, N, and O: a DFT study, RSC Adv. 7 (2017) 16064–16068.

[10] Q. Zhou, X. Su, W. Ju, Y. Yong, X. Li, Z. Fu, C. Wang, Adsorption of H_2S on graphane decorated with Fe, Co and Cu: A DFT study, RSC Adv. 7 (2017) 31457–31465.

[11] Y. Zhou, W. Chu, F. Jing, J. Zheng, W. Sun, Y. Xue, Enhanced hydrogen storage on Li-doped defective graphene with B substitution: A DFT study, Appl. Surf. Sci. 410 (2017) 166–176.

[12] T. Hussain, P. Panigrahi, R. Ahuja, Enriching physisorption of H_2S and NH_3 gases on a graphane sheet by doping with Li adatoms, Phys. Chem. Chem. Phys. 16 (2014) 8100–8105.

[13] X. Y. Liu, J. M. Zhang, K. W. Xu, V. Ji, Improving SO_2 gas sensing properties of graphene by introducing dopant and defect: A first-principles study, Appl. Surf. Sci. 313 (2014) 405–410.

[14] N. Tit, K. Said, N. M. Mahmoud, S. Kouser, Z. H. Yamani, Ab-initio investigation of adsorption of CO and CO_2 molecules on graphene: Role of intrinsic defects on gas sensing, Appl. Surf. Sci. 394 (2017) 219–230.

[15] L. Kong, A. Enders, T. S. Rahman, P. A. Dowben, Molecular adsorption on graphene, J. Phys. Condens. Matter. 26 (2014) 443001.

[16] H. Gao, Z. Liu, DFT study of NO adsorption on pristine graphene, RSC Adv. 7 (2017) 13082–13091.

[17] M. A. Kang, S. Ji, S. Kim, C. Y. Park, S. Myung, W. Song, S. S. Lee, J. Lim, K. S. An, Highly sensitive and wearable gas sensors consisting of chemically functionalized graphene oxide assembled on cotton yarn, RSC Adv. 8 (2018) 11991–11996.

[18] F. Schedin, A. K. Geim, S. V. Morozov, E. W. Hill, P. Blake, M. I. Katsnelson, K. S. Novoselov, Detection of individual gas molecules adsorbed on graphene, Nat. Mater. 6 (2007) 652–655.

[19] E. Akbari, Z. Buntat, A. Afroozeh, S. E. Pourmand, Y. Farhang, P. Sanati, Silicene and graphene nano materials in gas sensing mechanism, RSC Adv. 6 (2016) 81647–81653.

[20] T. O. Wehling, K. S. Novoselov, S. V. Morozov, E. E. Vdovin, M. I. Katsnelson, A. K. Geim, A. I. Lichtenstein, Molecular Doping of Graphene, Nano Lett. 8 (2008) 173–177.

[21] R. K. Joshi, H. Gomez, F. Alvi, A. Kumar, Graphene Films and Ribbons for Sensing of O_2, and 100 ppm of CO and NO_2 in Practical Conditions, J. Phys. Chem. C. 114 (2010) 6610–6613.

[22] W. Wang, Y. Zhang, C. Shen, Y. Chai, Adsorption of CO molecules on doped graphene: A first-principles study, AIP Adv. 6 (2016) 1–8.

[23] S. Yang, G. Lei, H. Xu, B. Xu, H. Li, Z. Lan, Z. Wang, H. Gu, A DFT study of CO adsorption on the pristine, defective, In-doped and Sb-doped graphene and the effect of applied electric field, Appl. Surf. Sci. 480 (2019) 205–211.

[24] J. Ni, M. Quintana, S. Song, Adsorption of small gas molecules on transition metal (Fe, Ni and Co, Cu) doped graphene: A systematic DFT study, Phys. E Low-Dimensional Syst. Nanostructures. 116 (2020) 113768.

[25] C. P. Zhang, B. Li, Z. G. Shao, First-principle investigation of CO and CO_2 adsorption on Fe-doped penta-graphene, Appl. Surf. Sci. 469 (2019) 641–646.

[26] A. S. Rad, S. S. Shabestari, S. Mohseni, S. A. Aghouzi, Study on the adsorption properties of O_3, SO_2, and SO_3 on B-doped graphene using DFT calculations, J. Solid State Chem. 237 (2016) 204–210.

[27] J. Dai, J. Yuan, P. Giannozzi, Gas adsorption on graphene doped with B, N, Al, and S: A theoretical study, Appl. Phys. Lett. 95 (2009) 232105.

[28] T. Vikramaditya, K. Sumithra, Effect of substitutionally boron-doped single-walled semiconducting zigzag carbon nanotubes on ammonia adsorption, J. Comput. Chem. 35 (2014) 586–594.

[29] D. Y. Usachov, A. V. Fedorov, O. Y. Vilkov, A. E. Petukhov, A. G. Rybkin, A. Ernst, M. M. Otrokov, E. V. Chulkov, I. I. Ogorodnikov, M. V. Kuznetsov, L. V. Yashina, E. Y. Kataev, A. V. Erofeevskaya, V. Y. Voroshnin, V. K. Adamchuk, C. Laubschat, and D. V. Vyalikh, Large-scale sublattice asymmetry in pure and boron-doped graphene, Nano Lett. 16 (2016) 4535–4543.

[30] X. Zhou, C. Zhao, G. Wu, J. Chen, Y. Li, DFT study on the electronic structure and optical properties of N, Al, and N-Al doped graphene, Appl. Surf. Sci. 459 (2018) 354–362.

[31] R. Skomski, P. A. Dowben, M. Sky Driver, J. A. Kelber, Sublattice-induced symmetry

breaking and band-gap formation in graphene, Mater. Horiz. 1 (2014) 563–571.

[32] K. Momma, F. Izumi, VESTA 3 for three-dimensional visualization of crystal, volumetric and morphology data, J. Appl. Crystallogr. 44 (2011) 1272–1276.

Chapter 4

[1] G. Hoek, R. M. Krishnan, R. Beelen, A. Peters, B. Ostro, B. Brunekreef, J. D. Kaufman, Long-term air pollution exposure and cardio- respiratory mortality: a review, J. Environ. Health. 12 (2013) 43–45.

[2] W. Yuan, G. Shi, Graphene-based gas sensors, J. Mater. Chem. A. 1 (2013) 10078-10091.

[3] F. Schedin, A. K. Geim, S. V. Morozov, E. W. Hill, P. Blake, M. I. Katsnelson, K. S. Novoselov, Detection of individual gas molecules adsorbed on graphene, Nat. Mater. 6 (2007) 652–655.

[4] L. Kong, A. Enders, T. S. Rahman, P. A. Dowben, Molecular adsorption on graphene, J. Phys. Condens. Matter 26 (2014), 443001.

[5] A. Lherbier, X. Blase, Y. M. Niquet, F. Triozon, S. Roche, Charge transport in chemically doped 2D graphene, Phys. Rev. Lett. 101 (2008), 036808.

[6] F. Cervantes-Sodi, G. Cs´anyi, S. Piscanec, A. C. Ferrari, Edge-functionalized and substitutionally doped graphene nanoribbons: electronic and spin properties, Phys. Rev. B Condens. Matter Mater. Phys. 77 (2008), 165427.

[7] S. Ullah, A. Hussain, W. A. Syed, M. A. Saqlain, I. Ahmad, O. Leenaerts, A. Karim, Band-gap tuning of graphene by Be doping and Be, B co-doping: a DFT study, RSC Adv. 5 (2015) 55762.

[8] P. Rani, V. K. Jindal, Designing band gap of graphene by B and N dopant atoms, RSC Adv. 3 (2013) 802–812.

[9] L. S. Panchakarla, K. S. Subrahmanyam, S. K. Saha, A. Govindaraj, H. R.

Krishnamurthy, U. V. Waghmare, C. N. R. Rao, Synthesis, structure, and properties of boron- and nitrogen-doped graphene, Adv. Mater. 21 (2009) 4726–4730.

[10] G. Bepete, D. Voiry, M. Chhowalla, Z. Chiguvare, N. J. Coville, Incorporation of small BN domains in graphene during CVD using methane, boric acid, and nitrogen gas, Nanoscale 5 (2013) 6552–6557.

[11] A. Sahithi, K. Sumithra, Adsorption and sensing of CO and NH_3 on chemically modified graphene surfaces, RSC Adv. 10 (2020) 42318–42326.

[12] J. Dai, J. Yuan, P. Giannozzi, Gas adsorption on graphene doped with B, N, Al, and S: a theoretical study, Appl. Phys. Lett. 95 (2009) 232103–232105.

[13] Y. H. Zhang, Y. Bin Chen, K. G. Zhou, C. H. Liu, J. Zeng, H. L. Zhang, Y. Peng, Improving gas sensing properties of graphene by introducing dopants and defects: a first-principles study, Nanotechnol 20 (2009), 185504.

[14] X. Jia, H. Zhang, Z. Zhang, L. An, Effect of doping and vacancy defects on the adsorption of CO on graphene, Mater. Chem. Phys. 249 (2020), 123114.

[15] S. Yang, Z. Lan, H. Xu, G. Lei, W. Xie, Q. Gu, A first-principles study on hydrogen sensing properties of pristine and Mo-Doped graphene, Nanotechnol (2018), 031805.

[16] W. Wang, Y. Zhang, C. Shen, Y. Chai, Adsorption of CO molecules on doped graphene: a first-principles study, AIP Adv. 6 (2016) 025317–025322.

[17] A. S. Rad, S. S. Shabestari, S. Mohseni, S. A. Aghouzi, Study on the adsorption properties of O_3, SO_2, and SO_3 on B-doped graphene using DFT calculations, J. Solid State Chem. 237 (2016) 204–210.

[18] I. Choudhuri, N. Patra, A. Mahata, R. Ahuja, B. Pathak, Highly Sensitive and Selective Gas Sensor, J. Phys. Chem. C 119 (2015) 24827–24836.

[19] T. O. Wehling, K. S. Novoselov, S. V. Morozov, E. E. Vdovin, M. I. Katsnelson, A. K. Geim, A. I. Lichtenstein, Molecular doping of graphene, Nano Lett. 8 (2008) 173–177.

[20] G. Ko, H. Y. Kim, J. Ahn, Y. M. Park, K. Y. Lee, J. Kim, Graphene based nitrogen dioxide gas sensors, Curr. Appl. Phys. 10 (2010) 1002–1004.

[21] M. Ali, N. Tit, Adsorption of NO and NO_2 molecules on defected-graphene and ozone-treated graphene: First-principles analysis, Surf. Sci. 684 (2019) 28–36.

[22] N. T. T. Tran, D. K. Nguyen, S. Y. Lin, G. Gumbs, M. F. Lin, Fundamental properties of transition metals adsorbed graphene, ChemPhysChem 20 (2019) 2473–2481.

[23] S. Yang, G. Lei, H. Xu, B. Xu, H. Li, Z. Lan, Z. Wang, H. Gu, A DFT study of CO adsorption on the pristine, defective, In-doped and Sb-doped graphene and the effect of applied electric field, Appl. Surf. Sci. 480 (2019) 198–205.

[24] C. P. Zhang, B. Li, Z. G. Shao, First-principle investigation of CO and CO_2 adsorption on Fe-doped penta-graphene, Appl. Surf. Sci. 469 (2019) 641–646.

[25] X. Jia, L. An, The adsorption of nitrogen oxides on noble metal-doped graphene: the first-principles study, Mod. Phys. Lett. B 33 (2019) 1-5.

[26] O. Leenaerts, B. Partoens, F. M. Peeters, Adsorption of H_2O, NH_3, CO, NO_2, and NO on graphene: a first-principles study, Phys. Rev. B Condens. Matter Mater. Phys. 77 (2008), 125416.

[27] X. Gao, Q. Zhou, J. Wang, L. Xu, W. Zeng, Performance of intrinsic and modified graphene for the adsorption of H2S and CH4: a DFT study, Nanomater. 10 (2020) 299-309.

[28] C. Kaykılarlı, D. Uzunsoy, E. D. S. Parmak, M. F. Fellah, O. Ç. Çakır, Boron and nitrogen doping in graphene: an experimental and density functional theory (DFT) study, Nano Express. 1 (2020), 010027.

[29] S. Tang, Z. Cao, Adsorption of nitrogen oxides on graphene and graphene oxides: insights from density functional calculations, J. Chem. Phys. 134 (2011), 044710.

[30] N. W. Ashcroft, H. Mermin, D. G. Crane, Solid State Physics, College Publishers, New

York, 1976, p. 29 C. 2.

[31] N. Tit, K. Said, N. M. Mahmoud, S. Kouser, Z. H. Yamani, Ab-initio investigation of adsorption of CO and CO_2 molecules on graphene: role of intrinsic defects on gas sensing, Appl. Surf. Sci. 394 (2017) 219–230.

[32] N. Tit, M. M. A. Ezzi, H. M. Abdullah, M. Yusupov, S. Kouser, H. Bahlouli, Z. H. Yamani, Detection of CO_2 using CNT-based sensors: role of Fe catalyst on sensitivity and selectivity, Mater. Chem. Phys. 186 (2017) 353–364.

[33] F. Haddadi, Q. S. Wu, A. J. Kruchkov, O. V. Yazyev, Moir´e flat bands in twisted double bilayer graphene, Nano Lett. 20 (2020) 2410–2415.

Chapter 5

[1] J. W. Schwank, M. Dibattista, Oxygen sensors: Materials and applications, MRS Bull 24 (1999) 44–47.

[2] R. Ramamoorty, P. K. Dutta, S. A. Akbar, Oxygen sensors: Materials, methods, designs and applications, J. Mater. Sci. 38 (2003) 4271–4282.

[3] M. Javaid, A. Haleem, S. Rab, R. P. Singh, R. Suman, Sensors for daily life: A review, Sens. International. 2 (2021) 100121.

[4] F. Schedin, A. K. Geim, S. V. Morozov, E. W. Hill, P. Blake, M. I. Katsenelson, and K. S. Novoselov, Detection of Individual Gas Molecules Adsorbed on Graphene, Nat. Mater. 6 (2007) 652–657.

[5] H. C. Chang, Y. J. Huang, H. Y. Chang, W. J. Su, Y. T. Shih, Y. S. Huang, and K. Y. Lee, Oxygen adsorption effect on nitrogen-doped graphene electrical properties, Appl. Phys. Express 7 (2014) 055101.

[6] C. J. Docherty, C. T. Lin, H. J. Joyce, R. J. Nicholas, L. M. Herz, L. J. Li, and M. B. Johnston, Extreme sensitivity of graphene photoconductivity to environmental gases, Nat. Commun. 3 (2012) 1228-1239.

[7] H. Nan, Z. Wang, W. Wang, Z. Liang, Y. Lu, Q. Chen, D. He, P. Tan, F. Miao, X. Wang, J. Wang, and Z. Ni, Strong Photoluminescence enhancement of MoS_2 through defect engineering and oxygen bonding, ACS Nano 8 (2014) 5738–5745.

[8] Y. Sato, K. Takai, and T. Enoki, Electrically Controlled Adsorption of Oxygen in Bilayer Graphene Devices, Nano Lett. 11 (2011) 3468–3475.

[9] L. Liu, S. Ryu, M. R. R. Tomasik, E. Stolyarova, N. Jung, M. S. S. Hybertsen, M. L. L. Steigerwald, L. E. E. Brus, and G. W. W. Flynn, Graphene Oxidation: Thickness-Dependent Etching and Strong Chemical Doping, Nano Lett. 8 (2008) 1965–1970.

[10] M. Zhou, Y. H. Lu, Y. Q. Cai, C. Zhang, and Y. P. Feng, Adsorption of gas molecules on transition metal embedded graphene: a search for high-performance graphene-based catalysts and gas sensors, Nanotechnology 22 (2011) 385502.

[11] F. Yavari, C. Kritzinger, C. Gaire, L. Song, H. Gulapalli, T. Borca-Tasciuc, P. M. Ajayan, and N. Koratkar, Tunable Bandgap in Graphene by the Controlled Adsorption of Water Molecules, Small 6 (2010) 2535–2538.

[12] T. O. Wehling, K. S. Novoselov, S. V. Morozov, E. E. Vdovin, M. I. Kats nelson, A. K. Geim, and A. I. Lichtenstein, Molecular Doping of Graphene, Nano Lett. 8 (2008) 173–177.

[13] J. Dai, J. Yuan, and P. Giannozzi, Gas adsorption on graphene doped with B, N, Al, and S: A theoretical study, Appl. Phys. Lett. 95 (2009) 232105.

[14] B. Kang, H. Liu, and J. Y. Lee, Oxygen adsorption on single layer graphyne: a DFT study, Phys. Chem. Chem. Phys.16 (2014) 974-980.

[15] O. Leenaerts, B. Partoens, and F. M. Peeters, Adsorption of H_2O, NH_3, CO, NO_2, and NO on graphene: A first-principles study, Phys. Rev. B 77 (2008) 125416.

[16] J. Dai, and J. M. Yuan, Adsorption of molecular oxygen on doped graphene: atomic, electronic, and magnetic properties, Phys. Rev. B 81 (2010) 165414.

[17] A. Sahithi, and K. Sumithra, Adsorption and sensing of CO and NH_3 on chemically modified graphene surfaces, RSC Adv. 10 (2020) 42318–42326.

[18] K. Nakada, and A. Ishii, DFT calculation for adatom adsorption on graphene, Graphene Simul. IntechOpen, London (2011) 1-18.

[19] A. Sahithi, and K. Sumithra, New insights in the electronic structure of doped graphene on adsorption with oxides of nitrogen, Mater. Today Commun. 27 (2021) 102417.

[20] Y. H. Zhang, Y. B. Chen, K. G. Zhou, C. H. Liu, J. Zeng, H. L. Zhang, and Y. Peng, Improving gas sensing properties of graphene by introducing dopants and defects: A first-principles study, Nanotechnology 20 (2009) 185504.

[21] I. Choudhuri, N. Patra, A. Mahata, R. Ahuja, and B. Pathak, B–N@graphene: highly sensitive and selective gas sensor, J. Phys. Chem. C. 119 (2015) 24827–24836.

[22] S. Yang, G. Lei, H. Xu, B. Xu, H. Li, Z. Lan, Z. Wang, and H. Gu, A DFT study of CO adsorption on the pristine, defective, In-doped and Sb-doped graphene and the effect of the applied electric field, Appl. Surf. Sci. 480 (2019) 205–211.

[23] J. Ni, M. Quintana, and S. Song, Adsorption of small gas molecules on transition metal (Fe, Ni and Co, Cu) doped graphene: A systematic DFT study, Phys. E. 116 (2020) 113768.

[24] L. S. Panchakarla, K. S. Subrahmanyam, S. K. Saha, A. Govindaraj, H. R. Krishnamurthy, U. V. Waghmare, and C. N. R. Rao, Synthesis, structure, and properties of boron- and nitrogen-doped graphene, Adv. Mater. 21 (2009) 4726–4730.

[25] D. Wei, Y. Liu, Y. Wang, H. Zhang, L. Huang, and G. Yu, Synthesis of n-doped graphene by chemical vapor deposition and its electrical properties, Nano Lett. 9 (2009) 1752–1758.

[26] J. Nakamura, J. Ito, and A. Natori, Structural bistability of the oxygen-adsorbed graphene sheet, J. Phys.: Conf. Ser. 100 (2008) 052019.

[27] C. W. Chen, S. C. Hung, M. D. Yang, C. W. Yeh, C. H. Wu, G. C. Chi, F. Ren, and S. J. Pearton, Oxygen sensors made by monolayer graphene under room temperature, Appl. Phys. Lett. 99 (2011) 243502.

[28] S. Rumyantsev, G. Liu, M. S. Shur, R. A. Potyrailo, and A. A. Balandin, Selective gas sensing with a single pristine graphene transistor, Nano Lett. 12 (2012) 2294–2298.

[29] F. R. Bagsican, A. Winchester, S. Ghosh, X. Zhang, L. Ma, M. Wang, H. Murakami, S. Talapatra, R. Vajtai, P. M. Ajayan, J. Kono, M. Tonouchi, and I. Kawayama, Adsorption energy of oxygen molecules on graphene and two-dimensional tungsten disulfide, Sci Rep. 7 (2017) 1774-1782.

[30] Y. Zou, F. Li, Z. H. Zhu, M. W. Zhao, X. G. Xu, and X. Y. Su, An ab initio study on gas sensing properties of graphene and Si-doped graphene, Eur. Phys. J. B 81 (2011) 475–479.

[31] H. Shin, Y. Luo, and A. Benali, Diffusion Monte Carlo study of O_2 adsorption on single layer graphene, Phys. Rev. B. 100 (2019) 075430.

[32] A. Pramanik, and H. S. Kang, Density functional theory study of O_2 and NO adsorption on heteroatom-doped graphenes including the van der Waals interaction, J. Phys. Chem. C. 115 (2011) 10971–10978.

[33] Y. Chena, X. C. Yang, Y. Liua, J. Zhaoa, Q. Cai, and X. Wang, Can Si-doped graphene activate or dissociate O_2 molecule? J. Mol. Graph. 39 (2013) 126–132.

[34] F. Mehmood, R. Pachter, W. Lu, and J. J. Boeckl, Adsorption and diffusion of oxygen on single-layer graphene with topological defects, J. Phys. Chem. C 117 (2013) 10366–10374.

[35] X. Zhu, K. Liu, Z. Lu, Y. Xu, S. Qi, and G. Zhang, Effect of oxygen atoms on graphene: adsorption and doping, Physica E. 117 (2020) 113827.

[36] L. H. Qu, X. L. Fu, C. G. Zhong, P. X. Zhou, and J. M. Zhang, Equibiaxial strained oxygen adsorption on pristine graphene, nitrogen/boron doped graphene, and defected graphene, Materials. 13 (2020) 4945-4953.

[37] J. Yan, B. Xu, S. Q. Shi, and C. Y. Ouyang, First-principles study of the oxygen adsorption and dissociation on graphene and nitrogen doped graphene for Li-air batteries, J. Appl. Phys. 112 (2012) 104316.

[38] K. Kinoshita, T. Saito, A. Ito, T. Kawakami, Y. Kitagawa, S. Yamanaka, K. Yamaguchi, and M. Okumura, Theoretical study on singlet oxygen adsorption onto surface of graphene-like aromatic hydrocarbon molecules, Polyhedron 30 (2011) 3249-3253.

[39] K. A. L. Lima, M. L. Pereira Jr, F. F. Monteiro, L. F. Roncaratti, and L. A. Ribeiro Jr, O_2 adsorption on defective Penta-Graphene lattices: A DFT study, Chem. Phys. Lett. 763 (2021) 138229.

[40] T. Saito, S. Nishihara, Y. Kataoka, Y. Nakanishi, T. Matsui, Y. Kitagawa, T. Kawakami, M. Okumura, and K. Yamaguchi, Transition state optimization based on approximate spin-projection (AP) method, Chem. Phys. Lett. 483 (2009) 168-176.

[41] K. Momma, and F. Izumi, "VESTA 3 for three-dimensional visualization of crystal, volumetric and morphology data," J. Appl. Crystallogr. 44 (2011) 1272-1276.

[42] Z. Zhang, P. Ma, L. Luo, X. Ding, S. Zhou and J. Zeng, Regulating spin states in oxygen electrocatalysis, Angew. Chem., Int. Ed., 2023, 62, e202216837.

Chapter 6

[1] S. A. Kharitonov, Biomarkers of some pulmonary diseases in exhaled breath, Biomarkers. 7 (2002) 1–32.

[2] K. Sawicka, P. Gouma, S. Simon, Electrospun biocomposite nanofibers for urea biosensing, Sens. Actuators B Chem., 108 (2005) 585–588.

[3] A. Srivastava, C. Bhat, S. K. Jain, P. K. Mishra, R. Brajpuriya, Electronic transport properties of BN sheet on adsorption of ammonia (NH_3) gas, J Mol Model. 21 (2015) 39–47.

[4] M. S. Khan, A. Srivastava, R. Chaurasiya, P. Dua, NH_3 and PH_3 adsorption through single walled ZnS nanotube: First principle insight, Chem. Phys. Lett. 636 (2015) 103–109.

[5] W. Wang, Y. Zhang, C. Shen and Y. Chai, Adsorption of CO molecules on doped graphene: a first-principles study, AIP Adv. 6 (2016) 025317–025322.

[6] O. Leenaerts, B. Partoens, F. Peeters, Adsorption of H_2O, NH_3, CO, NO_2, and NO on graphene: A first-principles study, Phys. Rev. B. 77 (2008) 125416.

[7] R. Miller, R. Outlaw, B. Holloway, Graphene double-layer capacitor with ac line-filtering performance, Science 329 (2010) 1637-1639.

[8] E. McCann, M. Koshino, The electronic properties of bilayer graphene, Rep. Prog. Phys. 76 (2013) 056503.

[9] M. Alattas, U. Schwingenschlögl, Band gap control in bilayer graphene by co-doping with B-N pairs, Sci Rep. 8 (2018) 1–6.

[10] C. Berger, Z. Song, X. Li, Electronic confinement and coherence in patterned epitaxial grapheme, Science. 312 (2006) 1191-1196.

[11] F. Schedin, A. K. Geim, S. V. Morozov, E. W. Hill, P. Blake, M. I. Katsnelson, K. S. Novoselov, Detection of individual gas molecules adsorbed on graphene, Nat. Mater. 6 (2007) 652-655.

[12] F. Shayeganfar, Energy gap tuning of graphene layers with single molecular F_2 adsorption, J. Phys. Chem. C. 119 (2015) 12681-12689.

[13] L. Kong, A. Enders, T. S. Rahman, P. A. Dowben, Molecular adsorption on graphene, J. Phys. Condens. Matar. 26 (2014) 443001.

[14] J. Dai, J. Yuan, P. Giannozzi, Gas adsorption on graphene doped with B, N, Al, and S: A theoretical study, Appl. Phys. Lett. 95 (2009) 232105.

[15] Y. Wang, Y. Shao, D. W. Matson, J. Li, Y. Lin, Nitrogen-doped graphene and its application in electrochemical biosensing, ACS nano. 4 (2010) 1790-1798.

[16] J. R. Williams, L. DiCarlo, C. M. Marcus, Quantum Hall effect in a gate-controlled p-n junction of graphene, Science. 317 (2007) 638-641.

[17] A. F. Young, P. Kim, Quantum interference and Klein tunnelling in graphene heterojunctions, Nat. Phys. 5 (2009) 222-226.

[18] E. Akbari, R. Yusof, M. T. Ahmadi, A. Enzevaee, M. J. Kiani, Bilayer graphene application on NO_2 sensor modelling, J. Nanomater. 7 (2014) 534105.

[19] Y. Fujimoto, S. Saito, Electronic structures and stabilities of bilayer graphene doped with boron and nitrogen, Surf. Sci. 634 (2015) 57-61.

[20] Y. Fujimoto, S. Saito, Gas adsorption, energetics and electronic properties of boron-and nitrogen-doped bilayer graphenes, Chem. Phys. 478 (2016) 55-61.

[21] M. L. Ould NE, M. Boujnah, A. Benyoussef, A. El Kenz, Electronic and electrical conductivity of ab and aa-stacked bilayer graphene with tunable layer separation, J. Supercond Nov Magn. 30 (2017) 1263–1267.

[22] M. Junaid and G. Witjaksono, Analysis of band gap in AA and AB stacked bilayer graphene by hamiltonian tight binding method, IEEE International Conference on Sensors and Nanotechnology (2019) 1-4.

[23] H. Santos, L. Henrard, Fluorine adsorption on single and bilayer graphene: role of sublattice and layer decoupling, J. Phys. Chem. C. 118 (2014) 27074-27080.

[24] R. M. Ribeiro, N. M. R. Peres, J. Coutinho, P. R. Briddon, Inducing energy gaps in monolayer and bilayer graphene: local density approximation calculations, Phys. Rev. B. 78 (2008) 075442.

[25] J. Sun, M. Muruganathan, H. Mizuta, Room temperature detection of individual molecular physisorption using suspended bilayer graphene, Sci. Adv. 2 (2016) e1501518.

[26] R. E. Mapasha, A. M. Ukpong, N. Chetty, *Ab initio* studies of hydrogen adatoms on bilayer graphene, Phys. Rev. B. 85 (2012) 205402.

[27] N. M. Caffrey, R. Armiento, R. Yakimova, I. A. Abrikosov, Changes in work function due to NO_2 adsorption on monolayer and bilayer epitaxial graphene on SiC (0001), Phys. Rev. B. 94 (2016) 205411.

[28] Y. Tang, Z. Liu, Z. Shen, W. Chen, D. Ma, X. Dai, Adsorption sensitivity of metal atom decorated bilayer graphene toward toxic gas molecules (CO, NO, SO_2 and HCN), Sens. Actuators B Chem. 238 (2017) 182-195.

[29] J. K. Lee, S. C. Lee, J. P. Ahn, The growth of AA graphite on (111) diamond, J. Chem. Phys. 129 (2008) 234709.

[30] T. Vikramaditya, K. Sumithra, Effect of substitutionally boron-doped single-walled semiconducting zigzag carbon nanotubes on ammonia adsorption, J. Comput. Chem. 35 (2014) 586–59.

[31] K. Momma, F. Izumi, VESTA 3 for three-dimensional visualization of crystal, volumetric, and morphology data. J. Appl. Crystallog. 44 (2011) 1272-1276.

Chapter 7

[1] M. Xu, T. Liang, M. Shi, H. Chen, Graphene-like two-dimensional materials, Chem. Rev. 113 (2013) 3766–3798.

[2] J. Lelieveld, J. S. Evans, M. Fnais, D. Giannadaki, A. Pozzer, The contribution of outdoor air pollution sources to premature mortality on a global scale, Nature. 525 (2015) 367–371.

[3] A. Hashmi, J. Hong, Transition metal doped phosphorene: First-principles study, J. Phys.

Chem. C. 119 (2015) 9198–9204.

[4] T. Hu, J. Hong, First-principles study of metal adatom adsorption on black phosphorene, J. Phys. Chem. C. 119 (2015) 8199–8207.

[5] N. Suvansinpan, F. Hussain, G. Zhang, C. H. Chiu, Y. Cai, Y. W. W. Zhang, Substitutionally doped phosphorene: electronic properties and gas sensing, Nanotechnology. 27 (2016) 065708.

[6] Y. Tang, Z. Liu, Z. Shen, W. Chen, D. Ma, X. Dai, Adsorption sensitivity of metal atom decorated bilayer graphene toward toxic gas molecules (CO, NO, SO_2 and HCN), Sensors Actuators, B Chem. 238 (2017) 182–195.

[7] L. Li, Y. Yu, G. J. Ye, Q. Ge, X. Ou, H. Wu, D. Feng, X. H. Chen, Y. Zhang, Black phosphorus field-effect transistors, Nat. Nanotechnol. 9 (2014) 372–377.

[8] H. Liu, A.T. Neal, Z. Zhu, Z. Luo, X. Xu, D. Tománek, P. D. Ye, Phosphorene: An unexplored 2D semi-conductor with a high hole mobility, ACS Nano. 8 (2014) 4033–4041.

[9] J. Qiao, X. Kong, Z. X. Hu, F. Yang, W. Ji, High-mobility transport anisotropy and linear dichroism in few-layer black phosphorus, Nat. Commun. 5 (2014) 4475-4483.

[10] W. Lei, D. Portehault, D. Liu, S. Qin, Y. Chen, Porous boron nitride nanosheets for effective water cleaning, Nat. Commun. 4 (2013) 1777-1786.

[11] F. Xia, H. Wang, Y. Jia, Rediscovering black phosphorus as an anisotropic layered material for optoelectronics and electronics, Nat. Commun. 5 (2014) 4458-4463.

[12] R. Fei, L. Yang, Strain-engineering the anisotropic electrical conductance of few-layer black phosphorus, Nano Lett. 14 (2014) 2884–2889.

[13] J. Dai, X. C. Zeng, Bilayer phosphorene: Effect of stacking order on bandgap and its potential applications in thin-film solar cells, J. Phys. Chem. Lett. 5 (2014) 1289–1293.

[14] H. Guo, N. Lu, J. Dai, X. Wu, X. C. Zeng, Phosphorene nanoribbons, phosphorus

nanotubes, and van der Waals multilayers, J. Phys. Chem. C. 118 (2014) 14051–14059.

[15] Y. Cai, G. Zhang, Y. W. Zhang, Layer-dependent band alignment and work function of few-layer phosphorene, Sci. Rep. 4 (2014) 6677-6685.

[16] Q. Wei, X. Peng, Superior mechanical flexibility of phosphorene and few-layer black phosphorus, Appl. Phys. Lett. 104 (2014) 251915-251923.

[17] R. Fei, A. Faghaninia, R. Soklaski, J. A. Yan, C. Lo, L. Yang, Enhanced thermoelectric efficiency via orthogonal electrical and thermal conductances in phosphorene, Nano Lett. 14 (2014) 6393–6399.

[18] Y. Cai, Q. Ke, G. Zhang, Y. P. Feng, V. B. Shenoy, Y. Zhang, Giant phononic anisotropy and unusual anharmonicity of phosphorene: Interlayer coupling and strain engineering, Adv. Funct. Mater. 25 (2015) 2230–2236.

[19] Y. Du, H. Liu, Y. Deng, P. D. Ye, Device perspective for black phosphorus field-effect transistors: Contact resistance, ambipolar behavior, and scaling, ACS Nano. 8 (2014) 10035–10042.

[20] S. Zhao, W. Kang, J. Xue, The potential application of phosphorene as an anode material in Li-ion batteries, J. Mater. Chem. A. 2 (2014) 19046–19052.

[21] L. Zhou, J. Zhang, Z. Zhuo, L. Kou, W. Ma, B. Shao, A. Du, S. Meng, T. Frauenheim, Novel excitonic solar cells in phosphorene-TiO_2 heterostructures with extraordinary charge separation efficiency, J. Phys. Chem. Lett. 7 (2016) 1880–1887.

[22] M. Z. Rahman, C. W. Kwong, K. Davey, S. Z. Qiao, 2D phosphorene as a water splitting photocatalyst: fundamentals to applications, Energy Environ. Sci. 9 (2016) 709–728.

[23] R. Babar, M. Kabir, Transition metal and vacancy defect complexes in phosphorene: A spintronic perspective, J. Phys. Chem. C. 120 (2016) 14991–15000.

[24] A. N. Abbas, B. Liu, L. Chen, Y. Ma, S. Cong, N. Aroonyadet, M. Ko, M. Köpf, T. Nilges, C. Zhou, Black Phosphorus Gas Sensors, ACS Nano. 9 (2015) 5618–5624.

[25] S. Cui, H. Pu, S. A. Wells, Z. Wen, S. Mao, J. Chang, M. C. Hersam, J. Chen, Ultrahigh sensitivity and layer-dependent sensing performance of phosphorene-based gas sensors, Nat. Commun. 6 (2015) 8632-8648.

[26] A. Sibari, Z. Kerrami, A. Kara, M. Hamedoun, A. Benyoussef, O. Mounkachi, M. Benaissa, Adsorption and diffusion on a phosphorene monolayer: a DFT study, J. Solid State Electrochem. 22 (2018) 11–16.

[27] Y. Wang, A. Pham, S. Li, J. Yi, Electronic and magnetic properties of transition-metal-doped monolayer black phosphorus by defect engineering, J. Phys. Chem. C. 120 (2016) 9773–9779.

[28] C. Zhai, X. Dai, W. Li, Y. Ma, T. Wang, Y. Tang, Strain tuning of magnetism in transition-metal atom doped phosphorene, Superlattices Microstruct. 101 (2017) 49–56.

[29] W. Yu, Z. Zhu, C. Y. Niu, C. Li, J. H. Cho, Y. Jia, Dilute magnetic semi-conductor and half-metal behaviors in 3d transition-metal doped black and blue phosphorenes: A first-principles study, Nanoscale Res. Lett. 11 (2016) 77-86.

[30] Y. Ding, Y. Wang, Structural, electronic, and magnetic properties of adatom adsorptions on black and blue phosphorene: A first-principles study, J. Phys. Chem. C. 119 (2015) 10610–10622.

[31] L. Goulart, L. da S. Fernandes, C. Lange dos Santos, J. Rossato, Electronic and structural properties of black phosphorene doped with Si, B and N, Phys. Lett. Sect. A Gen. At. Solid State Phys. 383 (2019) 125945-125956.

[32] W. Yu, Z. Zhu, C. Y. Niu, C. Li, J. H. Cho, Y. Jia, Anomalous doping effect in black phosphorene using first-principles calculations, Phys. Chem. Chem. Phys. 17 (2015) 16351–16358.

[33] L. Yang, W. Mi, X. Wang, Tailoring magnetism of black phosphorene doped with B, C, N, O, F, S and Se atom: A DFT calculation, J. Alloys Compd. 662 (2016) 528–533.

[34] L. Seixas, A. Carvalho, A. H. Castro Neto, Atomically thin dilute magnetism in Co-doped phosphorene, Phys. Rev. B. 91 (2015) 155138-155149.

[35] C. Guo, C. Xia, L. Fang, T. Wang, Y. Liu, Tuning anisotropic electronic transport properties of phosphorene: Via substitutional doping, Phys. Chem. Chem. Phys. 18 (2016) 25869–25878.

[36] Y. Guo, J. Robertson, Vacancy and Doping States in Monolayer and bulk Black Phosphorus, Sci. Rep. 5 (2015) 14165-14178.

[37] Q. Yang, R. S. Meng, J. K. Jiang, Q. H. Liang, C. J. Tan, M. Cai, X. Sun, D. G. Yang, T. L. Ren, X. P. Chen, First-Principles Study of Sulfur Dioxide Sensor Based on Phosphorenes, IEEE Electron Device Lett. 37 (2016) 660–662.

[38] P. Pyykkö, M. Atsumi, Molecular single-bond covalent radii for elements 1-118, Chem. - A Eur. J. 15 (2009) 186–197.

[39] Y. Jiang, J. B. Adams, First principle calculations of benzotriazole adsorption onto clean Cu (1 1 1), Surf. Sci. 529 (2003) 428–442.

[40] L. Bin Shi, Y. P. Wang, H. K. Dong, First-principle study of structural, electronic, vibrational and magnetic properties of HCN adsorbed graphene doped with Cr, Mn and Fe, Appl. Surf. Sci. 329 (2015) 330–336.

List of publications

- **A. Sahithi** and K. Sumithra

Adsorption and sensing of CO and NH_3 on chemically modified graphene surfaces, RSC Advances, 2020, 10, 42318–42326.

- **A. Sahithi** and K. Sumithra,

New insights in the electronic structure of doped graphene on adsorption with oxides of nitrogen, Materials Today Communications, 2021, 27, 102417.

- **A. Sahithi** and K. Sumithra

Adsorption of ammonia on p-doped graphene bilayer surface: Energetics and electronic Structure. Advances in Computational Modeling and Simulation. Lecture Notes in Mechanical Engineering. Springer Nature, Singapore., 2022, 1-13.

- **A. Sahithi** and K. Sumithra

Adsorption of singlet and triplet oxygen on B-doped graphene: Adsorption and electronic characteristics, RSC Advances, 2023, 13, 20868–20875.

- **A. Sahithi** and K. Sumithra

A first-principles research on adsorption of hydrogen cyanide and hydrogen isocyanides on non-metallic atom substituted phosphorene. (under communication)

List of Conferences

- **A. Sahithi**, K. Sumithra (Poster presentation)

Adsorption of gases on Boron and Nitrogen doped graphenes: A Computational study.

National Symposium on "Convergence of Chemistry & Materials". CCM-2019

BITS- PILANI, Hyderabad campus, Hyderabad, 17-18th DEC 2019.

- **A. Sahithi**, K. Sumithra (Poster presentation)

Computational study of adsorption of some gaseous moieties on chemically modified graphene. NFCFA- National conference on "new frontiers in chemistry –from fundamentals to applications-III, Birla Institute of Technology and Science, Pilani- K. K. Birla Goa Campus, Goa, 20-22nd DEC 2019.

- **A. Sahithi**, K. Sumithra (Oral presentation)

National Conference on Frontiers in Medicinal Chemistry and Nanochemistry. Directorate of Higher Education, Government of Goa, Goa, 14th- 15th February 2020.

- **A. Sahithi**, K. Sumithra (Poster presentation)

The adsorption and sensing of NO, N_2O and NO_2 on chemically modified graphene surfaces. DAE Symposium on Current Trends in Theoretical Chemistry (CTTC-2020) Conference Room, Training School Hostel, Anushaktinagar, Mumbai Organised by Chemistry Division, Bhabha Atomic Research Centre Mumbai, India In Association with Society for Materials Chemistry, Mumbai, India September 23-25, 2021.

- **A. Sahithi**, K. Sumithra (Poster presentation)

A first-principles study of gas sensing properties of NO, NO_2, N_2O gases on chemically modified graphene. 17th Theoretical Chemistry Symposium (TCS 2021), under the joint auspices of IISER Kolkata, IACS Kolkata, University of Kalyani and S.N Bose National Centre for Basic Sciences Kolkata. December 11-14, 2021.

- **A. Sahithi**, K. Sumithra (Poster presentation)

Ab initio study of gap opening and gas adsorption on p-doped bilayer graphene. The National Conference on Molecular Modelling and Simulations (NCMMS 2022), under the auspices of VIT Bhopal University, Bhopal, February 28 - March 02, 2022.

- **A. Sahithi**, K. Sumithra (Poster presentation)

Adsorption of molecular oxygen on B-doped graphene: Triplet and singlet electronic properties. International Conference on Energy Conversion and Storage(IECS-2023) was held in Chennai, IIT madras, 18-20 January-2023.

- **A. Sahithi**, K. Sumithra (Poster presentation)

Adsorption of singlet and triplet oxygen on chemically altered graphene surface. National Symposium on "Convergence of Chemistry & Materials". CCM-2023, BITS- PILANI, Hyderabad campus, Hyderabad, January 6-7, 2023.

Biography of Ms. Andru Sahithi

Ms. A. Sahithi was born in Hanumakonda (HNK), Hanamkonda District, Telangana. She completed her Bachelor of Science (B.Sc., with Biotechnology, Zoology and Chemistry) in 2016 from Kakatiya University, Warangal and Master of Science in Organic chemistry in the year 2018 from University College of Sciences, Osmania University Campus, Hyderabad, Telangana State. From Mid 2018-2019 she worked as project assistant in Indian Institute of Chemical Technology (CSIR-IICT), Hyderabad, Telangana.

She joined the department of chemistry, BITS-Pilani, Hyderabad campus for her doctoral research work in Computational Chemistry division under the supervision of Prof. K. Sumithra in 2019. During her doctoral study, she received a fellowship from BITS-Pilani, Hyderabad campus. She has published scientific publications in well-renowned international journals and a book chapter in Springer Nature. She also presented papers at various national and international conferences in India. Her research interests are adsorption studies of 2D materials and van der Waals nanostructures in sensor applications and also studying the optical and conductivity properties of various gas molecules which find applications in gas sensors and solar cells employing electronic structure calculations.

Biography of Prof. K. Sumithra

Prof. K. Sumithra is presently working as a professor in the Department of Chemistry at Birla Institute of Technology and Science, Pilani Hyderabad Campus, India, where she joined in July 2009. She received her Doctoral degree from Cochin University of Science and Technology, Cochin, Kerala, under the supervision of Prof. K. L. Sebastian. Her Ph.D. thesis is on the Statistical mechanics of polymer chains in disordered media and their adsorption on random surfaces. After Ph.D., she worked briefly as a lecturer and has worked in various institutes in Germany as a postdoctoral researcher on Monte Carlo simulations of polymer adsorption. After this, she worked in Martin Luther University on a C1 position equivalent to Assistant Professor in the Theoretical Physics division for six years.

She has been involved in teaching and research for the past 15 years. At present, she is working on Computational Material Science. Her research concentrates on adsorption on carbon nanotubes, Electronic structure calculations of organic semiconducting oligomeric and polymeric systems, etc. Her current research is adsorption studies on van der Waals 2D materials and chemically altered nano surfaces. She has published several research articles in various peer-reviewed international journals. She has also completed projects funded by DST and CSIR.